Development of the Numerical Simulation Method for Rocky Body Impacts and Theoretical Analysis of Asteroidal Shapes (固体天体衝突現象を扱う数値計算法の開発と小惑星形状の成因の理論的解析)

Keisuke Sugiura

Laboratory for Theoretical Astronomy & Astrophysics (Ta-Lab)
Department of Physics, Nagoya University
Furo-cho, Chikusa-ku, Nagoya, Aichi, 464-8602, Japan

February 8, 2019

Abstract

Many asteroids exist between the orbits of Mars and Jupiter in the present solar system. Asteroids are the remnants of minor bodies that existed in the primordial environment, and they are fossils holding information of the planet formation era since they do not experience significant melting thanks to those small sizes. Thus the detailed researches of asteroids lead to clarify the history of the solar system.

As we notice from the elongated shape of the asteroid Itokawa observed by the spacecraft Hayabusa, asteroids have not only spherical shapes but also variety of shapes. Now we know the shapes of about the 1,600 asteroids owing to the detailed light-curve observations. Since the shapes of asteroids are mainly formed through asteroidal collisions, we can statistically discuss the collisional history of asteroids if we clarify the relationship between impact conditions and the shapes of impact outcomes. Previous studies investigated the impact conditions of the collisions that produce the several asteroidal shapes, but they do not provide the comprehensive relationship between impact conditions and the shapes of impact outcomes. Thus, we conducted numerical simulations of impacts between rocky asteroids with various impact conditions and investigated the shapes of impact outcomes.

Firstly, we developed the numerical simulation code that treats rocky body impact phenomena. We developed the numerical simulation code based on the Smoothed Particle Hydrodynamics (SPH) method for elastic dynamics since particle methods are suitable for problems involving large deformation such as impacts. The SPH method for elastic dynamics has difficulty to treat tension dominated regions due to a numerical instability. We developed a new method to solve the numerical instability using the knowledge provided by the Godunov SPH method (Inutsuka 2002). To reproduce collisional destruction of rocky bodies and gravitational reaccumulation of fragments, we also introduced the self gravity, the model of fracture of rocky material (Benz and Asphaug 1995), and the model of friction of completely damaged rock (Jutzi 2015). Moreover, we parallelized our simulation code utilizing Framework for Developing Particle Simulator developed by RIKEN (Iwasawa et al. 2015, 2016), which enables massive parallel computing or wide parameter survey using supercomputers.

Secondly, to compare with the shapes of actual asteroids with diameters larger than 100 km, we reproduced the impacts with the target rocky asteroids with the diameter of 100 km. We conducted the impact simulations with the impact velocities of several 100 m/s that are realized in the planet formation era. As a result, we found that the similar-mass impacts with the mass

ratios of two impacting bodies larger than 0.5 produce various shapes including extremely flat shapes of the largest remnants, while those with the mass ratios smaller than 0.5 produce only spherical shapes with the ratio of the minor to major axis lengths larger than 0.5. Next, we conducted the impact simulations with the impact velocities of several km/s that are realized in the present solar system. As a result, we found that the impacts with the mass ratio of 1/64, which result in non-destructive impacts, only produce spherical shapes of the largest remnants with the ratio of the minor to major axis lengths larger than 0.7, and the similar-mass impacts with the mass ratios larger than 1/8, which mainly result in destructive impacts, only produce spherical or bilobed shapes. Therefore, we expect that flat shapes are produced only by low-velocity and similar-mass impacts in the primordial environment. To verify our prediction, we analyzed the shape models of actual asteroids obtained from Database of Asteroid Models from Inversion Technique, and investigated the shapes of family asteroids and non-family asteroids separately. Note that family asteroids are mainly produced by recent destructive impacts. We found that there are no flat family asteroids with the diameter larger than 100 km, while there are several flat non-family asteroids. We also found that the fraction of flat non-family asteroids larger than 10 km is more than twice as large as that of family asteroids. This suggests that flat asteroids are likely to be formed in the primordial environment, and especially flat asteroids larger than 100 km were formed in the planet formation era and remain the same until today.

Thirdly, we investigated impact conditions of collisions that produce the extremely elongated shape of 1I/′Oumuamua, which was found on October 2017. 1I/′Oumuamua has the mean radius of about 100 m, and the large light-curve amplitude of 1I/′Oumuamua suggests that this object has the elongated shape with the ratio of the intermediate to major axis lengths less than 0.3. To reproduce the extremely elongated shape of 1I/′Oumuamua, we conducted the impact simulations with the 50 m-sized rubble pile targets with various impact velocities, impact angles, mass ratios of two impacting bodies, and friction angles. As a result, we found that the formation of the extremely elongated shapes with the axis ratio less than 0.3 roughly requires the impact velocity less than 40 cm/s, the impact angle less than 30°, the mass ratio larger than 0.5, and the friction angle larger than 40°. This impact velocity is realized in the extremely primordial protoplanetary disks without the planetesimals with the radius larger than 7 km. Thus, 1I/′Oumuamua might have been formed in such an extremely primordial protoplanetary disk, then might have been ejected from the planetary system due to, for example, a stellar encounter, and then visited our solar system.

Contents

Chapter 1

Introduction

1.1 Asteroids in the Solar System

Our solar system is mainly composed of the planets orbiting around the sun. The solar system has eight planets, that is, Mercury, Venus, the Earth, Mars, Jupiter, Saturn, Uranus, and Neptune. They are the major bodies orbiting around the sun and account for the almost all mass of the solar system. However, not only the planets but also other minor bodies are orbiting around the sun. The minor objects include asteroids, comets, and trans-neptunian objects.

The number of the minor bodies in the solar system is clearly much larger than that of the major bodies. Especially, great number of asteroids are found so far. According to Small Body Database Search Engine of Jet Propulsion Laboratory[1], the number of all asteroids with known orbits is about 800,000. Even the number of the asteroids with the diameters larger than 1 km is more than 100,000. The largest asteroid (1) Ceres, which was discovered by Giuseppe Piazzi on 1801, has the diameter of about $1,000$ km (Note that (1) Ceres is no longer the asteroid but now classified to the dwarf planet). Thus more than 100,000 asteroids with the diameters of $1-1,000$ km are observed, and we can achieve statistical information regarding to the properties of the solar system from asteroids.

Figure 1.1 shows the positions of the inner six planets and the asteroids with the diameter larger than 1 km. It is clear at a glance that asteroids mainly exist between the orbits of Mars and Jupiter. The region where asteroids mainly exist is called the main belt, and the asteroids in this region are called main-belt asteroids. We also notice that there are two groups of asteroids existing in the Lagrange points of Jupiter. These asteroids are called Jupiter trojans. There are some asteroids that have the orbits close to that of the Earth. These asteroids are called

[1] https://ssd.jpl.nasa.gov/sbdb_query.cgi#x

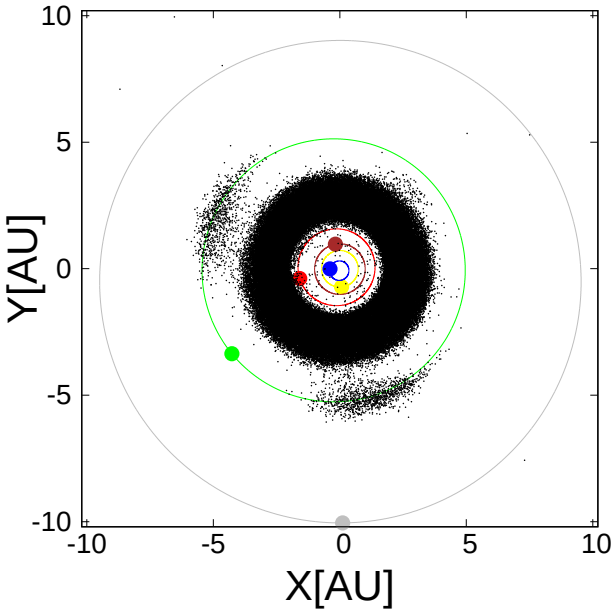

Figure 1.1: Positions of the inner six planets and the asteroids with the diameters larger than 1 km at 00:00:00 on 1st January, 2018. The orbits of the planets are indicated by the solid curves. The orbit of the Earth is on the XY plane, and X axis is in the direction of the vernal equinox. The positions and the orbits are calculated from the orbital elements of the planets and the asteroids obtained from Small Body Database Search Engine of Jet Propulsion Laboratory. The blue point and solid curve show the position and orbit of Mercury, the yellow ones show those of Venus, the brown ones show those of the Earth, the red ones show those of Mars, the green ones show those of Jupiter, and the gray ones show those of Saturn. The black dots show the positions of the asteroids.

near-Earth asteroids, which include the asteroids Itokawa and Ryugu visited by the spacecraft Hayabusa and Hayabusa 2. Almost all near-Earth asteroids have the diameters less than 10 km, and they are considered to be originated from the main belt through the migration due to the Yarkovsky effect or the scattering due to the planets (e.g., Binzel et al. 1992; Michel et al. 2005).

Figure 1.2 shows the incremental mass distribution of asteroids estimated using the diameters of asteroids obtained from Small Body Database Search Engine of Jet Propulsion Laboratory. From Fig. 1.2, we notice that the total mass of the asteroids with the diameters in each diameter bin increases with increasing the diameters of asteroids. We also notice that there is a peak of the mass around the diameter ≈ 100 km (see also Bottke et al. 2005; Kobayashi et al. 2016). Note that the two diameter bins with the diameter > 500 km in Fig. 1.2 include only three asteroids (Ceres, Pallas, and Vesta), and these points are statistically insignificant. Thus, the asteroids with the diameter ≈ 100 km account for large fraction of the total mass of

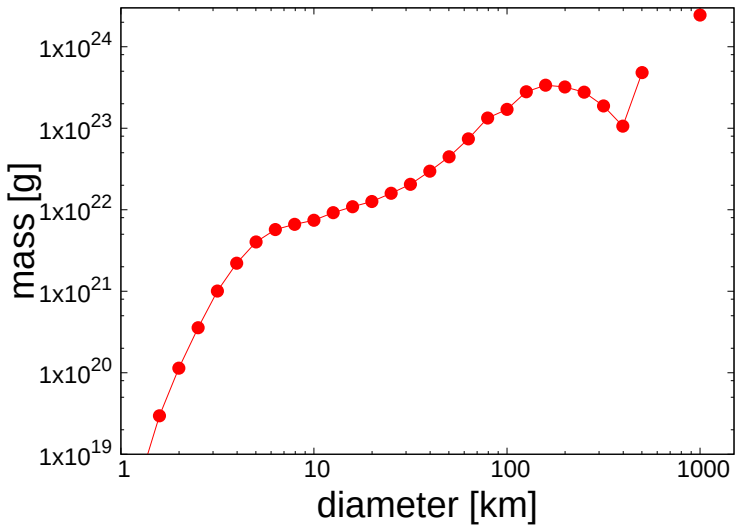

Figure 1.2: Incremental mass distribution of asteroids calculated from the diameters of the asteroids obtained from Small Body Database Search Engine of Jet Propulsion Laboratory. Here, we assume that the density of asteroids is $3\,\mathrm{g/cm^3}$. The horizontal axis represents the diameters of asteroids. Each point shows the diameter of the center of each diameter bin D_c, and each bin has the width of $D_c(10^{0.05} - 10^{-0.05})$. The vertical axis represents the total mass of the asteroids with the diameter in each diameter bin.

asteroids.

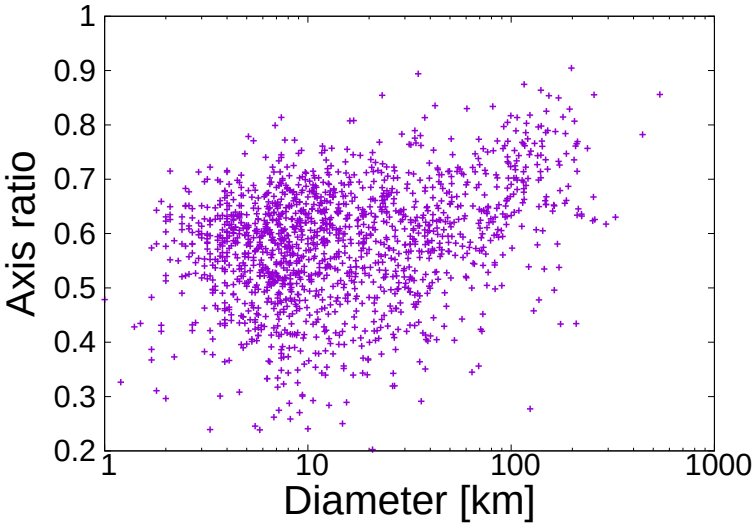

Figure 1.3: Axis ratios of asteroids obtained from the shape models stored in Database of Asteroid Models from Inversion Technique. The horizontal axis represents the diameters of asteroids, and the vertical axis represents the ratio of the minor to major axis lengths of asteroids. The axis ratios are measured through the bottom-up method (see Section 3.2).

The shapes of the planets or large satellites such as the moon are almost complete spheres. However, as we notice from the sea-otter shape of the asteroid Itokawa, many asteroids have irregular shapes that are different from spherical shapes. This is because material strength is dominant rather than the self gravity for small bodies such as asteroids (Hughes and Cole 1995; Lineweaver and Norman 2010). The shapes of asteroids are mainly measured using light curves, that is, luminosity variation of asteroids in time. The rotations of asteroids vary the cross section of asteroids with respect to observers, and this causes luminosity changes. Kaasalainen and Torppa (2001) and Kaasalainen et al. (2001) provide the novel technique that predicts the shapes of asteroids from the light curves of asteroids. The shape models of asteroids obtained from light curves are summarized in Database of Asteroid Models from Inversion Technique[2] (Ďurech et al. 2010). The shapes of asteroids are also measured by in-situ observations (e.g., Fujiwara et al. 2006), radar observations (e.g., Ostro et al. 2000), and the occultations of background stars due to asteroids (e.g., Satō et al. 2000), but the number of asteroidal shapes obtained from these methods is much smaller than those obtained from light curves. Fig. 1.3 shows the axis ratios of asteroids obtained from Database of Asteroid Models from Inversion Technique, and we notice that about half of asteroids have the irregular shapes with the ratio of the minor to major axis lengths less than 0.6.

There are several groups of asteroids that have similar proper orbital elements. Here, the proper orbital elements mean that quasi-invariants of motions of asteroids that are not affected by short-term perturbations such as the gravity from the gas giants (e.g., Knezevic et al. 2002). Groups of asteroids with similar proper orbital elements are called asteroid families. Japanese astronomer Kiyotsugu Hirayama firstly identified several asteroid families (Hirayama 1918), and thus asteroid families are also called Hirayama families. The asteroids in an asteroid family usually have similar spectral properties (e.g., Zappalá et al. 1995), so that the asteroids in a family are considered to be the fragments produced through collisional destruction of a parent body (e.g., Farinella et al. 1996).

There are several mechanisms that vary the proper orbital elements. One of them is the Yarkovsky effect (e.g., Farinella et al. 1998). The Yarkovsky effect mainly changes the orbital semi-major axis due to the torque induced by irradiation and the rotations of asteroids. The rotations of asteroids make differences between the directions of absorption of irradiation from the sun and the directions of re-emission of radiation, which exerts the torque on asteroids and causes the semi-major axis change. The Yarkovsky effect both increases and decreases

[2]http://astro.troja.mff.cuni.cz/projects/asteroids3D/web.php

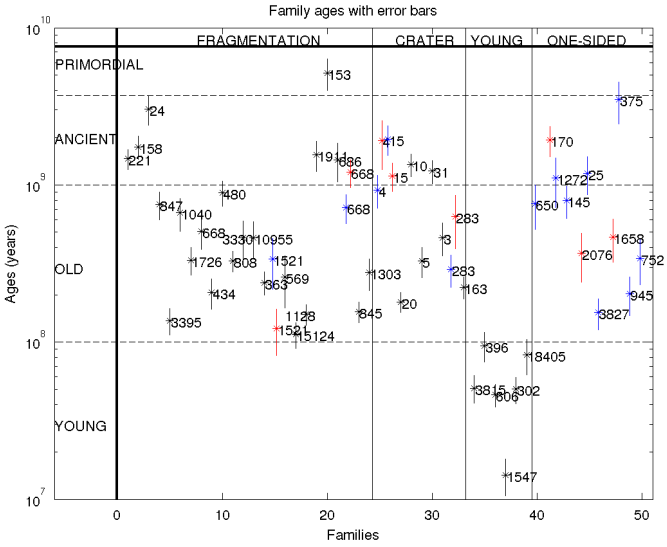

Figure 1.4: Ages of asteroid families estimated from the Yarkovsky "V-shape". The vertical axis represents the estimated ages of families, and the number nearby each plot indicates minor-planet designation of the largest member of each family. This figure is taken from Asteroid Dynamics Site 2 (http : //hamilton.dm.unipi.it/astdys2/fam_ages/index.html).

the semi-major axis depending on the direction of rotations, and is more effective for smaller asteroids, especially for the asteroids smaller than 10 km (Morbidelli and Vokrouhlický 2003). The Yarkovsky effect dissipates asteroids families for a very long period, and we can utilize this effect to measure the ages of asteroid families (Spoto et al. 2015). The semi-major axis change due to the Yarkovsky effect is faster for smaller asteroids, and thus if we plot the diameters and proper semi-major axes of the asteroids in a family on a graph that has the horizontal axis of the proper semi-major axis and the vertical axis of the inverse of the diameter, we can achieve "V-shape" occupied by the plots of asteroids. The opening angles of V-shapes are larger for older families, and thus the ages of asteroid families are estimated from the opening angles of V-shapes. Fig. 1.4 shows the estimated ages of asteroid families, and we notice that the most families have the ages younger than 1 Gyr, which is much shorter than the age of the solar system. Thus, asteroid families were mainly formed through recent asteroidal collisions.

Note that not all of asteroids were destructed by recent impacts but especially large asteroids may have the primordial origin. Fig. 1.5 shows the collisional lifetime of asteroids (or the timescale of the occurrence of destructive impacts) in the present main belt estimated in O'Brien and Greenberg (2005). From Fig. 1.5, we notice that the asteroids with the diameters larger than 100 km have the collisional lifetimes of about ten times longer than the age of the solar

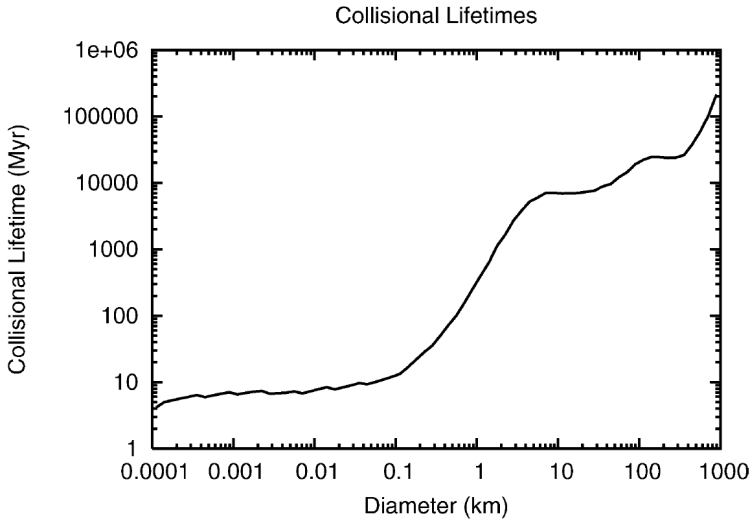

Figure 1.5: Collisional lifetime of asteroids (or the timescale of catastrophic disruptive impacts) in the present main belt. The horizontal axis represents the diameter of asteroids, and the vertical axis represents the collisional lifetime of asteroids with the diameter shown in the horizontal axis. This figure is taken from O'Brien and Greenberg (2005).

system. Thus these larger asteroids may be "fossils" of the primordial asteroids (Bottke et al. 2005). Fig. 1.5 also shows that the asteroids larger than 10 km have the collisional lifetime slightly longer than the age of the solar system, which means that some fraction of these asteroids may also be primordial.

1.2 Solar System Formation Scenario

Standard solar system formation scenarios are based on the model proposed by Safronov (1969) or the so-called Kyoto model proposed by Hayashi et al. (1985). Fig. 1.6 shows the schematic picture of the solar system formation scenario based on the Kyoto model. Planets are formed in a protoplanetary disk, which is composed of gas and solid dust particles. Gas is mainly composed of hydrogen and helium. The typical size of dust particles is considered to be sub micron, which is the typical size of interstellar dust particles (Mathis et al. 1977; Draine and Lee 1984). The existence of protoplanetary disks is already proved by many observations (e.g., Kitamura et al. 2002; Kwon et al. 2011), and nowadays Atacama Large Millimeter/submillimeter Array clarified even the spatial structures of the surface density of dust component for several protoplanetary disks (ALMA Partnership et al. 2015).

Dust particles grow up to be planetesimals, which are the bodies with the typical size

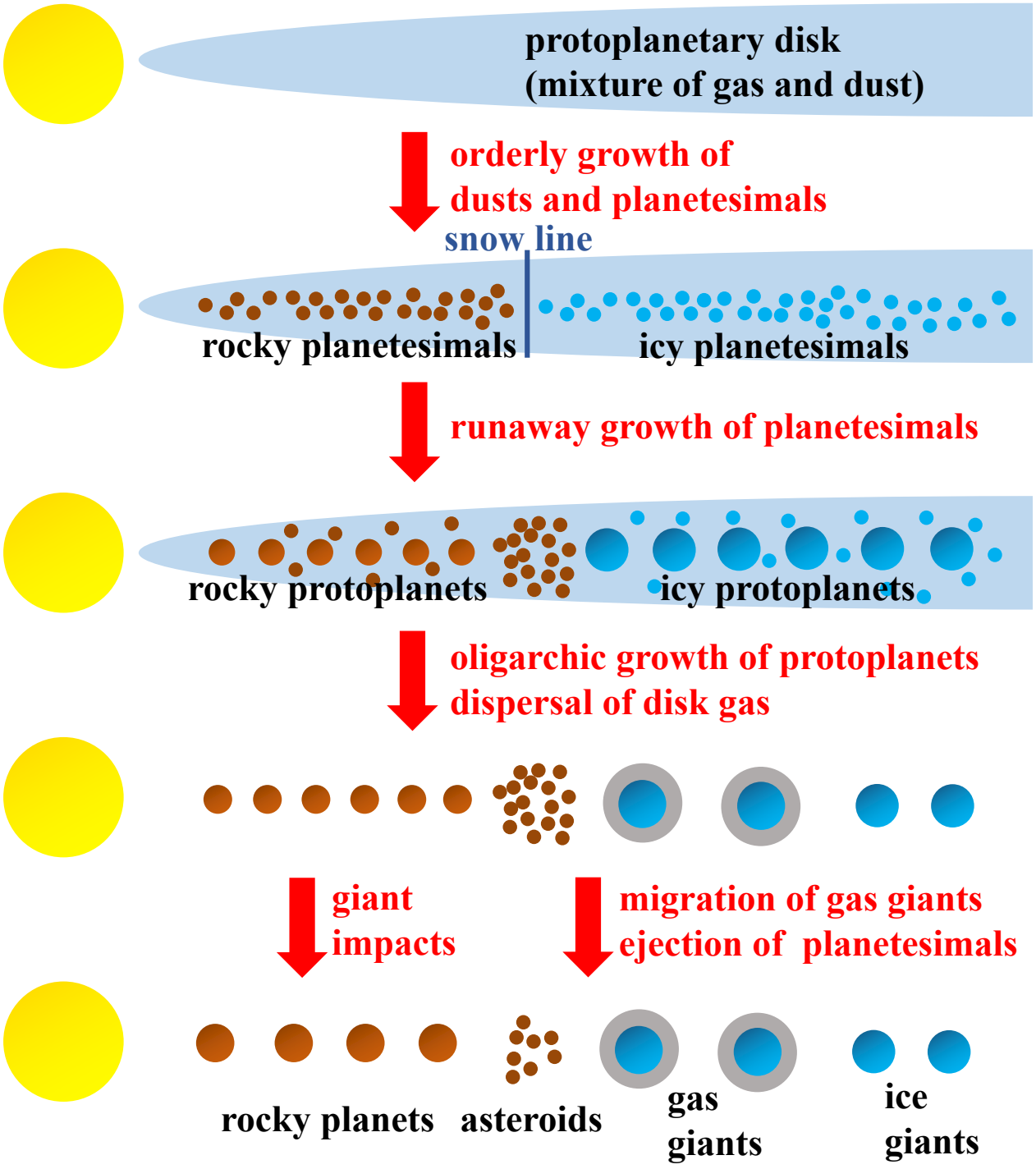

Figure 1.6: Schematic figure that shows the formation and evolution of the solar system.

of $1 - 100\,\mathrm{km}$, through collisional sticking of dust particles due to the van der Waals force. There are some difficulties for dust particles to grow to be planetesimals through collisional

coalescence, although we already found some mechanisms to avoid the difficulties. One of the difficulties is the radial drift problem. Gas component is orbiting around the sun with sub-Keplerian velocity because of radial gas-pressure gradient, and dust particles experience head wind and loose the angular momentum. If dust particles grow with keeping compact density, the timescale for the radial drift is shorter than the growth timescale when the size of compact dust reaches about 1 m (Weidenschilling 1977), which means that dust particles fall down to the central star before they grow to be planetesimals. However, collisional sticking of dust particles produces porous aggregates (e.g., Suyama et al. 2008), which accelerates the growth of dust particles to be faster than the radial drift (Okuzumi et al. 2012). Sufficiently grown dust aggregates are compressed through gas compression and self-gravity compression, and then planetesimals with the size ~ 1 km are formed (Kataoka et al. 2013). The radial drift problem is also overcome by the steaming instability (Johansen et al. 2014). The streaming instability produces overdense filaments composed of dust particles, and gravitational fragmentation of overdense regions directly produces planetesimals in a short timescale. The size of planetesimals produced through the streaming instability is estimated to be ~ 100 km.

Planetesimals grow through collisional coalescence of planetesimals, and here "glue" is the gravity between planetesimals. There are two types of the growth mode of planetesimals. If the relative velocity between planetesimals is smaller than the mutual escape velocity of planetesimals, the gravity is effective and collisional cross section is larger for larger planetesimals (gravitational focusing). This means that larger planetesimals grow faster than smaller ones, and smaller planetesimals are left behind the growth. This growth mode is called runaway growth (e.g., Wetherill and Stewart 1989; Kokubo and Ida 1996). In contrast, if the relative velocity is larger than the escape velocity, the gravity is not effective. In this case, the difference of the masses of two planetesimals decreases through the growth, and planetesimals with different masses grow with the similar growth rate. This growth mode is called orderly growth (e.g., Weidenschilling et al. 1997). In the orderly growth mode, the shape of the mass distribution of planetesimals merely shifts to massive side.

The relative velocity between the planetesimals with the radius larger than 1 km is mainly increased by the density fluctuation caused by turbulence (Ida et al. 2008; Okuzumi and Ormel 2013; Ormel and Okuzumi 2013), while the relative velocity is decreased by the collisional damping (e.g., Ohtsuki 1992). The equilibrium relative velocity between the planetesimals smaller than 100 km is larger than the escape velocity from these planetesimals, and thus the growth mode for smaller planetesimals is the orderly growth (Kobayashi et al. 2016). Note that

the relative velocity is surely larger than the escape velocity from the planetesimals smaller than 100 km but is still less than about ten times of the escape velocity, which does not result in the collisional destruction but results in the growth.

On the other hand, the escape velocity from the planetesimals larger than about 100 km is larger than the relative velocity (Kobayashi et al. 2016). Thus the growth mode of the planetesimals that reach the size of about 100 km changes to the runaway growth. Several larger planetesimals, or protoplanets, grow much faster than the planetesimals smaller than 100 km, and the runaway growth produces bimodal mass distribution that is composed of several protoplanets and remnant planetesimals with the radius $\sim$ 100 km (Kobayashi and Tanaka 2018). The mass distribution of remnant planetesimals has the peak around the radius of about 100 km, which probably remains the same until today and produces the peak around 100 km of the mass distribution of the asteroids in the main belt (Kobayashi and Tanaka 2018). Therefore, the asteroids are considered to be remnant planetesimals and they are essentially the same objects. Thus, in the explanation of the collisional simulations shown after Chapter 2, we only use the term of asteroid and do not use the term of planetesimal to avoid confusions.

The runaway growth does not continue eternally. Sufficiently grown protoplanets gravitationally scatter surrounding planetesimals and increase the relative velocity between protoplanets and planetesimals. Gravitational focusing is more effective with smaller relative velocity, and thus the heat up by the protoplanets decreases the growth rate of the protoplanets themselves. Eventually, several protoplanets with the similar masses and sufficient separations are formed, and they grow through coalescence of surrounding planetesimals. This growth mode is called oligarchic growth (Kokubo and Ida 1998, 2000). The separations between protoplanets are typically about 10 Hill radii (Kokubo and Ida 1995).

Inner protoplanetary disk is hotter due to the irradiation from the sun, while outer protoplanetary disk is colder. There is the orbital radius where disk temperature is the same as the water condensation temperature. This radius is called the snow line. Solid water, or ice, exists outside of the snow line, and thus the amount of solid components outside of the snow line is larger than that inside of the snow line (Hayashi 1981), which leads to the rapid growth of protoplanets outside of the snow line. If the mass of protoplanets exceeds about 10 Earth masses, protoplanets accumulate surrounding disk gas in a runaway manner (Mizuno et al. 1978; Mizuno 1980; Stevenson 1982), which leads to the formation of gas giants. The protoplanets that eventually become Jupiter and Saturn grow rapidly because of the existence of icy component outside of the snow line and become heavier than 10 Earth masses before the

dispersal of gas disk.

Disk gas damps the eccentricity of protoplanets, and protoplanets are orbiting around the sun with almost circular orbits and sufficient separations. However, after disk gas dissipates, the eccentricity increases due to the mutual gravitational perturbations between protoplanets, which leads to the orbital crossing of protoplanets and giant impacts (e.g., Wetherill 1985; Kokubo and Ida 1998). The final stage of the terrestrial planet formation is considered to be the giant impact stage. Giant impacts determine the characteristics of the present terrestrial planets, such as the number or the orbital elements of the planets (e.g., Agnor et al. 1999; Kokubo and Genda 2010). The moon is also considered to be formed by a giant impact (e.g., Ida et al. 1997; Canup 2004).

The total mass of the asteroids in the present main belt is much smaller than that of solid component of the protoplanetary disk (e.g., Petit et al. 2001; Nagasawa et al. 2002). The substantial fraction of asteroids are ejected from the solar system due to, for example, the migration of the gas giants (Walsh et al. 2011), which means that the impacts between planetesimals in the primordial environment are considered to be more frequent than those between asteroids in the present environment. Thus collisional deformation of planetesimals larger than 100 km probably occurs in the primordial environment although collisional destruction of 100 km-sized asteroids in the present solar system rarely occurs (see Fig. 1.5).

1.3 Planetesimal or Asteroidal Collisions

As we introduced in Section 1.2, impacts between various objects including dust particles, planetesimals, and protoplanets play the essential role for the formation of the solar system, that is to say, the impact is the most important physical process for the planet formation. Collisional merging of these objects leads to the growth of objects. However, impacts do not always result in merging but also result in destruction or other types of collisions depending mainly on the impact velocity and also the impact angle and the mass ratio of impacting two bodies. Therefore, the detailed understanding of impact outcomes is very important to discuss the details of the solar system formation scenario. Here, we especially focus on planetesimal or asteroidal impacts.

Numerical simulation is one of the most powerful tools to investigate the results of impacts, since the scale of planetesimals or asteroids (larger than km) is too large to be treated in laboratory experiments. Moreover, the self gravity of bodies plays important role, which is

also difficult to be investigated by room experiments. Certainly, laboratory experiments of impacts for m-sized targets (e.g., Fujiwara et al. 1989; Kato et al. 1995) are applicable not only to impacts between m-sized asteroids but also to those between much larger asteroids through scaling laws (e.g., Housen and Holsapple 1990; Mizutani et al. 1990), but the direct comparison between laboratory-scale-impacts and asteroid-scale-impacts is still difficult. Moreover, the recent improvement of computational power through the development of supercomputers such as K computer enhances the value of numerical simulations.

There are two major frameworks of simulation methods for impacts. One of them is shock physics codes, or hydrocodes, and the other one is particle based codes, or discrete element methods. In shock physics codes, we solve continuum equations for hydrodynamics or elastic dynamics and calculate the time evolution of field variables such as the velocity or density. Some studies include models for realistic rocky materials (e.g., Benz and Asphaug 1995; Jutzi 2015), and thus shock physics codes can treat the impacts between rocky bodies. Shock physics codes are roughly classified to particle methods and mesh methods depending on how to discretize continuum bodies. Particle methods, which include Smoothed Particle Hydrodynamics (SPH) method, utilize Lagrangian particles that mimic bulk of continuum bodies and move with the motion of continuum bodies (e.g., Jutzi and Asphaug 2015), while mesh methods utilize Eulerian meshes that are usually fixed to computational domain (e.g., Kraus et al. 2011). Impact phenomena accompany with large deformation, so that particle methods are more preferable than mesh methods. On the other hand, in particle based codes, we represent bodies as collection of particles with finite radii and rigid boundaries, and we directly assume interactions between particles. Particle based codes are also roughly classified to hard sphere models and soft sphere models. In hard sphere models, we assume the coefficient of restitution and only solve repulsion between particles (e.g., Richardson et al. 2000). In soft sphere models, we take into account finite interaction times and interactions are governed by elastic forces and frictional dissipation (e.g., Schwartz et al. 2018).

Both shock physics codes and particle based codes have merits and demerits. Shock physics codes can solve shock waves, so that they can treat hypervelocity impacts. However, time steps in shock physics codes are determined by the Courant condition and are much smaller than the timescale of gravitational reaccumulation especially for the impacts with bodies smaller than 100 km, so that it is difficult for shock physics codes to complete gravitational reaccumulation phases. On the other hand, particle based codes do not have the strict restriction for time steps especially for hard sphere models, so that the simulations of gravitational reaccumulation

phases are relatively easy. However, they can treat neither shock waves nor heats generated by shock waves. Recently, some studies conduct impact simulations with hybrid codes that utilize both shock physics codes and particle based codes; they calculate initial fragmentation phases using shock physics codes and subsequent gravitational reaccumulation phases using particle based codes (e.g., Michel et al. 2001).

Various impacts are investigated in various researches so far (e.g., Michel et al. 2011; Genda et al. 2012; Ballouz et al. 2014). In this section, we introduce the impact simulations in previous works in terms of the classification of impact outcomes based on Benz and Asphaug (1999) and Leinhardt and Stewart (2012) and asteroidal shapes formed through impacts based on Leinhardt et al. (2000), Jutzi and Asphaug (2015), Jutzi and Benz (2017), Schwartz et al. (2018), and Leleu et al. (2018).

1.3.1 Types of Collisional Outcomes

One of the most important measures of impact results is the mass of the largest remnants. If the mass of the largest remnants are larger than target bodies, impacts result in merging and bodies grow. Here, a target body means the larger body among two impacting objects, and an impactor body means the smaller one. Generally speaking, impacts with larger kinetic energy result in more destructive impacts. However, the degree of destruction also depends on the mass of target bodies. The larger target bodies are, the lesser the degree of destruction becomes with the same impact kinetic energy. Thus, the following total kinetic energy per unit mass Q_R will be a good measure of the degree of destruction:

$$Q_R = \frac{(1/2)\mu_{\rm imp} v_{\rm imp}^2}{M_{\rm tot}}, \tag{1.1}$$

where $v_{\rm imp}$ is the impact velocity, $\mu_{\rm imp} = M_i M_{\rm target}/M_{\rm tot}$ is the reduced mass, $M_{\rm tot} = M_i + M_{\rm target}$ is the total mass, and M_i and $M_{\rm target}$ are masses of impactor and target bodies, respectively. If the mass difference of two bodies is too large $M_i \ll M_{\rm target}$, Q_R is simply written as

$$Q = \frac{(1/2) M_i v_{\rm imp}^2}{M_{\rm target}}. \tag{1.2}$$

The specific kinetic energy Q_R when the mass of the largest remnant becomes just half of that of a target body is called the catastrophic disruption threshold Q^*_{RD}. If Q_R is much smaller than Q^*_{RD}, the impacts result in non-destructive or merging collisions. If Q_R is comparable to

or larger than Q^*_{RD}, the impacts result in catastrophic destruction. Therefore, Q^*_{RD} is one of good thresholds to judge that impacts become destructive or non-destructive. Destruction of larger bodies is prevented by the gravity (gravity-dominated regime), while destruction of smaller bodies is prevented by material strength (strength-dominated regime).

Benz and Asphaug (1999) derived the size dependence of Q^*_D, which is the catastrophic disruption threshold for Q in Eq (1.2), through SPH impact simulations with the material strength of intact rocks. They conducted impact simulations with various impact angles, mass ratios of two impacting bodies, and radii of target bodies but with fixed impact velocities of 3 km/s or 5 km/s, which are the typical impact velocities in the main belt, and they derived the impact-angle-averaged Q^*_D for various target radii, which is expressed as

$$\bar{Q}^*_D = Q_0 \Big(\frac{R_t}{1\,\mathrm{cm}} \Big)^{a_{\mathrm{pow}}} + B_0 \rho_0 \Big(\frac{R_t}{1\,\mathrm{cm}} \Big)^{b_{\mathrm{pow}}}, \tag{1.3}$$

where R_t is the radii of targets, ρ_0 is the mean density, and Q_0, B_0, a_{pow}, and b_{pow} are parameters depending on the impact velocity and target material. The detailed parameters are listed in Benz and Asphaug (1999), and the two exponents have the values of $a_{\mathrm{pow}} \approx -0.4$ and $b_{\mathrm{pow}} \approx 1.3$. Thus there is a radius that has minimum $\bar{Q}^*_D$ and this radius is the transition radius between strength- and gravity-dominated regimes. They found that the transition diameter of target bodies is about 300 m. Note that Q^*_D depends on the friction coefficient of completely damaged rock (Jutzi 2015) and also the resolution of numerical simulations (Genda et al. 2015). Q^*_D is used in theoretical works to assess how impacts are destructive (e.g., Bottke et al. 2005; Kobayashi and Tanaka 2018).

The comparison between Q^*_{RD} and Q_R roughly determines whether impacts result in destructive or non-destructive ones. However, there are other types of impacts such as hit-and-run collisions (e.g., Genda et al. 2012). Moreover, Q^*_{RD} depends not only on the sizes of target bodies as in Eq (1.3) but also on the impact angle or the mass ratio of two impacting bodies. Leinhardt and Stewart (2012) extended Q^*_{RD} in gravity-dominated regime to represent the dependence of the impact angle and the mass ratio as follows:

$$
\begin{aligned}
&Q^*_{RD} = \Big(\frac{\mu_{\rm imp}}{\mu_{{\rm imp},\alpha}}\Big)^{(3\bar{\mu}_{\rm mat}/2-2)} \Big(\frac{1}{4}\frac{(q+1)^2}{q}\Big)^{(2/(3\bar{\mu}_{\rm mat})-1)} Q^*_{RD,q=1,\theta_{\rm imp}=0},\\
&q = M_i/M_{\rm target},\\
&\mu_{{\rm imp},\alpha} = \frac{\alpha_{\rm imp} M_i M_{\rm target}}{\alpha_{\rm imp} M_i + M_{\rm target}},\\
&\alpha_{\rm imp} = \frac{3R_i l^2 - l^3}{4R_i^3},\\
&l = \begin{cases} (R_i + R_t)(1-\sin\theta_{\rm imp}) & R_t < R_i + (R_i + R_t)\sin\theta_{\rm imp} \\ 2R_i & R_t > R_i + (R_i + R_t)\sin\theta_{\rm imp} \end{cases},
\end{aligned}
\tag{1.4}
$$

where R_i is the radii of impactors, $\theta_{\rm imp}$ is the impact angle, $Q^*_{RD,q=1,\theta_{\rm imp}=0}$ is the catastrophic disruption threshold for equal-mass and head-on collisions, and $\bar{\mu}_{\rm mat}$ is the material dependent scaling parameter with $1/3 \leq \bar{\mu}_{\rm mat} \leq 2/3$. Leinhardt and Stewart (2012) determined $Q^*_{RD,q=1,\theta_{\rm imp}=0}$ using scaling laws, but it can also be determined by numerical simulations as done in Benz and Asphaug (1999). For detailed classification of impact types, they also set the following critical impact angle (see also Asphaug 2010):

$$
\theta_{\rm imp,crit} = \sin^{-1}\Big(\frac{R_t}{R_t + R_i}\Big). \tag{1.5}
$$

Using Q^*_{RD}, $\theta_{\rm imp,crit}$, and two-body escape velocity $v_{\rm esc}$, we can roughly classify impact types as follows: merging collisions for $v_{\rm imp} \leq v_{\rm esc}$, partial accretion for $\theta_{\rm imp} \leq \theta_{\rm imp,crit}$ and $Q_{RD} < Q^*_{RD}$, hit-and-run collisions for $\theta_{\rm imp} > \theta_{\rm imp,crit}$ and $Q_{RD} < Q^*_{RD}$, and catastrophic destruction for $Q_{RD} \geq Q^*_{RD}$.

1.3.2 Collisions as the Origin of Asteroidal Shapes

In Section 1.3.1, we focused on the types of impacts and the mass of the largest remnants, or the ejected masses. There are many other interesting features of the results of impacts such as the rotation of impact outcomes. In this dissertation, we especially focus on the shapes of impact outcomes, because the shapes of impact outcomes are sensitive to the impact conditions (e.g., Jutzi and Asphaug 2015) and we already know the shapes of many actual asteroids (see Fig. 1.3).

The shapes of asteroids are mainly determined by asteroidal collisions, although there are other mechanisms to deform asteroidal shapes such as the spin-up due to the Yarkovsky-O'Keefe-Radzievskii-Paddack (YORP) effect (e.g., Richardson et al. 2005) or tidal disruption due to planets (e.g., Walsh and Richardson 2006). The YORP effect is caused by irradiation

like the Yarkovsky effect, and the YORP effect changes the rotation rate of asteroids (Rubincam 2000). If the rotation rate becomes too large due to the YORP effect, the centrifugal force due to the rotation exceeds the self gravity and shapes are deformed (e.g., Pravec et al. 2002). However, the timescale of rotation-rate changes due to the YORP effect for the asteroids larger than 10 km is much longer than the age of the solar system (Rubincam 2000), and thus the YORP deformation is not important for the larger asteroids. The deformation due to tidal disruption is also inefficient, because tidal disruption of asteroids only occurs when the distance between planets and asteroids is comparable to the radii of planets albeit there are no large planets in the main belt.

The shapes of impact outcomes are investigated in several previous researches using the particle based method (Leinhardt et al. 2000), the SPH method (Jutzi and Asphaug 2015; Jutzi and Benz 2017; Leleu et al. 2018), and the hybrid method (Schwartz et al. 2018). Here, we briefly introduce each study.

Leinhardt et al. (2000) conducted the impact simulations between km-sized rubble pile bodies with impact velocities smaller than 10 m/s, which are comparable to the two-body escape velocity of considered rubble pile bodies. They investigated the dependence of impact outcomes on the impact velocity, the impact angle, the mass ratio of two impacting bodies, and even the rotation rate of impacting bodies. They found that the equal-mass impacts can form elongated or bilobed shapes, while all the shapes formed through unequal-mass impacts are spherical. However, although they investigated the detailed dependence of the shapes of impact outcomes on the impact velocity and angle, they only conducted simulations with two values of the mass ratios (1/1 and 1/8) and they also ignored destructive impacts.

Jutzi and Asphaug (2015), Jutzi and Benz (2017), and Schwartz et al. (2018) focus on how to form the bilobed shape of Comet 67P/Churyumov-Gerasimenko, which has the size of 1 km. Jutzi and Asphaug (2015) investigated similar-mass and low-velocity (≈ 1 m/s) impacts, and showed that the bilobed shapes are formed through the impacts with moderate initial angular momentum. However, the impacts with the impact velocity ≈ 1 m/s occurs only in the primordial environment, and it is quite unlikely that such shapes of km-sized bodies survive until today without experiencing destructive collisions. Jutzi and Benz (2017) showed that the sub-catastrophic destruction of rotating elongated body with the impact velocity of ≈ 300 m/s forms a bilobed shape through the fission of a rotating elongated body into two remnants and reaccumulation of the remnants. Schwartz et al. (2018) showed that bilobed shapes are also formed during the reaccumulation phase after catastrophic destruction through the coalescence

of two spherical remnants.

Leleu et al. (2018) investigated the production procedure of the peculiar shapes of inner and small Saturnian moons. Among six inner Saturnian moons, there are three irregularly shaped moons, that is, Pan and Atlas have the flat shapes and Prometheus has the elongated shapes. Moons produced from the rings of Saturn have similar masses and small orbital eccentricities due to the oblateness of Saturn, which leads to similar-mass and low-velocity impacts between Saturnian moons. They investigated the probability distribution of impact conditions at around Saturn and the shapes formed through the impacts with probable impact conditions, and they found that similar-mass and low-velocity impacts around Saturn can explain the current fraction of the irregular shapes of the small Saturnian moons.

Although there are several previous researches investigating shapes formed through impacts, almost all of them focus on the shapes of specific objects and do not investigated comprehensive shapes formed through various impacts. Crucially, none of them investigate shapes quantitatively, and then we cannot statistically compare the results of simulations with the shape distribution of actual asteroids. Thus, in this dissertation, we conduct various impact simulations and investigate the shapes of impact outcomes quantitatively in terms of the axis ratios.

Chapter 2

Method

In this chapter, we introduce the detailed methods necessary for the numerical simulations of asteroidal collisions and the formation of resultant shapes, which includes the equations for elastic dynamics, the descretized equations for the SPH method, the equation of state for impact simulations, the model for fracture of rock, the model for friction of damaged rock, the parallelization of simulation code, and the time development procedure. Some parts of this chapter are based on Sugiura and Inutsuka (2016), Sugiura and Inutsuka (2017), and Sugiura et al. (2018a).

2.1 Elastic Dynamics

2.1.1 Basic Equations for Elastic Dynamics

Elastic bodies mean bodies that always return to those initial shapes under any deformation owing to internal stresses. Basic equations include not only the equation of motion or the equation of continuity but also the equation to calculate the stress tensor from the strain. In this section, detailed equations utilized in elastic dynamics are introduced. Please note that the SPH method is a particle method, which basically requires Lagrangian formulation, and thus we introduce equations in Lagrange-type formulation.

The Hooke's law describes the relationship between the stress and the strain for elastic bodies with small deformation. According to the Hooke's law, the stress tensor $\sigma^{\alpha\beta}$ is proportional to the strain, which is the displacement per unit length. $\sigma^{\alpha\beta}$ means the force per unit area acting on a surface of a part of elastic bodies, and β indicates the direction of the force and α indicates the direction perpendicular to the surface. Here, Greek letters of α or β correspond to each direction x, y, or z. According to the Hooke's law, the stress tensor is expressed as

$$\sigma^{\alpha\beta} = 2\mu\left(\epsilon^{\alpha\beta} - \frac{1}{3}\epsilon^{\gamma\gamma}\delta^{\alpha\beta}\right) + K\epsilon^{\gamma\gamma}\delta^{\alpha\beta}, \tag{2.1}$$

where μ is the shear modulus, K is the bulk modulus, and $\delta^{\alpha\beta}$ is the Kronecker delta. We assume a summation convention over repeated indices of Greek letters. $\epsilon^{\alpha\beta}$ is strain tensor and written as,

$$\epsilon^{\alpha\beta} = \frac{1}{2}\left(\frac{\partial\zeta^{\alpha}}{\partial x^{\beta}} + \frac{\partial\zeta^{\beta}}{\partial x^{\alpha}}\right), \tag{2.2}$$

where $\zeta^{\alpha} = x^{\alpha} - x_0^{\alpha}$, $\boldsymbol{x}$ is the position vector, and $\boldsymbol{x}_0$ is the position vector when bodies are not deformed. The first term of Eq. (2.1) shows the deviatoric stress tensor, and we define

$$S^{\alpha\beta} \equiv 2\mu\left(\epsilon^{\alpha\beta} - \frac{1}{3}\epsilon^{\gamma\gamma}\delta^{\alpha\beta}\right). \tag{2.3}$$

The second term of Eq. (2.1) shows the isotropic stress, i.e., the pressure, and we define $P \equiv -K\epsilon^{\gamma\gamma}$. For numerical simulations, it is convenient to use the relationship between the pressure, density, and internal energy, i.e., the equation of state. $\epsilon^{\gamma\gamma}$ is related to the change of volume, and the pressure with small deformations is expressed as

$$P = \frac{K}{\rho_0}(\rho - \rho_0) = C_s^2(\rho - \rho_0), \tag{2.4}$$

where ρ is the density, ρ_0 is the density when bodies are not deformed, and $C_s = \sqrt{K/\rho_0}$ is the bulk sound speed. Note that positive pressures represent repulsive forces, while negative pressures represent tensile forces. Thus the stress tensor is represented as

$$\sigma^{\alpha\beta} = -P\delta^{\alpha\beta} + S^{\alpha\beta}. \tag{2.5}$$

However, the strain tensor defined as Eq. (2.2) does not become zero for rigid-body rotations, which leads to nonzero deviatoric stress tensor calculated from Eq. (2.3). Note that no deformation occurs for rigid-body rotations and the strain tensor should be zero. To avoid this problem, we solve the time-evolution equation of the deviatoric stress tensor (e.g., Libersky and Petschek 1991). The equation is achieved by differentiating Eq. (2.3) and represented as

$$\frac{dS^{\alpha\beta}}{dt} = 2\mu\left(\dot{\epsilon}^{\alpha\beta} - \frac{1}{3}\delta^{\alpha\beta}\dot{\epsilon}^{\gamma\gamma}\right) + S^{\alpha\gamma}R^{\beta\gamma} + S^{\beta\gamma}R^{\alpha\gamma}, \tag{2.6}$$

where d/dt represents Lagrangian time derivative and $\dot{\epsilon}^{\alpha\beta}$ and $R^{\alpha\gamma}$ represent strain rate tensor and rotation rate tensor, respectively. Strain rate tensor and rotation rate tensor are expressed as

$$\begin{aligned}\dot{\epsilon}^{\alpha\beta} &= \frac{1}{2}\Big(\frac{\partial v^{\alpha}}{\partial x^{\beta}} + \frac{\partial v^{\beta}}{\partial x^{\alpha}}\Big),\\ R^{\alpha\beta} &= \frac{1}{2}\Big(\frac{\partial v^{\alpha}}{\partial x^{\beta}} - \frac{\partial v^{\beta}}{\partial x^{\alpha}}\Big),\end{aligned} \tag{2.7}$$

where $\boldsymbol{v}$ is the velocity vector. The first term of Eq. (2.6) is achieved straightforwardly by differentiating Eq (2.3). Eq (2.3) is written for the coordinate system fixed to bodies, but we utilize the laboratory coordinate system. Thus we need to consider the difference of two coordinate systems when bodies rotate. The second term of Eq. (2.6) represents this difference and is derived from the derivative of the bases.

The acceleration of a part of elastic bodies is determined by the space derivative of the stress tensor. The equation of motion, which determines the acceleration of elastic bodies, is expressed as

$$\frac{dv^{\alpha}}{dt} = \frac{1}{\rho}\frac{\partial \sigma^{\alpha\beta}}{\partial x^{\beta}}. \tag{2.8}$$

The density change is determined by the divergence of the velocity field. The equation of continuity, which determines the change rate of the density, is expressed as

$$\frac{d\rho}{dt} = -\rho\frac{\partial v^{\alpha}}{\partial x^{\alpha}}. \tag{2.9}$$

We can treat the motion of elastic bodies by solving the equation of state (2.4), the time-evolution equation of the deviatoric stress tensor (2.6), the equation of motion (2.8), and the equation of continuity (2.9). However, if we want to solve the temperature change, we need to additionally solve the equation of energy. The change of the specific internal energy u due to the work done by internal stresses is basically determined by the product of the stress tensor and the velocity gradient, i.e., the deformation per unit time, and thus the equation of energy is expressed as,

$$\frac{du}{dt} = \frac{1}{\rho}\sigma^{\alpha\beta}\frac{\partial v^{\alpha}}{\partial x^{\beta}}. \tag{2.10}$$

2.1.2 Basic Concept of SPH Method

The SPH method is originally the numerical method for fluid dynamics using Lagrangian "particles". The SPH method is firstly developed by Gingold and Monaghan (1977) and Lucy (1977) to solve hydrodynamics problems in astrophysics fields. Each SPH particle mimics a fluid element, and we represent a fluid body as swarm of SPH particles. Recently, the SPH method is extended to elastic dynamics (e.g., Libersky and Petschek 1991; Gray et al. 2001; Sugiura and Inutsuka 2017), dynamics of brittle solids (Benz and Asphaug 1994, 1995), and dynamics of granular material (Jutzi 2015).

Each SPH particle is not a point particle but has a kind of finite radius. In the framework of the SPH method, the density at the position $\boldsymbol{x}$ is represented as

$$\rho(\boldsymbol{x}) = \sum_j m_j W(|\boldsymbol{x} - \boldsymbol{x}_j|, h), \tag{2.11}$$

where m_j is the mass of the j-th SPH particle, $\boldsymbol{x}_j$ is the position of the j-th particle, $W(|\boldsymbol{x} - \boldsymbol{x}_j|, h)$ is a kernel function, and h is a smoothing length. Hereafter, subscripts of Roman letters mean the particle number. The kernel function $W(|\boldsymbol{x} - \boldsymbol{x}_j|, h)$ represents shape of a kind of distribution of the j-th particle, and the smoothing length determines the width of the broadening of each SPH particle (h is usually set to be comparable to average particle spacing). In Eq. (2.11), $m_j W(|\boldsymbol{x} - \boldsymbol{x}_j|, h)$ represents the density distribution contributed from the j-th particle, and thus the total density distribution is represented by superposition of the density distribution contributed from nearby SPH particles. Note that the kernel function has following properties: (I) The kernel function converges to a Dirac δ function when $h \to 0$; (II) The kernel function is normalized so that the spatial integration of the kernel function becomes unity; (III) The kernel function $W(r, h)$becomes 0 for $r \to \infty$. The kernel function has various forms, and here we introduce two types of the kernel function; Gaussian and cubic spline kernels. The Gaussian kernel is expressed as

$$W(r, h) = \left[\frac{1}{h\sqrt{\pi}}\right]^{d_{\rm dim}} e^{-r^2/h^2}, \tag{2.12}$$

where $d_{\rm dim}$ is a spatial dimension, and the cubic spline kernel for three dimensional problems is expressed as

$$W(r,h) = \frac{1}{\pi h^3} \begin{cases} 1 - \frac{3}{2}\left(\frac{r}{h}\right)^2 + \frac{3}{4}\left(\frac{r}{h}\right)^3 & 0 \le \frac{r}{h} < 1 \\ \frac{1}{4}\left(2 - \frac{r}{h}\right)^3 & 1 \le \frac{r}{h} < 2 \\ 0 & 2 \le \frac{r}{h} \end{cases} . \tag{2.13}$$

Smoothing lengths should be comparable to local average particle spacing. Thus if the particle spacing, or the density, largely varies in space and in time, we need to adjust smoothing lengths to be local average particle spacing. However, all simulations in this dissertation do not accompany with large density variation. Thus we use constant smoothing lengths in space and in time, and we set smoothing lengths to be the initial particle spacing.

A physical quantity f_i at the position of the i-th particle $\boldsymbol{x}_i$ is approximated by the convolution of f at vicinity points, which is given by

$$f_i = \int f(\boldsymbol{x}) W(|\boldsymbol{x} - \boldsymbol{x}_i|, h) d\boldsymbol{x}. \tag{2.14}$$

In the same manner, the convolution of the spatial derivative of the physical quantity is given by

$$\begin{aligned} \frac{\partial f_i}{\partial x_i^\alpha} &= \int \frac{\partial f(\boldsymbol{x})}{\partial x^\alpha} W(|\boldsymbol{x} - \boldsymbol{x}_i|, h) d\boldsymbol{x} \\ &= \int f(\boldsymbol{x}) \frac{\partial}{\partial x_i^\alpha} W(|\boldsymbol{x} - \boldsymbol{x}_i|, h) d\boldsymbol{x}. \end{aligned} \tag{2.15}$$

Here, we have integrated by parts and used the relation $W(r,h) = W(-r,h)$. From Eq. (2.11), we achieve the following identity:

$$\sum_j \frac{m_j}{\rho(\boldsymbol{x})} W(|\boldsymbol{x} - \boldsymbol{x}_j|, h) = 1. \tag{2.16}$$

By using the identity Eq (2.16), we further modify Eq. (2.15) as

$$\frac{\partial f_i}{\partial x_i^\alpha} = \sum_j \int m_j \frac{f(\boldsymbol{x})}{\rho(\boldsymbol{x})} \frac{\partial}{\partial x_i^\alpha} W(|\boldsymbol{x} - \boldsymbol{x}_i|, h) W(|\boldsymbol{x} - \boldsymbol{x}_j|, h) d\boldsymbol{x}. \tag{2.17}$$

Basically, the spatial derivatives in Eqs. (2.6), (2.8), (2.9), and (2.10) are evaluated as Eq. (2.17). However, Eq. (2.17) includes the spatial integral and we cannot directly evaluate the gradients using Eq. (2.17).

2.1.3 Equations for Standard SPH Method

In the widely-used SPH method, the approximation of $W(|\boldsymbol{x}-\boldsymbol{x}_j|,h) \approx \delta(|\boldsymbol{x}-\boldsymbol{x}_j|)$ is utilized in the evaluation of Eq. (2.17), where $\delta(|\boldsymbol{x}-\boldsymbol{x}_j|)$ is the Dirac δ function. This approximation leads to

$$\frac{\partial f_i}{\partial x_i^\alpha} \approx \sum_j m_j \frac{f_j}{\rho_j} \frac{\partial}{\partial x_i^\alpha} W(|\boldsymbol{x}_i-\boldsymbol{x}_j|,h). \tag{2.18}$$

Then spatial gradients are straightforwardly evaluated using information of neighbor SPH particles as Eq. (2.18).

There are several types of the final forms of Eqs. (2.6), (2.8), (2.9), and (2.10) for the standard SPH method with small differences. Although the final forms are depending on the detailed procedure how to transform the equations, the final forms of the equations can be basically derived by replacing the spacial derivatives in Eqs. (2.6), (2.8), (2.9), and (2.10) with those in Eq. (2.18).

For example, Sugiura et al. (2018a) use the following types of the equation of continuity, motion, and energy:

$$\frac{d\rho_i}{dt} = -\sum_j m_j \frac{\rho_i}{\rho_j}(v_j^\alpha - v_i^\alpha) \frac{\partial}{\partial x_i^\alpha} W(|\boldsymbol{x}_i-\boldsymbol{x}_j|,h), \tag{2.19}$$

$$\frac{dv_i^\alpha}{dt} = \sum_j m_j \Big[\frac{\sigma_i^{\alpha\beta}}{\rho_i^2} + \frac{\sigma_j^{\alpha\beta}}{\rho_j^2} - \Pi_{ij}\delta^{\alpha\beta}\Big] \frac{\partial}{\partial x_i^\beta} W(|\boldsymbol{x}_i-\boldsymbol{x}_j|,h), \tag{2.20}$$

$$\begin{aligned}\frac{du_i}{dt} = &-\sum_j \frac{1}{2} m_j \Big[\frac{p_i}{\rho_i^2} + \frac{p_j}{\rho_j^2} + \Pi_{ij}\Big](v_j^\alpha - v_i^\alpha) \frac{\partial}{\partial x_i^\alpha} W(|\boldsymbol{x}_i-\boldsymbol{x}_j|,h) \\ &+ \sum_j \frac{1}{2} m_j \frac{S_i^{\alpha\beta}}{\rho_i\rho_j} \Big[(v_j^\alpha - v_i^\alpha)\frac{\partial}{\partial x_i^\beta} + (v_j^\beta - v_i^\beta)\frac{\partial}{\partial x_i^\alpha}\Big] W(|\boldsymbol{x}_i-\boldsymbol{x}_j|,h),\end{aligned} \tag{2.21}$$

where Π_{ij} is the artificial viscosity term, which is necessary to treat shock waves and stabilize numerical simulations. There are many forms of the artificial viscosity term, but the most common form of Π_{ij} is as follows (Monaghan 1992):

$$\begin{aligned}\Pi_{ij} &= \begin{cases} \frac{-\alpha_{\rm vis}\mu_{ij}(C_{s,i}+C_{s,j})/2 + \beta_{\rm vis}\mu_{ij}^2}{(\rho_i+\rho_j)/2} & (\boldsymbol{v}_i-\boldsymbol{v}_j)\cdot(\boldsymbol{x}_i-\boldsymbol{x}_j) < 0 \\ 0 & (\boldsymbol{v}_i-\boldsymbol{v}_j)\cdot(\boldsymbol{x}_i-\boldsymbol{x}_j) > 0 \end{cases}, \\ \mu_{ij} &= \frac{h(\boldsymbol{v}_i-\boldsymbol{v}_j)\cdot(\boldsymbol{x}_i-\boldsymbol{x}_j)}{(\boldsymbol{x}_i-\boldsymbol{x}_j)^2 + 0.01h^2}.\end{aligned} \tag{2.22}$$

Here, $\alpha_{\rm vis}$ and $\beta_{\rm vis}$ are the parameters for the artificial viscosity, and throughout this dissertation we use $\alpha_{\rm vis} = 1.0$ and $\beta_{\rm vis} = 2.0$.

Sugiura et al. (2018a) also use the following form of the time-evolution equation of the deviatoric stress tensor:

$$\frac{dS_i^{\alpha\beta}}{dt} = 2\mu\Big(\epsilon_i^{\alpha\beta} - \frac{1}{3}\epsilon_i^{\gamma\gamma}\delta^{\alpha\beta}\Big) + S_i^{\alpha\gamma}R_i^{\beta\gamma} + S_i^{\beta\gamma}R_i^{\alpha\gamma}, \tag{2.23}$$

where

$$\epsilon_i^{\alpha\beta} = \frac{1}{2}\Big(\frac{\partial v_i^\alpha}{\partial x_i^\beta} + \frac{\partial v_i^\beta}{\partial x_i^\alpha}\Big), \tag{2.24}$$

$$R_i^{\alpha\beta} = \frac{1}{2}\Big(\frac{\partial v_i^\alpha}{\partial x_i^\beta} - \frac{\partial v_i^\beta}{\partial x_i^\alpha}\Big), \tag{2.25}$$

and the velocity gradients are evaluated as

$$\begin{aligned}\frac{\partial v_i^\alpha}{\partial x_i^\beta} &= \sum_j \frac{m_j}{\rho_j}(v_j^\alpha - v_i^\alpha)\mathrm{L}_i^{\beta\gamma}\frac{\partial}{\partial x_i^\gamma}W(|\boldsymbol{x}_i - \boldsymbol{x}_j|, h),\\ \mathbf{L}_i &= \Big(\sum_j \frac{m_j}{\rho_j}\frac{\partial}{\partial \boldsymbol{x}_i}W(|\boldsymbol{x}_i - \boldsymbol{x}_j|, h)\otimes(\boldsymbol{x}_j - \boldsymbol{x}_i)\Big)^{-1}.\end{aligned} \tag{2.26}$$

Here, $\mathbf{L}_i$ is the correction matrix necessary to describe rigid body rotations correctly (Bonet and Lok 1999), and $\otimes$ represents the tensor product. We leave the detailed explanation of the correction matrix to Section 2.1.7.

The density is calculated using both Eqs. (2.11) and (2.19). However, Eq. (2.11) causes problems around surfaces of solid bodies. The density around free surfaces calculated through Eq. (2.11) is smaller than the uncompressed density, and the pressure is negative through the equation of state. Thus such unphysical pressure around free surfaces deforms solid bodies (Monaghan 1988). The problem is prevented by setting the initial density of all SPH particles to undeformed density and calculating the density using Eq. (2.19), which represents the time-evolution equation for the density.

2.1.4 Equations for Godunov SPH Method and Tensile Instability

Now we have the complete set of the equations for elastic dynamics in the standard SPH method listed in Section 2.1.3. However, the SPH method has one serious problem especially

in simulations of pure elastic dynamics; the tensile instability (e.g., Swegle et al. 1995). The tensile instability is a numerical instability that is prominent in tension-dominated regions, or negative pressure regions and produces unphysical clustering of SPH particles, which leads to unphysical fracturing of elastic bodies (see Swegle et al. 1995 and Gray et al. 2001). Thus, we need to suppress the tensile instability for the correct treatment of pure elastic bodies.

Several methods have been proposed to solve the tensile instability (e.g., Randles and Libersky 1996; Chen et al. 1999; Sigalotti and López 2008). The most common way to remove the tensile instability is the method utilizing an artificial stress (Monaghan 2000; Gray et al. 2001). The artificial stress is an additional repulsive force. Perturbations with longer wavelengths are not affected by the artificial stress, and thus it safely removes the tensile instability, which is the instability with short wavelength of $2h$.

We also develop another way to remove the tensile instability based on the Godunov SPH (Inutsuka 2002), which utilizes so-called Riemann solver to accurately resolve extremely strong shock waves. Another prominent feature of the Godunov SPH method is that they evaluate the convolution Eq. (2.17) more correctly by interpolating the distribution of the density and other physical quantities. Let us briefly introduce the equations and the properties of the Godunov SPH method according to Sugiura and Inutsuka (2016, 2017). We only introduce how to formulate the equation of motion. See Appendix A.1 for the detailed formulations of the equation of energy and the equation for time development of the deviatoric stress tensor.

We use the Gaussian kernel Eq. (2.12) for the Godunov SPH method. We formulate the equation of motion for the Godunov SPH method through the convolution of Eq. (2.8), which is represented as

$$\frac{dv_i^\alpha}{dt} \equiv \int \frac{dv^\alpha(\boldsymbol{x})}{dt} W(|\boldsymbol{x}-\boldsymbol{x}_i|,h)d\boldsymbol{x} = \int \frac{1}{\rho(\boldsymbol{x})}\frac{\partial}{\partial x^\beta}\sigma^{\alpha\beta}(\boldsymbol{x})W(|\boldsymbol{x}-\boldsymbol{x}_i|,h)d\boldsymbol{x}. \tag{2.27}$$

We further transform Eq. (2.27) using the identity Eq. (2.16) and integration by parts, and then we achieve

$$\frac{dv_i^\alpha}{dt} = \sum_j m_j \int \frac{\sigma^{\alpha\beta}(\boldsymbol{x})}{\rho^2(\boldsymbol{x})}\Big[\frac{\partial}{\partial x_i^\beta} - \frac{\partial}{\partial x_j^\beta}\Big] W(|\boldsymbol{x}-\boldsymbol{x}_i|,h)W(|\boldsymbol{x}-\boldsymbol{x}_j|,h)d\boldsymbol{x}, \tag{2.28}$$

which is similar to Eq. (2.17). To evaluate the integral in Eq. (2.28), we interpolate the distribution of the density and the stress tensor around the i-th and j-th particles. The interpolated distributions are constructed from the density, the stress tensor, and the gradients of the density at the i-th and j-th particles. The gradients are calculated using, for example, Eq. (2.18).

Then we approximate the distribution of the stress tensor as constant for the direction perpendicular to $\boldsymbol{x}_i - \boldsymbol{x}_j$ and linear for the direction parallel to $\boldsymbol{x}_i - \boldsymbol{x}_j$. Similarly, we approximate the distribution of ρ^{-2} as linear for the direction perpendicular to $\boldsymbol{x}_i - \boldsymbol{x}_j$ and the distribution of ρ^{-1} as linear, cubic spline, and quintic spline for the direction parallel to $\boldsymbol{x}_i - \boldsymbol{x}_j$. This approximation leads to

$$\frac{dv_i^\alpha}{dt} = \sum_j 2m_j \sigma_{ij}^{\alpha\beta *} V_{ij}^2 \frac{\partial}{\partial x_i^\beta} W(|\boldsymbol{x}_i - \boldsymbol{x}_j|, \sqrt{2}h), \tag{2.29}$$

$$\sigma_{ij}^{\alpha\beta *} = -P_{ij}^* \delta^{\alpha\beta} + S_{ij}^{\alpha\beta *}, \tag{2.30}$$

$$S_{ij}^{\alpha\beta *} = \frac{S_i^{\alpha\beta} + S_j^{\alpha\beta}}{2} + s_{ij}^* \frac{S_i^{\alpha\beta} - S_j^{\alpha\beta}}{|\boldsymbol{r}_i - \boldsymbol{r}_j|}. \tag{2.31}$$

Here, the formulas of V_{ij}^2 and s_{ij}^* depend on the interpolation method of ρ^{-1} for $\boldsymbol{x}_i - \boldsymbol{x}_j$ direction, i.e., linear, cubic spline, and quintic spline interpolation. See Sugiura and Inutsuka (2016) or Appendix A.1 for the detailed equations of V_{ij}^2 and s_{ij}^*. Moreover, the pressure resulted from the Riemann solver is used for P_{ij}^*. The way to calculate P_{ij}^* using the quantities at the i-th and j-th particles is described in Appendix A.2. Note that P_{ij}^* is close to $(P_i + P_j)/2$ for smooth pressure distributions.

Sugiura and Inutsuka (2016) investigated the stability of Eq. (2.29) through the linear stability analysis. As a result, we found that the stability depends on the spatial dimensions, the sign of pressure, and the interpolation method of ρ^{-2}. See Appendix B for the detailes of the linear stability analysis. We summarize the stability in Table 2.1. According to the columns of Table 2.1 for two- and three-dimensions, the equation for the linear interpolation is stable in positive pressure regions, and that for the cubic spline interpolation is stable in negative pressure regions. Thus we can conduct numerical simulations of elastic dynamics stably if we use the linear interpolation in regions with positive pressure and the cubic spline interpolation in those with negative pressure.

2.1.5 Time Development Method

Now, we have the time development equations for the velocity (2.20) or (2.29), the density (2.19), the specific internal energy (2.21), and the deviatoric stress tensor (2.23). There are several time advancing schemes such as Euler, Runge-Kutta, and leapfrog integrator. In this dissertation, we utilize the leapfrog integrator shown in Sugiura et al. (2018a), which has the second-order accuracy in time.

	$P > 0$, $d_{\rm dim} = 1$	$P < 0$, $d_{\rm dim} = 1$	$P > 0$, $d_{\rm dim} = 2$ or 3	$P < 0$, $d_{\rm dim} = 2$ or 3
Linear	◯	×	◯	×
Cubic	◯	×	×	◯
Quintic	×	◯	×	◯

Table 2.1: Dependence of the stability on the spatial dimension, the interpolation methods, and the sing of pressure. Circles (◯) show stable interpolations and crosses (×) show unstable interpolations. $d_{\rm dim}$ shows the number of dimensions and P shows the pressure. This table is the same as Table 1 of Sugiura and Inutsuka (2016).

The detailed procedures of the leapfrog integrator are as follows: At the n-th step we update the position of the i-th particle $\boldsymbol{x}_i^n$ and other quantities of the i-th particle q_i^n as

$$\begin{aligned} \boldsymbol{x}_i^{n+1} &= \boldsymbol{x}_i^n + \boldsymbol{v}_i^n \Delta t + \frac{1}{2}\Big(\frac{d\boldsymbol{v}_i}{dt}\Big)^n \Delta t^2, \\ q_i^{n+1} &= q_i^n + \frac{1}{2}\Big[\Big(\frac{dq_i}{dt}\Big)^n + \Big(\frac{dq_i}{dt}\Big)^{n+1}\Big]\Delta t, \end{aligned} \tag{2.32}$$

where Δt is the timestep and $q = \rho, u, \boldsymbol{v}, S^{\alpha\beta}$.

In Eq. (2.32), for example, $\boldsymbol{v}_i^{n+1}$ is determined by $(d\boldsymbol{v}_i/dt)^{n+1}$. However, to calculate $(d\boldsymbol{v}_i/dt)^{n+1}$ with the equation of motion (2.20), we need $\boldsymbol{v}_i^{n+1}$ and we cannot directly derive $\boldsymbol{v}_i^{n+1}$. Thus we update physical quantities as following procedure: Firstly, we predict the quantities of the $(n+1)$-th step only using the quantities of the n-th step as

$$q_i^* = q_i^n + \Big(\frac{dq_i}{dt}\Big)^n \Delta t. \tag{2.33}$$

At the same time we update the positions as Eq. (2.32). Then we calculate $(dq_i/dt)^{n+1}$ using q_i^* and $\boldsymbol{x}_i^{n+1}$, and we obtain q_i^{n+1} from Eq. (2.32). We can reuse $(dq_i/dt)^{n+1}$ at the next step, so that we calculate the derivatives of the variables only once at every step. Moreover, if all variables vary linearly in time, this procedure does not produce any integration error. Therefore, this integration scheme has second-order accuracy in time.

According to the Courant condition, the timestep Δt is given by

$$\Delta t = \min_i C_{\rm CFL} \frac{h}{C_{s,i}}, \tag{2.34}$$

where $C_{s,i}$ is the local bulk sound speed at the i-th particle. Bulk sound speed for elastic dynamics is defined as in Eq. (2.4). Even for other equation of state, $C_{s,i}$ is expressed as

$C_{s,i} = \sqrt{dP_i/d\rho_i}$ and is calculated using ρ, u, and P of the i-th particle. We adopt the value of $C_{\rm CFL} = 0.5$.

2.1.6 Test Simulations of SPH Method for Elastic Dynamics

We implemented both the standard SPH method and the Godunov SPH method in our simulation code of elastic dynamics. We validate the Godunov SPH method through test simulations for elastic bodies as shown in following subsections. These tests are also shown in Sugiura and Inutsuka (2017). The standard SPH method cannot treat elastic dynamics problems stably due to the tensile instability, but it only needs a low computational cost. Note that the tensile instability is insignificant for asteroidal collisions because fractures of rocky material quickly release negative pressure, and we can still utilize the standard SPH method for such problems.

Elastic Rings Collision

Firstly, let us introduce the test simulation that reproduces the collision of two elastic rings in a two-dimensional configuration. We use the following unit system: The density is scaled using undeformed density ρ_0, the velocity is scaled using the bulk sound speed C_s, and the length is scaled using the widths of rings w. Initially two rings are put with the distance between the centers of two rings of $9w$. The rings have the inner radii of $3w$ and the outer radii of $4w$. We put particles on square lattices within two rings with the smoothing length of $h = 0.1w$. The shear modulus is set to $\mu = 0.22C_s^2\rho_0$. The rings are not deformed initially, so that all the densities are set to undeformed density ρ_0, and all the deviatoric stress tensors are set to 0. These rings collide with the relative velocity of $0.118C_s$.

Figure 2.1 shows the behavior of the elastic rings calculated using the Godunov SPH method, which validates the stability of the Godunov SPH method for the simulation of bounce off of the two rings. The configurations of the colliding two rings are similar to those of Gray et al. (2001).

Elastic Plate Oscillation

Secondly, to validate the Godunov SPH method in three-dimensional configurations, we simulate the oscillation of elastic plate with fixed end. The similar simulation but in two dimensions was conducted by Gray et al. (2001). Lifshitz et al. (1986) provide the analytical solution for extremely-thin-plate oscillations.

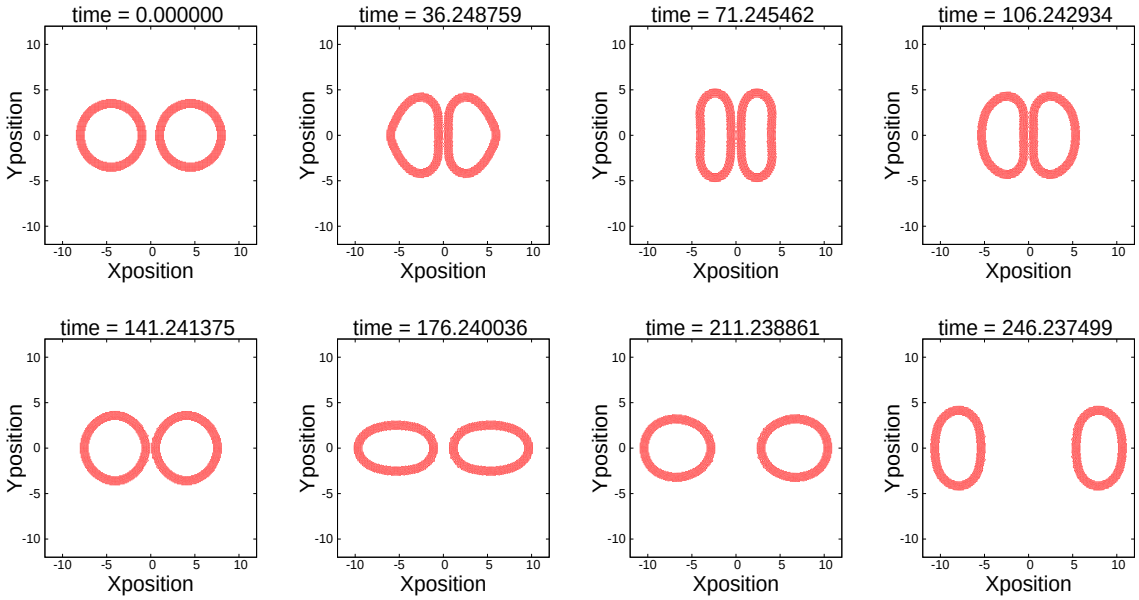

Figure 2.1: Rubber rings collision calculated by the Godunov SPH method. This figure is the same as Fig. 3 of Sugiura and Inutsuka (2017).

The same unit system as in the previous subsection is used except for the unit of length, which is scaled by the thickness of the plate H. The plate has the length of $L = 11H$ and the width of $W = 2H$. We put particles on square lattices within the plate with $h = 0.1w$. μ is set to $0.5C_s^2\rho_0$. The positions of particles that exist within $1H$ from left end of the plate are fixed to represent fixed end of the plate. As in the previous subsection, we set initial densities to ρ_0 and initial deviatoric stress tensors to 0.

y component of the velocity v_y at the initial condition is given as

$$\frac{v_y}{C_s} = V_f \frac{[M(\cos(kx) - \cosh(kx)) - N(\sin(kx) - \sinh(kx))]}{Q}, \tag{2.35}$$

where x is the x position, V_f is the velocity normalized by the bulk sound speed at the free edge of the plate,

$$\begin{aligned} M &= \sin(kL) + \sinh(kL), \\ N &= \cos(kL) + \cosh(kL), \\ Q &= 2(\cos(kL)\sinh(kL) - \sin(kL)\cosh(kL)), \end{aligned} \tag{2.36}$$

and k is a kind of the wave number, which is given by the solution of

$$\cos(kL)\cosh(kL) = -1, \tag{2.37}$$

$kL = 1.875$ for a fundamental mode. In this simulation, we set $V_f = 0.05$.

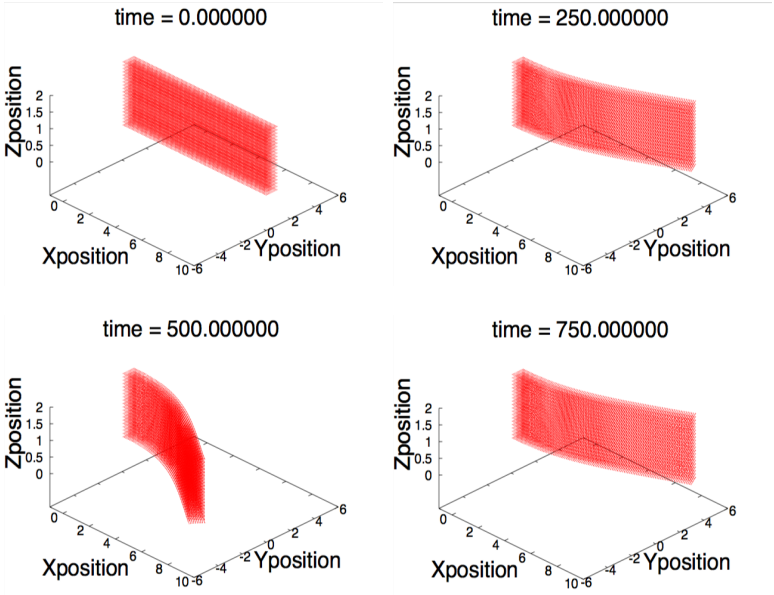

Figure 2.2: Oscillation of plate calculated by the Godunov SPH method. This figure is taken from Fig. 5 of Sugiura and Inutsuka (2017).

Figure 2.2 shows the result of the simulation using the Godunov SPH method, which shows that our method calculates the oscillation stably.

According to Lifshitz et al. (1986), the angular frequency (=2π/oscillation period) of an extremely thin plate is written as

$$\omega^2 = \frac{EH^2k^4}{12\rho(1-\nu^2)}, \tag{2.38}$$

where E represents the Young's modulus and ν represents the Poisson's ratio, which are expressed using the bulk modulus K and the shear modulus μ as

$$\begin{aligned} E &= \frac{9K\mu}{3K+\mu}, \\ \nu &= \frac{3K-2\mu}{2(3K+\mu)}. \end{aligned} \tag{2.39}$$

The angular frequency using the parameters utilized in our simulation then becomes $\omega = 0.01201C_s/H$, which leads to the analytical period of the oscillation of the extremely thin plate

$$T_{\text{theo}} = \frac{2\pi}{\omega} = 523.2H/C_s. \tag{2.40}$$

Our simulation gives the period of $T_{\text{sim}} \approx 665H/C_s$. The difference between the analytical and simulated periods is expected to decrease with decreasing the ratio of the width to length of the plate W/L. We also conduct the same simulations but with $L = 15H$ and $L = 20H$. The oscillation periods with $L = 15H$ and $L = 20H$ are $1406H/C_s$ and $2353H/C_s$, respectively. The errors between simulated and theoretical results $(=(T_{\text{theo}} - T_{\text{sim}})/T_{\text{theo}})$ is 27.3% for $L = 10H$, 19.5% for $L = 15H$, and 12.5% for $L = 20H$, respectively: The errors significantly decrease with decreasing W/L.

2.1.7 Correction Matrix and Rigid Body Rotation

In this section, we will explain why we need the correction matrix $\mathbf{L}_i$ in the calculation of the velocity gradient Eq. (2.26).

The velocity gradient is also calculated without the correction matrix as follows (Libersky and Petschek 1991):

$$\frac{\partial v_i^\alpha}{\partial x_i^\beta} = \sum_j \frac{m_j}{\rho_j}(v_j^\alpha - v_i^\alpha)\frac{\partial}{\partial x_i^\beta}W(|\boldsymbol{x}_i - \boldsymbol{x}_j|, h). \tag{2.41}$$

However, this equation leads to the erroneous velocity gradient around surfaces of bodies. To show this, we consider a body doing a rigid body rotation with an angular velocity vector $\boldsymbol{\omega} = (\omega_x, \omega_y, \omega_z)$ and the center of the rotation at the origin of a coordinate. The velocity at the position $\boldsymbol{x}$ is expressed as

$$\boldsymbol{v} = \boldsymbol{\omega} \times \boldsymbol{x}. \tag{2.42}$$

Here, we define the velocity gradient matrix $\mathbf{W}$ so that $\alpha\beta$ component of $\mathbf{W}$ has $\partial v^\alpha/\partial x^\beta$. For the rigid body rotation, $\mathbf{W}$ is expressed as

$$\mathbf{W} = \begin{bmatrix} 0 & -\omega_z & \omega_y \\ \omega_z & 0 & -\omega_x \\ -\omega_y & \omega_x & 0 \end{bmatrix}. \tag{2.43}$$

We also notice the following relationship:

$$\boldsymbol{v} = \mathbf{W}\boldsymbol{x}. \tag{2.44}$$

The velocity gradient evaluated by SPH approximation Eq. (2.41) becomes

$$\begin{aligned}\mathbf{W}_{\mathrm{SPH}} &= \sum_j \frac{m_j}{\rho_j}(\mathbf{W}\boldsymbol{x}_j - \mathbf{W}\boldsymbol{x}_i) \otimes \frac{\partial}{\partial \boldsymbol{x}_i} W(|\boldsymbol{x}_i - \boldsymbol{x}_j|, h) \\ &= \mathbf{W}\Big(\sum_j \frac{m_j}{\rho_j}(\boldsymbol{x}_j - \boldsymbol{x}_i) \otimes \frac{\partial}{\partial \boldsymbol{x}_i} W(|\boldsymbol{x}_i - \boldsymbol{x}_j|, h)\Big), \end{aligned} \tag{2.45}$$

where $\partial/\partial \boldsymbol{x}_i = (\partial/\partial x_i, \partial/\partial y_i, \partial/\partial z_i)$. The velocity gradient obtained from SPH approximation $\mathbf{W}_{\mathrm{SPH}}$ matches the correct velocity gradient $\mathbf{W}$ only when

$$\sum_j \frac{m_j}{\rho_j}(\boldsymbol{x}_j - \boldsymbol{x}_i) \otimes \frac{\partial}{\partial \boldsymbol{x}_i} W(|\boldsymbol{x}_i - \boldsymbol{x}_j|, h) = \mathbf{I}, \tag{2.46}$$

where $\mathbf{I}$ is an identity matrix. However, Eq. (2.46) is not satisfied around surfaces of bodies, which leads to the incorrect treatment of rigid body rotations.

To solve this problem, Bonet and Lok (1999) introduced the correction matrix $\mathbf{L}_i$ and they replaced $(\partial/\partial \boldsymbol{x}_i)W(|\boldsymbol{x}_i - \boldsymbol{x}_j|, h)$ with $\mathbf{L}_i(\partial/\partial \boldsymbol{x}_i)W(|\boldsymbol{x}_i - \boldsymbol{x}_j|, h)$. This replacement modifies Eq. (2.46) as

$$\begin{aligned}&\sum_j \frac{m_j}{\rho_j}(\boldsymbol{x}_j - \boldsymbol{x}_i) \otimes \mathbf{L}_i \frac{\partial}{\partial \boldsymbol{x}_i} W(|\boldsymbol{x}_i - \boldsymbol{x}_j|, h) \\ &= \Big(\sum_j \frac{m_j}{\rho_j}(\boldsymbol{x}_j - \boldsymbol{x}_i) \otimes \frac{\partial}{\partial \boldsymbol{x}_i} W(|\boldsymbol{x}_i - \boldsymbol{x}_j|, h)\Big)\mathbf{L}_i^{\mathrm{T}} = \mathbf{I}. \end{aligned} \tag{2.47}$$

To satisfy Eq. (2.47), $\mathbf{L}_i$ should be determined as in Eq. (2.26). Introduction of $\mathbf{L}_i$ leads to the equation of the velocity gradient Eq. (2.26) and we can correctly describe rigid body rotations.

To show the validity of the correction matrix, we conduct a simple test simulation of the rotation of an elastic sphere. We utilize the standard SPH method, and model the elastic sphere using about 500 SPH particles. Here, we use the following unit system: The density is scaled using undeformed density ρ_0, the velocity is scaled using the bulk sound speed C_s, and the length is scaled using the radius of the sphere R_s. The shear modulus is set to $\mu = 1.0C_s^2\rho_0$. We initially put a rigid body rotation around z-axis with an angular frequency of $\omega_z = (2\pi/100)(C_s/R_s)$ to the sphere, and calculate the motion of the sphere until one rotation.

Figure 2.3 shows the results of the simulations with and without the correction matrix. As we notice from Fig. 2.3, in the simulation without the correction matrix, the rotation speed decreases with time and the sphere finally does a counter rotation. This nonconservation of the

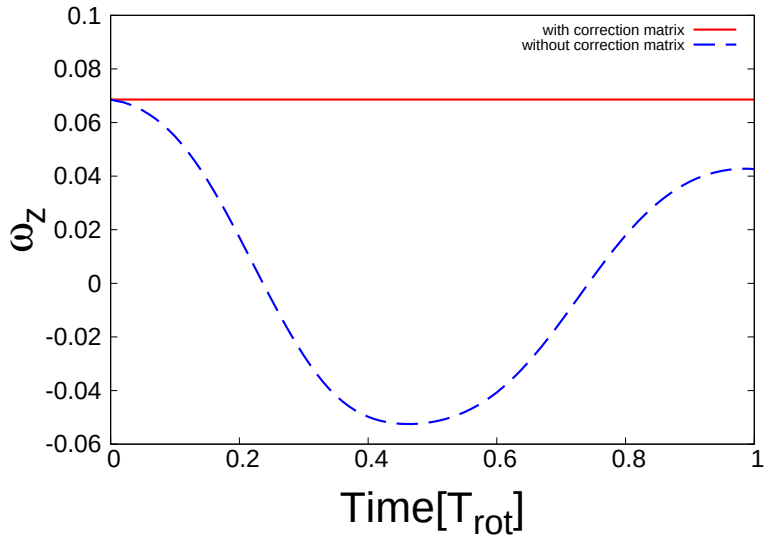

Figure 2.3: Time evolution of the angular frequency of the rotating elastic sphere calculated using the standard SPH method. The horizontal axis represents the elapsed time normalized by the initial rotation period, and the vertical axis represents the angular frequency of the sphere. The red solid curve shows the simulation with the correction matrix (Eq. (2.26)), and the blue dashed curve shows the simulation without the correction matrix (Eq. (2.41)).

rotation speed or angular momentum is caused by unphysical torque due to the error of the velocity gradient. In contrast, in the simulation with the correction matrix, the rotation speed of the sphere is well conserved at least until one rotation. Thus the correction matrix is valid for rigid body rotation problems.

2.2 Tillotson Equation of State

For elastic dynamics, we use the simple equation of state Eq. (2.4) where the pressure is proportional to the density. However, Eq. (2.4) cannot treat the states caused by hypervelocity impacts such as melting, vaporization, and extreme pressure produced by shock waves.

The tillotson equation of state is one of the most frequently used equation of states for numerical simulations of celestial body impacts (e.g., Genda et al. 2012; Jutzi and Asphaug 2015; Leleu et al. 2018). Tillotson (1962) developed the tillotson equation of state for metallic materials through laboratory experiments of impacts. For low-energy and low-deformation states, the tillotson equation of state converges to elastic equation of state Eq. (2.4), and for high-energy states, i.e., vaporized states, this converges to the ideal-gas equation of state. Thus the tillotson equation of state can treat both low-energy elastic solids and high-energy

vaporized gas. The tillotson equation of state has ten material dependent parameters. Later, these material dependent parameters for basalt and ice are derived (O'Keefe and Ahrens 1982a; O'Keefe and Ahrens 1982b; Lange and Ahrens 1983; Nakamura and Fujiwara 1991; Benz and Asphaug 1999).

The tillotson equation of state has three different forms depending on the values of the density and the specific internal energy. For $\rho > \rho_0$ or $u < u_{\rm iv}$, where ρ_0 is the uncompressed density and $u_{\rm iv}$ is the specific internal energy for incipient vaporization, the equation is

$$P = P_s(\rho, u) = \left[a_{\rm til} + \frac{b_{\rm til}}{(u/(u_{0,\rm til}\eta^2) + 1)}\right]\rho u + A_{\rm til}\mu + B_{\rm til}\mu^2, \tag{2.48}$$

where $\eta = \rho/\rho_0$ and $\mu = \eta - 1$. Eq. (2.48) is for compressed or cold expanded states. For $\rho < \rho_0$ and $u > u_{\rm cv}$, where $u_{\rm cv}$ is the specific internal energy for complete vaporization, the equation is

$$P = P_g(\rho, u) = a_{\rm til}\rho u + \left[\frac{b_{\rm til}\rho u}{(u/(u_{0,\rm til}\eta^2) + 1)} + A_{\rm til}\mu e^{-\beta_{\rm til}(\rho_0/\rho - 1)}\right] e^{-\alpha_{\rm til}(\rho_0/\rho - 1)^2}. \tag{2.49}$$

Eq. (2.49) is for expanded and completely vaporized states. Finally, for $\rho < \rho_0$ and $u_{\rm iv} < u < u_{\rm cv}$, the equation is

$$P = \frac{(u - u_{\rm iv})P_g(\rho, u_{\rm cv}) + (u_{\rm cv} - u)P_s(\rho, u_{\rm iv})}{u_{\rm cv} - u_{\rm iv}}. \tag{2.50}$$

Eq. (2.50) is for expanded and partially vaporized states. Here, ρ_0, $u_{\rm iv}$, $u_{\rm cv}$, $u_{0,\rm til}$, $A_{\rm til}$, $B_{\rm til}$, $a_{\rm til}$, $b_{\rm til}$, $\alpha_{\rm til}$, and $\beta_{\rm til}$ are the material dependent tillotson parameters.

Eq. (2.48) converges to elastic equation of state Eq. (2.4) if $u \to 0$ and $\rho \approx \rho_0$. We also notice that $A_{\rm til}$ is corresponding to the bulk modulus for low-temperature and nearly-uncompressed states, and thus the bulk sound speed of the tillotson equation of state for such state is calculated as

$$C_{s,\rm til} = \sqrt{\frac{A_{\rm til}}{\rho_0}}. \tag{2.51}$$

Eq. (2.49) converges to the ideal gas equation of state if $u \to \infty$, and $\alpha_{\rm til}$ and $\beta_{\rm til}$ control the speed of the convergence to the ideal gas equation of state.

2.3 Self Gravity

2.3.1 Self Gravity for SPH Method

The SPH method uses particles that mimic small fractions of fluid or elastic bodies, and each SPH particle has its own mass. Thus, as in the case of N-body orbital simulations, the self-gravity between the i-th and j-th SPH particles is directly calculated as

$$\boldsymbol{g}_{ij,\mathrm{simple}} = -Gm_j \frac{\boldsymbol{x}_i - \boldsymbol{x}_j}{|\boldsymbol{x}_i - \boldsymbol{x}_j|^3}, \tag{2.52}$$

where G is the gravitational constant.

However, Eq. (2.52) is not correct especially for close pairs of particles, because Eq. (2.52) is derived using the assumption that all particles are point masses. As we introduced in Section 2.1.2, SPH particles are not point masses but have a kind of radii. We cannot ignore the broadening of SPH particles especially for the calculation of the self gravity between close pairs of particles. Crucially, Eq. (2.52) diverges if two particles are completely overlapped, but this does not occur if we correctly treat the broadening of SPH particles.

Here, for the calculation of the self gravity between a pair of SPH particles, we only consider the broadening of one particle of the pair. This seems to break the action-reaction principle, which leads to nonconservation of the momentum, but our simulations do not have such problem since we use the same broadening radius, or the smoothing length, for all SPH particles. Then Eq. (2.52) is modified as

$$\begin{aligned} \boldsymbol{g}_{ij} &= -G\hat{m}_j \frac{\boldsymbol{x}_i - \boldsymbol{x}_j}{|\boldsymbol{x}_i - \boldsymbol{x}_j|^3}, \\ \hat{m}_j &= \int_0^{|\boldsymbol{x}_i - \boldsymbol{x}_j|} 4\pi r^2 m_j W(r,h) dr. \end{aligned} \tag{2.53}$$

Eq. (2.53) converges to zero if $|\boldsymbol{x}_i - \boldsymbol{x}_j| \to 0$.

The detailed expression of $\hat{m}_j$ in the case of the Gaussian kernel is

$$\frac{\hat{m}_j}{m_j} = \Big[\mathrm{erf}\Big(\frac{|\boldsymbol{x}_i - \boldsymbol{x}_j|}{h}\Big) - \frac{2|\boldsymbol{x}_i - \boldsymbol{x}_j|}{h\sqrt{\pi}} \exp\Big(-\frac{|\boldsymbol{x}_i - \boldsymbol{x}_j|^2}{h^2}\Big)\Big], \tag{2.54}$$

where erf is the error function, while that in the case of the cubic spline kernel is

$$\frac{\hat{m}_j}{m_j} = \begin{cases} \frac{4}{3}(\Delta_{ij})^3 - \frac{6}{5}(\Delta_{ij})^4 + \frac{1}{2}(\Delta_{ij})^5 & 0 \le \Delta_{ij} < 1 \\ \frac{8}{3}(\Delta_{ij})^3 - 3(\Delta_{ij})^4 + \frac{6}{5}(\Delta_{ij})^5 - \frac{1}{6}(\Delta_{ij})^6 - \frac{1}{15} & 1 \le \Delta_{ij} < 2 \\ 1 & 2 \le \Delta_{ij} \end{cases}, \tag{2.55}$$

where $\Delta_{ij} = |\boldsymbol{x}_i - \boldsymbol{x}_j|$.

If we want to calculate the self gravity, the equation of motion Eq. (2.20) is modified as

$$\frac{dv_i^\alpha}{dt} = \sum_j m_j \Big[\frac{\sigma_i^{\alpha\beta}}{\rho_i^2} + \frac{\sigma_j^{\alpha\beta}}{\rho_j^2} - \Pi_{ij}\delta^{\alpha\beta} \Big] \frac{\partial}{\partial x_i^\beta} W(|\boldsymbol{x}_i - \boldsymbol{x}_j|, h) + \sum_j g_{ij}^\alpha. \tag{2.56}$$

2.3.2 Acceleration Scheme of Computation of Self Gravity

If we directly compute the self gravity between all pairs of SPH particles, the computational cost increases with $\mathcal{O}(N^2)$, where N is the total number of SPH particles. Thus the computational cost is proportional to N^2, which means that the direct computation of the self gravity is difficult especially for large number of particles (typically more than 100,000).

Barnes and Hut (1986) developed a novel technique that utilizes a tree structured subdivision of space, which enables us to reduce the computational cost to $\mathcal{O}(N \log N)$. In this technique, firstly we divide whole space that includes all SPH particles (root cell) into eight subcells, and then we recursively divide each subcell into eight subcells whenever more than several particles occupy the same cell. Then we calculate the total mass and the center of mass of SPH particles that are included in each subcell. Finally we calculate the self gravity on an SPH particle from all other particles as the following recursive procedure:

- We assess whether a subcell is sufficiently faraway from the particle or not with inequality $l/d < \theta$, where l is the side length of this subcell, d is the distance from the particle to the center of mass of this subcell, and θ determines the accuracy and has $0.3 - 1.0$ (A).

- If yes, we calculate the self gravity on the particle from the center of mass of this subcell as the representative gravity from all particles in this subcell.

- If no, we do the same assessment (A) for direct subcells of this subcell.

The assessment (A) is firstly done for the root cell. If leaf cells do not satisfy the condition $l/d < \theta$, then we directly calculate the gravity from the particles in leaf cells. Following this procedure, we can reduce the computational cost to $\mathcal{O}(N \log N)$.

2.4 Fracture Model

In Section 2.1, we introduced how to simulate the dynamics of elastic bodies. Asteroids are certainly elastic bodies if deformation is small. However, asteroids are rocky material, which is fractured under large deformation. Thus we need an appropriate model for the fracture to describe collisional destruction. In this section, we will explain the fracture model for the SPH method introduced by Benz and Asphaug (1995), who follow the fracture model of brittle solids developed by Grady and Kipp (1980).

2.4.1 Concept of Fracture Model

Rock is fractured under large tensile forces. Rocks do not have uniform strength, but there are some weak parts and also some strong parts. Fractures are typically generated at weak parts and extended to other parts.

Benz and Asphaug (1995) assume the existence of explicit incipient flaws in rocky material. The probability distribution of the strength of incipient flaws is expressed as Weibull distribution (Weibull 1939). The probable number of flaws per unit volume that have the failure strain smaller than ϵ is expressed as a power law form

$$n(\epsilon) = k_w \epsilon^{m_w}, \tag{2.57}$$

where k_w and m_w are the Weibull parameters, which can be determined from laboratory experiments. The parameter k_w determines the number of flaws per unit volume and widely varies between various rock types. The parameter m_w determines the dispersion of strengths; small m_w means rocks with widely varying strengths, while large m_w means homogeneous rocks. m_w typically has the value from 6 to 12. Note that the Weibull distribution itself does not have the information about the position or direction of flaws. Using Eq. (2.57), we can also derive a flaw's activation threshold of strain ϵ for a flaw.

Here, we consider a part of a rock. When local tensile strain has exceeded a threshold of strain for a flaw, a crack is generated and allowed to grow. According to Lawn (1993), the speed of crack extension is a constant C_g, which is about 0.4 times the speed of a longitudinal sound wave. Thus the length of the growing crack l_c is expressed as

$$l_c = C_g(t - t_0), \tag{2.58}$$

where t_0 is the time of crack generation. Grady and Kipp (1980) introduced a damage parameter D that has the range of $0-1$. $D=0$ represents an intact rock, while $D=1$ represents a completely damaged rock that does not feel any tensile stress. A rock with $D=0.5$ feels only half of the original tensile stress calculated from elastic dynamics equations. Benz and Asphaug (1995) defined D as the local fraction of volume that has relieved stress by cracks. According to Walsh (1965), the volume that has relieved stress by a crack approximately equals to the volume of the sphere with the radius of the crack length. Thus D is expressed as

$$D = \frac{(4/3)\pi l_c^3}{V_s}, \tag{2.59}$$

where $V_s = (4/3)\pi R_s^3$ is the volume of the part of a rock that we consider now. Using Eqs. (2.58) and (2.59), we can derive the differential equation for D as

$$\frac{dD^{1/3}}{dt} = \frac{C_g}{R_s}. \tag{2.60}$$

Tensile force, that is, negative pressure is relieved by fractures. According to the definition of D, the pressure is modified as

$$P_D = \begin{cases} (1-D)P & P < 0 \\ P & P > 0 \end{cases}. \tag{2.61}$$

P_D is used in the equation of motion and so on as the pressure. Shear force, that is, the deviatoric stress is also affected by fractures. However, the deviatoric stress in a part with $D=1$ is mainly determined by the friction between completely destructed rock. Thus we leave the explanation of the treatment of the deviatoric stress for damaged rock to Section 2.5.

2.4.2 SPH Implementation of Fracture Model

According to Benz and Asphaug (1995), we explicitly assign threshold strains for crack activation to each SPH particle when we prepare initial conditions. We consider an asteroid with total volume of V. The weakest flaw has the threshold strain of

$$\epsilon_1^{\rm act} = \left[\frac{1}{k_w V}\right]^{1/m_w}. \tag{2.62}$$

In the same manner, the p-th weakest flaw has the threshold strain of

$$\epsilon_p^{\rm act} = \left[\frac{p}{k_w V}\right]^{1/m_w}. \tag{2.63}$$

We randomly choose an SPH particle and assign a threshold $\epsilon_p^{\rm act}$ with $p = 1$ to this particle, and next we choose another SPH particle randomly and assign a threshold $\epsilon_p^{\rm act}$ with $p = 2$, and next we choose another one and assign that with $p = 3 \cdots$. We continue this procedure until all SPH particles have at least one activation threshold. Each SPH particle has, on average, $\ln N$ flaws, where N is the number of SPH particles. Hereafter, we represent the threshold strain for the p-th weakest flaw assigned to the i-th SPH particle as $\epsilon_{i,p}^{\rm act}$.

According to Melosh et al. (1992) or Benz and Asphaug (1995), the local strain at the i-th SPH particle is calculated from the damage-relieved stress tensor $\sigma_{D,i}^{\alpha\beta} = -P_{D,i}\delta^{\alpha\beta} + S_{D,i}^{\alpha\beta}$, where $S_{D,i}^{\alpha\beta}$ is the damage-relieved deviatoric stress tensor and will be introduced in Section 2.5. We firstly calculate the three principal stresses $\sigma_{D,i}^1$, $\sigma_{D,i}^2$, and $\sigma_{D,i}^3$, which are the eigenvalues of the damage-relieved stress tensor. Then we find the maximum principal stress $\sigma_{D,i}^{\rm m}$, which is the maximum tensile stress among the three principal stresses. The local strain at the i-th SPH particle ϵ_i is calculate as

$$\epsilon_i = \frac{\sigma_{D,i}^{\rm m}}{(1 - D_i)E}, \tag{2.64}$$

where $E = 9K\mu/(3K + \mu)$ is the Young's modulus.

If at least one of the flaws inside of the i-th particle is activated, i.e, at least one of $\epsilon_{i,p}^{\rm act}$ is smaller than ϵ_i, the damage parameter D_i increases according to

$$\frac{dD_i^{1/3}}{dt} = \frac{C_g}{R_s}. \tag{2.65}$$

Here, $R_s = 4h$ for the Gaussian kernel and $R_s = 2h$ for the cubic spline kernel. However, D_i is only allowed to accumulate to a maximum value given by

$$D_i^{\rm max} = \left(\frac{n_i}{n_i^{\rm tot}}\right)^{1/3}, \tag{2.66}$$

where $n_i^{\rm tot}$ is the total number of flaws inside of the i-th particle, and n_i is the number of activated flaws inside of the i-th particle. If multiple flaws are activated, the damage parameter will increase faster, and thus we multiply n_i to the right hand side of Eq. (2.65). According to Eq. (2.61), the pressure of the i-th particle is modified as

$$P_{D,i} = \begin{cases} (1 - D_i)P_i & P_i < 0 \\ P_i & P_i > 0 \end{cases}. \tag{2.67}$$

2.5 Pressure Dependent Failure Model and Friction Model

Benz and Asphaug (1995) set $S_{D,i}^{\alpha\beta} = (1-D)S_i^{\alpha\beta}$ for damaged SPH particles. This means that completely damaged SPH particles with $D = 1$ behave like fluid that does not feel any tensile and shear stresses. However, completely damaged rocks, or granular material, have the friction between granular particles. The frictional forces are shear forces and play the crucial role for the shape formation of rubble pile bodies. Jutzi (2015) introduced the friction model to the SPH method, and he also introduced the pressure dependent failure model for intact rocks. In this section, we will introduce these models. We also show the results of the test simulations using our SPH code with the friction model, since the friction is the most important effect for the formation of the shapes of rubble pile bodies.

2.5.1 Description of Models

Actual metals are not perfect elastic bodies but plastic deformation occurs under large deformation. It is called as yielding, and the criterion of yielding for metallic material is described by the pressure independent von Mises yield criterion. However, yielding criterion of rocky material is pressure dependent, and the shear strength of intact rocks increases with increasing confining pressure. According to Collins et al. (2004) or Jutzi (2015), the pressure dependent yielding strength for the intact rock at the i-th SPH particle Y_i is expressed as

$$\begin{aligned} Y_i &= Y_{I,i} = \Big(Y_0 + \frac{\mu_I P_{\mathrm{pos},i}}{1 + \mu_I P_{\mathrm{pos},i}/(Y_M - Y_0)}\Big)\Big(1 - \frac{u_i^{'}}{u_{\mathrm{melt}}}\Big), \\ P_{\mathrm{pos},i} &= \max[P_i, 0], \\ u_i^{'} &= \min[u_i, u_{\mathrm{melt}}], \end{aligned} \tag{2.68}$$

where Y_0 and Y_M are the yielding strength at zero pressure and infinite pressure, respectively, μ_I is the coefficient of internal friction, and u_{melt} is the specific internal energy for melting.

For completely damaged rocks, the yielding strength is determined by the friction. As we know, the friction is proportional to confined pressure. Thus the yielding strength for the completely damaged rock at the i-th SPH particle is expressed as

$$Y_i = Y_{D,i} = \mu_d P_{i,\mathrm{pos}}, \tag{2.69}$$

where μ_d is the friction coefficient, which is the most important parameter for our study. The angle of friction is defined as $\phi_d = \arctan(\mu_d)$ and generally the same as the angle of repose. Note that μ_d here merely determines the ratio of frictional stress to confined pressure.

For partially damaged rocks, we use the following yielding strength that allows a smooth transition between Eqs. (2.68) and (2.69) according to Jutzi (2015):

$$Y_i = (D_i - 1)Y_{I,i} + D_i Y_{D,i}. \tag{2.70}$$

Here, we use the following limitations $Y_{D,i} \leq Y_{I,i}$ and $Y_i \leq Y_{I,i}$.

To implement the yielding, we usually utilize the second invariant of the deviatoric stress tensor $J_{2,i}$, which is computed as

$$J_{2,i} = \frac{1}{2} S_i^{\alpha\beta} S_i^{\alpha\beta}. \tag{2.71}$$

$\sqrt{J_{2,i}}$ is a kind of the magnitude of the deviatoric stress tensor $S_i^{\alpha\beta}$, and $S_i^{\alpha\beta}/\sqrt{J_{2,i}}$ represents a kind of the unit vector of this deviatoric stress tensor. Thus $Y_i S_i^{\alpha\beta}/\sqrt{J_{2,i}}$ has the magnitude of Y_i and the direction of $S_i^{\alpha\beta}$; $Y_i S_i^{\alpha\beta}/\sqrt{J_{2,i}}$ represents the shear stress under the yielding. If the magnitude $\sqrt{J_{2,i}}$ is larger than Y_i, the yielding occurs and the deviatoric stress tensor should be modified to $Y_i S_i^{\alpha\beta}/\sqrt{J_{2,i}}$. Thus we modify the deviatoric stress tensor as

$$\begin{aligned} S_{D,i}^{\alpha\beta} &= f S_i^{\alpha\beta}, \\ f &= \min\Big[\frac{Y_i}{\sqrt{J_{2,i}}}, 1\Big]. \end{aligned} \tag{2.72}$$

In each time step, we also modify $S_i^{\alpha\beta}$ as $S_i^{\alpha\beta} = S_{D,i}^{\alpha\beta}$.

2.5.2 Test Simulations for Friction Model

To confirm the validity of the friction model implemented in our simulation code, we conduct the test simulations that reproduce cliff collapse experiments following the test simulations in Jutzi (2015). Lajeunesse et al. (2005) conducted the laboratory experiments of the cliff collapse of glass beads in a two-dimensional configuration. They conducted the experiments with grass beads with diameters of 1.15 mm and 3 mm, various initial height of cliff H_0, and various initial ratios of length of cliff L_0 to height of cliff H_0. As a result, they found that final configurations are only depending on the friction angle of granular material and the initial aspect ratio L_0/H_0.

They also found that the profiles of cliffs at different times and different experiments are barely distinguishable when the profiles are scaled by L_0 and the times are scaled by the characteristic time $\tau = \sqrt{H_0/g}$, where g is the gravitational acceleration on surfaces of the Earth.

For the simulation of the cliff collapse, we use the standard SPH method and the cubic spline kernel. The damage parameters of all SPH particles are initially set to unity, and thus SPH particles mimic granular material. The friction coefficient is set to $\mu_d = \tan(20.9°)$ according to Jutzi (2015). We use the simple equation of state Eq. (2.4) with $C_s = 500\,\mathrm{m/s}$ and $\rho_0 = 1500\,\mathrm{kg/m^3}$, which are the typical values for granular material. We do not calculate the self gravity, but add the downward gravitational acceleration g to the equation of motion of SPH particles. To mimic the wall and floor in the experiments, we put several layers of SPH particles with fixed positions on just outside of the simulation space. We set $L_0 = 1,000\,\mathrm{m}$ to avoid too small time steps (see Eq. (2.34)). Although the length of cliff is much larger than the experimental scale, this is not the problem because results can be scaled by L_0 and τ.

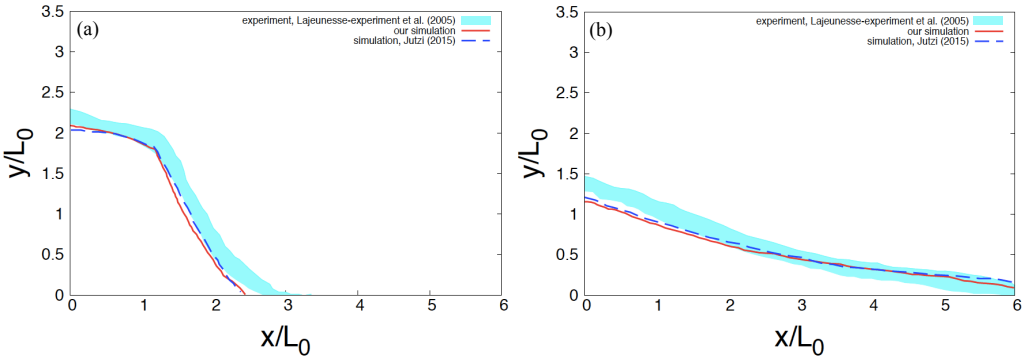

Figure 2.4: The profiles of collapsing cliff with $H_0/L_0 = 3.2$ at (a) $t = \tau$ and (b) $t = \infty$. The red solid curves show the results of our simulations, the blue dashed curves show the results of the simulations of Jutzi (2015), and the cyan shaded regions show the results obtained from the experiments of Lajeunesse et al. (2005). The results of the experiments are shown in shaded regions because we describe the profiles obtained from several experiments with the same L_0/H_0 and the friction angle together, which have small scatters.

Figure 2.4 shows the comparison between our simulations, the simulations of Jutzi (2015), and the experiments of Lajeunesse et al. (2005), and we notice that these results agree well with each other. Therefore, our simulation code can well reproduce behaviors of granular bodies.

2.6 Parallelization of Simulation Code Using FDPS

In this dissertation, we reproduce the three-dimensional shapes of asteroids through numerical simulations using the SPH method. Three-dimensional simulations require larger number of SPH particles compared to one- or two-dimensional simulations. Especially, to investigate the shapes of smaller remnants produced through disruptive impacts, we need much larger number of SPH particles of about several millions. We cannot complete such high-resolution simulations with a normal laptop PC within acceptable computational time, and we need to utilize supercomputers. This means that we have to parallelize our simulation code to utilize many CPU cores.

Usual supercomputers are composed of PC clusters with distributed memories. Thus for efficient parallelization, we have to consider the amount of sending/receiving data and load balancing between CPU cores. If the amount of sending/receiving data is too large or workload balance is not good, the parallelization efficiency becomes significantly low, which means that it is meaningless to utilize many CPU cores. However, in general, it is very difficult to parallelize particle-based simulation codes so that they achieve high parallelization efficiency, because particles move from one CPU domain to the other. Thus we need to reassign SPH particles to other CPU cores so as to keep good workload balance. Moreover, the simulation codes that calculate the self gravity using the tree method (see Section 2.3.2) are so complex that usual researchers cannot parallelize such codes with acceptable efforts.

To support the parallelization of codes based on particle methods, the particle simulator research team, AICS, RIKEN developed Framework for Developing Particle Simulator (FDPS: Iwasawa et al. 2015, 2016). FDPS is a framework to support developing efficiently-parallelized simulation codes that are based on particle methods. FDPS provides functions for exchanging information of particles between CPUs and those for load balancing. FDPS also provides a function to calculate the self gravity using the tree method shown in Section 2.3.2. We parallelize our simulation code using FDPS. Therefore, thanks to FDPS, we effectively use parallel computers for our simulations.

We checked the parallelization efficiency of our simulation code. We calculated the parallelization efficiency through the strong scaling, i.e., we measured the elapsed times needed to simulate the problem with fixed number of SPH particles but with various number of CPU cores. We used the standard SPH method with the cubic spline kernel. We used about 10^8 SPH particles and solved an elastic problem for 10 time steps. We utilized XC30 system of

Center for Computational Astrophysics, National Astronomical Observatory of Japan.

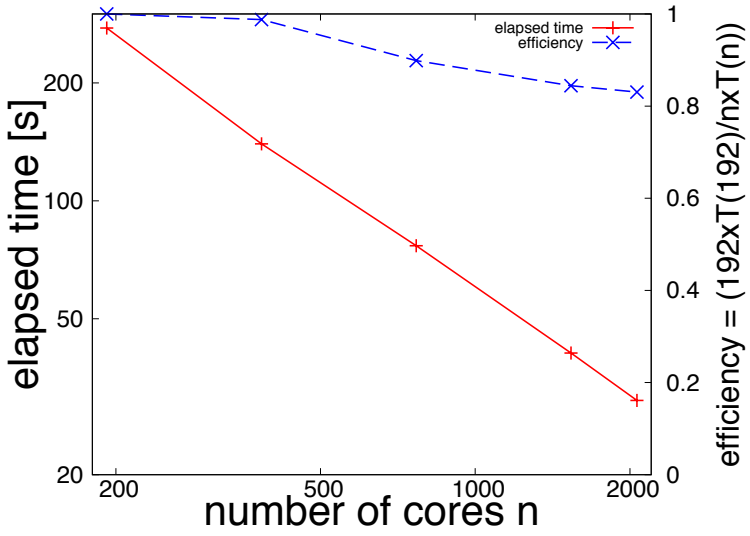

Figure 2.5: Parallelization efficiency of our simulation code. The red solid line shows elapsed times and the blue dashed line shows parallelization efficiency defined as Eq. (2.73). The horizontal axis represents the number of utilized CPU cores, the left vertical axis represents the elapsed time, and the right vertical axis represents the parallelization efficiency.

We vary utilized CPU cores from 192 to 2,064. The parallelization efficiency is calculated based on the elapsed time when we use 192 cores as

$$\text{efficiency} = 192T(192)/(nT(n)), \tag{2.73}$$

where n is the number of utilized CPU cores and $T(n)$ shows the elapsed time to simulate the elastic problem when we use n CPU cores. From Fig. 2.5, we notice that the elapsed time decreases linearly with increasing the number of utilized CPU cores. We also notice that the parallelization efficiency when we use 2,064 CPU cores is about 0.8, which is the quite high efficiency. This means that the elapsed time with 2064 CPU cores is about nine times shorter than that with 192 CPU cores. Thus, our simulation code is well efficiently parallelized thanks to FDPS.

2.7 Summary of Utilized Methods and Parameters

As we explain in Section 2.1.6, the tensile instability is insignificant for simulations of asteroidal impacts. Thus hereafter, we utilize the standard SPH method that needs low computational

costs to conduct detailed parameter surveys or high-resolution simulations. We also utilize the following methods or models: the leap-frog integrator (Section 2.1.5), the correction matrix for rigid body rotations (Section 2.1.7), the tillotson equation of state (Section 2.2), the self gravity (Section 2.3), the fracture model (Section 2.4), the pressure dependent failure model (Section 2.5), and the friction model (Section 2.5).

μ(Pa)	K(Pa)
2.27×10^{10}	2.67×10^{10}

Table 2.2: Parameters for elastic dynamics. μ shows the shear modulus and K shows the bulk modulus.

ρ_0(kg/m^3)	$u_{\rm iv}$(J/kg)	$u_{\rm cv}$(J/kg)	$u_{0,\rm til}$(J/kg)	$A_{\rm til}$(Pa)	$B_{\rm til}$(Pa)	$a_{\rm til}$	$b_{\rm til}$	$\alpha_{\rm til}$	$\beta_{\rm til}$
2.7×10^3	4.72×10^6	1.82×10^7	4.87×10^8	2.67×10^{10}	2.67×10^{10}	0.5	1.5	5.0	5.0

Table 2.3: Tillotson parameters for basalt. These values are listed in Benz and Asphaug (1999).

k_w(m^{-3})	m_w
4.0×10^{35}	9.0

Table 2.4: Parameters for the fracture model, or Weibull parameters. These values are listed in Benz and Asphaug (1999).

Y_0(Pa)	Y_M(Pa)	μ_I	$u_{\rm melt}$(J/kg)
1.0×10^8	3.5×10^9	1.5	3.4×10^6

Table 2.5: Parameters for the pressure dependent failure model. The values for Y_0, Y_M, and μ_I are taken from Jutzi (2015). The value for $u_{\rm melt}$ is listed in Benz and Asphaug (1999).

Throughout this dissertation, we assume the material of asteroids as basalt. There are many material dependent parameters required for the simulations of asteroidal collisions such as the shear modulus or tillotson parameters. Here, we summarize the parameters utilized for the simulations in following sections. These parameters are summarized in Table 2.2 - 2.5. Note that we vary the friction angle in Chapter 5 and we do not list the value of the friction angle here.

Chapter 3

Results: Shapes of Impact Outcomes

In this chapter, we introduce the results of our simulations that investigate the shapes of asteroids formed through various impacts. DAMIT database provides almost all of the shapes of the asteroids with the diameters larger than 100 km. Thus, throughout this chapter, the radius of target asteroids is fixed to 50 km to allow us to directly compare the results of our simulations with the shapes of actual asteroids. We vary the impact angle, the impact velocity, and the ratio of the mass of impactor asteroids to that of target asteroids, and we conduct various impact simulations. Some parts of this chapter are based on Sugiura et al. (2018a).

3.1 Initial Conditions of Impacts

For simplicity, we use a sphere of basalt with zero rotation as an initial asteroid. The radius of target asteroids is set to $R_t = 50\,\mathrm{km}$, and thus the mass of target asteroids is $M_{\mathrm{target}} = 4\pi\rho_0 R_t^3/3$, where ρ_0 is the uncompressed density of basalt, which is the same as ρ_0 of the tillotson parameter.

For a basaltic asteroid with the radius of 50 km or smaller, the density at the center in hydrostatic equilibrium is almost the same as uncompressed density. Thus we set initial asteroids to be uniform spheres with the mean density of basalt. To do so, an isotropic SPH particle distribution is more preferable than, for example, particles placed on cubic lattices, so that we prepare a particle distribution with uniform disposition from a random distribution. Detailed procedures to produce the uniform and isotropic particle distribution are as follows: Firstly we put SPH particles within a cubic domain with periodic boundary conditions randomly so that desired resolution and desired mean density are achieved. Secondly we let the particles move under the forces anti-parallel to density gradients that make the particle distribution uniform until the standard deviation of density becomes less than 0.1% of the mean density. Finally,

we remove particles outside a shell with the desired radius, and then a uniform and isotropic sphere is obtained.

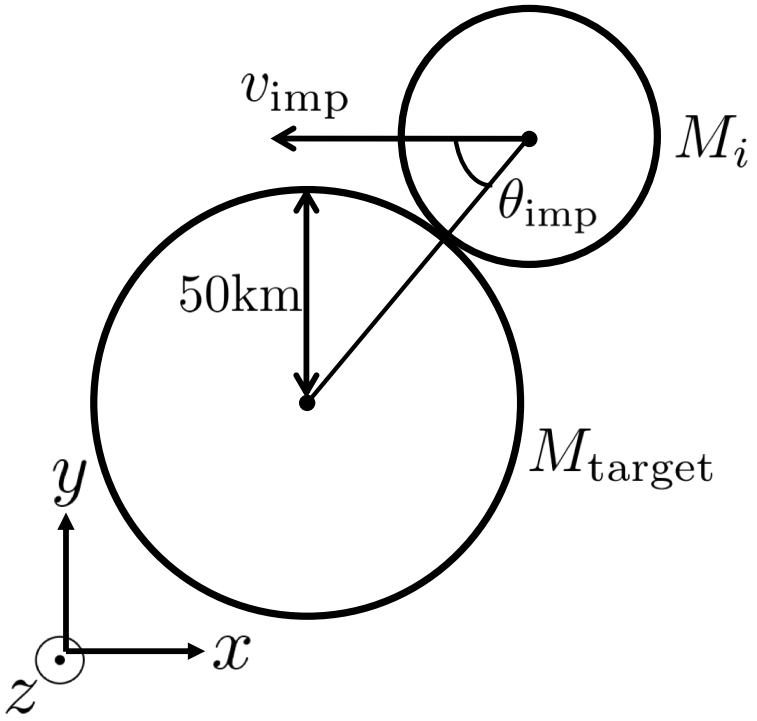

Figure 3.1: Impact geometry, coordinate system, and the definition of the impact velocity $v_{\rm imp}$ and angle $\theta_{\rm imp}$.

We define the impact velocity $v_{\rm imp}$ as the relative velocity between two asteroids at the time of impact, and the impact angle $\theta_{\rm imp}$ as the angle between the line joining centers of two asteroids and the relative velocity vector at the time of impact. Thus the impact angle of 0° means a head-on collision, and that of 90° means a grazing collision. We also define the mass ratio $q = M_i/M_{\rm target}$, where $M_i = (4/3)\pi R_i^3 \rho_0$ is the mass of impactor asteroids and R_i is the radius of impactor asteroids. Fig. 3.1 schematically shows the definition of the impact velocity and angle. At the beginning of simulations, centers of two asteroids are apart at a distance of $2(R_t + R_i)$.

We assume the friction coefficient for completely damaged material of $\mu_d = \tan(40°) = 0.839$, which corresponds to a material with the angle of friction of $\phi_d = 40°$. Note that the angle of friction of lunar sand is estimated to be $30° - 50°$ (e.g., Heiken et al. 1991), which is consistent with the angle of friction estimated from surface slopes of the asteroid Itokawa (Fujiwara et al. 2006).

3.2 Analysis of Results

We conduct simulations of impacts and subsequent gravitational reaccumulation over a period of 1.0×10^5 s. The typical timescale of reaccumulation is estimated as $t_{\rm acc} = 2R_t/v_{\rm esc,t}$, where $v_{\rm esc,t}$ is the escape velocity from target asteroids. The value of $t_{\rm acc}$ is calculated as

$$t_{\rm acc} = \frac{2R_t}{v_{\rm esc}} = \sqrt{\frac{3}{2\pi G\rho_0}} \simeq 1600\,{\rm s}. \tag{3.1}$$

Thus 1.0×10^5 s is about 100 times longer than the typical timescale of reaccumulation, and we also confirmed that gravitational reaccumulation is sufficiently finished after 1.0×10^5 s.

After collisional simulations, we identify remnants using a friends-of-friends algorithm (e.g., Huchra and Geller 1982). We find swarms of SPH particles with spacing less than $1.5h$ and swarms are identified with remnants. Then we evaluate the shapes of remnants. To do so, we quantitatively measure the axis lengths of remnants using the inertia moment tensor. We approximate a remnant as an ellipsoid that has the same inertia moment tensor and mass, and then we identify the axis lengths of the ellipsoid with those of the remnant. The inertia moment tensor of a remnant composed of k SPH particles is calculated as

$$I^{\alpha\beta} = \sum_k m_k \Big[(x_k^\gamma - x_{\rm CoM}^\gamma)(x_k^\gamma - x_{\rm CoM}^\gamma)\delta^{\alpha\beta} - (x_k^\alpha - x_{\rm CoM}^\alpha)(x_k^\beta - x_{\rm CoM}^\beta) \Big], \tag{3.2}$$

where $\boldsymbol{x}_{\rm CoM}$ is the position vector at the center of mass of the remnant. Then, three principal moments of inertia I_1, I_2, and I_3 are obtained from $I^{\alpha\beta}$. Here, $I_1 > I_2 > I_3$. For a uniform ellipsoid with the length of major axis a, intermediate axis b, and minor axis c, the three principal moments of inertia are represented as

$$\begin{aligned} I_1 &= \frac{1}{20}(a^2 + b^2)M, \\ I_2 &= \frac{1}{20}(a^2 + c^2)M, \\ I_3 &= \frac{1}{20}(b^2 + c^2)M, \end{aligned} \tag{3.3}$$

where M is the mass of this ellipsoid. Eq. (3.3) is rewritten as

$$a = \sqrt{\frac{10(I_1 + I_2 - I_3)}{M}},$$
$$b = \sqrt{\frac{10(I_1 - I_2 + I_3)}{M}},$$
$$c = \sqrt{\frac{10(-I_1 + I_2 + I_3)}{M}}. \tag{3.4}$$

Therefore, we obtain I_1, I_2, I_3, and M of remnants through simulations, and then derive those a, b, and c from Eq. (3.4).

It should be noted that the bodies resulting from simulations are not perfect ellipsoids. The obtained axis ratios are thus different from those measured in, e.g., the bottom-up method that is usually used in laboratory experiments (e.g., Fujiwara et al. 1978). In this method, the axis lengths of a remnant are defined as distances between a pair of parallel plates that contact with the remnant. The detailed procedure to measure the axis lengths in the bottom-up method is as follows: Firstly, we identify the minor axis length c with the minimum distance among distances between parallel plates, and define the direction normal to the plates when the distance is minimum as the minor axis. Secondly, we identify the intermediate axis length b with the minimum distance among distances between parallel plates when the directions normal to the plates are perpendicular to the minor axis, and also define the intermediate axis. Finally, we identify the major axis length a as the distance between the parallel plates when the direction normal to the plates is perpendicular to both the minor and intermediate axes.

As shown in Appendix A of Michikami et al. (2018), the difference of axis ratios obtained from different methods is at most about 0.1; the axis ratios include measurement errors of ~ 0.1. If the difference of the axis ratios of two different remnants are larger than 0.1, these remnants have quantitatively different shapes.

3.3 Equal-Mass and Non-Destructive Impacts

In this section, we will introduce the results of our simulations of equal-mass and non-destructive impacts. We set the mass of impactor asteroids to $M_i = M_{\rm target}$, and we conduct various impact simulations with various impact velocities and angles. We focus on non-destructive impacts that have the mass of the largest remnants larger than $0.4M_{\rm target}$, and investigate the shapes of the largest remnants. The total number of SPH particles for each impact simulation is set to $100,000$, which is relatively low resolution but enables to reveal the detailed dependence of

resultant shapes on impact velocities and angles. The validity of this number of SPH particles is investigated in Section 3.3.1.

3.3.1 Resolution Dependence on the Resultant Shape

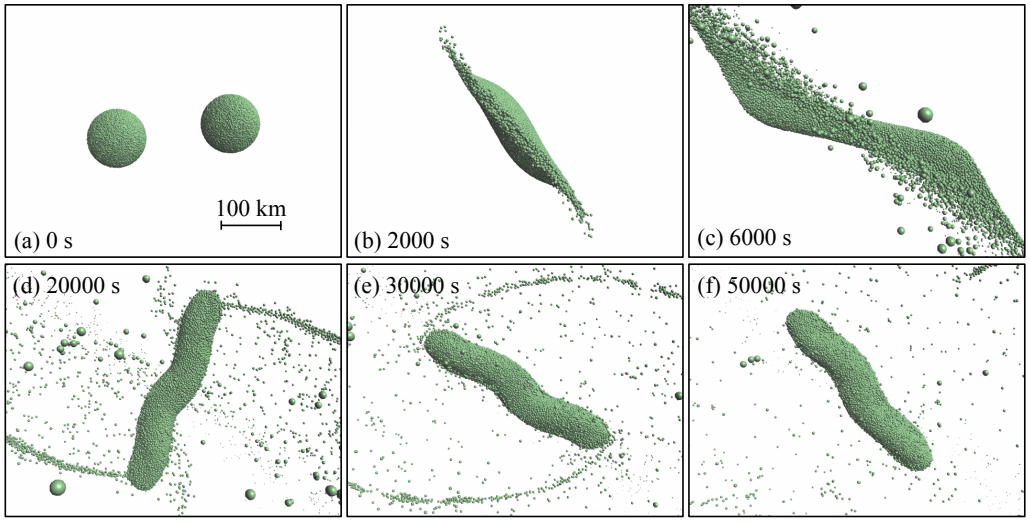

Figure 3.2: Snapshots of the impact simulation with the impact angle $\theta_{\rm imp}$ of 15°, the impact velocity $v_{\rm imp}$ of 200 m/s and the total number of SPH particles $N_{\rm total}$ of 1×10^5 at 0.0 s(a), 2.0×10^3 s(b), 6.0×10^3 s(c), 2.0×10^4 s(d), 3.0×10^4 s(e), and 5.0×10^4 s(f). Scale on the panel (a) is also valid for all the panels (b)-(f). This figure is the same as Fig. 2 of Sugiura et al. (2018a).

Figure 3.2 represents snapshots of the SPH simulation with the impact angle $\theta_{\rm imp}$ of 15° and the impact velocity $v_{\rm imp}$ of 200 m/s. In Fig. 3.2b, the collision induces shattering of asteroids. Then two asteroids are stretched in the direction perpendicular to the line joining centers of two contacting asteroids and fragments are ejected (Fig. 3.2c). Ejected materials are mainly reaccumulated from the direction of the long axis of the largest remnant (Fig. 3.2d). Finally a very elongated shape with the ratio b/a of about 0.2 is formed (Fig. 3.2f). The accretion on the largest body is mostly done within $t \sim 5.0 \times 10^4$ s.

Figure 3.3 shows the shapes of the largest remnants at 5.0×10^4 s with three different resolutions (the total number of SPH particles $N_{\rm total}$ of 5×10^4(a), 2×10^5(b), and 8×10^5(c)). Even if $N_{\rm total}$ becomes ten times larger, the characteristic of elongated shapes does not change. Figure 3.4 shows the dependence of the mass and axis ratios of the largest remnants on the number of SPH particles $N_{\rm total}$. The mass of the largest remnants slightly decreases with

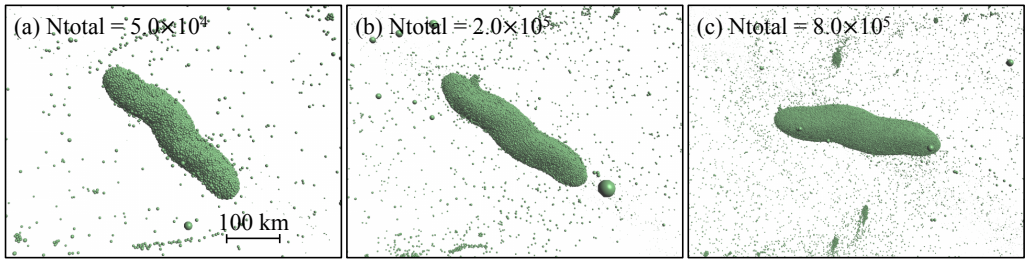

Figure 3.3: Shapes of the largest remnants at 5.0×10^4 s for the impact simulations with $v_{\rm imp} = 200\,{\rm m/s}$, $\theta_{\rm imp} = 15°$, and $N_{\rm total} = 5 \times 10^4$(a), 2×10^5(b), and 8×10^5(c), respectively. This figure is the same as Fig. 3 of Sugiura et al. (2018a).

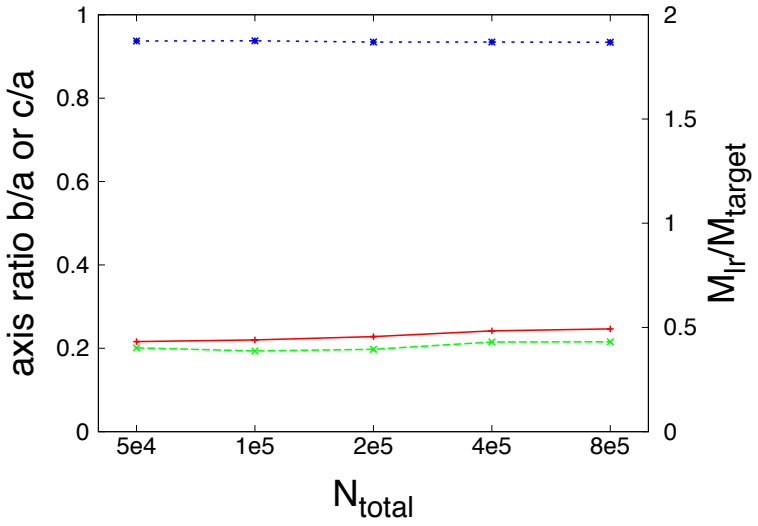

Figure 3.4: Dependence of the mass and axis ratios of the largest remnants on the number of SPH particles $N_{\rm total}$ for the impact with $\theta_{\rm imp} = 15°$ and $v_{\rm imp} = 200\,{\rm m/s}$. The red solid line shows the ratio b/a, the green dashed line shows the ratio c/a, and the blue dotted line shows the mass of the largest remnants $M_{\rm lr}$ normalized by the mass of an initial asteroid $M_{\rm target}$. The left vertical axis represents the axis ratios, and the right vertical axis represents the mass of the largest remnant. This figure is the same as Fig. 4 of Sugiura et al. (2018a).

increasing $N_{\rm total}$ because the numerical dissipation by the artificial viscosity decreases for higher resolutions. This tendency is the same as the results of Genda et al. (2015). The axis ratios slightly increase with increasing $N_{\rm total}$, and the difference of b/a between $N_{\rm total}$ of 5×10^4 and 8×10^5 is about 0.03. Difference of axis ratios less than 0.1 is unimportant for the analysis of asteroidal shapes because difference of axis measurements also causes such minor errors as discussed above. Therefore, the number of SPH particles of 10^5 is sufficient to capture at least the feature of shapes for non-destructive impacts.

3.3.2 Mass of the Largest Remnants

Hereafter, we use 10^5 SPH particles for a simulation, and we measure the mass and axis ratios of the largest remnants at 1.0×10^5 s after impacts.

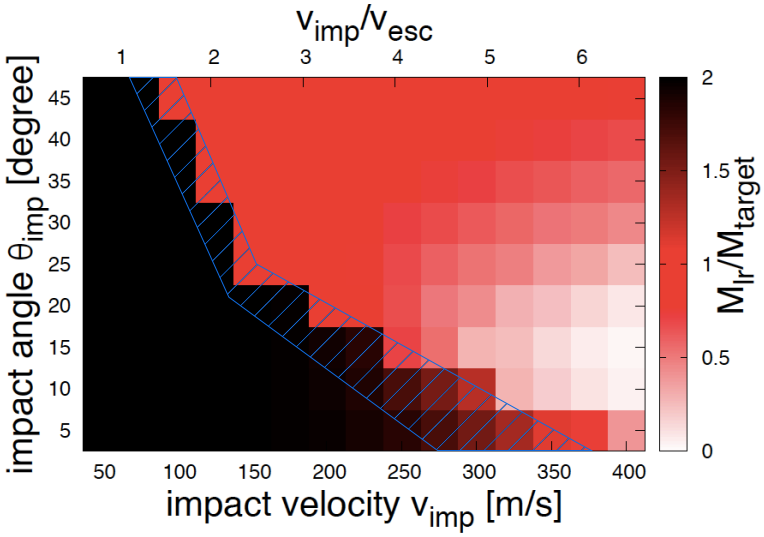

Figure 3.5: Dependence of the mass of the largest remnants on the impact velocity $v_{\rm imp}$ and the impact angle $\theta_{\rm imp}$. The upper horizontal axis represents $v_{\rm imp}$ normalized by two-body escape velocity $v_{\rm esc}$. The color shows the mass of the largest remnants $M_{\rm lr}$ normalized by the mass of an initial asteroid $M_{\rm target}$. Thus $M_{\rm lr}/M_{\rm target} = 2.0$ means complete merging. The hatched region approximately shows the transitional parameters from merging collisions to hit-and-run or elosive collisions. This figure is the same as Fig. 5 of Sugiura et al. (2018a).

Figure 3.5 shows the mass of the largest remnants $M_{\rm lr}$ formed through collisions with $v_{\rm imp} = 50\,{\rm m/s} - 400\,{\rm m/s}$ and $\theta_{\rm imp} = 5^\circ - 45^\circ$. The increment of the velocity is 25 m/s, and that of the angle is 5°. For $\theta_{\rm imp} \leq 15^\circ$, $M_{\rm lr} \sim 2M_{\rm target}$ due to collisional merging for low $v_{\rm imp}$, and $M_{\rm lr}$ gradually decreases with increasing $v_{\rm imp}$ because of erosive collisions. The impact parameters for the transition between merging and erosive collisions are highlighted in Fig. 3.5. On the other hand, for $\theta_{\rm imp} \geq 20^\circ$, sharp variation in $M_{\rm lr}$ from $\sim 2M_{\rm target}$ to $\sim M_{\rm target}$ is seen around $v_{\rm imp} \sim 100\,{\rm m/s}$. This is because collisions with high $v_{\rm imp}$ result in a "hit-and-run" process where two asteroids moving apart after the collision. The transition parameters between merging and hit-and-run collisions are also highlighted in Fig. 3.5. Erosive nature for low $\theta_{\rm imp}$ and merging/hit-and-run nature for high $\theta_{\rm imp}$ are also observed in previous collisional simulations (Agnor and Asphaug 2004; Leinhardt and Stewart 2012).

For $v_{\rm imp} > 300\,{\rm m/s}$, $M_{\rm lr}$ has a minimum value at $\theta_{\rm imp} \approx 15^\circ$ (see Fig. 3.5). For head-on

collisions, the most of the impact energy is dissipated and not transformed to the ejection processes, which results in large $M_{\rm lr}$. For slightly higher $\theta_{\rm imp}$, the impact energy is more effectively used for ejection, and thus the mass of the largest remnant $M_{\rm lr}$ becomes smaller. However, for much higher $\theta_{\rm imp}$, the velocity component normal to colliding bodies is small, so that the impact energy is not effectively used for destruction and ejection, which results in larger $M_{\rm lr}$. Therefore, an intermediate $\theta_{\rm imp}$ yields smallest $M_{\rm lr}$.

We note that collisions with $v_{\rm imp} > 400\,{\rm m/s}$ and low $\theta_{\rm imp}$ result in $M_{\rm lr} \leq 0.1 M_{\rm target}$. The largest remnants resulting from such impacts are composed of less than about 5,000 SPH particles, and resolved by less than 20 SPH particles along each axis direction. Thus axis ratios obtained from such a small number of SPH particles are not measured accurately. Our simulations of impacts with parameters outside those of Fig.3.5 show that impacts with $v_{\rm imp} = 500\,{\rm m/s}$ and $\theta_{\rm imp} = 5 - 25^\circ$ result in $M_{\rm lr}/M_{\rm target} = 0.01 - 0.07$. For $\theta_{\rm imp} > 45^\circ$, only edges of asteroids are destroyed by collisions rather than overall deformation, so that the investigation of such impact angles is not interesting. For example, our impact simulations with $\theta_{\rm imp} = 60^\circ$ and $v_{\rm imp} = 100-500\,{\rm m/s}$ result in $M_{\rm lr}/M_{\rm target} = 0.91-0.99$, which means merely partial destruction. Therefore, we investigate the collisions with $50\,{\rm m/s} \leq v_{\rm imp} \leq 400\,{\rm m/s}$ and $5^\circ \leq \theta_{\rm imp} \leq 45^\circ$, because in this parameter range the resolution of the largest remnants is mainly sufficient and significant shape deformation occurs.

3.3.3 Characteristic Shapes Formed by Collisions

As a result of impact simulations with $50\,{\rm m/s} \leq v_{\rm imp} \leq 400\,{\rm m/s}$ and $5^\circ \leq \theta_{\rm imp} \leq 45^\circ$, we find that resultant shapes of the largest remnants are roughly classified into five categories. Here, we introduce the results of typical impacts to form five different characteristic shapes, catastrophic collisions, and the impacts with the second collision.

Bilobed Shapes

If the impact velocity is very small, the initial spherical shapes of colliding bodies are preserved and collisional merging forms bilobed shape. Fig. 3.6 shows impact snapshots with $v_{\rm imp} = 50\,{\rm m/s}$ and $\theta_{\rm imp} = 30^\circ$. The impact forms a bilobed shape (Fig. 3.6). The two-body escape velocity $v_{\rm esc}$ is about 60 m/s, which is slightly larger than the impact velocity of this simulation. For $v_{\rm imp} < v_{\rm esc}$, the impact energy is too small to largely deform the initial spherical shapes (see Fig. 3.6b,c), and colliding bodies are gravitationally bound. Thus the bilobed shapes resulting from such low velocity impacts are independent of $\theta_{\rm imp}$.

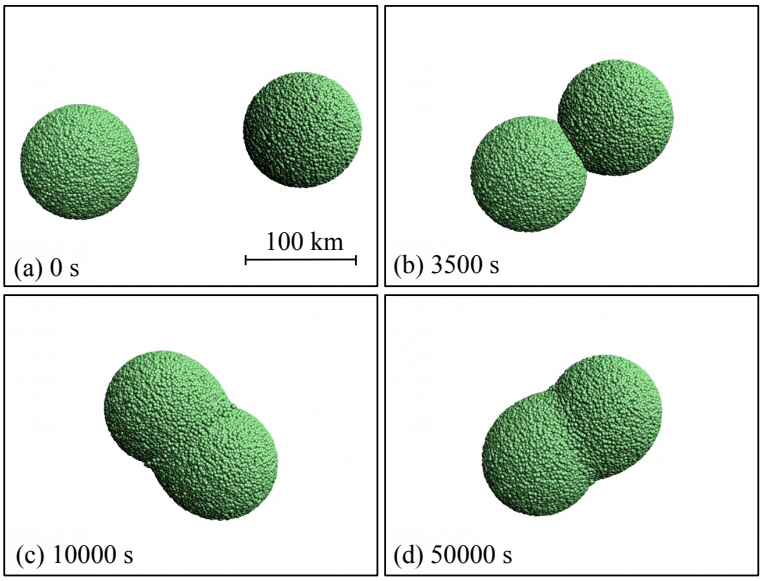

Figure 3.6: Snapshots of the impact simulation with $\theta_{\rm imp} = 30°$ and $v_{\rm imp} = 50\,{\rm m/s}$ at $0.0\,{\rm s}$(a), $3.5 \times 10^3\,{\rm s}$(b), $1.0 \times 10^4\,{\rm s}$(c), and $5.0 \times 10^4\,{\rm s}$(d). This figure is the same as Fig. 6 of Sugiura et al. (2018a).

Spherical Shapes

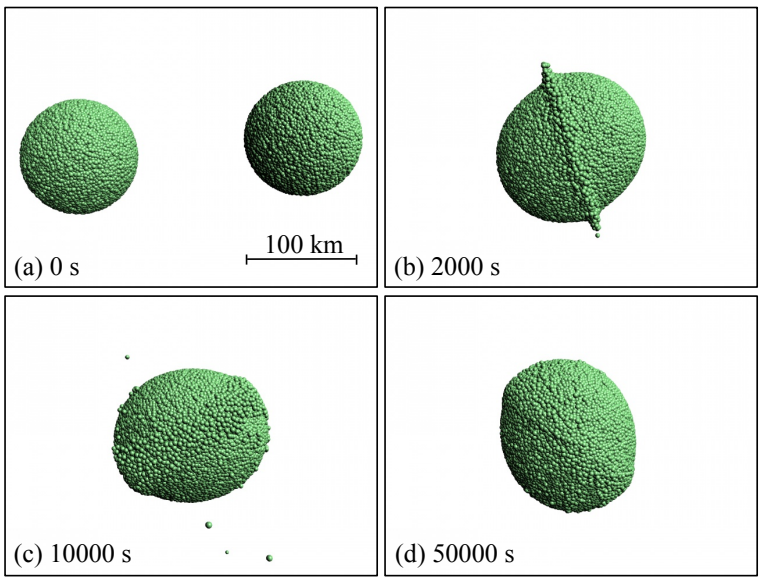

Figure 3.7: Snapshots of the impact simulation with $\theta_{\rm imp} = 10°$ and $v_{\rm imp} = 100\,{\rm m/s}$ at $0.0\,{\rm s}$(a), $2.0 \times 10^3\,{\rm s}$(b), $1.0 \times 10^4\,{\rm s}$(c), and $5.0 \times 10^4\,{\rm s}$(d). This figure is the same as Fig. 7 of Sugiura et al. (2018a).

The initial spherical shape is sufficiently deformed with $v_{\rm imp} \sim 100\,{\rm m/s}$, which results in a single sphere due to merging of two asteroids. Fig. 3.7 shows an impact producing a spherical shape with $v_{\rm imp} = 100\,{\rm m/s}$ and $\theta_{\rm imp} = 10°$. Collisional deformation (Fig. 3.7b) and gravitational reaccumulation (Fig. 3.7c,d) results in a spherical shape.

It should be noted that a relatively low speed collision with $\theta_{\rm imp} \geq 40°$ results in local destruction due to hit-and-run, whose outcome is also close to two spheres.

Flat Shapes

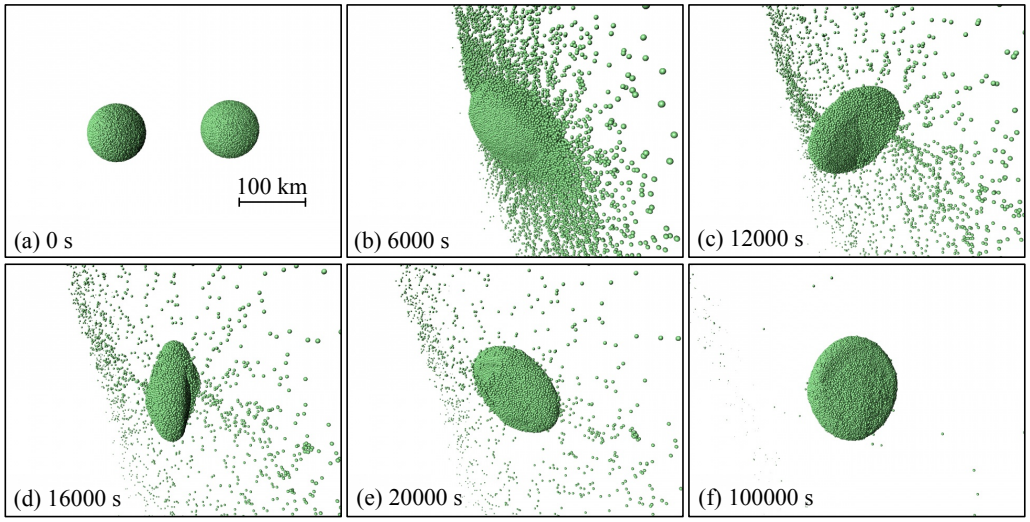

Figure 3.8: Snapshots of the impact simulation with $\theta_{\rm imp} = 5°$ and $v_{\rm imp} = 200\,{\rm m/s}$ at $0.0\,{\rm s}$(a), $6.0 \times 10^3\,{\rm s}$(b), $1.2 \times 10^4\,{\rm s}$(c), $1.6 \times 10^4\,{\rm s}$(d), $2.0 \times 10^4\,{\rm s}$(e), and $1.0 \times 10^5\,{\rm s}$(f). This figure is the same as Fig. 8 of Sugiura et al. (2018a).

Figure 3.8 shows impact snapshots with $v_{\rm imp} = 200\,{\rm m/s}$ and $\theta_{\rm imp} = 5°$. The initial spherical shapes are completely deformed (Fig. 3.8b,c), and the resultant shape is flat (Fig. 3.8d-f). The flat bodies are close to oblate shapes. The minor axis is formed in the direction perpendicular to the angular momentum vector.

Elongated Shapes

A collision forming extremely elongated shape is shown in Fig. 3.2. The collision results in $M_{\rm lr} \sim 2M_{\rm target}$; collisional merging mainly occurs.

Some hit-and-run collisions also produce elongated shapes. Fig. 3.9 shows snapshots of the impact with $v_{\rm imp} = 250\,{\rm m/s}$ and $\theta_{\rm imp} = 20°$, and Fig. 3.10 shows a zoom out view of

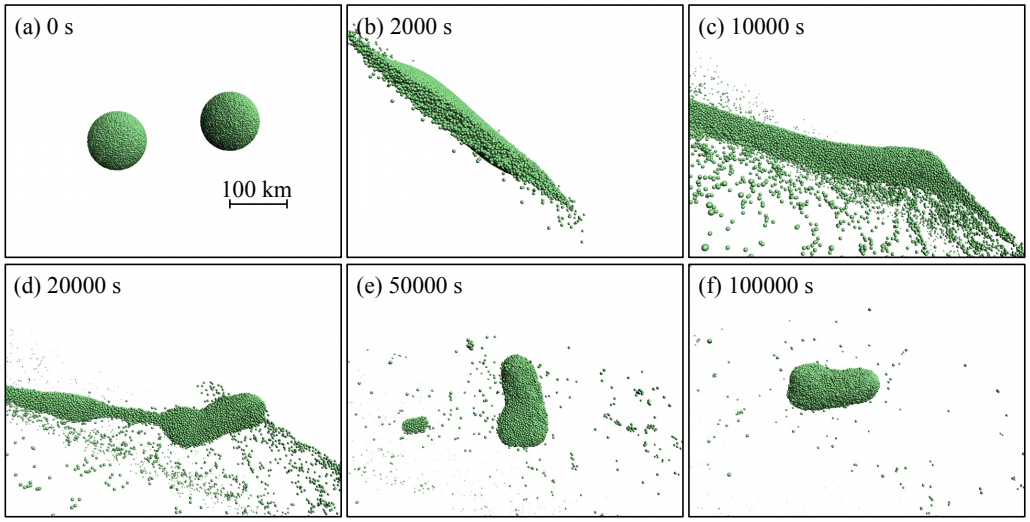

Figure 3.9: Snapshots of the impact simulation with $\theta_{\rm imp} = 20^\circ$ and $v_{\rm imp} = 250\,{\rm m/s}$ at $0.0\,{\rm s}$(a), $2.0 \times 10^3\,{\rm s}$(b), $1.0 \times 10^4\,{\rm s}$(c), $2.0 \times 10^4\,{\rm s}$(d), $5.0 \times 10^4\,{\rm s}$(e), and $1.0 \times 10^5\,{\rm s}$(f). This figure is the same as Fig. 9 of Sugiura et al. (2018a).

Fig. 3.9f. The impact results in significant destruction and deformation (Fig. 3.9b,c). Although two asteroids do not merge (Fig. 3.10), the reaccretion of surrounding fragments produces two elongated shapes (Fig. 3.9d-f and Fig. 3.10). Note that the largest and second largest objects in hit-and-run collisions have almost the same shape (Fig. 3.10).

Hemispherical Shapes

In Fig. 3.11, we show an impact forming hemispherical shapes. Significant destruction occurs around the impact point and a large amount of fragments is ejected straightforwardly (Fig. 3.11b). This collisional truncation results in hemispherical shapes (Fig. 3.11c-e).

Super-Catastrophic Destruction

Figure 3.12 represents the result of the impact simulation with $v_{\rm imp} = 400\,{\rm m/s}$ and $\theta_{\rm imp} = 5^\circ$. The impact of very high $v_{\rm imp}$ produces a large curtain of ejected fragments (Fig. 3.12b), and the gravitational fragmentation of the curtain forms many clumps (Fig. 3.12c). Then the largest remnant is formed through the coalescence of clumps (Fig. 3.12d-f).

In collisions with $M_{\rm lr} < 0.4 M_{\rm target}$, the largest bodies are formed through significant reaccretion of ejecta. Even small difference of initial conditions produces significant difference of the distribution of ejecta, which leads to variety of shapes. Therefore, high-resolution simulations

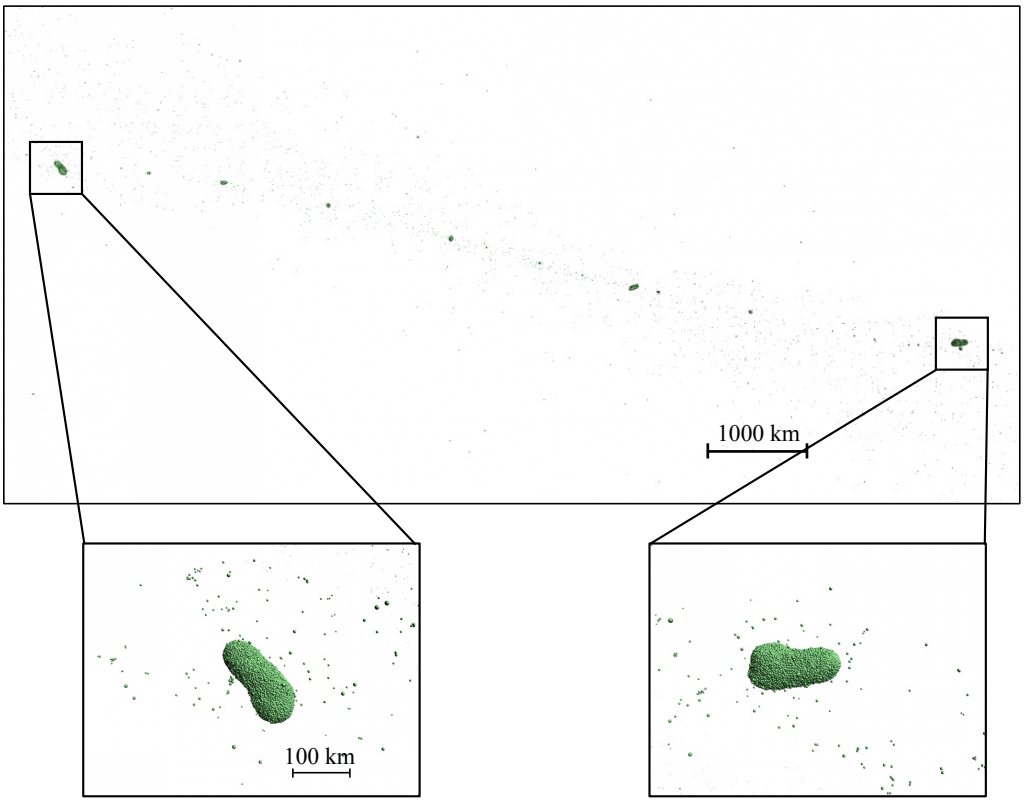

Figure 3.10: Zoom out view of the impact simulation with $v_{\rm imp} = 250\,{\rm m/s}$ and $\theta_{\rm imp} = 20^\circ$ at $1.0 \times 10^5\,{\rm s}$. Two enlarged figures represent the shape of the largest and second largest remnant, respectively. This figure is the same as Fig. 10 of Sugiura et al. (2018a).

are required. We will introduce the results of high-resolution simulations of destructive impacts in Section 3.5. Here, we just call impacts with $M_{\rm lr} < 0.4 M_{\rm target}$ super-catastrophic destruction, and do not classify shapes for such destructive impacts.

Elongated-Shape-Forming Impacts with the Second Collision

Figure 3.13 represents a collision with $v_{\rm imp} = 175\,{\rm m/s}$ and $\theta_{\rm imp} = 20^\circ$, which results in the second collision of two elongated objects. As in Fig 3.2, the first collision produces two elongated objects (Fig 3.13b,c). However, the energy dissipation by the collision makes colliding bodies gravitationally bounded (Fig. 3.13d), and the resultant body formed by the merging is no longer elongated object (Fig. 3.13e). Although the resultant body is not elongated, this impact is a kind of elongated-shape-forming collision.

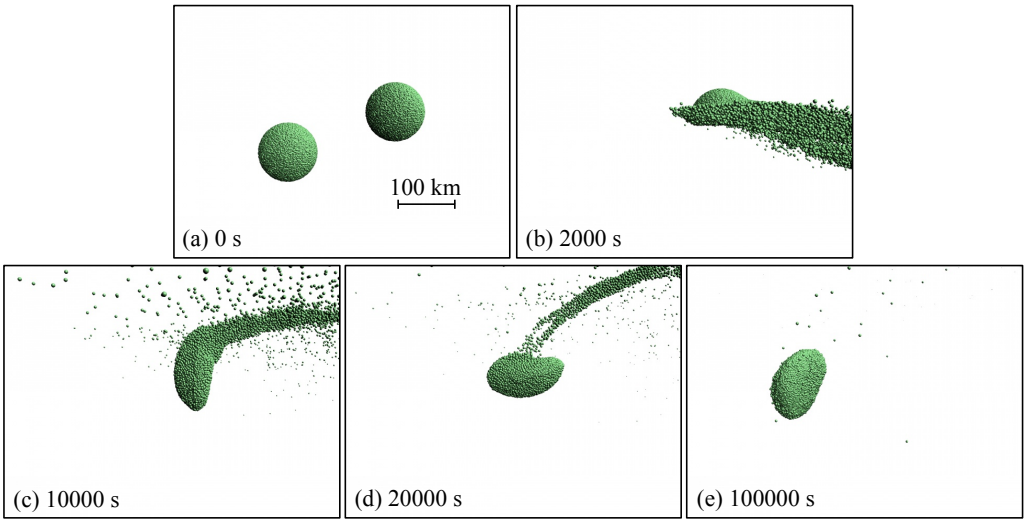

Figure 3.11: Snapshots of the impact simulation with $\theta_{\rm imp} = 45°$ and $v_{\rm imp} = 350\,{\rm m/s}$ at 0.0 s(a), 2.0×10^3 s(b), 1.0×10^4 s(c), 2.0×10^4 s(d), and 1.0×10^5 s(e). This figure is the same as Fig. 11 of Sugiura et al. (2018a).

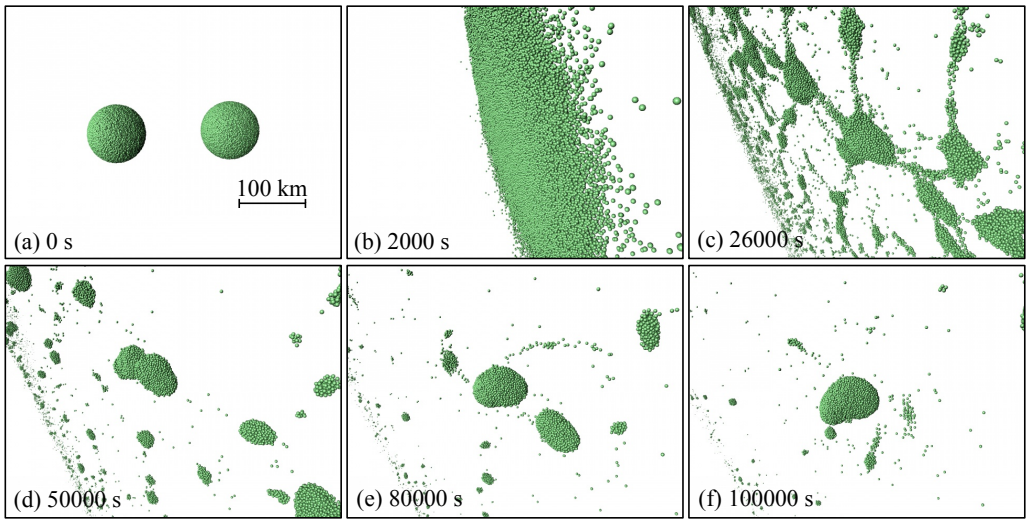

Figure 3.12: Snapshots of the impact simulation with $v_{\rm imp} = 400\,{\rm m/s}$ and $\theta_{\rm imp} = 5°$ at 0.0 s(a), 2.0×10^3 s(b), 2.6×10^4 s(c), 5.0×10^4 s(d), 8.0×10^4 s(e), and 1.0×10^5 s(f). This figure is the same as Fig. 12 of Sugiura et al. (2018a).

3.3.4 Summary of Shapes Formed by Collisions

Figure 3.14 shows the axis ratios of the largest remnants formed through impacts with various impact velocities and angles. For hit-and-run collisions, the largest and second largest bodies

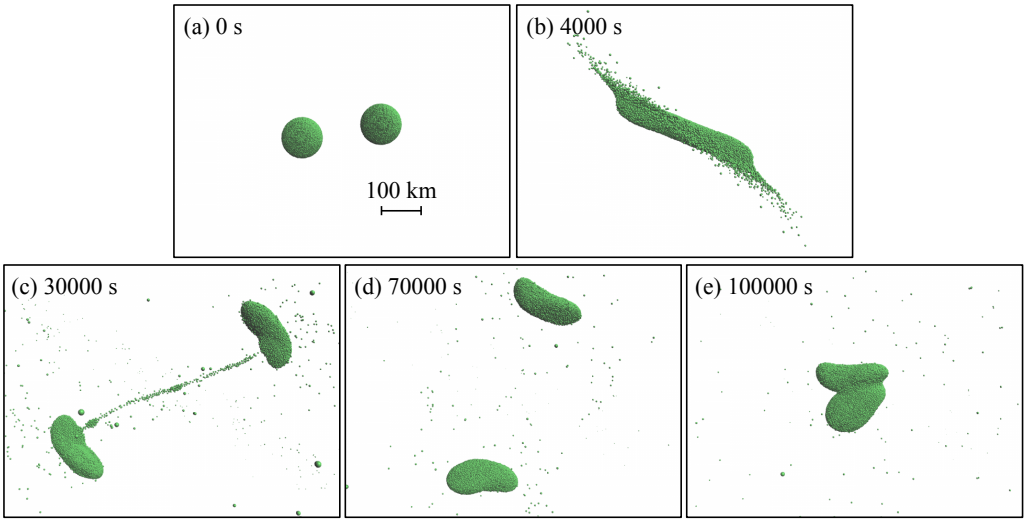

Figure 3.13: Snapshots of the impact simulation with $v_{\rm imp} = 175\,{\rm m/s}$ and $\theta_{\rm imp} = 20^\circ$ at 0.0 s(a), 4.0×10^3 s(b), 3.0×10^4 s(c), 7.0×10^4 s(d), and 1.0×10^5 s(e). This figure is the same as Fig. C.1 of Sugiura et al. (2018a).

have similar shapes as shown in Fig. 3.10. Thus if the mass ratio of the first to second largest bodies is smaller than 2.0, we use the averaged values among two bodies for b/a and c/a. Note that sharp variation of axis ratios at the hatched regions in Fig. 3.14 is caused by the transition between merging and erosive or hit-and-run collisions.

Figure 3.15 shows the summary of the axis ratios of the largest remnants produced through the non-destructive impacts with $50\,{\rm m/s} \leq v_{\rm imp} \leq 400\,{\rm m/s}$, $5^\circ \leq \theta_{\rm imp} \leq 45^\circ$, and $M_{\rm lr} > 0.4 M_{\rm target}$. From Fig. 3.15, we notice that the equal-mass and non-destructive impacts produce extremely elongated shapes with $b/a < 0.4$ and extremely flat shapes with $b/a > 0.8$ and $c/a < 0.6$.

We categorize shapes of collisional outcomes into bilobed, spherical, flat, elongated, hemispherical, and super-catastrophic destruction as shown in Table 3.1. The classification given by Table 3.1 mainly corresponds to the shapes formed via the processes shown in Section 4.3. Fig. 3.16 shows impact parameters producing the classified shapes, which indicates $v_{\rm imp} \sim 50\,{\rm m/s}$ or $v_{\rm imp} \sim 100\,{\rm m/s}$ and $\theta_{\rm imp} > 25^\circ$ (bilobed shapes), $v_{\rm imp} \sim 100\,{\rm m/s}$ and $\theta_{\rm imp} < 25^\circ$ (spherical shapes), $v_{\rm imp} > 100\,{\rm m/s}$ and $v_{\rm imp} \sin\theta_{\rm imp} < 30\,{\rm m/s}$ (flat shapes), $v_{\rm imp} > 100\,{\rm m/s}$, $v_{\rm imp} \sin\theta_{\rm imp} > 30\,{\rm m/s}$, and $\theta_{\rm imp} < 30^\circ$ (elongated shapes), and $v_{\rm imp} > 100\,{\rm m/s}$ and $\theta_{\rm imp} > 30^\circ$ (hemispherical shapes).

Note that two impacts resulting in flat shapes are in the elongated-shape region ($v_{\rm imp} =$

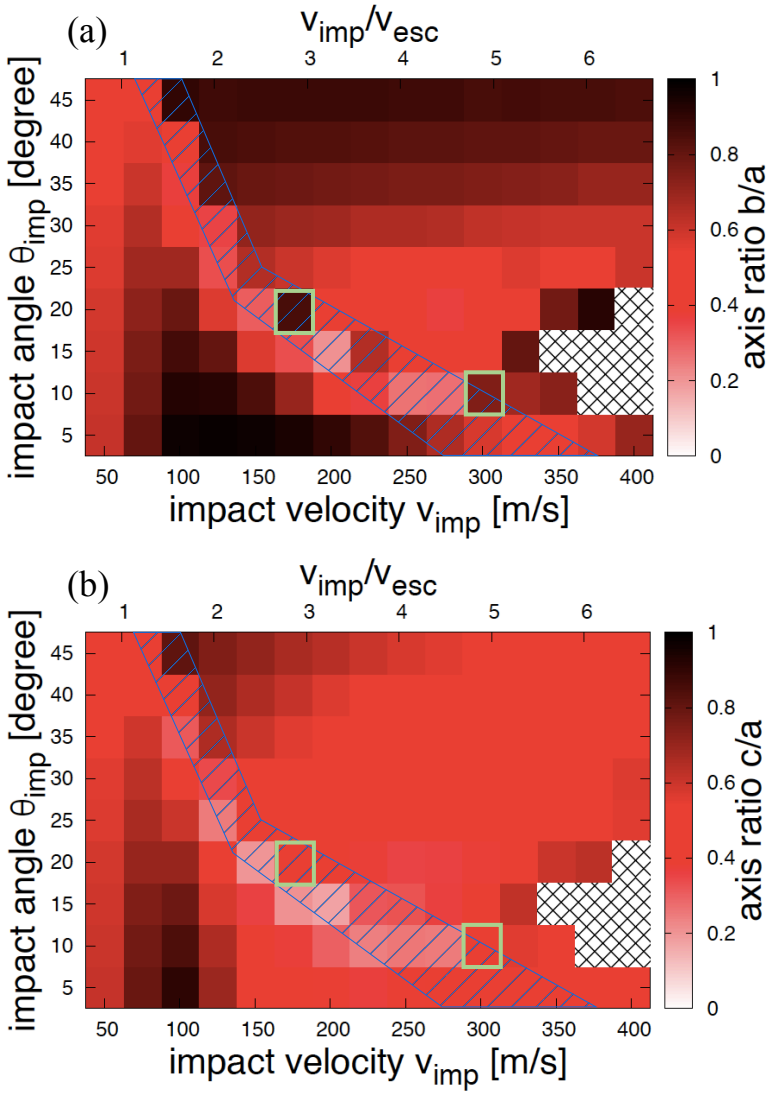

Figure 3.14: Dependence of the ratios b/a and c/a of the largest remnants on $v_{\rm imp}$ and $\theta_{\rm imp}$. The color represents (a) the ratio b/a, (b) the ratio c/a, respectively. For impacts in cross-hatched region, we do not measure the axis ratios of the largest remnants, because the mass of the largest remnants is too small (smaller than 0.15 $M_{\rm target}$). The meaning of the hatched regions is the same as in Fig. 3.5. Two parameters surrounded by green boxes represent impacts with the second collision as shown in Fig 3.13. This figure is the same as Fig. 13 of Sugiura et al. (2018a).

175 m/s, $\theta_{\rm imp} = 20°$ and $v_{\rm imp} = 300$ m/s, $\theta_{\rm imp} = 10°$). These impacts correspond to elongated-shape-forming collisions with the second collision as shown in Fig. 3.13. We consider these impacts as elongated-shape-forming collisions from the shapes observed in the simulations.

Based on the classification in Fig 3.16, we find the specific conditions to determine the shapes, which are written as

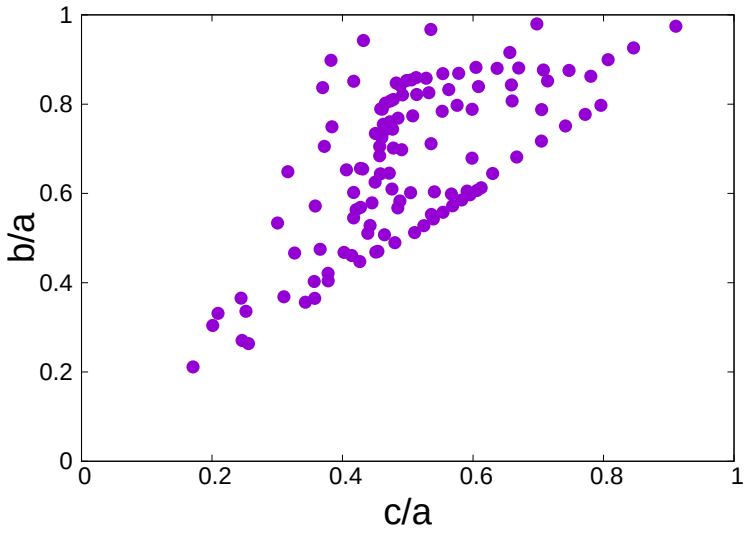

Figure 3.15: Axis ratios of the largest remnants with $M_{\rm lr} > 0.4M_{\rm target}$ produced through equal-mass and non-destructive impacts. The horizontal axis represents the ratio c/a, and the vertical axis represents the ratio b/a. Each point shows the axis ratios of the largest remnant produced through a non-destructive impact.

Shape	Thresholds		
Bilobed	$b/a < 0.7$	$c/a < 0.7$	$M_{\rm lr}/M_{\rm tot} = 1.0$
Spherical	$b/a > 0.7$	$c/a > 0.7$	$\cdots$
Flat	$b/a > 0.7$	$c/a < 0.7$	$M_{\rm lr}/M_{\rm target} > 1.0$
Elongated	$b/a < 0.7$	$c/a < 0.7$	$M_{\rm lr}/M_{\rm tot} < 1.0$
Hemispherical	$b/a > 0.7$	$c/a < 0.7$	$M_{\rm lr}/M_{\rm target} < 1.0$
Super-catastrophic	$\cdots$	$\cdots$	$M_{\rm lr}/M_{\rm target} < 0.4$

Table 3.1: Thresholds of b/a, c/a, $M_{\rm lr}/M_{\rm target}$, and $M_{\rm lr}/M_{\rm tot}$ of the largest remnants for the categorization of shapes, where $M_{\rm tot} = M_{\rm target} + M_i$ shows the total mass used in each impact simulation. All impacts with $M_{\rm lr}/M_{\rm target} < 0.4$ are classified to super-catastrophic destruction regardless of the values of b/a and c/a of the largest remnants.

- bilobed and spherical shapes: $v_{\rm imp} < 1.6v_{\rm esc}$,
- flat shapes: $v_{\rm imp} > 1.6v_{\rm esc}$ and $v_{\rm imp} \sin\theta_{\rm imp} < 0.5v_{\rm esc}$,
- hemispherical shapes: $v_{\rm imp} > 1.6v_{\rm esc}$ and $\theta_{\rm imp} > 30°$,

and

- elongated shapes: $v_{\rm imp} > 1.6v_{\rm esc}$, $\theta_{\rm imp} < 30°$, $v_{\rm imp} \sin\theta_{\rm imp} > 0.5v_{\rm esc}$, and $M_{\rm lr} > 0.4M_{\rm target}$,

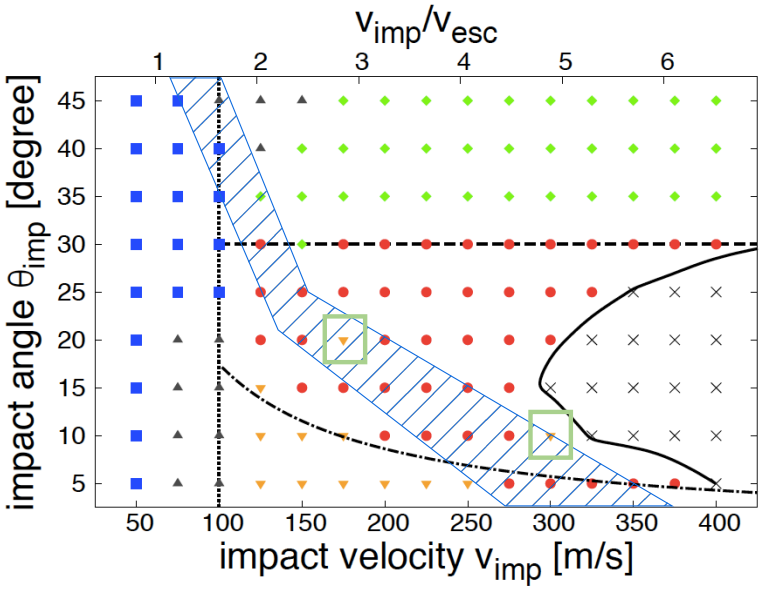

Figure 3.16: Summary of the classification of resultant shapes. The blue squares represent the impact parameters, $v_{\rm imp}$ and $\theta_{\rm imp}$, producing bilobed shapes, the gray triangles represent those of spherical shapes, the orange inverted triangles represent those of flat shapes, the red circles represent those of elongated shapes, the light green diamonds represent those of hemispherical shapes, and the black crosses represent those for super-catastrophic destruction. The dotted line shows $v_{\rm imp} = 1.6 v_{\rm esc} = 100\,{\rm m/s}$, the dashed line shows $\theta_{\rm imp} = 30°$, the chain curve shows $v_{\rm imp} \sin\theta_{\rm imp} = 0.5 v_{\rm esc} = 30\,{\rm m/s}$, and the solid curve shows $M_{\rm lr} = 0.4 M_{\rm target}$. The meanings of the hatched region and green boxes are the same as in Fig. 3.5 and Fig. 3.14. This figure is the same as Fig. 14 of Sugiura et al. (2018a).

where two-body escape velocity $v_{\rm esc} \approx 60\,{\rm m/s}$. The hatched region in Fig. 3.16 divides the elongated-shape region into two parts. Elongated shapes formed with parameters in the left part of the hatched region are formed by merging collisions (see Fig. 3.2), and those in the right part are formed by hit-and-run collisions (see Fig. 3.9).

3.3.5 Discussion: Four Conditions Required for the Formation of Elongated Shapes

The threshold of $v_{\rm imp} > 1.6 v_{\rm esc}$ is required for significant deformation. We estimate necessary impact velocity to deform asteroids as follows. Frictional force of $\mu_d P$ acts on the area of $\sim \pi R_t^2$ and the energy dissipation occurs due to frictional deformation on the length scale of $\sim 4R_t$. The dissipated energy $E_{\rm dis}$ is estimated as

$$E_{\rm dis} = 4\pi R_t^3 \mu_d P. \tag{3.5}$$

The timescale for deformation of whole bodies is estimated to be $2R_t/v_{\rm imp}$, which is much longer than the shock passing time $\sim 2R_t/C_s$, where $C_s \approx 3\,{\rm km/s}$ is the sound speed. High pressure states caused by shocks are already relaxed before the end of the deformation, and shocks do not contribute to the pressure for frictional force given in Eq. (3.5). Therefore, the pressure is mainly determined by the self-gravity and estimated to be central pressure of an asteroid with the radius of R_t and uniform density of ρ_0, given by

$$P = \frac{2}{3}\pi G\rho_0^2 R_t^2. \tag{3.6}$$

Equating the total initial kinetic energy for two equal-mass bodies $(1/4)M_{\rm target}v_{\rm imp}^2$ to $E_{\rm dis}$, we obtain the critical deformation velocity as

$$\begin{aligned} v_{\rm imp,crit} &= \sqrt{4E_{\rm dis}/M_{\rm target}} = \sqrt{3\mu_d}v_{\rm esc} \\ &= 1.587\Big(\frac{\mu_d}{\tan(40^\circ)}\Big)v_{\rm esc}. \end{aligned} \tag{3.7}$$

The impact velocity obtained in Eq. (3.7) well agrees with $v_{\rm imp} = 1.6v_{\rm esc}$ in spite of rough estimation of the dissipated energy $E_{\rm dis}$.

The condition of $\theta_{\rm imp} < 30^\circ$ is needed for the avoidance of hemispherical shapes caused by hit-and-run collisions. For $\theta_{\rm imp} \geq 30^\circ$ half or smaller of a target is directly interacted by an impactor, resulting in hit-and-run collisions (Asphaug 2010; Leinhardt and Stewart 2012). To form elongated shapes, it is necessary for almost whole volume of two asteroids to be deformed. For $\theta_{\rm imp} < 30^\circ$ most of two asteroids are directly affected by collisions, which leads to deformation to be elongated shapes.

Collisional elongation requires large shear velocity $v_{\rm imp}\sin\theta_{\rm imp} > 0.5v_{\rm esc}$, while impacts with $v_{\rm imp}\sin\theta_{\rm imp} < 0.5v_{\rm esc}$ produce flat shapes. Elongated shapes are formed through stretch of asteroids in the direction of shear velocity (see Figs. 3.2 and 3.9). However, the self-gravity prevents deformation, which occurs if $v_{\rm imp}\sin\theta_{\rm imp} \ll v_{\rm esc}$. We find that elongation needs $v_{\rm imp}\sin\theta_{\rm imp} > v_{\rm esc}/2$.

Super-catastrophic destruction with $M_{\rm lr} < 0.4M_{\rm target}$ produces many small remnants, which mainly have spherical shapes as shown in Fig. 3.12. Elongated shapes may not be formed through super-catastrophic destruction. Thus for certain formation of elongated shapes, $M_{\rm lr} > 0.4M_{\rm target}$ is required.

Distribution of pressure is determined by the self-gravity unless the impact velocity is comparable to or larger than the sound speed. Since frictional force is proportional to the pressure,

the friction is also determined by the self-gravity. Thus, unless the material strength is dominant, force on bodies (the right hand side of the equation of motion) is solely determined by the self-gravity, so that results of impacts are characterized by dimensionless velocity $v_{\rm imp}/v_{\rm esc}$ regardless of the scale or size of asteroids. For rocky asteroids with $R_t \geq 0.5\,{\rm km}$, the friction is dominant rather than the material strength. For $R_t \leq 200\,{\rm km}$, $v_{\rm esc}$ is smaller than $0.1C_s$. Therefore, the conditions to form elongated shapes and the shape classification of Fig. 3.16 with upper horizontal axis are also valid for equal-mass impacts with the angle of friction of 40° and $10^0\,{\rm km} \lesssim R_t \lesssim 10^2\,{\rm km}$.

3.4 Unequal-Mass and Non-Destructive Impacts

In this section, we will introduce the asteroidal shapes formed through non-destructive impacts, but we consider the cases that the mass of impactor asteroids is different from that of target asteroids. We again focus on non-destructive impacts with $M_{\rm lr} > 0.4M_{\rm target}$ and investigate the shapes of the largest remnants. Except for the impact simulations with the mass ratio $q = 1/64$, the number of SPH particles for target asteroids is fixed to $50,000$, which is the same resolution as that in Section 3.3. For the simulations with $q = 1/64$, we use $100,000$ SPH particles for target asteroids to use sufficient number of SPH particles for impactor asteroids.

3.4.1 Similar-Mass Impacts

Firstly, we will introduce the simulation results of impacts between two asteroids that have relatively similar masses. We conduct the simulations with the mass ratios of $q = 0.75$, 0.50, and 0.25. We vary the impact angle from 5° to 45° with the increment of 5°. We also vary the impact velocity from $50\,{\rm m/s}$ to $600\,{\rm m/s}$ with the increment of $50\,{\rm m/s}$, which is the wider range but the larger increment of the impact velocity compared to the parameter survey for the equal-mass impacts in Section 3.3.

Figure 3.17 shows the summary of the mass and axis ratios of the largest remnants. From the panels of $M_{\rm lr}/M_{\rm target}$ in Fig. 3.17, we observe clear boundaries between merging collisions and erosive/hit-and-run collisions for all of three mass ratios. We also notice that the impacts with $v_{\rm imp} = 600\,{\rm m/s}$ and $\theta_{\rm imp} = 5°$ result in $M_{\rm lr} < 0.4M_{\rm target}$, i.e., catastrophic disruption, even with $q = 0.25$. Thus the impacts with $50\,{\rm m/s} \leq v_{\rm imp} \leq 600\,{\rm m/s}$ include various types of collisions, namely, merging collisions, hit-and-run collisions, and catastrophic disruptions.

From panels of b/a and c/a in Fig. 3.17, we observe the entire tendency that the axis ratios

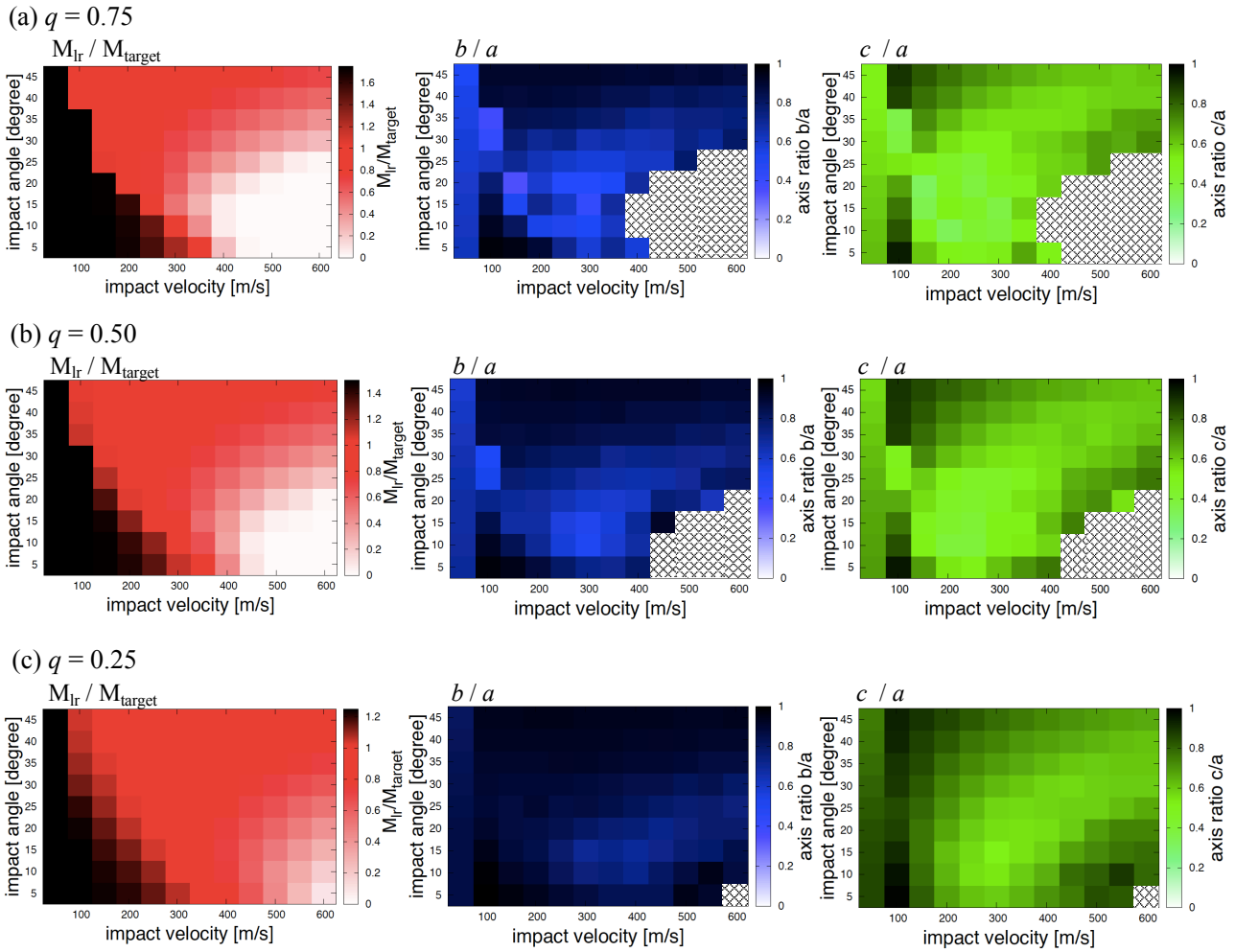

Figure 3.17: Summary of the mass and axis ratios of the largest remnants produced through the impacts with three different mass ratios. Each row shows the results of the impacts with (a) $q = 0.75$, (b) $q = 0.50$, and (c) $q = 0.25$, respectively. Each color of contour shows $M_{\rm lr}/M_{\rm target}$ (red), b/a (blue), and c/a (green) of the largest remnants, respectively. In the panels that show $M_{\rm lr}/M_{\rm target}$, black regions show the impacts with $M_{\rm lr} \approx M_{\rm tot}$, i.e., the impacts resulting in merging collisions. In each panel, the horizontal axis represents the impact velocity, and the vertical axis represents the impact angle. The impacts in cross-hatched region have $M_{\rm lr} < 0.15 M_{\rm target}$, and we do not measure the axis ratios.

increase with decreasing the mass ratios. This means that the impacts with high-mass ratios are difficult to produce irregular shapes. Especially, this tendency is clear for b/a; $b/a \approx 1$ for almost all of impacts with $q = 0.25$. Thus, non-destructive impacts with high-mass ratios do not produce elongated shapes of the largest remnants.

The left panels of Fig. 3.18 show the shape classification of the largest remnants for similar-mass impacts. We use the same threshold in Table 3.1 for the classification as that for the

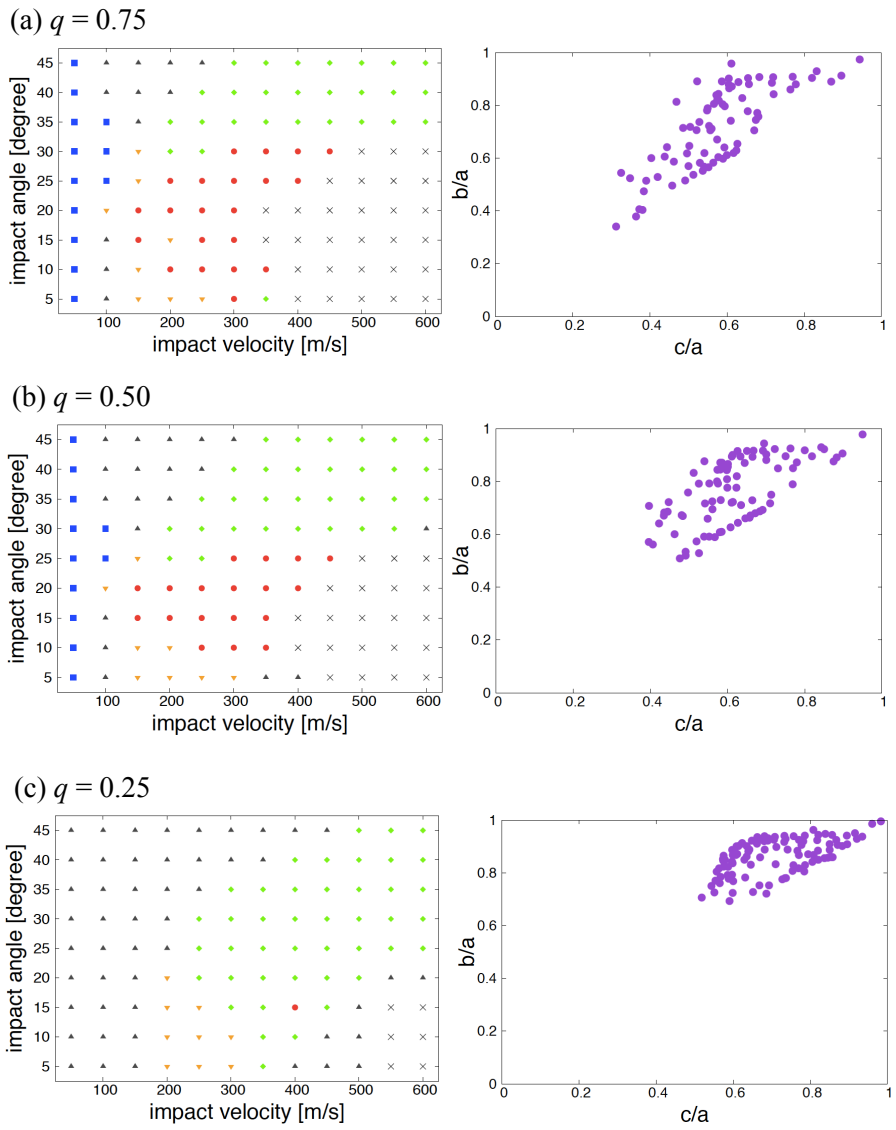

Figure 3.18: Summary of the classification of resultant shapes and the shape distribution of the largest remnants produced through the impacts with three different mass ratios. Each row shows the results of the impacts with (a) $q = 0.75$, (b) $q = 0.50$, and (c) $q = 0.25$, respectively. The left panels show the results of shape classification according to Table 3.1 with the horizontal axis of the impact velocity and the vertical axis of the impact angle. The meanings of symbols are the same as those of Fig. 3.16. The right panels show the axis ratios with the horizontal axis of c/a and the vertical axis of b/a.

equal-mass impacts. From Fig 3.18a and b, we notice that the results of the classification for $q = 0.75$ and $q = 0.50$ are similar to that of the equal-mass impacts (Fig. 3.16): In the impact velocity-angle diagram, the left parts are for bilobed shapes, the left-bottom parts are for spherical shapes, the bottom parts are for flat shapes, the middle parts are for elongated

shapes, the upper parts are for hemispherical shapes, and the right parts are for catastrophic disruptions [1]. However, the result of the shape classification for $q = 0.25$ is distinctly different from that of the equal-mass impacts. There is no clear region for bilobed shapes and elongated shapes. This is because the impacts with high-mass ratios tend to result in partial destruction rather than overall deformation. Thus the various shapes of the largest remnants are only formed through the impacts with $q \geq 0.5$.

The right panels of Fig. 3.18 show the shape distribution of the largest remnants produced through the similar and non-destructive impacts with $M_{\rm lr} > 0.4M_{\rm target}$. From these panels, we observe clearly that the number of elongated shapes of impact outcomes decreases with decreasing the mass ratio q. Especially for $q = 0.25$, even flat shapes with $c/a \approx 0.5$ are not found. Thus, to produce extreme shapes, we need non-destructive impacts with $q \geq 0.5$.

3.4.2 Impacts with Large Mass Ratios

Secondly, we will introduce the results of the impacts between two asteroids that have large mass differences. We investigate asteroidal collisions with the mass ratios of $q = 1/8$ and $1/64$, i.e., even the ratio of the radius R_i/R_t is smaller than 0.5. For $q = 1/8$, we vary the impact velocity from 125 m/s to 2,500 m/s with the increment of 125 m/s and the impact angle from 0° to 45° with the increment of 5°. For $q = 1/64$, we vary the impact velocity from 500 m/s to 3,000 m/s with the increment of 250 m/s and the impact angle from 0° to 40° with the increment of 10°.

Figure 3.19 summarizes the mass and the axis ratios of the largest remnants produced through the high-mass-ratio impacts. From the panels of $M_{\rm lr}/M_{\rm target}$ in Fig. 3.19, we notice that our investigation of the high-mass-ratio impacts covers various impacts from non-destructive impacts to destructive impacts especially for $q = 1/8$. The parameter survey for $q = 1/64$ also includes destructive impacts with $M_{\rm lr} < 0.4M_{\rm target}$.

Figure 3.19 shows that the shapes of the largest remnants produced through the high-mass-ratio impacts are only spherical and hemispherical shapes. The minimum b/a of the largest remnants produced through the impacts with $q = 1/8$ is about 0.8. All largest remnants produced through the impacts with $q = 1/64$ have $b/a > 0.9$. Thus, high-mass-ratio and non-destructive impacts do not produce elongated shapes.

From the panels of c/a in Fig. 3.19, we also notice the tendency that c/a increases with

[1] We notice that there are some exceptions, but these exceptions are mainly caused by the thresholds we determined for the equal-mass impacts. If we could find better thresholds, we might remove the exceptions.

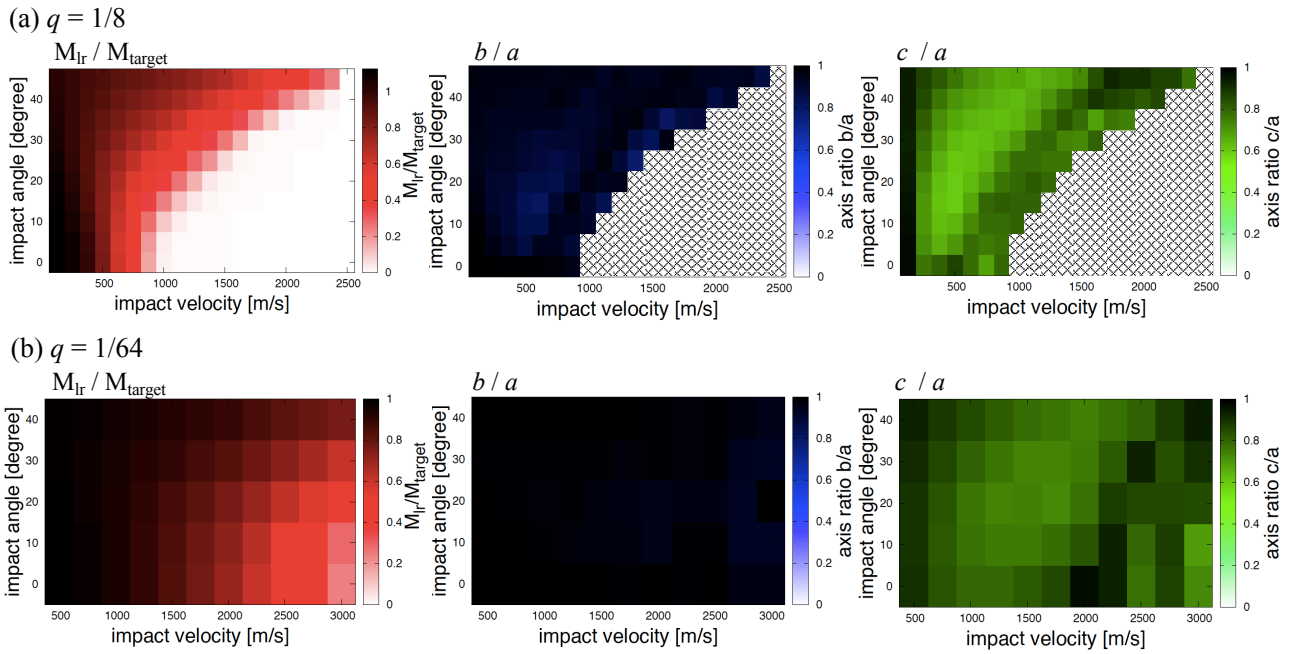

Figure 3.19: Summary of the mass and axis ratios of the largest remnants produced through the high-mass-ratio impacts. Each row shows the results of the impacts with (a) $q = 1/8$ and (b) $q = 1/64$, respectively. Each color of contour shows $M_{\rm lr}/M_{\rm target}$ (red), b/a (blue), and c/a (green) of the largest remnants, respectively. In each panel, the horizontal axis represents the impact velocity, and the vertical axis represents the impact angle. The impacts in cross-hatched region have $M_{\rm lr} < 0.15 M_{\rm target}$, and we do not measure the axis ratios.

decreasing q. The minimum c/a resulted from the impacts with $q = 1/8$ is about 0.6, while that resulted from the impacts with $q = 1/64$ is about 0.7. This is because high-mass-ratio and non-destructive impacts mainly result in cratering. High-mass-ratio impacts do not produce largely irregular shapes even if the impacts result in relatively destructive impacts with $M_{\rm lr} \approx 0.5 M_{\rm target}$, because such impacts mainly eject materials around impact cites rather than overall deformation. Therefore, our simulations suggest that high-mass-ratio and non-destructive impacts with $q \leq 1/64$ do not produce irregular shapes of the largest remnants.

3.5 Destructive Impacts

To investigate the shapes of small remnants produced through destructive impacts, we conduct high-resolution simulations of catastrophic destruction. We use about 4 million SPH particles for each impact simulation and conduct four simulations with the following conditions: $q = 1$, $\theta_{\rm imp} = 15°$, $v_{\rm imp} = 350\,{\rm m/s}$; $q = 1/4$, $\theta_{\rm imp} = 15°$, $v_{\rm imp} = 700\,{\rm m/s}$; $q = 1/8$, $\theta_{\rm imp} = 0°$,

$v_{\rm imp} = 1,000\,{\rm m/s}$; and $q = 1/16$, $\theta_{\rm imp} = 15^\circ$, $v_{\rm imp} = 1,700\,{\rm m/s}$.

Figure 3.20 shows the snapshots of the impacts with $q = 1$, $\theta_{\rm imp} = 15^\circ$, $v_{\rm imp} = 350\,{\rm m/s}$ and $q = 1/8$, $\theta_{\rm imp} = 0^\circ$, $v_{\rm imp} = 1,000\,{\rm m/s}$. We notice that the catastrophic destruction produces large ejecta curtains regardless of the detailed impact conditions such as the mass ratio (Fig. 3.20a-2 and c-2). The destructive impacts produce thin ejecta curtains (Fig. 3.20b-2 and d-2), and the gravitational instability and fragmentation of the curtains produce many filamentary structures (Fig. 3.20a-4 and c-4). The gravitational reaccumulation of fragments in the filamentary structures (Fig. 3.20a-5 and c-5) eventually leads to the formation of many small remnants (Fig. 3.20a-6 and c-6). Note that these processes do not depend on the detailed impact conditions as long as impacts result in catastrophic destruction.

Figure 3.21 shows the cumulative mass distributions of the remnants produced through four destructive impacts. From Fig. 3.21, we notice that the masses of the largest remnants produced through the impacts with $q = 1$, $\theta_{\rm imp} = 15^\circ$ $v_{\rm imp} = 350\,{\rm m/s}$; $q = 1/4$, $\theta_{\rm imp} = 15^\circ$, $v_{\rm imp} = 700\,{\rm m/s}$; and $q = 1/16$, $\theta_{\rm imp} = 15^\circ$, $v_{\rm imp} = 1,700\,{\rm m/s}$ are about $0.1 M_{\rm target}$, while that with $q = 1/8$, $\theta_{\rm imp} = 0^\circ$, $v_{\rm imp} = 1,000\,{\rm m/s}$ is about $0.01 M_{\rm target}$. We also notice that the ratios of the mass of the largest to that of the second largest for the impacts with $q = 1$, $\theta_{\rm imp} = 15^\circ$, $v_{\rm imp} = 350\,{\rm m/s}$ and $q = 1/8$, $\theta_{\rm imp} = 0^\circ$, $v_{\rm imp} = 1,000\,{\rm m/s}$ are about unity, while those with $q = 1/4$, $\theta_{\rm imp} = 15^\circ$, $v_{\rm imp} = 700\,{\rm m/s}$ and $q = 1/16$, $\theta_{\rm imp} = 15^\circ$, $v_{\rm imp} = 1,700\,{\rm m/s}$ are less than 0.1. We do not investigate the dependence of the feature of cumulative mass distributions on the impact conditions in more detail, but it should be noted that not only the mass of the largest remnants but also the ratios of the mass of the largest to the second largest probably have important information to reveal impact conditions to form asteroid families.

If a remnant is composed of 5,000 SPH particles, this remnant is resolved by about 20 SPH particles along axis directions. This number of SPH particles is considered to be sufficient to measure the shape of such remnant. Thus, we measure the axis ratios of remnants composed of 5,000 or more SPH particles. From Fig. 3.21, we notice that the number of the remnants with 5,000 or more SPH particles for the impacts with $q = 1$, $\theta_{\rm imp} = 15^\circ$ $v_{\rm imp} = 350\,{\rm m/s}$ is 69, that with $q = 1/4$, $\theta_{\rm imp} = 15^\circ$, $v_{\rm imp} = 700\,{\rm m/s}$ is 24, that with $q = 1/8$, $\theta_{\rm imp} = 0^\circ$, $v_{\rm imp} = 1,000\,{\rm m/s}$ is 30, and that with $q = 1/16$, $\theta_{\rm imp} = 15^\circ$, $v_{\rm imp} = 1,700\,{\rm m/s}$ is 13. Thus the total number of the remnants with measured shapes is sufficient to statistically discuss the shape distribution of remnants produced through destructive impacts.

Figure 3.22 shows the snapshots of the main remnants produced through the impact with $q = 1$, $\theta_{\rm imp} = 15^\circ$ $v_{\rm imp} = 350\,{\rm m/s}$. From Fig. 3.22, we notice that the most remnants have

the rounded shapes rather than irregular shapes. This is because the remnants are produced through violent reaccumulation of fragments; strong gravitational effect tends to produce spherical bodies. However, we also notice that some remnants have the characteristic shapes with two lobes. These bilobed shapes are formed through coalescence of two rounded remnants. Fig. 3.22 shows the tendency that the smaller remnants have more rounded shapes. This may be caused by the weak mutual gravity between smaller remnants; they do not coalesce each other due to the weak mutual gravity, which leads to let these shapes remain spherical ones.

Figure 3.23 shows the dependence of $\sqrt{bc}/a$ on the mass of the remnants. As shown in Schwartz et al. (2018), $\sqrt{bc}/a$ represents the shape irregularity of remnants, and smaller $\sqrt{bc}/a$ means more irregular shapes. From Fig. 3.23, we notice the tendency that the smaller remnants have more rounded shapes for all the impacts, especially for the equal-mass impact as we already notice in Fig. 3.22. Schwartz et al. (2018) also investigated the shape distribution of remnants produced through several catastrophic impacts through simulations using the particle based code of the soft sphere model. However, they do not observe the tendency of $\sqrt{bc}/a$ on the mass of the remnants. This discrepancy may be caused by the difference of simulation methods. Thus, in our future works, we will investigate the detailed dependence of shape distribution of produced remnants on simulation methods.

Figure 3.24 shows the shape distribution of the remnants produced through the destructive impacts. From Fig. 3.24, we notice that all the destructive impacts mainly produce the spherical shapes and also the irregular shapes with $b/a \approx c/a \approx 0.5$ that are mainly the bilobed shapes. We also notice that the destructive impacts are difficult to produce flat shapes. Among the remnants produced through the four impacts investigated here, there are only two flat shapes with $b/a > 0.8$ and $c/a < 0.6$, and these flat shapes are produced by the equal-mass and relatively low-velocity impact. Therefore, destructive impacts, especially high-velocity impacts, do not produce flat shapes of asteroids.

In this section, we investigated the shapes of small remnants produce through destructive impacts. However, small remnants are also ejected by relatively non-destructive impacts (see, e.g., Fig. 3.11b). The shapes of fine remnants produced through non-destructive impacts are also determined by the reaccumulation of fragments. Thus we expect that the shapes of such remnants resemble those formed through destructive impacts.

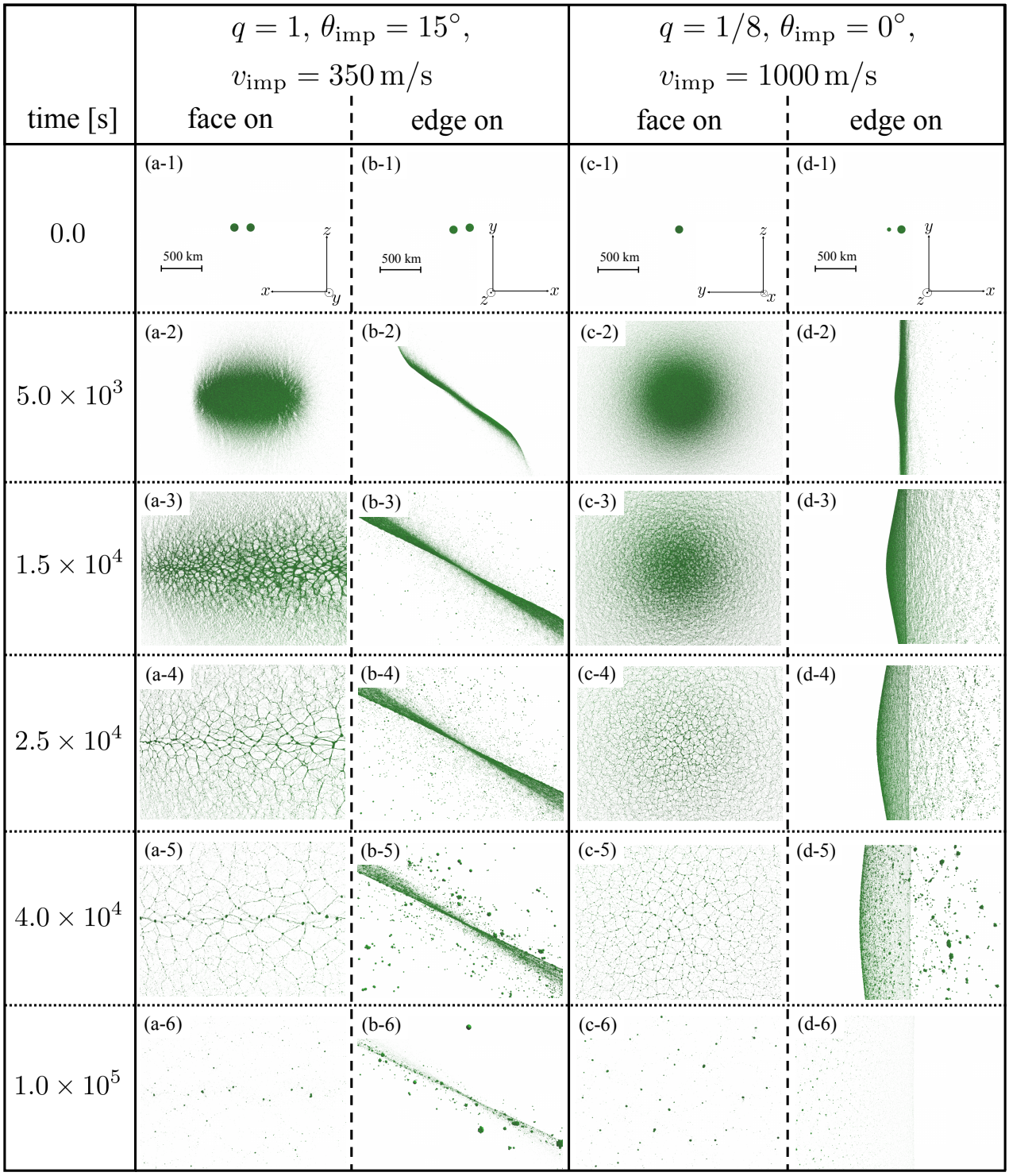

Figure 3.20: Snapshots of the simulations of the destructive impacts. The panels (a-1) - (a-6) and (b-1) - (b-6) show the face on views and the edge on views of the ejecta curtain produced through the impact with $q = 1$, $\theta_{\rm imp} = 15°$, $v_{\rm imp} = 350\,{\rm m/s}$, respectively. The panels (c-1) - (c-6) and (d-1) - (d-6) show the face on views and the edge on views of the ejecta curtain produced through the impact with $q = 1/8$, $\theta_{\rm imp} = 0°$, $v_{\rm imp} = 1,000\,{\rm m/s}$, respectively. Each row shows the snapshots at 0.0s, 5.0×10^3s, 1.5×10^4s, 2.5×10^4s, 4.0×10^4s, and , 1.0×10^5s. In the panels (a-1), (b-1), (c-1), and (d-1), we show the scales and the coordinate systems that are valid for each column.

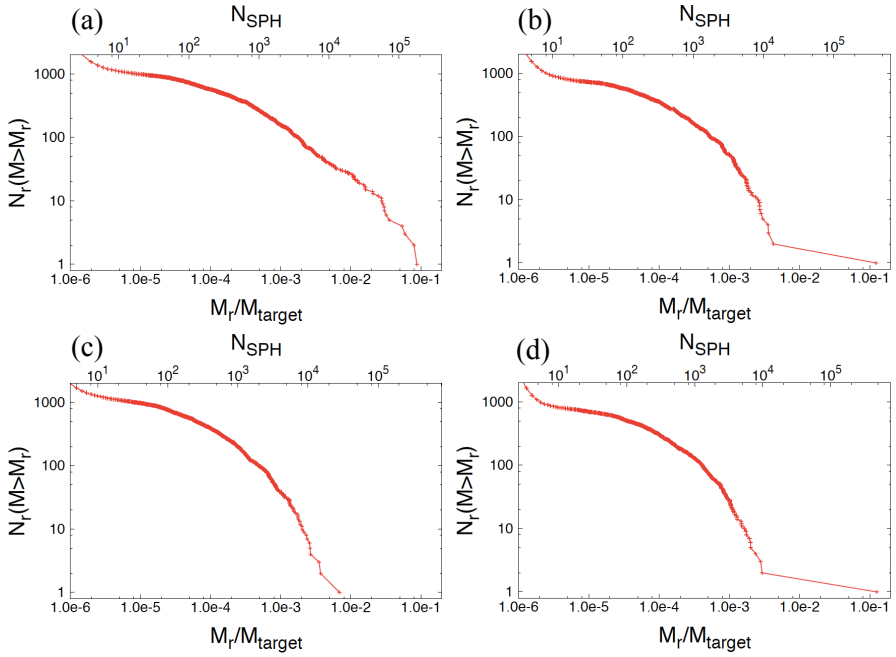

Figure 3.21: Cumulative mass distributions of the remnants produced through the destructive impacts. In each panel, the horizontal axis represents the mass of remnants M_r normalized by the mass of the target asteroids $M_{\rm target}$, and the vertical axis represents the cumulative number of remnants that have the mass larger than M_r. The upper horizontal axis represents the number of SPH particles that compose a remnant with the mass of M_r. The panel (a) shows the cumulative mass distribution resulted from the impact with $q = 1$, $\theta_{\rm imp} = 15°$, $v_{\rm imp} = 350\,{\rm m/s}$, the panel (b) shows that with $q = 1/4$, $\theta_{\rm imp} = 15°$, $v_{\rm imp} = 700\,{\rm m/s}$, the panel (c) shows that with $q = 1/8$, $\theta_{\rm imp} = 0°$, $v_{\rm imp} = 1,000\,{\rm m/s}$, and the panel (d) shows that with $q = 1/16$, $\theta_{\rm imp} = 15°$, $v_{\rm imp} = 1,700\,{\rm m/s}$.

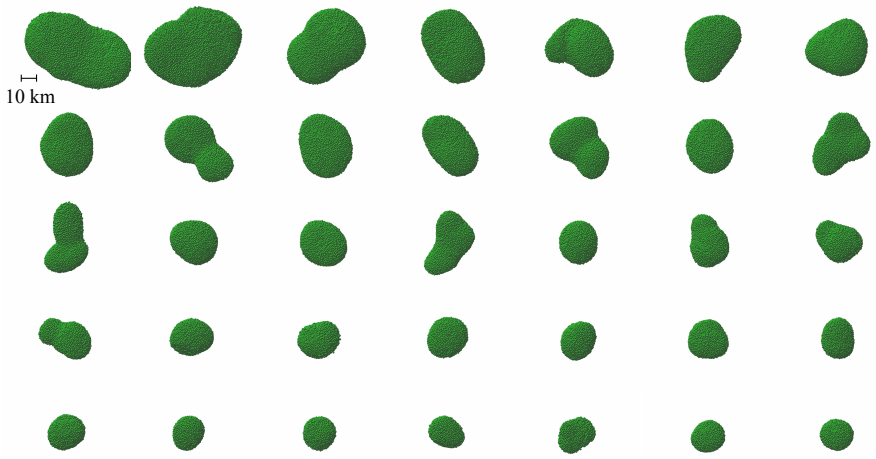

Figure 3.22: Snapshots of the remnants produced through the impact with $q = 1$, $\theta_{\rm imp} = 15°$, $v_{\rm imp} = 350\,{\rm m/s}$. We show the shapes of from the largest remnants (the remnant at the left upper corner) to the 35th largest remnant (the remnant at the right bottom corner).

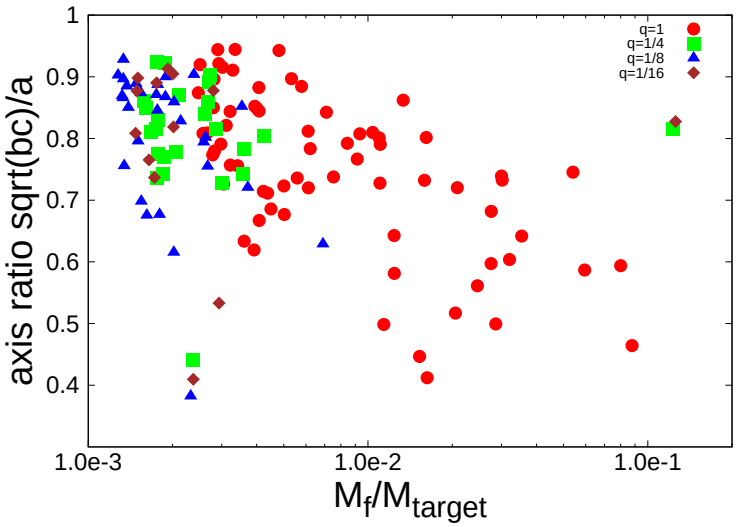

Figure 3.23: Dependence of the shape irregularity on the mass of the remnants. The horizontal axis represents the mass of the remnants normalized by that of the target asteroids, and the vertical axis represents $\sqrt{bc}/a$ of the remnants. The red circles show the remnants produced through the impact with $q = 1$, $\theta_{\rm imp} = 15°$, $v_{\rm imp} = 350\,{\rm m/s}$, the green squares show those with $q = 1/4$, $\theta_{\rm imp} = 15°$, $v_{\rm imp} = 700\,{\rm m/s}$, the blue triangles show those with $q = 1/8$, $\theta_{\rm imp} = 0°$, $v_{\rm imp} = 1,000\,{\rm m/s}$, and the brown diamonds show those with $q = 1/16$, $\theta_{\rm imp} = 15°$, $v_{\rm imp} = 1,700\,{\rm m/s}$.

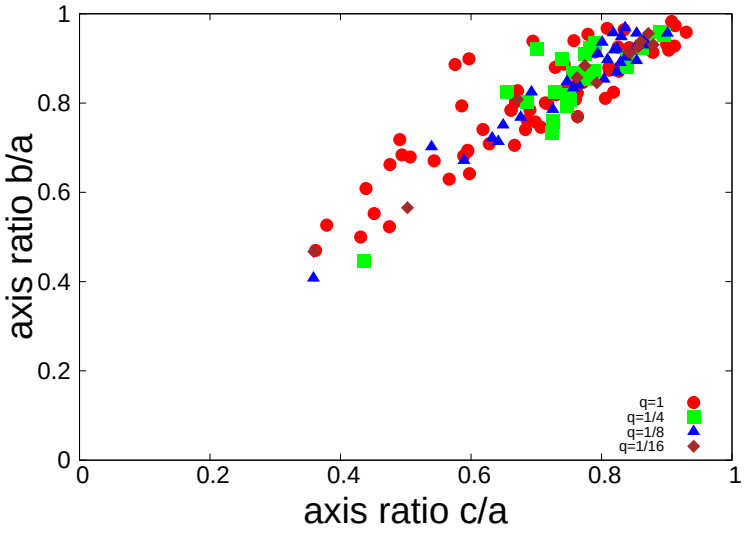

Figure 3.24: Shape distribution of the remnants produced through the destructive impacts. The horizontal axis represents c/a of the remnants, and the vertical axis represents b/a of the remnants. The red circles show the remnants produced through the impact with $q = 1$, $\theta_{\rm imp} = 15°$, $v_{\rm imp} = 350\,{\rm m/s}$, the green squares show those with $q = 1/4$, $\theta_{\rm imp} = 15°$, $v_{\rm imp} = 700\,{\rm m/s}$, the blue triangles show those with $q = 1/8$, $\theta_{\rm imp} = 0°$, $v_{\rm imp} = 1,000\,{\rm m/s}$, and the brown diamonds show those with $q = 1/16$, $\theta_{\rm imp} = 15°$, $v_{\rm imp} = 1,700\,{\rm m/s}$.

Chapter 4

Discussion: Collisional History of Asteroids

In Chapter 3, we investigated shapes of asteroids formed through various impacts and found the relationship between resultant shapes of collisional outcomes and the impact conditions such as the impact velocity. The impact velocity is strongly affected by the environments of planetary systems such as the exsitence of gas components or giant planets. Thus we may connect shapes of asteroids to the environments or era when asteroids were formed. In this chapter, we discuss the connection between shapes of asteroids and formation era. We investigate information of actual asteroids including those shapes obtained from several databases, and we discuss the suggestions obtained from shapes of actual asteroids.

4.1 Connection Between Shapes of Asteroids and Collisional Environments

4.1.1 Summary of Shapes of Impact Outcomes

In Chapter 3, we investigated asteroidal shapes produced through the impacts with the 100 km target asteroids. We classified impacts into three categories; equal-mass and non-destructive impacts, unequal-mass and non-destructive impacts, and destructive impacts. Non-destructive impacts mean the impacts with the mass of the largest remnants larger than $0.4M_{\rm target}$. We will briefly introduce the shapes of asteroids produced through the three types of impacts.

Equal-mass and non-destructive impacts with $v_{\rm imp} \leq 400\,{\rm m/s}$ produce various shapes including extremely elongated shapes (Fig. 3.2) and extremely flat shapes (Fig. 3.8). The shapes of impact outcomes are depending on the impact conditions. Elongated shapes are formed through the impacts with $2v_{\rm esc} \lesssim v_{\rm imp} \lesssim 5v_{\rm esc}$ and $15^\circ \lesssim \theta_{\rm imp} \lesssim 30^\circ$, and flat shapes are formed

through the impacts with $2v_{\rm esc} \lesssim v_{\rm imp} \lesssim 4v_{\rm esc}$ and $\theta_{\rm imp} \lesssim 15^\circ$ (Fig. 3.16). The most elongated shape produced through the equal-mass and non-destructive impacts has $b/a \approx 0.2$ and the most flat shape has $c/a \approx 0.4$ (Fig. 3.15).

Unequal-mass and non-destructive impacts are more difficult to produce irregular shapes compared to equal-mass impacts. The impacts with $q = 0.5$ still produce elongated shapes with $b/a \approx 0.6$ (Fig. 3.18b) and those with $q = 0.25$ still produce flat shapes with $c/a \approx 0.6$ (Fig. 3.18c). However, the most irregular shape produced through the impacts with $q = 1/8$ has $b/a \approx 1$ and $c/a \approx 0.6$ (Fig. 3.19a), and that produced through the impacts with $q = 1/64$ has $b/a \approx 1$ and $c/a \approx 0.7$ (Fig. 3.19b). Thus, the impacts with $q < 1/8$ do not produce the irregular shapes with $c/a < 0.6$.

Destructive impacts mainly produce spherical and bilobed shapes (Fig 3.22). Intense gravitational reaccumulation of fragments after destructive impacts produce spherical remnants, and the coalescence of spherical remnants produce bilobed shapes. We conduct the simulations of the destructive impacts with various mass ratios and impact velocities up to about 2 km/s and find that every destructive impact produces spherical and bilobed shapes (Fig. 3.24). Some bilobed remnants have $b/a \approx 0.4$. However, flat shapes are difficult to be formed through destructive impacts; among about 100 remnants produced through our destructive impacts, there are only two flat remnants with $c/a \approx 0.6$, and there are no flat remnants with $c/a \leq 0.5$.

4.1.2 Impact Velocity and Collisional Environments

Primordial Environment

We will estimate the typical relative velocity between asteroids in the primordial environment. We consider the era when protoplanets are under oligarchic growth, i.e., several protoplanets with sufficient separations grow through the accretion of surrounding asteroids. In this era, gas component of the protoplanetary disk still exists because Jupiter is not yet formed. The random velocity between asteroids increases through viscous stirring of protoplanets, while the random velocity decreases through gas drag.

The timescale of the viscous stirring is estimated as (e.g., Ida and Makino 1993)

$$t_{\rm vis} = \frac{1}{n_{\rm proto}\sigma_{\rm scat}v_{\rm rel}} = \frac{1}{n_{\rm proto}v_{\rm rel}}\frac{1}{\pi R_{\rm proto}^2}\left(\frac{v_{\rm rel}}{v_{\rm esc,p}}\right)^4, \tag{4.1}$$

where $n_{\rm proto}$ is the number density of protoplanets, $\sigma_{\rm scat} = \pi R_{\rm proto}^2 (v_{\rm esc,p}/v_{\rm rel})^4$ is the scattering cross section of protoplanets, $R_{\rm proto}$ is the radius of protoplanets, $v_{\rm esc,p}$ is the escape velocity

from protoplanets, and $v_{\rm rel}$ is the typical relative velocity between asteroids. We also denote the mass of protoplanets as $M_{\rm proto} = (4/3)\pi R_{\rm proto}^3 \rho_s$, where ρ_s is solid density. The number density of protoplanets is estimated as

$$n_{\rm proto} = \frac{1}{2\pi a \cdot b_{\rm sep} \cdot h_{\rm ast}}, \tag{4.2}$$

where a is the orbital semi-major axis, $b_{\rm sep}$ is the orbital separation between protoplanets, and $h_{\rm ast}$ is the scale height of asteroid disk. $h_{\rm ast}$ is estimated as $e_{\rm ast}a$, where $e_{\rm ast}$ is the typical eccentricity of asteroids. Since $e_{\rm ast}v_{\rm K} = v_{\rm rel}$, where $v_{\rm K}$ is the Keplerian velocity, $h_{\rm ast}$ is written as

$$h_{\rm ast} = a v_{\rm rel}/v_{\rm K}. \tag{4.3}$$

The orbital separations between protoplanets are maintained to be several times of the mutual hill radius (e.g., Kokubo and Ida 2002), and thus $b_{\rm sep}$ is written as

$$b_{\rm sep} = \tilde{b}_{\rm sep}\Big(\frac{2M_{\rm proto}}{3M_s}\Big)^{1/3} a, \tag{4.4}$$

where $\tilde{b}_{\rm sep}$ is a factor and typically has $\tilde{b}_{\rm sep} \approx 10$, and M_s is the mass of the sun.

The timescale of the gas damping is estimated to be stopping time. For large asteroids with the radius $R_{\rm ast} = 50\,{\rm km}$, gas drag law is described by Newton law. The stopping time is written as (e.g.,Whipple 1972; Weidenschilling 1977)

$$t_s = \frac{6\rho_s R_{\rm ast}}{\rho_{\rm gas} v_{\rm rel}}, \tag{4.5}$$

where $\rho_{\rm gas}$ is the density of gas.

Equating Eq. (4.1) and Eq. (4.5), we achieve the relative velocity between asteroids at the equilibrium as

$$\begin{aligned} v_{\rm rel} =& 300\Big(\frac{R_{\rm ast}}{50\,{\rm km}}\Big)^{1/5}\Big(\frac{M_{\rm proto}}{M_{\rm Mars}}\Big)^{1/3}\Big(\frac{a}{3{\rm AU}}\Big)^{-7/10} \\ &\times \Big(\frac{\rho_{\rm gas}}{2\times 10^{-9}\,{\rm g/cm^{-3}}}\Big)^{-1/5}\Big(\frac{\tilde{b}_{\rm sep}}{10}\Big)^{-1/5}\Big(\frac{\rho_s}{1\,{\rm g/cm^3}}\Big)^{1/5}{\rm m/s}, \end{aligned} \tag{4.6}$$

where $M_{\rm Mars}$ is the mass of Mars and $2\times10^{-9}\,{\rm g/cm^3}$ is the typical gas density obtained from the minimum mass solar nebula model (Hayashi 1981). Eq. (4.6) shows that the relative velocity between asteroids is comparable to the escape velocity from asteroids with the radius 50 km

until the mass of protoplanets grows to be Mars mass. Thus non-destructive impacts mainly occur when the planet formation is ongoing.

Present Environment

In the present solar system, the impact velocity between asteroids is comparable to the Keplerian velocity because of the existence of the planets. The average relative velocity of asteroids is roughly estimated as $\sqrt{e_{\rm ave}^2 + i_{\rm ave}^2} v_{\rm K}$, where $e_{\rm ave}$ and $i_{\rm ave}$ are the average orbital eccentricity and inclination, respectively. In the main belt, the Keplerian velocity is $v_{\rm K} \approx 20\,{\rm km/s}$. We achieve the orbital elements of all observed asteroids from Jet Propulsion Laboratory (JPL) Small-Body Database [1], and the average eccentricity and inclination are calculated as $e_{\rm ave} = 0.15$ and $i_{\rm ave} = 0.13$ (cf. Ueda et al. 2017). Thus, the average relative velocity is calculated as $\approx 4\,{\rm km/s}$.

We will also estimate the distribution of impact velocities between main-belt asteroids according to the method for obtaining the relative velocity at the orbital crossing described in Whitmire et al. (1998) and Kobayashi and Ida (2001). We consider two asteroids 1 and 2 orbiting around the sun. The orbital elements of asteroid 1 and 2 have subscripts of 1 and 2, respectively. r, f, a, e, i, Ω, and ω represent orbital radius, true anomaly, semi-major axis, eccentricity, inclination, longitude of ascending node, and argument of pericenter, respectively, and $p = a(1-e^2)$. $\Delta\tilde{\omega}$ shows the difference of longitude of pericenters of two asteroids and is defined as $\Delta\tilde{\omega} = \tilde{\omega_2} - \tilde{\omega_1} = (\Omega_2 + \omega_2) - (\Omega_1 + \omega_1)$.

We assume the inclinations of two asteroids are small and set $i_1 = i_2 = 0$, which leads to the simple condition of the orbital crossing of $r_1 = r_2$. Thus the orbital crossing occurs when

$$\left(\frac{1}{r_1} - \frac{1}{r_2}\right)_{f_2 = f_{2,c}} = 0 = \frac{1}{p_1} - \frac{1}{p_2} + \frac{e_1 \cos(f_{2,c} - \Delta\tilde{\omega})}{p_1} - \frac{e_2 \cos f_{2,c}}{p_2}, \tag{4.7}$$

where $f_{2,c}$ is the true anomaly of asteroid 2 at the orbital crossing. Note that we have the relation of $f_1 = f_2 - \Delta\tilde{\omega}$ when two asteroids are located on the same line connecting the asteroids and the sun. The solution for $f_{2,c}$ of Eq (4.7) is given by

$$\cos f_{2,c} = \frac{-AB \pm C\sqrt{C^2 + B^2 - A^2}}{B^2 + C^2}, \tag{4.8}$$

where

[1] https://ssd.jpl.nasa.gov/sbdb_query.cgi#x

$$A = p_2 - p_1,$$
$$B = e_1 p_2 \cos\Delta\tilde{\omega} - e_2 p_1,$$
$$C = e_1 p_2 \sin\Delta\tilde{\omega}. \tag{4.9}$$

If the orbits of two asteroids intersect each other, Eq. (4.8) has physical solutions, which requires

$$C^2 + B^2 - A^2 \geq 0. \tag{4.10}$$

Note that Eq. (4.8) has two solutions, and thus $f_{2,c}$ has two values if Eq. (4.10) is satisfied.

If Eq. (4.10) is satisfied, the orbits of two asteroids are crossing under the assumption of $i_1 = i_2 = 0$. Then, we assess whether two asteroids collide each other or not in three-dimensional space when $f_2 = f_{2,c}$ and $f_1 = f_{2,c} - \Delta\tilde{\omega}$. The heights of two asteroids from the equatorial plane of the sun are

$$z_1 = r_c \sin(f_{2,c} - \Delta\tilde{\omega} + \omega_1) i_1,$$
$$z_2 = r_c \sin(f_{2,c} + \omega_2) i_2, \tag{4.11}$$

where r_c is the orbital radius at the orbital crossing given by

$$r_c = \frac{p_2}{1 + e_2 \cos f_{2,c}}. \tag{4.12}$$

Note that we still assume i_1 and i_2 are small, which leads to $\sin i_1 \approx i_1$, $\cos i_1 \approx 0$, $\sin i_2 \approx i_2$, and $\cos i_2 \approx 0$. The collision occurs if $|z_1 - z_2|$ is smaller than $(D_1 + D_2)/2$, where D_1 and D_2 are the diameters of asteroid 1 and 2, respectively. Here, to increase the number of samples, we use the more loose condition of

$$|z_1 - z_2| < 5(D_1 + D_2). \tag{4.13}$$

If Eqs (4.10) and (4.13) are satisfied, we calculate the relative velocity between two asteroids v_{12} at the orbital crossing as follows:

$$v_{12}^2 = GM_s \Big[\Big(\frac{e_1 \sin(f_{2,c} - \Delta\tilde{\omega})}{\sqrt{p_1}} - \frac{e_2 \sin f_{2,c}}{\sqrt{p_2}} \Big)^2 + \Big(\frac{\sqrt{p_1}}{r_c} - \frac{\sqrt{p_2}}{r_c} \Big)^2 + \Big(\frac{i_1[\cos(f_{2,c} - \Delta\tilde{\omega} + \omega_1) + e_1 \cos\omega_1]}{\sqrt{p_1}} - \frac{i_2[\cos(f_{2,c} + \omega_2) + e_2 \cos\omega_2]}{\sqrt{p_2}} \Big)^2 \Big]. \tag{4.14}$$

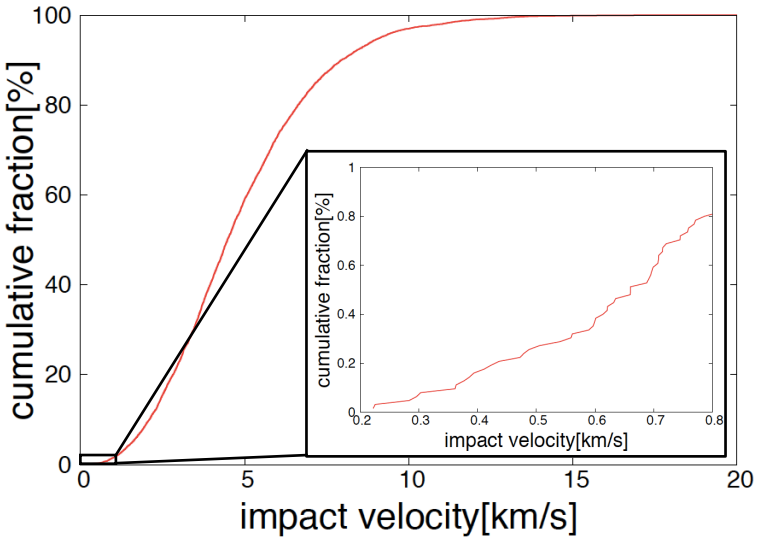

Figure 4.1: Cumulative distribution of impact velocities of possible collisions between main-belt asteroids. The horizontal axis represents estimated impact velocity, and the vertical axis represents the fraction of the impact velocity that is smaller than the value in the horizontal axis. Blow-up figure shows the distribution for the lower impact velocity.

We evaluate whether the orbital crossing occurs or not using Eqs (4.10) and (4.13) for each pair of all observed asteroids in the main belt, and we calculate possible impact velocity as Eq (4.14) if Eqs (4.10) and (4.13) are satisfied. The orbital elements of asteroids are obtained from JPL Small-Body Database. Fig. 4.1 shows the distribution of the possible impact velocity between main-belt asteroids in the present main belt. The average impact velocity is calculated as 5 km/s, which is consistent with the rough estimation using the average eccentricity and inclination. The fraction of the impact velocity smaller than 400 m/s is only about 0.2%. The impact simulations in Section 3.3 show that equal-mass and non-destructive impacts require $v_{\rm imp} < 400\,{\rm m/s}$, and thus similar-mass impacts in the present environment mainly result in catastrophic destruction.

4.1.3 Shapes Formed in the Primordial and Present Environments

The impact velocity is comparable to the escape velocity from asteroids with the diameter $D = 100\,{\rm km}$ in the primordial environment before the formation of Mars-mass protoplanets (see Section 4.1.2). The asteroids with $D > 100\,{\rm km}$ are mainly the largest bodies among asteroids (see Fig. 1.2), and thus they mainly collide with similar-mass or smaller asteroids. As we

investigated in Sections 3.3 and 3.4.1, similar-mass impacts, especially equal-mass impacts, produce various (bilobed, spherical, flat, elongated, and hemispherical) shapes including extremely elongated and flat shapes. High-mass-ratio impacts in the primordial environment merely result in crater formation or coalescence, and such impacts do not deform target asteroids. Although high-mass-ratio impacts are more frequent than similar-mass impacts, the shapes of 100 km asteroids are probably determined by the last similar-mass impacts.

In the present environment, the typical impact velocity is much larger than the escape velocity from 100 km asteroids. The impacts with the impact velocity comparable to the escape velocity may occur, but the fraction of such impacts is about 0.2%; such impacts rarely occur (see Fig. 4.1). Relatively similar-mass impacts with the impact velocity much larger than the escape velocity result in destructive impacts. As we investigated in Section 3.5, destructive impacts mainly produce spherical and bilobed shapes. Larger mass-ratio impacts may result in non-destructive impacts with overall deformation of target asteroids. However, as we investigated in Section 3.4.2, such impacts do not produce the irregular shapes of target asteroids with $c/a \leq 0.6$.

4.2 Comparison with Actual Asteroids

4.2.1 Databases Utilized in Our Analysis

DAMIT

Database of Asteroid Models from Inversion Technique[2] (DAMIT: Ďurech et al. 2010) is a database that mainly includes the shape models of asteroids. The shape models of asteroids stored in DAMIT are mainly obtained from light curves of asteroids through light curve inversion technique (Kaasalainen and Torppa 2001; Kaasalainen et al. 2001). As of November 2018, DAMIT provides the shape models of 1,609 asteroids.

Light curve inversion technique accurately measures the shapes of asteroids, at least the axis ratio b/a of elongated asteroids. For example, b/a of the asteroid Itokawa obtained from the light curve is about 0.5 (Kaasalainen et al. 2003), while that measured by the in-situ observation is 0.55 (Fujiwara et al. 2006). Thus the shape models obtained from light curves has enough accuracy to analyze the axis ratios of asteroids.

The shape models in DAMIT are represented as polyhedrons with triangular surface facets. For each asteroids, DAMIT provides the file that includes the information of coordinates x,

[2]http://astro.troja.mff.cuni.cz/projects/asteroids3D/web.php

y, and z on the surface of the shape model. We utilize the coordinates of the surface of the shape model to derive the axis ratios of asteroids. To measure the axis ratios of the shape models of asteroids, we follow the bottom-up method (Fujiwara et al. 1978, see also Section 3.2). Note that the coordinates x, y, and z for the most shape models are normalized by the volume of each shape model, so that we cannot achieve the information of the size of asteroids from DAMIT.

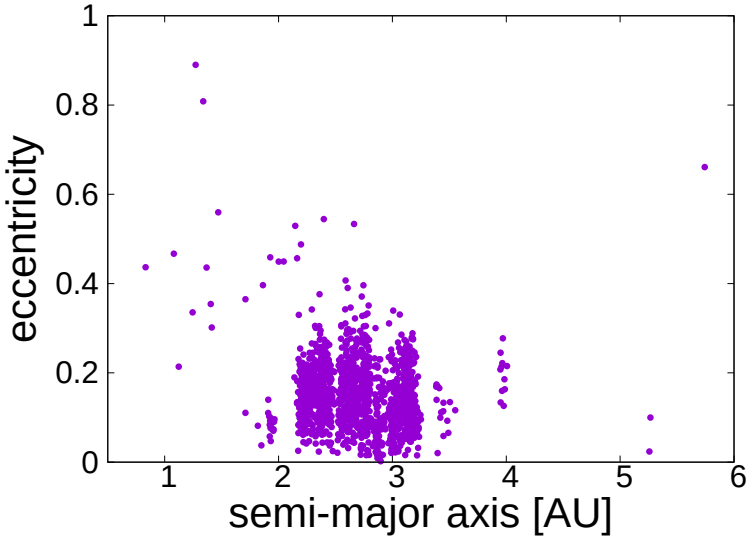

Figure 4.2: Orbital elements of the asteroids of which shape models are stored in DAMIT. The horizontal axis represents the orbital semi-major axis of the asteroids, and the vertical axis represents the orbital eccentricity of the asteroids.

Figure 4.2 shows the orbital semi-major axis and eccentricity of the asteroids of which shape models are stored in DAMIT. From Fig. 4.2, we notice that the most asteroids in DAMIT are the main-belt asteroids, but some of them are the near-Earth asteroids, Hilda asteroids, and Trojan asteroids.

Figure 4.3 shows the ratio of the number of the asteroids that are included in DAMIT to that of all observed asteroids. We notice that DAMIT includes more than 50% of the asteroids with the diameter D larger than 100 km, and thus the shapes of the almost all of the asteroids ≥ 100 km are measured. However, the shapes of only about 10% of asteroids with $D > 10$ km are measured. For the asteroids ≤ 10 km, the fraction of the asteroids with known shapes is less than 1%.

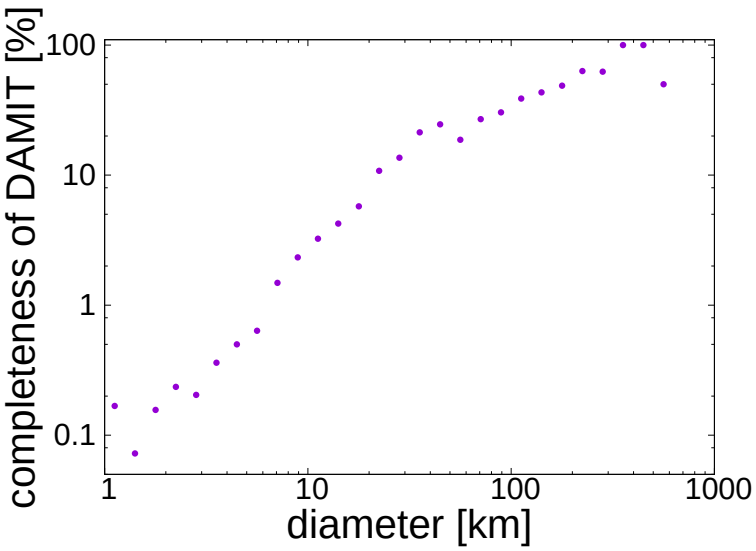

Figure 4.3: The ratio of the number of DAMIT asteroids to that of all observed asteroids. The vertical axis represents the fraction, and the horizontal axis represents the diameter of asteroids.

JPL Small-Body Database

Small-Body Database of Jet Propulsion Laboratory (JPL) provides the orbital and physical information of the asteroids. The physical information includes the diameter, absolute magnitude, albedo, and rotation period. We utilize the diameters of asteroids listed in JPL Small-Body Database to distinguish the shapes of larger asteroids and smaller asteroids.

The diameters of asteroids cannot be determined by solely the absolute magnitude in visible light, because the absolute magnitude depends on both of the diameter and the albedo, and albedo is not well determined. Thus, the almost all of the diameters of asteroids in JPL Small-Body Database are obtained from NEOWISE mission. NEOWISE mission was conducted by the spacecraft Wide-field Infrared Survey Explorer (WISE). WISE observed various objects including asteroids in infrared wavelengths. The magnitude of asteroids in infrared wavelength is mainly determined by the temperature of asteroids and not strongly depends on the albedo. Therefore, if we utilize both the magnitudes in visible and infrared wavelength, we can accurately determine the diameters of asteroids.

AstDyS-2

Asteroid Dynamics Site-2[3] (AstDyS-2) summarizes the orbital information of asteroids. The information in AstDyS-2 includes that of asteroid families. From this database, we can find that each asteroid is belonging to any family or not and the name of a family that each asteroid belongs to. Asteroid families were formed through relatively recent impacts, and thus we distinguish the asteroids that were affected by recent impacts and those are not affected using the family information obtained from AstDyS-2.

The family classification of AstDyS-2 is based on Milani et al. (2014). Note that the results of family classification depend on classification method. Throughout this study, we utilize the family information obtained from AstDyS-2.

4.2.2 Fraction of Family Asteroids

Asteroids in asteroid families were formed in recent impacts. Although asteroid families are dissipated with the typical timescale of about 1 Gyr, the fraction of family asteroids may tell us how many asteroids were affected by recent destructive impacts. Thus, we will calculated the dependence of the fraction of family asteroids on the diameters of asteroids. We use the information of asteroid families obtained from AstDyS-2 and the diameters of asteroids obtained from JPL Small Body Database.

Shapes of asteroids in asteroid families were mainly formed through recent destructive impacts. However, the largest bodies of cratering families are not the case because those shapes were not affected by family-forming impacts. To correctly detect the effect of recent destructive impacts onto shapes of asteroids, we should remove the largest bodies of cratering families from our analysis. Here, we consider the families with $M_{\rm lr}/M_{\rm pb} > 0.8$ as cratering families, where $M_{\rm lr}$ is the mass of the largest bodies among asteroids in each family and $M_{\rm pb}$ is the total mass of each family, i.e., the mass of the parent body. We calculate the ratio $M_{\rm lr}/M_{\rm pb}$ using the diameters of member asteroids as follows:

$$\frac{M_{\rm lr}}{M_{\rm pb}} = \frac{D_{\rm lr}^3}{\sum_n D_n^3}, \tag{4.15}$$

where $D_{\rm lr}$ is the diameters of the largest bodies, D_n is the diameters of member asteroids, and $\sum_n$ denotes the summation for all member asteroids. Here, we assume the density for all asteroids is the same. Hereafter, family asteroids mean the asteroids in any families except

[3]http://hamilton.dm.unipi.it/astdys/index.php?pc=0

for the largest asteroids in the cratering families, and non-family asteroids mean the largest asteroids in the cratering families in addition to the asteroids that do not belong to any families.

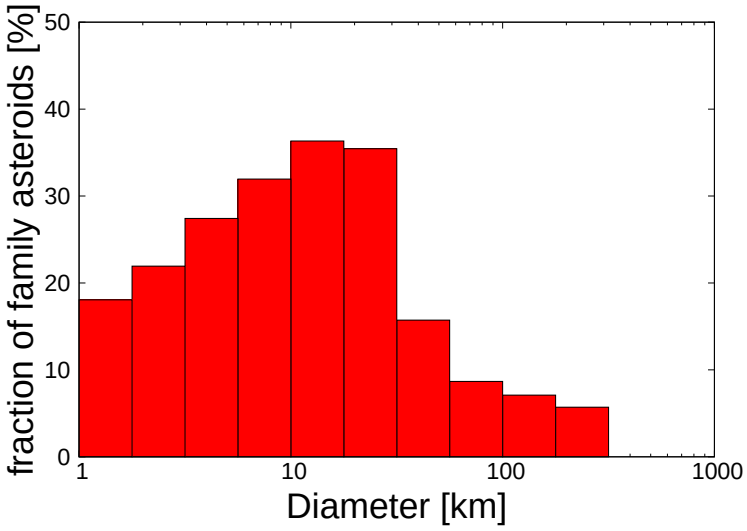

Figure 4.4: The fraction of family asteroids. The vertical axis represents the fraction, i.e., the ratio of the number of family asteroids to that of all asteroids, and the horizontal axis represents the diameters of asteroids.

Figure 4.4 shows the dependence of the fraction of family asteroids on the diameters of asteroids. As we notice from Fig 4.4, the fraction is less than 10% for the asteroids with $D > 100\,\mathrm{km}$, which is significantly smaller than that for smaller asteroids $\approx 30\%$. This is because the larger asteroids are difficult to be disrupted and the collisions that destroy the larger asteroids are not frequent. Thus about 90% of asteroids with $D > 100\,\mathrm{km}$ are probably not affected by the recent destructive impacts. This is consistent with the collisional lifetime estimated in O'Brien and Greenberg (2005); the collisional lifetimes for the asteroids $> 100\,\mathrm{km}$ are estimated to be about ten times longer than the age of the solar system (see Fig. 1.5), which means that only about one tenth of asteroids are destructed within the timescale comparable to the age of the solar system. Therefore, the shapes of larger asteroids may keep those formed in the primordial environment.

We also notice from Fig 4.4 that the fraction decreases with decreasing the diameters for the asteroids with $D < 10\,\mathrm{km}$. The timescale of the Yarkovsky effect for the asteroids with $D = 1\,\mathrm{km}$ is about ten times longer than the collisional lifetime (e.g., Morbidelli and Vokrouhlický 2003). Thus this tendency is probably not caused by the dissipation due to the Yarkovsky effect. Although we have not yet specified the reason of this tendency, we assume that this tendency

is merely caused by the error of orbital elements or incompleteness of family classification due to the smaller size of asteroids.

4.2.3 Asteroids Larger Than 100 km

As we showed in Section 4.2.2, the fraction of family asteroids with the diameter $D \geq 100\,\mathrm{km}$ is significantly smaller than that with $D < 100\,\mathrm{km}$, which means that the shapes of the larger asteroids may be formed in the primordial environment. We showed in Section 4.1.2 that low-velocity impacts in the primordial environment mainly result in non-destructive impacts, while high-velocity impacts in the present environment mainly result in destructive impacts. Thus, the comparison between the shapes of non-family and family asteroids with $D \geq 100\,\mathrm{km}$ may suggest the difference of the formation era, which leads to constrain when these asteroids were formed. We also discuss the comparison between the results of our collisional simulations and the shapes of actual asteroids.

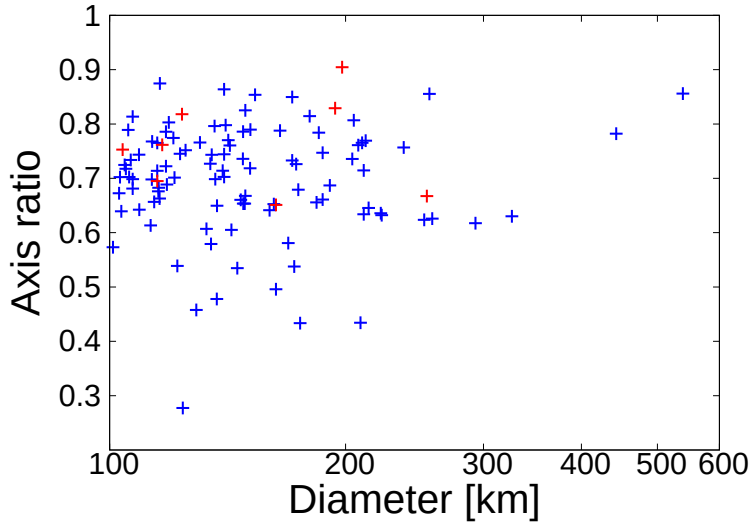

Figure 4.5: The axis ratio c/a of the asteroids with the diameters D larger than 100 km. The vertical axis represents c/a, and the horizontal axis represents the diameter. The blue points show the non-family asteroids, while the red points show the family asteroids.

Figure 4.5 shows the axis ratio c/a of the non-family and family asteroids with the diameters $> 100\,\mathrm{km}$. All family asteroids, which were affected by recent destructive impacts, have the axis ratio $c/a > 0.6$, i.e., they have rounded shapes, while some of non-family asteroids have the irregular shapes with $c/a < 0.6$. This may suggest the difference of the formation environment. However, this tendency is not statistically significant. The number of the family asteroids that

have the irregular shapes with $c/a < 0.6$ is zero among eight family asteroids, while the number of the non-family asteroids that have the irregular shapes with $c/a < 0.6$ is 12 among 107 non-family asteroids. The fraction of the irregular shapes of family asteroids is not so different from that of non-family asteroids.

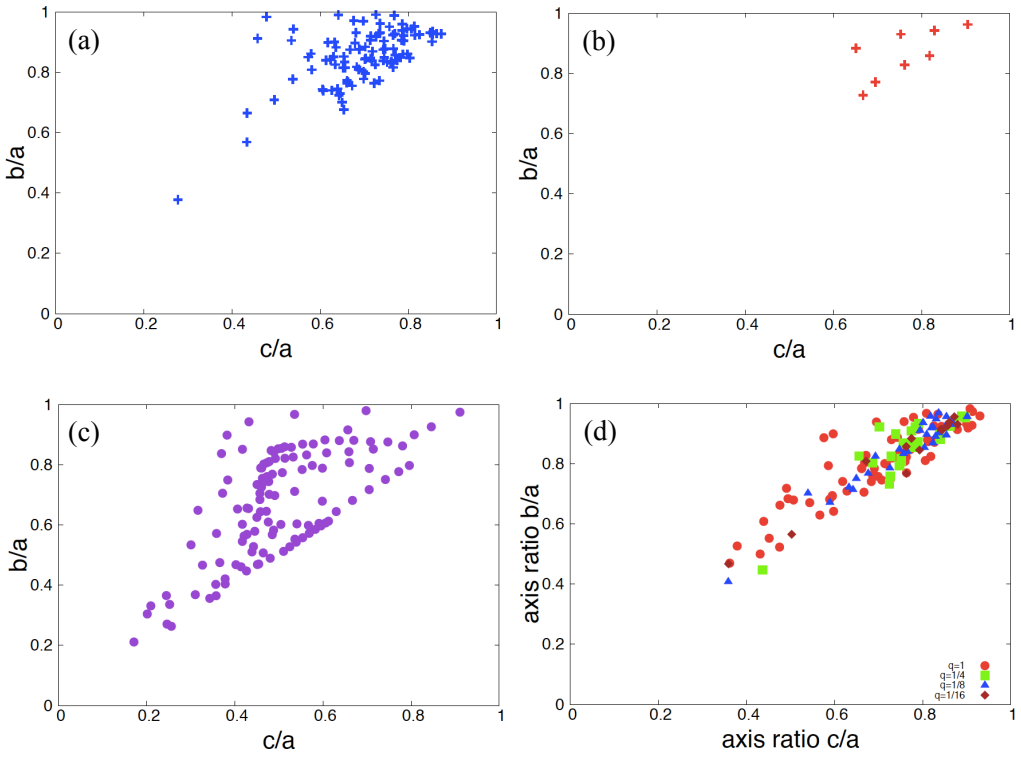

Figure 4.6: Shape distributions of the actual asteroids and the remnants produced through our simulations. In each panel, the horizontal axis represents the axis ratio c/a, and the vertical axis represents the axis ratio b/a. The panel (a) shows the shape distribution of the actual non-family asteroids with $D > 100\,\mathrm{km}$, and the panel (b) shows that of the actual family asteroids. The panels (c) and (d) show those of the remnants produced through our non-destructive and equal-mass impacts (see Fig. 3.15) and destructive impacts (see Fig. 3.24), respectively.

Figure 4.6a and b show the axis ratios of actual non-family and family asteroids, respectively. Fig. 4.6b again shows that all of the shapes of the family asteroids with $D > 100\,\mathrm{km}$ are rounded shapes with $c/a > 0.6$, while Fig. 4.6a shows that the shapes of the non-family asteroids include the extremely elongated shape with $b/a \approx 0.4$ or the extremely flat shapes with $c/a \approx 0.4$. From the comparison between the shapes of the remnants produced through our simulations of the destructive impacts (Fig. 4.6d) and those of actual non-family asteroids (Fig. 4.6a), we notice that the destructive impacts, especially the unequal-mass impacts, are difficult to produce the

flat shapes of the actual asteroids with $c/a \approx 0.4$. Note that the impacts with $q = 1$ in Fig 4.6d has the impact velocity of $v_{\rm imp} = 350\,{\rm m/s}$, which is still difficult to occur in the present environment. In contrast, Fig. 4.6c shows that non-destructive and equal-mass impacts can produce flat shapes with $c/a \approx 0.4$.

As we discussed in Section 4.1.2, the impacts in the present environment mainly result in destructive impacts, which do not lead to the formation of flat shapes. In contrast, the impacts in the primordial environment mainly result in non-destructive impacts, so that the similar-mass impacts in the primordial environment lead to the formation of flat shapes. Therefore, the flat shapes of non-family asteroids with $D > 100\,{\rm km}$ are likely to be formed in the primordial environment before the formation of Jupiter, and remain the same until today.

Family asteroids were formed through recent destructive impacts (see Fig. 1.4). However, non-family asteroids were not necessarily formed in the primordial environment. They may have been formed through recent destructive impacts, but they are no longer family asteroids due to, for example, scattering through mean motion resonances with gas giants. The information of shapes, especially flat shapes of asteroids, tells us they were surely formed in the primordial environment through low-velocity impacts.

4.2.4 Asteroids Larger Than 10 km

The fraction of the family asteroids with $D > 10\,{\rm km}$ is much higher than that of the asteroids with $D > 100\,{\rm km}$ (see Fig. 4.4). Thus, it is less likely that the shapes of the asteroids with $D > 10\,{\rm km}$ also keep those formed in the primordial environment. However, O'Brien and Greenberg (2005) show that the collisional lifetimes for the asteroids with $D = 10\,{\rm km}$ are comparable to the age of the solar system, which suggests that about half of such asteroids may not experience recent destructive impacts. Moreover, Fig. 4.4 shows that about two third of the asteroids with $D \approx 10\,{\rm km}$ still do not belong to any family, which means that they may not be affected by recent impacts. Thus, we may also find the difference of the shapes between family and non-family asteroids with $D > 10\,{\rm km}$.

Figure 4.7 is the same as Fig. 4.5, but for the asteroids with $D > 10\,{\rm km}$. As we notice from Fig. 4.7, the difference of c/a between the family and non-family asteroids is not apparent compared to the asteroids with $D > 100\,{\rm km}$. The fraction of the asteroids with $c/a < 0.6$ is similar for the family and non-family asteroids. The number of the family asteroids with $c/a < 0.6$ is 120 among 237 family asteroids with $D > 10\,{\rm km}$; the fraction is 50.6%. The number of the non-family asteroids with $c/a < 0.6$ is 255 among 591 non-family asteroids

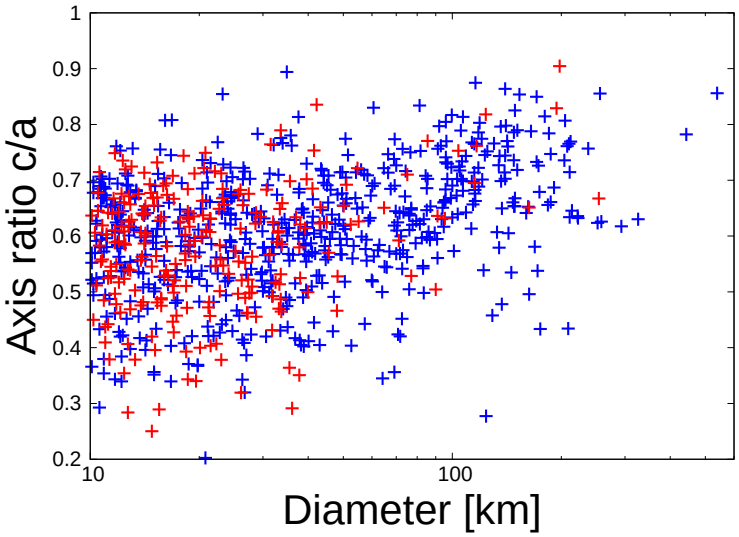

Figure 4.7: Axis ratio c/a of the asteroids with $D > 10\,\mathrm{km}$. The vertical axis represents c/a, and the horizontal axis represents the diameter. The blue points show the non-family asteroids, while the red points show the family asteroids.

with $D > 10\,\mathrm{km}$; the fraction is 43.1%. Both non-destructive and destructive impacts produce irregular shapes with smaller c/a; non-destructive impacts produce various irregular shapes (see Fig. 3.15), and destructive impacts produce bilobed shapes (see Fig. 3.24). This suggests that we cannot distinguish the family and non-family asteroids only with the ratio c/a.

As we investigated in Section 3.5, the destructive impacts are difficult to produce flat shapes. Thus the fraction of flat shapes of family asteroids may be different from that of non-family asteroids. Fig. 4.8 shows the shape distribution of the asteroids with $D > 10\,\mathrm{km}$. Here, we define the flat shapes as the shape with $c/a < 0.6$ and $b/a > 0.8$, and count the number of the flat shapes for non-family and family asteroids. We find 50 non-family asteroids with the flat shapes among 591 non-family asteroids; the fraction of the flat shapes is 8.5%. In contrast, we find 9 family asteroids with the flat shapes among 237 family asteroids; the fraction is 3.8%. Therefore, the fraction of the flat shapes of the non-family asteroids is more than twice as high as that of the family asteroids; the fraction of the flat shapes of the family asteroids, which are affected by recent destructive impacts, is significantly small. It is consistence with the result of our simulations that destructive impacts are difficult to produce flat shapes.

Our simulations predict that destructive impacts do not produce flat shapes, and thus we expect that the family asteroids do not include flat shapes. However, Fig. 4.8 shows that there are several family asteroids with flat shapes. This may be caused by observational errors; it

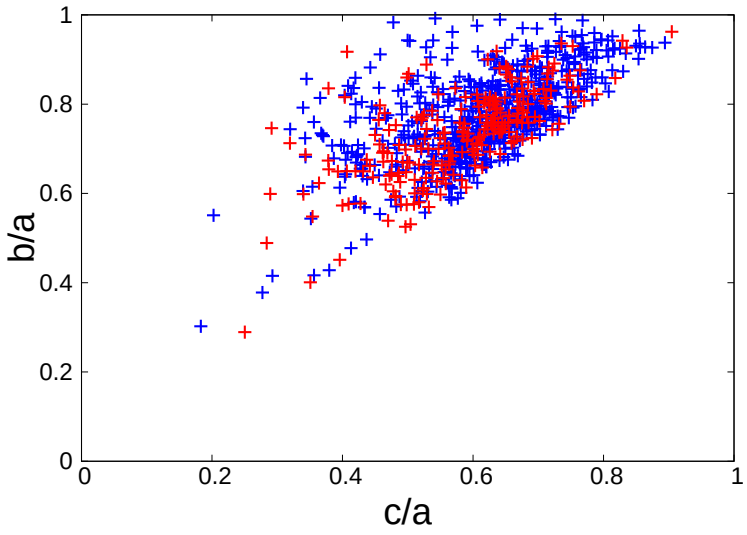

Figure 4.8: Shape distribution of the asteroids with $D > 10\,\mathrm{km}$. The horizontal axis represents the ratio c/a, and the vertical axis represents the ratio b/a. The blue points show the non-family asteroids, while red points show the family asteroids.

might be difficult to distinguish flat shapes and elongated shapes solely by light curves because both flat and elongated shapes cause brightness variations due to rotations, and flat shapes of the family asteroids may be elongated shapes.

Although we have not yet specified the reason why the family asteroids with $D > 10\,\mathrm{km}$ include flat shapes, there is one possible mechanism. The dispersion speed of family asteroids just after the shattering of parent bodies is estimated to be $\sim 100\,\mathrm{m/s}$ (e.g., Michel et al. 2001); the dispersion speed is comparable to the impact velocity of non-destructive impact in the primordial environment. Shuttered bodies return to the place where family-forming impacts occur after one or more revolutions around the sun, and they may collide with each other with low impact velocities, which may result in the formation of flat shapes of family asteroids if colliding two bodies have similar masses.

The reason why the family asteroids with $D > 100\,\mathrm{km}$ do not include flat shapes is expected to be rack of similar-mass family members. The family asteroids with $D > 100\,\mathrm{km}$ are mainly the largest bodies among family members. The number of family members increases with decreasing the size of members, and thus the number of similar-mass members for $D > 100\,\mathrm{km}$ is small: Similar-mass impacts between family members with $D > 100\,\mathrm{km}$ are difficult to occur, which may lead to the rack of flat family asteroids. We counted the number of similar-mass asteroids (the mass ratio is larger than 0.5) among the members in the same families for eight

family asteroids with $D > 100\,\mathrm{km}$ ((5) Astraea, (15) Eunomia, (423) Diotima, (85) Io, (104) Klymene, (24) Themis, (171) Ophelia, and (221) Eos). The number of similar-mass members is as follows: 1 for (5) Astraea, 0 for (15) Eunomia, 0 for (423) Diotima, 1 for (85) Io, 3 for (104) Klymene, 0 for (24) Themis, 4 for (171) Ophelia, and 5 for (221) Eos. Thus the number of similar-mass family members is in fact small for the family asteroids with $D > 100\,\mathrm{km}$.

In contrast, the number of similar-mass members for the family asteroids with $D > 10\,\mathrm{km}$ is relatively large because they are not the largest bodies among asteroids in the same families. We also counted the number of similar-mass members for nine family asteroids with the flat shapes and $D > 10\,\mathrm{km}$ ((135) Hertha, (355) Gabriella, (1040) Klumpkea, (1286) Banachiewicza, (2962) Otto, (6905) Miyazaki, (3261) Tvardovskij, (608) Adlfine, and (1836) Komarov). Six asteroids among them indeed have large number of similar-mass members: 133 for (1286) Banachiewicza, 9 for (2962) Otto, 62 for (6905) Miyazaki, 90 for (3261) Tvardovskij, 151 for (608) Adlfine, and 8 for (1836) Komarov. Thus the flat shapes of these family asteroids are possible to be formed through low-velocity and similar-mass impacts between member asteroids. However, the number of similar-mass members for three of them is very small: 0 for (135) Hertha, 0 for (355) Gabriella, and 3 for (1040) Klumpkea. We do not know any mechanism to produce the flat shapes of these family asteroids, and they may be interlopers that were non-family asteroids in past.

4.2.5 Direction of Rotation Axis

We investigated collisional formation of elongated and flat shapes through equal-mass and low-velocity impacts in Section 3.3. Our simulations predict that the rotation axis of elongated bodies are perpendicular to the major axis and those of flat bodies are perpendicular to the minor axis if these bodies are formed through equal-mass and low-velocity impacts. To verify our prediction, we investigate the angles between rotation axis and the major or minor axis of actual asteroids.

Figure 4.9a shows the angles between the rotation axis and the major axis of the elongated asteroids with $b/a < 0.6$ and $c/a < 0.6$. From Fig. 4.9a, we notice that all the elongated asteroids have the rotation axis almost perpendicular to the major axis, which means that the rotation axis almost aligns with the minor axis. The directions of the rotation axis of the elongated asteroids are consistent with those of the elongated remnants formed through our simulations of the equal-mass and low-velocity impacts (see e.g., Fig. 3.2). From Fig. 4.9b, we notice that the almost all of the flat asteroids have the rotation axis aligned to the minor axis.

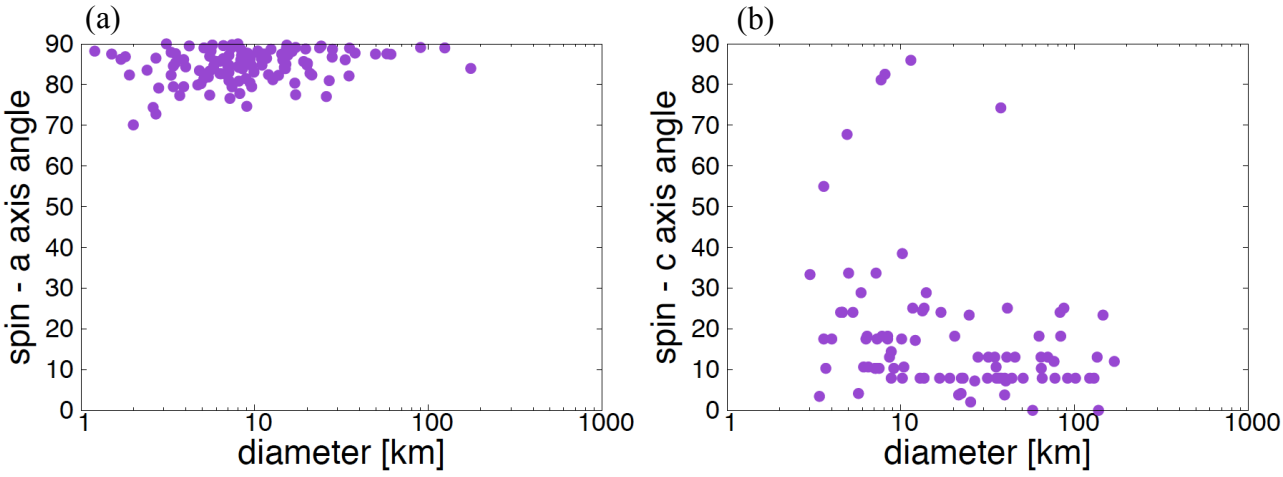

Figure 4.9: Angles between rotation axis and the major or minor axis of the elongated or flat asteroids, respectively. The horizontal axes for two panels show the diameters of the asteroids. In the panel (a), the vertical axis represents the angles between the rotation axis and the major axis of the elongated asteroids with $b/a < 0.6$ and $c/a < 0.6$. In the panel (b), the vertical axis represents the angles between the rotation axis and the minor axis of the flat asteroids with $b/a > 0.8$ and $c/a < 0.6$.

The directions of the rotation axis of the flat remnants produced through our simulations of the equal-mass and low-velocity impacts are perpendicular to the minor axis (see Fig. 3.8), and thus the directions of the rotation axis of the actual flat asteroids are inconsistent with the results of our simulations.

In Section 4.2.3, we argued that the flat asteroids with $D > 100\,\mathrm{km}$ were formed in the primordial environment before the formation of Jupiter through similar-mass and low-velocity impacts (see Fig. 3.8). The rotation axis of the produced flat remnants is perpendicular to the minor axis and they rotate around the major axis. Rotation energy of the rotation around the major axis is larger than that around the minor axis, and thus internal energy dissipation causes gradual alignment of the rotation axis with the minor axis. Internal energy dissipation is mainly caused by the deformation stress due to the gyroscopic torque and the stress due to the deformation of the centrifugal bulge during wobble motions (Burns and Safronov 1973). Note that the flat remnant in Fig. 3.8 also does the wobble motion with much longer period than the duration of the simulation. Burns and Safronov (1973) estimated the timescale of the alignment as

$$\tau_{\mathrm{align}} = \frac{\mu Q}{\rho K_3^2 R_{\mathrm{ast}}^2 \omega_{\mathrm{rot}}^3}, \tag{4.16}$$

where μ is the rigidity of asteroids, ρ is its density, $R_{\rm ast}$ is its radius, and $\omega_{\rm rot}$ is its rotational angular frequency. Q is the material's quality factor, which is roughly defined as the ratio of the total stored strain energy to the energy loss per cycle of wobble motion. K_3^2 is a shape factor, and $K_3^2 \approx 10^{-2}$ for spherical bodies and $K_3^2 \approx 0.1[(a-c)/c]^2$ for irregular shaped bodies. With the probable parameters shown in Burns and Safronov (1973), the alignment timescale is estimated to be

$$\tau_{\rm align} = 1.0 \times 10^6 \Big(\frac{R_{\rm ast}}{50\,{\rm km}}\Big)^{-2} \Big(\frac{T_{\rm rot}}{8\,{\rm hour}}\Big)^3 {\rm year}, \tag{4.17}$$

where $T_{\rm rot}$ is the rotation period. Thus, the timescale for the alignment of the rotation axis with the minor axis is about 1 Myr, which is much shorter than the age of the solar system. Therefore, we suggest that the flat asteroids with $D > 100\,{\rm km}$ were formed in the primordial environment and initially had the rotation axis perpendicular to the minor axis, but the rotation axis now aligns with the minor axis due to the internal energy dissipation.

Chapter 5

Application: Extremely Elongated Shape of 1I/′Oumuamua

As we showed in Section 3.3, equal-mass and non-destructive impacts can produce extremely elongated shapes of asteroids. Recently, an interstellar object 1I/′Oumuamua that has the extremely elongated shape was discovered. In this chapter, we will introduce the results of our simulations that investigate detailed impact conditions to form extremely elongated asteroids. Almost all parts of this chapter are based on Sugiura et al. (2018b).

5.1 Introduction of 1I/′Oumuamua

1I/′Oumuamua was discovered by Pan-STARRS1 on October 2017 (Meech et al. 2017). It is recognized to be an interstellar object because of its high orbital eccentricity $e \approx 1.2$. A considerable fraction of planetesimals are ejected from planetary systems during the planet formation stage (Bottke et al. 2005; Raymond et al. 2018; Jackson et al. 2018); thus it is no wonder that interstellar objects exist. Moreover, the velocity at infinity $v_\infty \approx 26\,\mathrm{km/s}$ of 1I/′Oumuamua is close to relative velocities of stars in the solar neighborhood. Therefore this object is likely to come from a nearby planetary system (Meech et al. 2017; de la Fuente Marcos and de la Fuente Marcos 2017).

The absolute magnitude of 1I/′Oumuamua is $H_\mathrm{V} \approx 22\,\mathrm{mag}$, which corresponds to a mean radius of about 100 m with albedo 0.04 (Meech et al. 2017; Bolin et al. 2018; Bannister et al. 2017). The rotation period of 1I/′Oumuamua is about 8 hours (e.g., Bolin et al. 2018). Its spectral feature is consistent with that of D-type asteroids or comets (Meech et al. 2017). Although no cometary activity is confirmed through imaging observations (Meech et al. 2017; Ye et al. 2017; Jewitt et al. 2017), non-gravitational acceleration of 1I/′Oumuamua is measured

later (Micheli et al. 2018), which may be the result of mild cometary activity. Thus the composition of 1I/′Oumuamua is still under debate.

An interesting characteristic of 1I/′Oumuamua is the large light curve amplitude of about 2.5 mag (Meech et al. 2017). If this light curve variation is caused by the change of cross section due to rotation around the minor axis, 1I/′Oumuamua has an extremely elongated shape. Although its dimensions are not yet fully specified because of the short observational period, the ratio of the intermediate axis length b to the major axis length a is estimated in several studies as follows: $b/a < 0.19$ (Bannister et al. 2017), $0.10 < b/a < 0.29$ (Bolin et al. 2018), $b/a < 0.22$ (Drahus et al. 2018), $b/a < 0.20$ (Fraser et al. 2018), $b/a < 0.33$ (Knight et al. 2017), and $b/a \approx 0.1$ (Meech et al. 2017). Therefore, the ratio b/a is estimated to be smaller than about 0.3.

Several mechanisms to produce extremely elongated objects were suggested in the past. Impact experiments in laboratory show that some fragments among several thousands may have $b/a < 0.3$ (Michikami et al. 2016). Tidal disruption may also produce elongated objects (Ćuk 2018). Simulations for the tidal destruction of 3 km-sized rubble piles reproduced with N-body particles show that about 0.5% of resultant bodies produced in all simulations have $b/a < 0.3$ (Walsh and Richardson 2006). Simulations for the spin deformation of rubble piles show that rubble piles with spin states close to equilibrium limits may evolve to elongated shapes (Richardson et al. 2005). Recently it is suggested that extremely elongated objects may be formed through abrasion due to micro particle collisions (Domokos et al. 2009, 2017).

Collisions of bodies can also form elongated objects (e.g., Leinhardt et al. 2000, 2010; Sugiura et al. 2018a). In this chapter, we will investigate the possibility to form extremely elongated objects through collisions in more detail. Here, we will focus on impact simulations with much smaller (50 m sized) asteroids to reproduce extremely elongated objects with the size similar to that of 1I/′Oumuamua, and constrain detailed impact conditions to form shapes with $b/a < 0.3$: we focus on the formation of extremely elongated objects. Here, we define remnants with $b/a < 0.3$ as extremely elongated remnants (hereafter EERs).

5.2 Initial Conditions of Simulations for 1I/′Oumuamua

We use almost the same methods and initial conditions as in Chapter 3. Here, we describe different points from Chapter 3.

To reproduce collisional formation of elongated objects with size similar to 1I/′Oumuamua, the radius of target asteroids is set to $R_t = 50\,\mathrm{m}$. We use about 50,000 SPH particles for a target asteroid because Fig. 3.4 shows that this resolution is sufficient to achieve the converged value of axis ratios of the largest remnants.

We assume that asteroids have primordial property before they melt due to the decay energy of ^{26}Al, i.e, they do not have the tensile strength of solid body and shear strength is determined by the friction of granular material (Richardson et al. 2002). Thus damage parameters D of all SPH particles are initially set to unity.

We use the tillotson equation of state and the parameter set for basalt described in Benz and Asphaug (1999) as in Chapter 3. However, there is a problem if we straightforwardly utilize the original tillotson parameters for basalt. A time step determined by the sound speed of basaltic body $C_s \approx 3\,\mathrm{km/s}$ is calculated to be $\sim 10^{-3}\,\mathrm{s}$, which is much smaller than the time scale of gravitational reaccumulation $\approx 1,600\,\mathrm{s}$ estimated in Eq. (3.1). Thus it is difficult to complete a simulation in an acceptable computation time with the original value of C_s for basalt. However, if impact velocities are much smaller than C_s and shear strength is determined by the friction, results of simulations do not depend on C_s. The validity of this simplification is explained as follows: Motion of each SPH particle is determined by the self-gravity, pressure distribution, and deviatoric stress distribution. If impact velocities are much smaller than the sound speed, pressure distribution is determined by the self-gravity because pressure induced by the impact is immediately relaxed. Here, deviatoric stress is determined by the friction, and frictional force is proportional to the pressure; deviatoric stress distribution is also determined by the self-gravity. Therefore, motion of each SPH particle is solely determined by the self-gravity, and thus the sound speed does not affect results of impacts.

We conduct simulations of the impact with the mass ratio of impacting two bodies $q = 1$, the impact angle $\theta_{\mathrm{imp}} = 15^\circ$, the angle of friction $\phi_d = 40^\circ$, the impact velocity $v_{\mathrm{imp}} = 20\,\mathrm{cm/s}$, and two different values of sound speed, or tillotson parameters of A_{Til} and B_{Til}. Figs. 5.1a and b show snapshots of the impact outcomes with $A_{\mathrm{Til}} = B_{\mathrm{Til}} = 2.67 \times 10^4\,\mathrm{Pa}$ and $A_{\mathrm{Til}} = B_{\mathrm{Til}} = 2.67 \times 10^5\,\mathrm{Pa}$, respectively. From Fig. 5.1, we find that the results of the simulations become almost the same even if we use different values of A_{Til} or B_{Til}.

Thus we set A_{Til} and B_{Til} to $2.67 \times 10^4\,\mathrm{Pa}$, which corresponds to $C_s \approx 3\,\mathrm{m/s}$. This sound speed is still much larger than impact velocities treated in our simulations $\leq 40\,\mathrm{cm/s}$. The same approach utilizing reduced sound speed is adopted in Jutzi and Asphaug (2015).

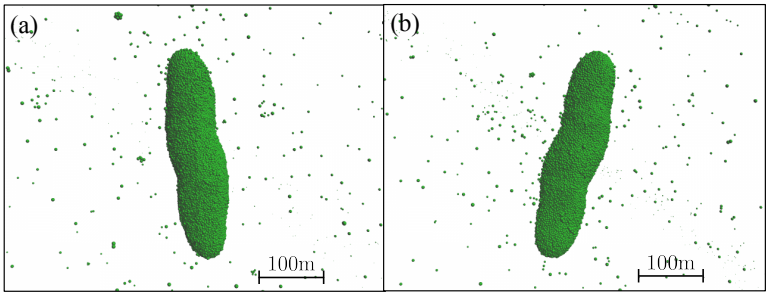

Figure 5.1: Snapshots of the impact with $R_t = 50\,\mathrm{m}$, $q = 1$, $\phi_d = 40°$, $\theta_{\mathrm{imp}} = 15°$, and $v_{\mathrm{imp}} = 20\,\mathrm{cm/s}$ at $t = 1.0 \times 10^5\,\mathrm{s}$. The panel (a) shows the result of the simulation with $A_{\mathrm{Til}} = B_{\mathrm{Til}} = 2.67 \times 10^4\,\mathrm{Pa}$, and the panel (b) shows that with $A_{\mathrm{Til}} = B_{\mathrm{Til}} = 2.67 \times 10^5\,\mathrm{Pa}$. This figure is the same as Fig. 9 of Sugiura et al. (2018b).

5.3 Results of Simulations for 1I/′Oumuamua

We will introduce the results of simulations with various mass ratios q, impact angles θ_{imp}, impact velocities v_{imp}, and friction angles ϕ_d. Table 5.1 summarizes the conditions of the simulations.

q	$\phi_d(°)$	v_{imp}(cm/s)	Δv_{imp}(cm/s)	$\theta_{\mathrm{imp}}(°)$	$\Delta\theta_{\mathrm{imp}}(°)$	Remark
1	40	$12-36$	3	$5-30$	5	Fig. 5.3a
1	40	$15-30$	1	$7.5-20$	2.5	Fig. 5.3b
1	50	$12.5-40$	2.5	$5-40$	5	Fig. 5.5
1	30	$12.5-35$	2.5	$5-20$	5	Fig. 5.6
0.5	50	$15-35$	2	$10-35$	5	Fig. 5.9
0.25	50	$15-55$	4	$10-35$	5	Fig. 5.10

Table 5.1: Conditions of the simulations. Δv_{imp} and $\Delta\theta_{\mathrm{imp}}$ show the increments of v_{imp} and θ_{imp} in the parameter survey, respectively.

5.3.1 Equal-Mass Impacts with $\phi_d = 40°$

Figure 5.2 shows snapshots of the impact simulation with $q = 1$, $\theta_{\mathrm{imp}} = 15°$, $v_{\mathrm{imp}} = 20\,\mathrm{cm/s}$, and $\phi_d = 40°$. The collision induces elongation of the body (Fig.5.2b,c), which leads to the formation of an EER (Fig.5.2d,e). The ratio b/a of the largest remnant is 0.24. The rotation period of the largest remnant is 9.36 hours, which is comparable to that of 1I/′Oumuamua. As shown in Fig. 5.2, we confirm that the shape of the EER is stable at least until 1.0×10^5 s, which is correspoding to about three rotations of this object.

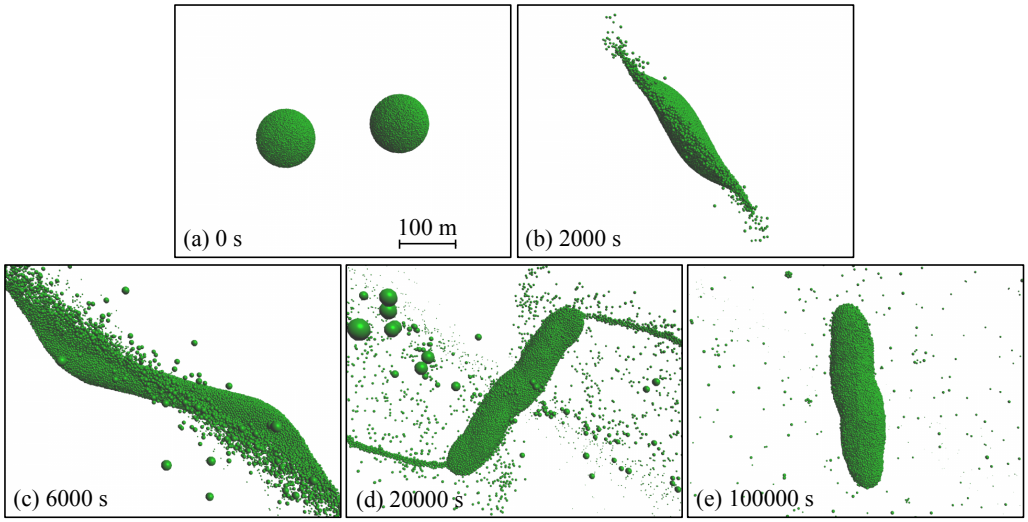

Figure 5.2: Snapshots of the impact simulation with $q = 1$, $\theta_{\rm imp} = 15°$, $v_{\rm imp} = 20\,{\rm cm/s}$, and $\phi_d = 40°$ at $0.0\,{\rm s}$(a), $2.0 \times 10^3\,{\rm s}$(b), $6.0 \times 10^3\,{\rm s}$(c), $2.0 \times 10^4\,{\rm s}$(d), and $1.0 \times 10^5\,{\rm s}$(e). This figure is the same as Fig. 1 of Sugiura et al. (2018b).

Figure 5.3 shows b/a of the largest remnants, which mainly become the most elongated objects, formed through impacts with $q = 1$ and $\phi_d = 40°$. From Fig. 5.3a, we find that EERs are formed through impacts with $\theta_{\rm imp} \approx 15°$ and $v_{\rm imp} \approx 15 - 20\,{\rm cm/s}$. A more detailed parameter survey (Fig. 5.3b) shows that impacts with $v_{\rm imp} \sin\theta_{\rm imp} \approx 5.1\,{\rm cm/s}$ form EERs. Here, all the largest remnants with $b/a < 0.3$ have the mass of $\approx 2.0 M_{\rm target}$, which means almost complete merging.

According to the results in Section 3.3, the formation of elongated bodies needs large shear velocity $v_{\rm imp} \sin\theta_{\rm imp}$, which induces elongation of asteroids. However, impacts with too large $v_{\rm imp} \sin\theta_{\rm imp}$ result in splitting of colliding bodies and do not lead to the formation of EERs. $v_{\rm imp} \sin\theta_{\rm imp} \approx 5.1\,{\rm cm/s}$ is sufficiently large to form extremely elongated objects and sufficiently small to form bodies with $\approx 2.0 M_{\rm target}$. Even if $v_{\rm imp} \sin\theta_{\rm imp} \approx 5.1\,{\rm cm/s}$, impacts with $v_{\rm imp} \geq 25\,{\rm cm/s}$ mainly result in catastrophic destruction, and those with $\theta_{\rm imp} \geq 20°$ mainly result in hit-and-run collisions; both of them are not likely to form elongated objects. Therefore impacts with $\theta_{\rm imp} \leq 20°$, $v_{\rm imp} \leq 25\,{\rm m/s}$ and $v_{\rm imp} \sin\theta_{\rm imp} \approx 5.1\,{\rm cm/s}$ form EERs for $q = 1$ and $\phi_d = 40°$.

The impact with $\theta_{\rm imp} = 15°$ and $v_{\rm imp} = 24\,{\rm cm/s}$ produces an EER that is formed from the third largest remnant as shown in Fig 5.4. The impact with the larger impact velocity compared to that in Fig. 5.2 produces a large ejecta curtain (Fig. 5.4b), and then a filamentary structure is formed through reaccumulation of fragments to the direction perpendicular to the impact

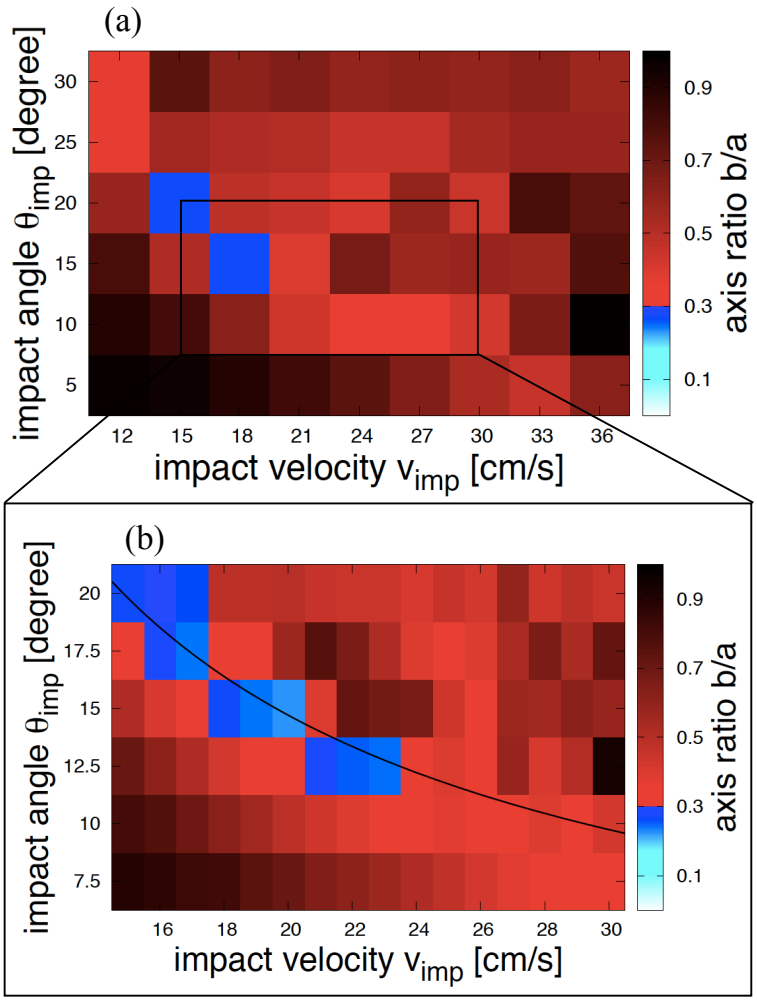

Figure 5.3: b/a of the largest remnants resulting from various impact simulations with $q = 1$ and $\phi_d = 40°$. The horizontal axis represents $v_{\rm imp}$, and the vertical axis represents $\theta_{\rm imp}$. The blue regions show parameters forming EERs, which have $b/a < 0.3$. In the panel (a), we vary the parameters within $12\,{\rm cm/s} \leq v_{\rm imp} \leq 36\,{\rm cm/s}$ and $5° \leq \theta_{\rm imp} \leq 30°$ with the increments of $3\,{\rm cm/s}$ and $5°$. In the panel (b), we vary the parameters within $15\,{\rm cm/s} \leq v_{\rm imp} \leq 30\,{\rm cm/s}$ and $7.5° \leq \theta_{\rm imp} \leq 20°$ with the increments of $1\,{\rm cm/s}$ and $2.5°$. The black curve in the panel (b) represents $v_{\rm imp} \sin\theta_{\rm imp} = 5.1\,{\rm cm/s}$. This figure is the same as Fig. 2 of Sugiura et al. (2018b).

velocity vector (Fig. 5.4c). Gravitational fragmentation of the filament leads to the formation of an EER (Fig. 5.4d,e), which has the mass of $0.24 M_{\rm target}$ and b/a of 0.27. However, the other EERs are obtained from the largest remnants.

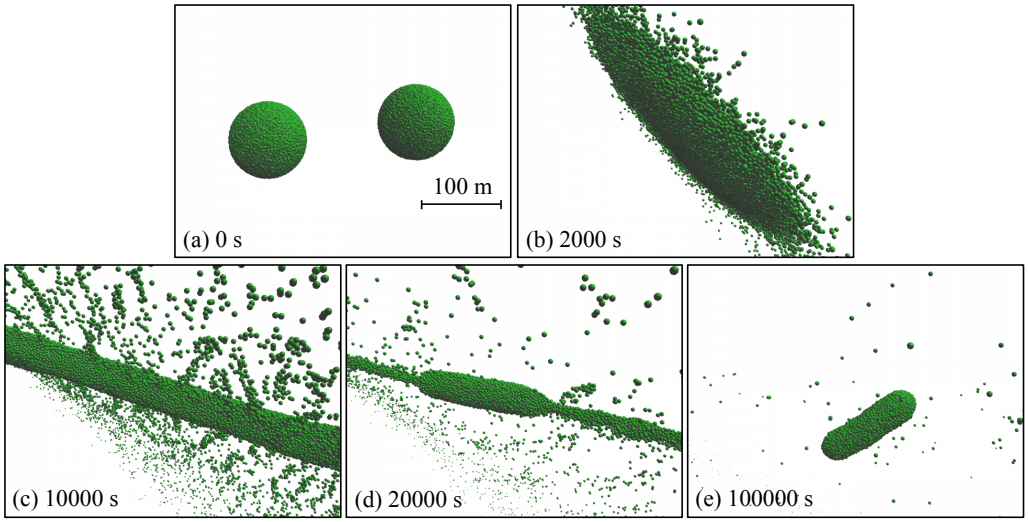

Figure 5.4: Snapshots of the third largest remnant formed through the impact with $q = 1$, $\theta_{\rm imp} = 15°$, $v_{\rm imp} = 24\,{\rm cm/s}$, and $\phi_d = 40°$ at 0.0 s(a), 2.0×10^3 s(b), 1.0×10^4 s(c), 2.0×10^4 s(d), and 1.0×10^5 s(e). This figure is the same as Fig. 3 of Sugiura et al. (2018b).

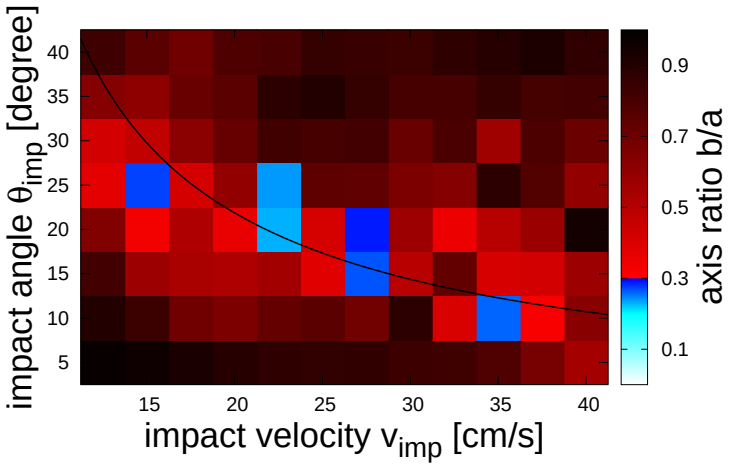

Figure 5.5: b/a of the largest remnants resulting from various impact simulations with $q = 1$ and $\phi_d = 50°$. We vary the parameters within $12.5\,{\rm cm/s} \leq v_{\rm imp} \leq 40\,{\rm cm/s}$ and $5° \leq \theta_{\rm imp} \leq 40°$ with the increments of 2.5 cm/s and 5°. The black curve shows $v_{\rm imp} \sin\theta_{\rm imp} = 7.4\,{\rm cm/s}$. This figure is the same as Fig. 4 of Sugiura et al. (2018b).

5.3.2 Dependence on the Friction Angle

Figure 5.5 represents b/a of the largest remnants formed through various impacts with $q = 1$ and $\phi_d = 50°$. b/a does not seem to be smooth function of $v_{\rm imp}$ and $\theta_{\rm imp}$ because of a smaller number of simulations in almost the same parameter space as that of Fig. 5.3b. The formation

of EERs occurs in a wider parameter space than that for $\phi_d = 40°$. We find that the parameters producing EERs concentrate around $v_{\rm imp} \sin\theta_{\rm imp} \approx 7.4\,{\rm cm/s}$ with $\theta_{\rm imp} \leq 30°$ and $v_{\rm imp} \leq 35\,{\rm m/s}$. Note that EERs are also formed from smaller remnants in four parameters with $\theta_{\rm imp} \approx 25°$ and $v_{\rm imp} \approx 20 - 30\,{\rm cm/s}$ in the impacts with $\phi_d = 50°$.

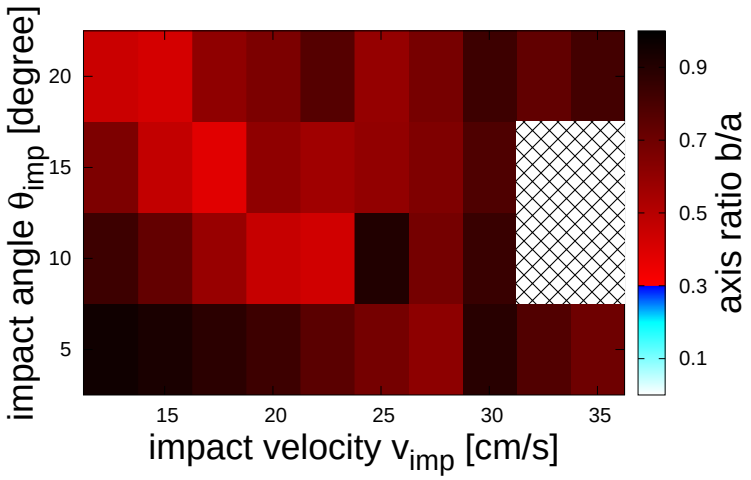

Figure 5.6: b/a of the largest remnants resulting from various impact simulations with $q = 1$ and $\phi_d = 30°$. We vary the parameters within $12.5\,{\rm cm/s} \leq v_{\rm imp} \leq 35\,{\rm cm/s}$ and $5° \leq \theta_{\rm imp} \leq 20°$ with the increments $2.5\,{\rm cm/s}$ and $5°$. The cross-hatched region shows the impacts with $M_{\rm lr} < 0.15 M_{\rm target}$, and thus the shapes resulting from these impacts are not measured.

We also conducted impact simulations with $q = 1$, $\phi_d = 30°$ as shown in Fig. 5.6. Although the ranges of impact velocities and angles are almost the same as those in Fig. 5.3 or Fig. 5.5, no EERs are formed through impacts with $\phi_d = 30°$. Thus the formation of EERs needs the friction angle $\phi_d \geq 40°$.

Let us roughly estimate the critical friction angle required for the formation of EERs theoretically. As shown in Fig. 5.2 or Fig. 5.4, EERs are formed through collisional elongation of asteroids and reaccumulation of fragments from the direction of the long axis. In reaccumulation phase, if the friction angle is small, the friction cannot stop fragments with small displacement, and resultant shapes become more round shapes. Total kinetic energy of fragments that compose an EER during reaccumulation phase is estimated as

$$E_{\rm kin} = \frac{1}{2} M_r v_{{\rm esc},r}^2, \tag{5.1}$$

where M_r is the mass of this EER and $v_{{\rm esc},r}$ is the escape velocity from this EER. According

to Sugiura et al. (2018a), total dissipated energy due to the friction with displacement L is estimated as

$$E_{\rm dis} = \pi R_r^2 L \mu_d P_c,$$
$$P_c = \frac{2}{3}\pi G \rho_0^2 R_r^2, \tag{5.2}$$

where G is the gravitational constant and R_r and P_c are the mean radius and the central pressure of this EER, respectively. Equating $E_{\rm kin}$ and $E_{\rm dis}$, we achieve

$$\frac{L}{R_r} \approx \frac{1}{\mu_d}. \tag{5.3}$$

If $L/R_r \gg 1$, i.e., $\mu_d \ll 1$, EERs are not formed because of large deformation due to reaccumulation of fragments. Thus the formation of EERs roughly requires μ_d larger than unity, or ϕ_d larger than 45°. Interestingly, this condition solely depends on μ_d, and thus it is applicable to impacts with different scale.

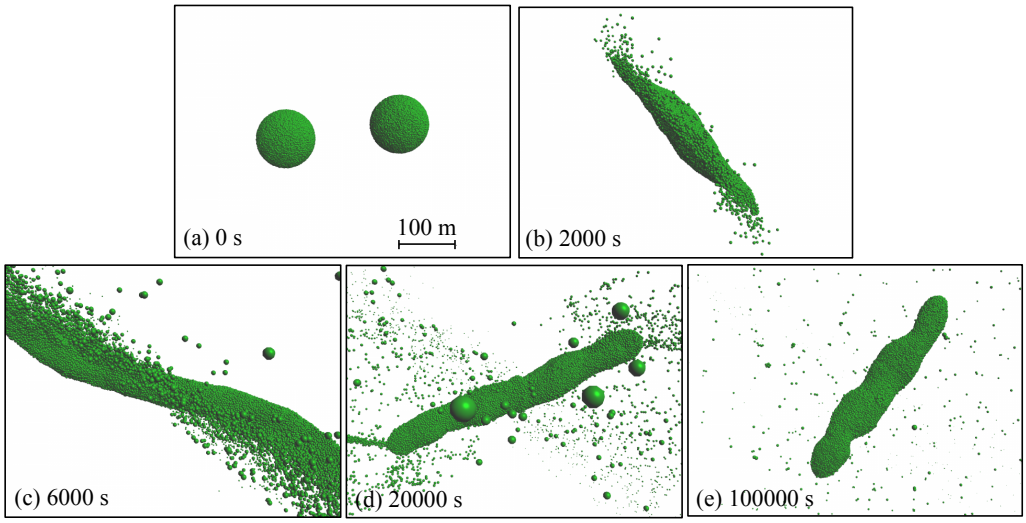

Figure 5.7: Snapshots of the impact simulation with $q = 1$, $\theta_{\rm imp} = 15°$, $v_{\rm imp} = 22.5\,{\rm cm/s}$, and $\phi_d = 60°$ at $0.0\,{\rm s}$(a), $2.0 \times 10^3\,{\rm s}$(b), $6.0 \times 10^3\,{\rm s}$(c), $2.0 \times 10^4\,{\rm s}$(d), and $1.0 \times 10^5\,{\rm s}$(e).

Impacts with larger friction angles generally form more irregular shapes. We found one impact simulation that forms the EER with $b/a = 0.16$. Fig. 5.7 shows the result of the impact simulation with $\theta_{\rm imp} = 15°$, $v_{\rm imp} = 22.5\,{\rm cm/s}$, and the friction angle $\phi_d = 60°$. The snapshots of this figure are similar to those of Fig. 5.2, and the impact with the slightly larger impact

velocity and the slightly larger friction angle forms the more elongated shape with $b/a = 0.16$, which explains the axis ratio of 1I/′Oumuamua estimated in Bannister et al. (2017) or Fraser et al. (2018). Although the friction angle of $\phi_d = 60°$ is too large for usual terrestrial granular material (Heiken et al. 1991), granular material on small bodies may achieve the angle of repose of 60° owing to the existence of cohesion.

5.3.3 Dependence on the Mass Ratio

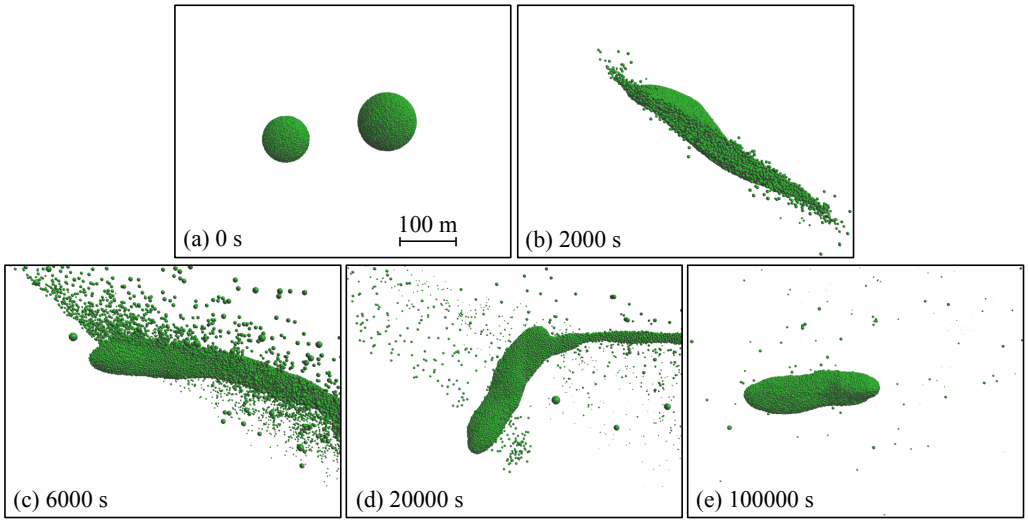

Figure 5.8: Snapshots of the largest remnant formed through the impact with $q = 0.5$, $\theta_{\rm imp} = 20°$, $v_{\rm imp} = 25\,{\rm cm/s}$, and $\phi_d = 50°$ at $0.0\,{\rm s}$(a), $2.0 \times 10^3\,{\rm s}$(b), $6.0 \times 10^3\,{\rm s}$(c), $2.0 \times 10^4\,{\rm s}$(d), and $1.0 \times 10^5\,{\rm s}$(e). This figure is the same as Fig. 5 of Sugiura et al. (2018b).

Figure 5.8 shows snapshots of the impact with $q = 0.5$, $\phi_d = 50°$, $\theta_{\rm imp} = 20°$, and $v_{\rm imp} = 25\,{\rm cm/s}$. The asymmetric destruction of asteroids occurs because of the unequal-mass impact (Fig. 5.8b). The collision induces elongation (Fig. 5.8c), which leads to the formation of an EER (Fig. 5.8d,e). This remnant has the mass of $1.1 M_{\rm target}$ and b/a of 0.27.

Figure 5.9 represents b/a of the largest remnants in various impact simulations with $q = 0.5$ and $\phi_d = 50°$. We find that the three impacts with $\theta_{\rm imp} = 20°$ and $v_{\rm imp} \approx 25\,{\rm cm/s}$ form EERs.

We also conducted impact simulations with $q = 0.25$ and $\phi_d = 50°$ as shown in Fig. 5.10. Although impacts in this parameter range include various types of collisions (merging, hit-and-run, and catastrophic destruction), no impacts with $q = 0.25$ form EERs. Overall deformation of target asteroid requires $q \sim 1$ because collisions with small impactors induce local deformation with the size comparable to that of impactors. Therefore the formation of EERs requires

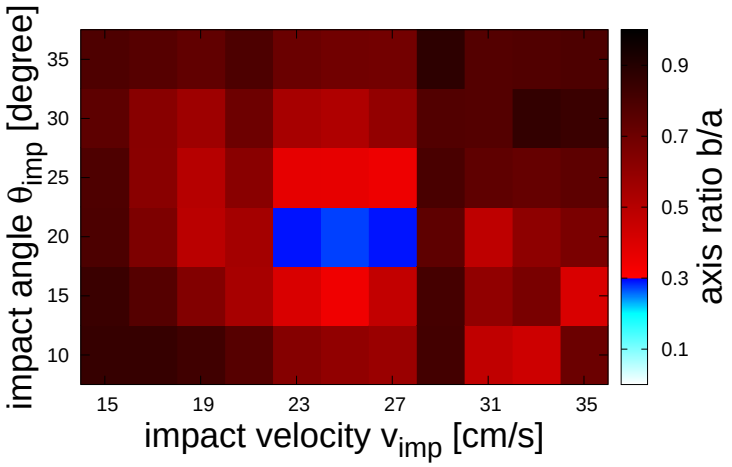

Figure 5.9: b/a of the largest remnants resulting from various impacts with $q = 0.5$ and $\phi_d = 50°$. We vary the parameters within $15\,\mathrm{cm/s} \leq v_{\mathrm{imp}} \leq 35\,\mathrm{cm/s}$ and $10° \leq \theta_{\mathrm{imp}} \leq 35°$ with the increments of $2\,\mathrm{cm/s}$ and $5°$. This figure is the same as Fig. 6 of Sugiura et al. (2018b).

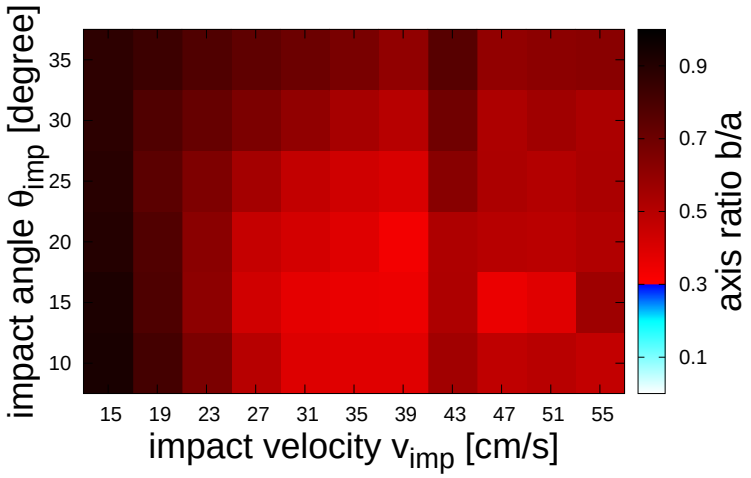

Figure 5.10: b/a of the largest remnants resulting from various impacts with $q = 0.25$ and $\phi_d = 50°$. We vary the parameters within $15\,\mathrm{cm/s} \leq v_{\mathrm{imp}} \leq 55\,\mathrm{cm/s}$ and $10° \leq \theta_{\mathrm{imp}} \leq 35°$ with the increments of $4\,\mathrm{cm/s}$ and $5°$.

$q \geq 0.5$.

5.4 Discussion: Environments for 1I/′Oumuamua Formation

In Figs 5.3, 5.5, and 5.9, the parameters forming EERs are limited and the collisional probability for EER formation is low. However, the formation of extremely elongated objects through other processes is also difficult. For example, if four spherical asteroids with equal size stick together in a completely straight line, an object with $b/a = 0.25$ is formed. To make a body with $b/a < 0.25$ through this process, it requires at least three times of impacts with very limited collisional directions and velocities; such probability might be smaller than that of EER formation due to elongation through single collision. Thus, we focus on EER formation through collisional elongation, and estimate the dynamical environment for such collisions.

Impact velocities required to produce EERs ($15\,\mathrm{cm/s} \leq v_{\mathrm{imp}} \leq 40\,\mathrm{cm/s}$) are much smaller than typical random velocity of objects orbiting around a star $\sim 1\,\mathrm{km/s}$ (e.g., the mean impact velocity at the main belt $\approx 5\,\mathrm{km/s}$). To realize such small impact velocities, dynamically cold environment in protoplanetary disks is necessary. Here, we focus on turbulence and gravitational interaction with large bodies as the sources of dynamical excitation of asteroids in protoplanetary disks, and give some constraints for environment such that $v_{\mathrm{imp}} \leq 40\,\mathrm{cm/s}$.

It should be noted that the impact velocity to form extremely elongated objects may be increased if we additionally consider cohesion of granular material. The cohesion of lunar soil is estimated to be 1 kPa (Heiken et al. 1991). In contrast, central pressure of an asteroid with the radius 50 m is about 10 Pa, which gives the typical value of frictional stress. Thus impact velocity for collisional elongation may become ten times larger if cohesion is included. However, cohesion may prevent the elongation due to its large tensile strength. The effect of cohesion will be investigated in our future works.

5.4.1 Turbulence

We will estimate the relative velocity between asteroids with the radius of $s = 100\,\mathrm{m}$ and the density of $\rho_s = 1\,\mathrm{g/cm^3}$ in a protoplanetary disk with a central star that has the same mass $M_\odot$ and luminosity as the Sun. The sound speed $C_{s,g}$, the density at the mid plane ρ_g, and the surface density Σ_g of gas at orbital radius r are given by those of the minimum mass solar nebula model (Hayashi 1981):

$$C_{s,g} = 1.0 \times 10^5 \left(\frac{r}{1\,\mathrm{au}}\right)^{-1/4} \mathrm{cm/s},$$
$$\rho_g = 1.4 \times 10^{-9} \left(\frac{r}{1\,\mathrm{au}}\right)^{-11/4} \mathrm{g/cm^3}, \tag{5.4}$$
$$\Sigma_g = 1.7 \times 10^3 \left(\frac{r}{1\,\mathrm{au}}\right)^{-3/2} \mathrm{g/cm^2}. \tag{5.5}$$

Asteroids are dragged by gas. A time scale of velocity variation due to gas drag is called the stopping time t_s and defined by the ratio of momentum to gas drag force. t_s for various gas drag laws is expressed as

$$t_s = \begin{cases} \frac{\rho_s s}{\rho_g \bar{v}_{\mathrm{th}}} & \text{for} \quad s < \frac{9}{4}\lambda & \text{(Epstein law)} \\ \frac{4\rho_s s^2}{9\rho_g \lambda \bar{v}_{\mathrm{th}}} & \text{for} \quad R_e < 1 & \text{(Stokes law 1)} \\ \frac{4^{3/5}\rho_s s^{8/5}}{9\rho_g \lambda^{3/5} \bar{v}_{\mathrm{th}}^{3/5} \Delta v^{3/5}} & \text{for} \quad 1 < R_e < 800 & \text{(Stokes law 2)} \\ \frac{6\rho_s s}{\rho_g \Delta v} & \text{for} \quad R_e > 800 & \text{(Newton law)} \end{cases}, \tag{5.6}$$

where $\bar{v}_{\mathrm{th}} = \sqrt{\pi/8} C_{s,g}$ is the mean thermal velocity of molecules, $\lambda = m_{\mathrm{H_2}}/\rho_g \sigma_{\mathrm{H_2}}$ is the mean free path of gas particles, $R_e = 4s\Delta v/\bar{v}_{\mathrm{th}}\lambda$ is the Reynolds number, Δv shows relative velocity between gas and asteroids, $m_{\mathrm{H_2}} = 3.4 \times 10^{-24}\,\mathrm{g}$ is the mass of a hydrogen molecule, and $\sigma_{\mathrm{H_2}} = 2.0 \times 10^{-15}\mathrm{cm^2}$ is the cross section of a hydrogen molecule (e.g.,Whipple 1972; Weidenschilling 1977; Birnstiel et al. 2010). In protoplanetary disks, Δv is mainly determined by the difference between the Keplerian velocity $v_{\mathrm{K}} = \sqrt{GM_\odot/r}$ and the rotation velocity of gas with pressure-gradient support. From the relation of isothermal gas pressure $P = \rho_g C_{s,g}^2$ and Eq. (5.5),

$$\Delta v = \frac{1}{2}\frac{r}{\rho_g v_{\mathrm{K}}}\frac{dP}{dr} = 5.4 \times 10^3\,\mathrm{cm/s}, \tag{5.7}$$

and λ and R_e are expressed as

$$\lambda = 1.2 \left(\frac{r}{1\,\mathrm{au}}\right)^{11/4} \mathrm{cm},$$
$$R_e = 2.9 \times 10^3 \left(\frac{r}{1\,\mathrm{au}}\right)^{-5/2}. \tag{5.8}$$

From Eqs. (5.5), (5.7), and (5.8), r dependence of t_s is expressed as

$$t_s = \begin{cases} 2.2 \times 10^1 \left(\frac{r}{1\,\mathrm{AU}}\right)^{3/2} \Omega_\mathrm{K}^{-1} & \text{for} \quad r > 19\,\mathrm{AU} \\ 3.6 \times 10^3 \left(\frac{r}{1\,\mathrm{AU}}\right)^{-1/4} \Omega_\mathrm{K}^{-1} & \text{for} \quad 1.6\,\mathrm{AU} < r < 19\,\mathrm{AU} \\ 1.8 \times 10^3 \left(\frac{r}{1\,\mathrm{AU}}\right)^{5/4} \Omega_\mathrm{K}^{-1} & \text{for} \quad r < 1.6\,\mathrm{AU} \end{cases}, \tag{5.9}$$

where Ω_K is the Keplerian angular frequency. The gas drag is determined by the Epstein law for $r > 19\,\mathrm{AU}$, the Stokes law for $1.6\,\mathrm{AU} < r < 19\,\mathrm{AU}$, and the Newton law (high Reynolds number) for $r < 1.6\,\mathrm{AU}$. For $t_s \Omega_\mathrm{K} \gg 1$, v_rel controlled by turbulent stirring is given by (Cuzzi et al. 2001; Ormel and Cuzzi 2007)

$$v_\mathrm{rel} \approx C_{s,g} \sqrt{3\alpha (\Omega_\mathrm{K} t_s)^{-1}}, \tag{5.10}$$

where α is the strength of turbulence in Shakura-Sunyaev prescription. Figure 5.11 shows v_rel as a function of r and α, and we find that $\alpha < 5 \times 10^{-4}$ for $1\,\mathrm{AU} < r < 20\,\mathrm{AU}$ and $\alpha < 5 \times 10^{-4} (r/20\,\mathrm{AU})^2$ for $r > 20\,\mathrm{AU}$ are roughly required for $v_\mathrm{imp} \leq 40\,\mathrm{cm/s}$.

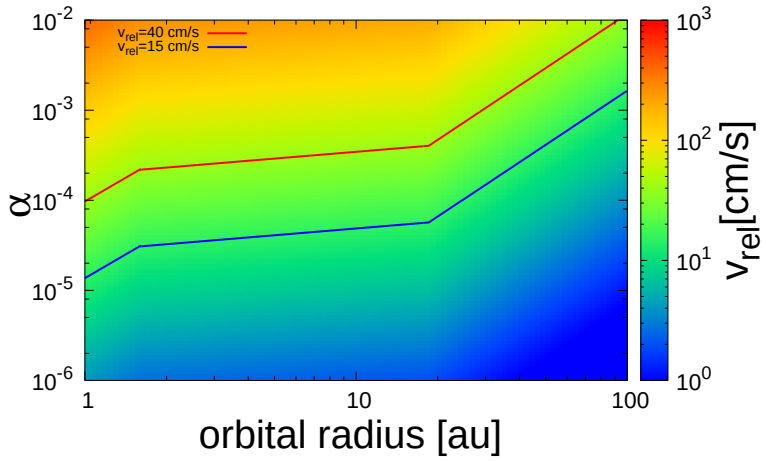

Figure 5.11: Relative velocity between asteroids with the radius 100 m induced by turbulence in a disk with the minimum mass solar nebula model. The horizontal axis represents the distance from the central star, and the vertical axis represents the Shakura-Sunyaev α parameter. The red and blue solid curves show the contours of $v_\mathrm{rel} = 40\,\mathrm{cm/s}$ and $v_\mathrm{rel} = 15\,\mathrm{cm/s}$, respectively. This figure is the same as Fig. 7 of Sugiura et al. (2018b).

Magnetorotational instability (MRI) is a dominant source of turbulence. MRI is active in vicinities of a central star with high ionized fraction ($r < 0.1\,\mathrm{AU}$) or sufficiently distant from a central star with low surface density of gas ($r > 10\,\mathrm{AU}$), and MRI produces strong

turbulence with $\alpha \sim 10^{-2}$ (e.g., Flock et al. 2017). MRI non-active regions (dead zones) are roughly considered to be the mid-plane with $0.1\,\mathrm{AU} < r < 10\,\mathrm{AU}$ (e.g., Kretke et al. 2009). The strength of turbulence in dead zones is estimated to be $10^{-6} < \alpha < 10^{-3}$ (e.g., Flock et al. 2017; Ilgner and Nelson 2008; Mori et al. 2017). Thus impacts with $v_{\rm imp} \leq 40\,\mathrm{cm/s}$ between 100 m-sized asteroids could occur in dead zones with $1\,\mathrm{AU} < r < 10\,\mathrm{AU}$.

On the other hand, observations of a protoplanetary disk suggest that α for the outer disk is smaller than values expected from MRI turbulence. Pinte et al. (2016) show that apparent gaps of HL Tau require $\alpha \sim 10^{-4}$. Note that such a small α is favorable for creating the observed multiple ring-like structure in HL Tau through secular gravitational instability (Takahashi and Inutsuka 2014, 2016; Tominaga et al. 2018). Thus impact velocities of $v_{\rm imp} \leq 40\,\mathrm{cm/s}$ are realized in protoplanetary disks such as HL Tau.

5.4.2 Size of Larger Bodies

Gravitational stirring by larger bodies increases the relative velocity between surrounding smaller asteroids. We will estimate the sizes of larger bodies that result in relative velocities between 100 m-sized asteroids less than 40 cm/s.

We consider two groups of bodies: One of them is small asteroids with the radius 100 m, and the other one is large bodies with the radius R. Through viscous stirring of large bodies, the relative velocity of small asteroids u increases at a rate of (Ida and Makino 1993)

$$\left.\frac{1}{u}\frac{du}{dt}\right|_{\rm vs} \sim +\Omega_{\rm K}\frac{\Sigma}{\rho_s R}\left(\frac{v_{\rm esc}}{u}\right)^4, \tag{5.11}$$

where Σ is the surface density of large bodies and $v_{\rm esc}$ is the escape velocity from a large body. The relative velocity decreases through gas drag at a rate of

$$\left.\frac{1}{u}\frac{du}{dt}\right|_{\rm gd} \sim -\frac{1}{t_s}, \tag{5.12}$$

which is inversely proportional to the stopping time. The balance between the increasing rate Eq. (5.11) and the decreasing rate Eq. (5.12) gives the relative velocity at a steady state

$$u = \left(\frac{t_s\Omega_{\rm K}\Sigma}{\rho_s R}\right)^{1/4} v_{\rm esc}. \tag{5.13}$$

Figure 5.12 shows the relative velocity in the minimum mass solar nebula. Here, we put 10^{-2} times the solid surface density for Σ. From Fig. 5.12, we find that $R < 2\,\mathrm{km}$ for $r \approx 1\,\mathrm{AU}$ and

$R < 7\,\mathrm{km}$ for $r > 20\,\mathrm{AU}$ are required to achieve $u < 40\,\mathrm{cm/s}$. Therefore, the formation of the extremely elongated shape of 1I/′Oumuamua through a collision requires an extremely young protoplanetary disk without bodies larger than 7 km.

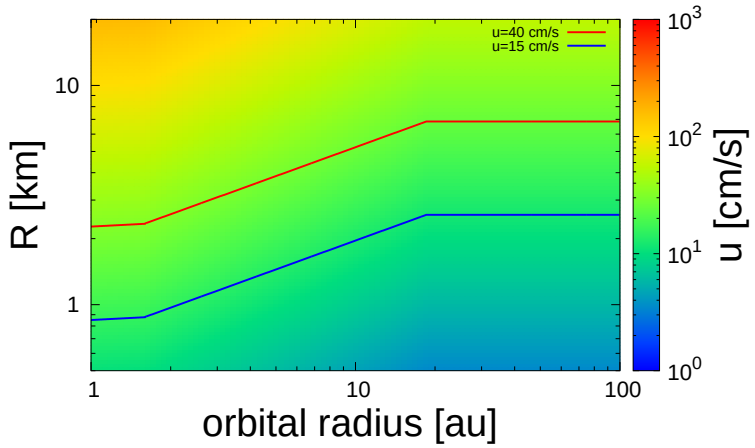

Figure 5.12: Relative velocity between asteroids with the radius 100 m induced by large bodies with the radius R in a disk with the minimum mass solar nebula model. The horizontal axis represents the distance from the central star, and the vertical axis represents the radius of bodies R. The red and blue solid curves show the contours of $u = 40\,\mathrm{cm/s}$ and $u = 15\,\mathrm{cm/s}$, respectively. This figure is the same as Fig. 8 of Sugiura et al. (2018b).

1I/′Oumuamua is thought to be ejected from another planetary system, and the ejection requires large scattering sources such as gas giants or central binary stars. However, such scattering sources significantly increase the relative velocity between asteroids. Thus the shape of 1I/′Oumuamua was probably formed in a place without large bodies, which may be in an outer protoplanetary disk, and then 1I/′Oumuamua drifted inward to the vicinity of gas giants or central binary stars to be ejected (e.g., Raymond et al. 2011, 2018; Jackson et al. 2018). Ejection by central binary stars may be favorable to explain lack of cometary activity of 1I/′Oumuamua because close encounter with binary stars evaporate volatile substances (Jackson et al. 2018). In contrast, an early stellar encounter ejects asteroids from an outer disk (e.g., Kobayashi et al. 2005).

5.4.3 Survivability of Extremely Elongated Shapes Through Ejection Processes

As we discussed in the previous subsection, 1I/′Oumuamua is thought to be ejected from another planetary system. However, ejection requires close encounter with gas giants or binary stars, and the extremely elongated shape of 1I/′Oumuamua may be destroyed due to tidal force. Here, we discuss the survivability of the shape of 1I/′Oumuamua through ejection processes.

Let us estimate the Roche radius for a prolate object with the major axis length a, the intermediate axis length b, and the density ρ_m. For simplicity, we consider the prolate object orbiting around a central body with the density ρ_m, the radius R_M, and the mass $M = (4/3)\pi R_M^3 \rho_m$. The prolate body is efficiently deformed when the major axis is pointing toward the central body, and tidal force per unit mass at the surface of the prolate object is

$$F_t = \frac{GMa}{d^3}, \tag{5.14}$$

where d is the distance between the prolate object and the central body. According to Chandrasekhar (1969), self-gravitational force per unit mass at the surface on the major axis is calculated as

$$F_s = \pi G \rho_m A_1 a, \tag{5.15}$$

where

$$\begin{aligned} A_1 &= \frac{1-e^2}{e^3}\ln\Big(\frac{1+e}{1-e}\Big) - 2\frac{1-e^2}{e^2}, \\ e &= \sqrt{1-\frac{b^2}{a^2}}. \end{aligned} \tag{5.16}$$

Equating F_t and F_s, we achieve the Roche radius $d_{\rm R}$ as

$$d_{\rm R} = R_M \sqrt[3]{\frac{4}{3}A_1^{-1}}. \tag{5.17}$$

Even for an extreme shape with $b/a = 0.1$, $d_{\rm R} = 3.2R_M$; the Roche radius is comparable to the radius of the central body.

Binary stars eject asteroids from inside of the critical orbital semi-major axis a_c (Holman and Wiegert 1999). An equal-mass binary with zero orbital eccentricity and orbital separation

of a_b has $a_c = 2.4a_b$. Since a_b is AU scale, a_c is much larger than radii of stars; asteroids are ejected before they experience tidal disruption.

In protoplanetary disks, asteroids drift inward due to angular momentum loss through gas drag. The orbital eccentricities of asteroids that drift to the vicinity of gas giants increase through moderate close encounters with gas giants. The distance of close encounters required for the increase of the eccentricities is about the Hill radius (Ohtsuki et al. 2002), which is much larger than the Roche radius. The asteroids with the eccentricities larger than 0.4 are efficietly ejected by gas giants (Bandermann and Wolstencroft 1971; Higuchi et al. 2006), and the typical distance of close encounters that eject asteroids is also about the Hill radius (Fernandez 1978; Ida 1990). In the case of Jupiter, Hill radius is about 760 times larger than the Jupiter radius, and thus asteroids rarely experience tidal disruption when they are ejected by gas giants.

Chapter 6

Summary and Future Prospects

6.1 Summary

Asteroids in the present solar system are the fossils of planetesimals that existed in the primordial solar system. Thus the information obtained from asteroids is very useful to reveal the history of the solar system, and such information is also used to reveal the collisional history of asteroids themselves, i.e., how impacts they experienced or when they were formed. Asteroids have variety of shapes and we can directly connect the shapes of asteroids to the collisional history of asteroids since asteroidal shapes are mainly formed through collisions.

We firstly developed the numerical simulation method for rocky body collisions. Then we investigated the shapes of asteroids formed through various impacts through numerical simulations. We also analyzed the shapes of actual asteroids and compare them with the results of our simulations. Finally we applied our simulations to the formation of the extremely elongated shapes of 1I/′Oumuamua. In this chapter, we will summarize our study.

6.1.1 Development of the Numerical Simulation Method

Our simulation method is based on elastic dynamics because rocky bodies have elastic properties when deformation is small. We developed our simulation code for rocky body impacts based on the SPH method for elastic dynamics because impact phenomena involve large deformation and particle methods are suitable to compute such phenomena. However, the standard SPH method has the serious problem in tension dominated regions, which is the tensile instability and causes numerical instability in tension dominated regions. We developed the new method to solve the tensile instability based on the Godunov SPH method (Inutsuka 2002). We evaluated the stability of the Godunov SPH method through the linear stability analysis and clarified

the stability with several interpolation methods of density distribution as shown in Table 2.1 (Sugiura and Inutsuka 2016, 2017). We also found that we can conduct numerical simulations without the tensile instability if we select stable interpolation methods, which depend on the sign of pressure. Our test simulations show that the Godunov SPH method for elastic dynamics well reproduces the dynamics of elastic bodies (Figs. 2.1, 2.2 or Sugiura and Inutsuka 2017).

However, asteroids are not elastic bodies but rocky bodies and we need appropriate methods to describe impact phenomena. The equation of state that is appropriate to describe impact phenomena is different from that of elastic dynamics. Many studies investigating impact phenomena with the SPH method utilize the tillotson equation of state (e.g., Genda et al. 2012; Jutzi and Asphaug 2015), and thus we also utilize the tillotson equation of state. Large deformation of rocky bodies causes the fracturing, which relieves tensile forces of intact rock. We included the fracture model for brittle solid described in Benz and Asphaug (1995). Friction between completely fractured rock, or granular material, is very important to describe the shapes of rubble pile bodies such as the asteroid Itokawa. Thus we included the friction model for granular material described in Jutzi (2015). Our test simulations show that our simulation code well reproduces the dynamics of granular material (Fig. 2.4). To reproduce the collisional formation of the shapes of rubble pile bodies, we also need to describe reaccumulation of fragments ejected by impacts, and thus we included the self gravity.

Catastrophic collisions produce fine remnants. To reproduce and investigate the shapes of such fine remnants, we need to conduct high-resolution simulations. To do so, we need to parallelize our simulation code to utilize supercomputers. Thus we parallelized our simulation code utilizing FDPS developed by RIKEN. As we notice from Fig. 2.5, our simulation code successfully achieves the high parallelization efficiency even if we utilize 2,000 CPU cores.

6.1.2 Asteroidal Shapes Formed Through Collisions

DAMIT provides the shape models of asteroids obtained through light curve observations of asteroids, and almost all of the shapes of the asteroids with the diameters larger than 100 km are already measured (Fig. 4.3). Moreover, the collisional lifetimes of asteroids larger than 100 km are much longer than the age of the solar system (Fig. 1.5), and many of them are not probably affected by recent impacts (Fig. 4.4). Therefore, the information of the asteroids larger than 100 km is desirable to investigate the long collisional history of those asteroids, and in this study we mainly focus on the shapes of the asteroids larger than 100 km.

Impact Velocity in the History of the Solar System

In the early planet formation era, planetesimals are under orderly growth until the largest bodies grow up to be the size of about 100 km. In this stage, the impact velocities between planetesimals are comparable to or slightly larger than the escape velocity from planetesimals (Kobayashi et al. 2016). Then, several planetesimals larger than 100 km grow up to be protoplanets rapidly under runaway growth, and evolutionary stage moves on to oligarchic growth stage. The impact velocities between planetesimals are controlled by the mass of protoplanets, and the impact velocity is kept to be as low as several 100 m/s until the mass of protoplanets becomes that of Mars (see Eq. (4.6)). Since the escape velocity from the planetesimal with the diameter of 100 km is about 100 m/s, the impact velocities between 100 km-sized planetesimals are always comparable to the escape velocity until the mass of protoplanets reaches to that of Mars. Therefore, the impacts in the primordial environment mainly result in non-destructive impacts.

In contrast, the impact velocities between asteroids in the present solar system are much larger than the escape velocities from asteroids because of the existence of gas giants. The average impact velocity in the main belt is about 5 km/s, and the occurrence rate of the impact velocity less than 400 m/s is only about 0.2% (Fig. 4.1). Therefore, the impacts in the present environment mainly result in destructive impacts.

Shapes Formed Through Various Impacts

We investigated the shapes of remnants produced through various impacts of asteroids by means of numerical simulations. We consider the impacts between basaltic asteroids that initially have spherical shapes and no rotation. The diameter of a target asteroid, i.e., larger asteroid among impacting two asteroids, is fixed to be 100 km, and we vary the impact velocity, the impact angle, and the mass ratio of impacting two asteroids.

Firstly, we investigated the shapes of the largest remnants produced through non-destructive impacts that have the mass of the largest remnants larger than $0.4M_{\rm target}$, where $M_{\rm target}$ is the mass of initial target asteroids. Note that fine remnants other than the largest remnants are also produced through non-destructive impacts, and we expect that the shapes of such fine remnants are similar to those produced through destructive impacts because those shapes are formed through gravitational reaccumulation of fine fragments ejected by impacts, which is the same mechanism observed in destructive impacts. Our simulations of the equal-mass impacts

with the impact velocity comparable to the escape velocity show that these impacts produce various shapes including extremely flat shapes of the largest remnants (Fig. 3.15). However, we notice that the impacts with smaller mass ratios of impacting two asteroids are more difficult to produce irregular shapes (Fig. 3.18), and the impacts with the mass ratio of 1/64 only produce the spherical largest remnants with the ratio of the minor to major axis lengths larger than 0.7 (Fig. 3.19).

Secondly, we investigated the shapes of fine remnants produced through destructive impacts by means of high-resolution simulations. We conducted four simulations of destructive impacts with various mass ratios and impact velocities. The highest impact velocity among four simulations is about 2 km/s, which is close to the average impact velocity in the present solar system. As a result, we found that the destructive impacts mainly produce spherical and bilobed shapes of fine remnants (Fig. 3.22). We also found that flat shapes are difficult to be formed through destructive impacts (Fig. 3.24).

Shapes Formed in Primordial and Present Environment

The impact velocities between planetesimals in the planet formation era are comparable to the escape velocity from planetesimals. Thus similar-mass impacts in the primordial environment forms various shapes including extremely flat shapes. Although similar mass impacts between 100 km-sized asteroids in the present solar system are very rare, similar-mass impacts between planetesimals in the primordial environment are more frequent compared to the present environment because Jupiter formation depleted planetesimals. Even in the primordial environment, impacts with large mass difference of two impacting planetesimals are more frequent than similar-mass impacts. However, low-velocity impacts with large mass difference do not result in the deformation of target planetesimals. Since 100 km-sized planetesimals are mainly the largest bodies among planetesimals in the primordial environment (Kobayashi and Tanaka 2018), the shapes of 100 km-sized planetesimal are mainly determined by similar-mass impacts, which leads to the formation of various shapes including flat shapes.

The impact velocities between asteroids in the present solar system are much larger than the escape velocity from asteroids, which mainly result in destructive impacts. Our simulations of destructive impacts show that these impacts only produce spherical and bilobed shapes. Even in the present environment, the impacts with large mass difference of impacting two asteroids may not result in destructive impacts. However, our simulations with the mass ratio of 1/64 only produce the spherical largest remnants even with the impact velocity realized in

the present solar system. Therefore, we expect that impacts in the present solar system do not produce flat shapes of asteroids.

6.1.3 Comparison with Actual Asteroids

From the results of our simulations, we predict that destructive impacts that are realized in the present solar system are difficult to produce flat shapes. To verify this prediction, we investigated the shapes of actual asteroids obtained from DAMIT. Asteroid families are mainly formed by recent destructive impacts, and thus we can assess the effect of destructive impacts on the asteroidal shapes through the comparison between the shapes of family and non-family asteroids. The information of asteroid families is obtained from AstDyS-2.

As a result of the investigation, we found that the family asteroids with the diameters larger than 100 km do not include flat asteroids, while non-family asteroids larger than 100 km include six flat asteroids with $c/a < 0.6$ and $b/a > 0.8$ (Fig. 4.6). This is consistent with the results of our simulations that the destructive impacts do not produce flat shapes. Thus, the flat shapes of the asteroids with the diameters larger than 100 km were formed in the primordial environment and remain the same until today. This conclusion is consistent with the collisional lifetime estimated in O'Brien and Greenberg (2005).

In contrast, the family asteroids with the diameters larger than 10 km include flat asteroids. These flat asteroids in asteroid families may be formed through low-velocity collisions between similar-sized members in the same family. However, the fraction of flat asteroids with $c/a < 0.6$ and $b/a > 0.8$ shows the clear difference between the family and non-family asteroids. The fraction of the flat shapes for the non-family asteroids is 8.5%, while that for family asteroids is 3.8% (Fig. 4.8); the fraction of the flat shapes for the non-family asteroids is more than twice as large as that for family asteroids. This difference also suggests that destructive impacts are difficult to produce flat asteroids.

6.1.4 Formation of Extremely Elongated Shape of 1I/′Oumuamua

As shown in Fig. 5.2, collisions can form extremely elongated shapes of asteroids. Recently, Meech et al. (2017) discovered the interstellar asteroid 1I/′Oumuamua that has the extremely elongated shape. Owing to the large amplitude of the light curve of 1I/′Oumuamua, the axis ratio b/a of this object is estimated to be 0.3 or smaller, and the nominal value of b/a is considered to be 1/6. To investigate detailed impact conditions to form extremely elongated

remnants (EERs) with $b/a < 0.3$ and the size similar to that of 1I/′Oumuamua, we conducted impact simulations with 50 m-sized rubble pile targets. We varied the impact velocity, the impact angle, the mass ratio of impacting two asteroids, and the friction angle and searched for the impact conditions to form EERs.

As a result, we found that the formation of EERs roughly requires the impact velocity smaller than 40 cm/s (Fig. 5.5), the impact angle smaller than 30° (Fig. 5.5), the mass ratio larger than 0.5 (Figs. 5.9 and 5.10), and the friction angle larger than 40° (Figs. 5.5 and 5.6).

The most difficult condition to be realized is the impact velocity. The realization of such low impact velocity requires dynamically extremely cold environment such as in a protoplanetary disk. We estimated the required condition of such protoplanetary disk in terms of turbulence and the size of large planetesimals. As a result, we found that the impact velocity smaller than 40 cm/s is realized in the environments with Shakura-Sunyaev $\alpha < 10^{-4}$ such as in MRI dead zones (Fig. 5.11) and without planetesimals larger than 7 km (Fig. 5.12). Small size of planetesimals requires the environments in an extremely young protoplanetary disk. Thus, 1I/′Oumuamua might have been formed in such an extremely young protoplanetary disk, then might have been ejected from the planetary system due to, for example, a stellar encounter, and then visited our solar system.

6.2 Future Prospects

6.2.1 Application to Other Phenomena

Cratering

In this study, we focus on the collisions that deform overall structures of asteroids. However, as we notice from surfaces of terrestrial objects such as the moon, collisions also produce craters. Since collisions due to smaller objects are more frequent than those between similar-mass bodies, craters give us the opportunity to statistically discuss the collisional history in the solar system.

There are various types of craters. Small craters are generally the simple craters that have bowl-like structures. Large craters have, in contrast, more complex structures such as central peaks or ring-like structures. Some celestial objects have craters that cover the large fraction of the surfaces of objects. For example, Phobos, the satellite of Mars, has Stickney crater on its surface (e.g., Bruck Syal et al. 2016). The size of Stickney crater ≈ 9 km is comparable to the size of Phobos ≈ 22 km. Craters are not necessarily symmetric but some craters have asymmetric structures, which are considered to be formed by oblique impacts (Goeritz et al.

2009) or impacts to surface slopes (Krohn et al. 2014). These variety of crater types give us more detailed clues to reveal impact conditions that form craters or surface conditions of celestial bodies.

Although there are numerous works on the formations of craters through experimental (e.g., Housen and Holsapple 1999; Michikami et al. 2014) or numerical (e.g., Jutzi et al. 2010; Potter et al. 2018) methods, knowledge for the formations of complex craters or asymmetric craters is limited. In the case of numerical simulations, the investigations of asymmetric craters need three-dimensional simulations. However, three-dimensional simulations of crater formations are difficult because of high-computational costs. Since our simulation code can be applied to the simulations of crater formations and are suitable for high-resolution simulations owing to the parallelization, the crater formation is a good target of our future works.

Tidal Disruption

Tidal disruption of asteroids due to close encounters with planets also changes asteroidal shapes. Some studies argue that the extremely elongated shape of 1I/′Oumuamua is formed through tidal disruption (e.g. Ćuk 2018). Although close encounters that cause tidal disruption are rare because of the smallness of the Roche radius, the constraint on the shapes of asteroids formed though tidal disruption leads to more detailed constraint on the origin of asteroids.

Walsh and Richardson (2006) well investigated the properties of tidal disruption in terms of the formation of binary asteroids through numerous simulations. However, shapes of remnants produced through tidal disruption are not well investigated so far. Since tidal disruption includes complex processes of approach to planets, disruption, and leaving from planets, numerical simulations are unique method to investigate tidal disruption. Our simulation code is applicable to tidal disruption problems easily.

Rotational Deformation

The spacecraft Hayabusa 2 recently clarified the diamond-like shape, or the top shape, of the asteroid Ryugu. There are other examples of asteroids that have top shapes. The target of OSIRIS-REx mission, the asteroid Bennu, also has the top shape. These top shapes are considered to be formed by rotational deformation due to the acceleration of rotation caused by the YORP effect (Walsh et al. 2008). The equatorial ridge of the asteroid Ryugu is also considered to be formed by the rotation of the asteroid.

Although Walsh et al. (2008) showed that top shapes are formed by rotations, we have not

yet known the detailed dependence of internal structures or properties such as the friction angle of granular material on the shapes of asteroids produced by rotations. Since the shapes formed by rotations may depend on internal structures such as the existence of rigid cores or the values of the friction angle or cohesion, the detailed investigations of rotational deformation leads to not only constrain internal structures or properties of granular material but also constrain the formation processes of asteroids. Thus rotational deformation is one of the targets of our future works.

6.2.2 Addition of Other Models

Cohesion

The equation for shear strength of granular material is composed of two terms. One of them is the term that is proportional to confine pressure, and the other one is the constant term that is corresponding to the shear strength at zero confine pressure. The latter term is corresponding to the cohesion of granular material. The typical strength of the cohesion is about 1 kPa (Heiken et al. 1991), which is comparable to the central pressure of 1 km-sized asteroids. For the simulations of the collisional deformation of asteroids larger than 10 km, the cohesion is negligible because the confine pressure due to the gravity is so large. However, the cohesion may play significant roles for the simulations for asteroids smaller than 1 km or small structures such as mountains on asteroids. Especially, the cohesion probably affects the formation of extreme shapes of minor bodies such as the extremely elongated shape of 1I/′Oumuamua. We have not yet introduced the model of the cohesion to our simulation code, and thus we will include the cohesion referring to, for example, Alduán and Otaduy (2011) in our future works.

Porosity

Some rocky materials such as pumice have the micro porosity, that is, they have void spaces inside of themselves. The materials that compose asteroids, e.g., chondrites, also have porosity. The mean value of porosity of chondrites is about 10% (Britt et al. 2002). This porosity may affect the results of impacts because crushing of porous material also dissipates impact energy.

Jutzi et al. (2008) introduced the effect of crushing of micro porosity to the SPH simulations. Their porosity model is based on the P-α model (Herrmann 1969; Carroll and Holt 1972), where distension parameter α, or porosity, is determined by the pressure. Jutzi (2015) showed that the inclusion of the porosity model increases the catastrophic disruption threshold Q^*_{RD} by about factor two. Thus the porosity affects at least how impacts are destructive. We have

not yet investigated the dependence of the porosity on the shapes of asteroids formed through impacts, so that we will also introduce the porosity model to our simulation code.

6.2.3 Comparison with Particle Based Codes

We conducted the simulations of catastrophic disruption only with the SPH method. However, simulation methods for fluid dynamics including the SPH method have a limitation of time step, that is, the CFL condition. Time step determined by the CFL condition is generally much smaller than the timescale of gravitational reaccumulation. Thus, some researches utilize particle based codes to simulate gravitational reaccumulation phase (e.g., Michel and Richardson 2013; Schwartz et al. 2018).

Except for the self gravity, the equations utilized in the SPH method and particle based codes are completely different. Moreover, the SPH method includes additional dissipation due to the artificial viscosity, while particle based codes do not include such additional dissipation. Although we expect that the shapes of remnants produced in reaccumulation phase of catastrophic disruption are not affected by the difference of simulation methods because the shapes are mainly controlled by the self gravity, we should take note of the difference of simulation methods. We also should note that the difference of the definition of the friction angle. The friction angle in the SPH method means that of granular material, while the friction angle in particle based codes means that between modeled particles. This difference of the definition may cause the difference of the shapes of produced remnants. In our future works, we will directly compare the results of the same impact obtained from both simulation methods.

Acknowledgement

I would like to show my greatest appreciation to Shu-ichiro Inutsuka for giving me the guidance regarding to the direction of my researches. I would like to express my gratitude to Hiroshi Kobayashi for giving me really detailed comments to the papers and knowledge about planet formation and celestial mechanics. I am deeply grateful to Hidekazu Tanaka for giving me useful comments when I visited Tohoku University. I would like to thank Kazunari Iwasaki and Yusuke Tsukamoto for the discussion and helps regarding to the numerical simulation method and coding technique. I would like to thank Ryuki Hyodo for useful comments on our third paper. I would like to thank Natsuki Hosono for helping me to parallelize our simulation code using FDPS. I would like to thank Ryo Suetsugu for giving me an opportunity to start the research about 1I/′Oumuamua. I would like to thank Martin Jutzi for giving me an opportunity to introduce my research in Bern University.

KS is supported by JSPS KAKENHI Grant Number JP 17J01703. Numerical simulations in this work were carried out on Cray XC30 and Cray XC50 at the Center for Computational Astrophysics, National Astronomical Observatory of Japan.

Appendix A

Extension of Godunov SPH Method to Elastic Dynamics

In this chapter, we will summarize the equations for the Godunov SPH method for elastic dynamics. This chapter is mainly based on Sugiura and Inutsuka (2016) and Sugiura and Inutsuka (2017).

A.1 Equations for Godunov SPH Method

The equation of continuity is the same as that for the standard SPH method (Eq. (2.19)) because the difference of the equation of continuity does not affect the stability of the SPH method (see Sugiura and Inutsuka 2017).

The equation of motion (EoM) is defined by the convolution of Eq. (2.8). Note that we use the Gaussian kernel (Eq. (2.12)) in the Godunov SPH method. The acceleration of the i-th particle is expressed as

$$\frac{dv_i{}^{\alpha}}{dt} \equiv \int \frac{dv^{\alpha}(\boldsymbol{x})}{dt} W(|\boldsymbol{x}-\boldsymbol{x}_i|,h)d\boldsymbol{x} = \int \frac{1}{\rho(\boldsymbol{x})}\frac{\partial}{\partial x^{\beta}}\sigma^{\alpha\beta}(\boldsymbol{x})W(|\boldsymbol{x}-\boldsymbol{x}_i|,h)d\boldsymbol{x}. \tag{A.1}$$

The right hand side of Eq. (A.1) is transformed using Eq. (2.16) and integration by parts as

$$\frac{dv_i^{\alpha}}{dt} = \sum_j m_j \int \frac{\sigma^{\alpha\beta}(\boldsymbol{x})}{\rho^2(\boldsymbol{x})}\Big[\frac{\partial}{\partial x_i^{\beta}} - \frac{\partial}{\partial x_j^{\beta}}\Big]W(|\boldsymbol{x}-\boldsymbol{x}_i|,h)W(|\boldsymbol{x}-\boldsymbol{x}_j|,h)d\boldsymbol{x}. \tag{A.2}$$

Similarly, the equation of energy (EoE) is defined by the convolution of Eq. (2.10) and is expressed as

$$\frac{du_i}{dt} \equiv \int \frac{du(\boldsymbol{x})}{dt} W(|\boldsymbol{x}-\boldsymbol{x}_i|,h)d\boldsymbol{x} = \int \frac{1}{\rho(\boldsymbol{x})}\sigma^{\alpha\beta}(\boldsymbol{x})\frac{\partial}{\partial x^\beta}v^\alpha(\boldsymbol{x})W(|\boldsymbol{x}-\boldsymbol{x}_i|,h)d\boldsymbol{x}. \tag{A.3}$$

The right hand side of Eq. (A.3) is transformed through integration by parts as

$$\begin{aligned}&\int \frac{1}{\rho(\boldsymbol{x})}\sigma^{\alpha\beta}(\boldsymbol{x})\frac{\partial}{\partial x^\beta}v^\alpha(\boldsymbol{x})W(|\boldsymbol{x}-\boldsymbol{x}_i|,h)d\boldsymbol{x}\\ &= \int \frac{1}{\rho(\boldsymbol{x})}\frac{\partial}{\partial x^\beta}(\sigma^{\alpha\beta}(\boldsymbol{x})v^\alpha(\boldsymbol{x}))W(|\boldsymbol{x}-\boldsymbol{x}_i|,h)d\boldsymbol{x} + \int \frac{1}{\rho(\boldsymbol{x})}v^\alpha(\boldsymbol{x})\frac{\partial}{\partial x^\beta}\sigma^{\alpha\beta}(\boldsymbol{x})W(|\boldsymbol{x}-\boldsymbol{x}_i|,h)d\boldsymbol{x}.\end{aligned} \tag{A.4}$$

Here, we use the following approximation:

$$\int \frac{1}{\rho(\boldsymbol{x})}v^\alpha(\boldsymbol{x})\frac{\partial}{\partial x^\beta}\sigma^{\alpha\beta}(\boldsymbol{x})W(|\boldsymbol{x}-\boldsymbol{x}_i|,h)d\boldsymbol{x} \approx \int \frac{1}{\rho(\boldsymbol{x})}v_i^\alpha\frac{\partial}{\partial x^\beta}\sigma^{\alpha\beta}(\boldsymbol{x})W(|\boldsymbol{x}-\boldsymbol{x}_i|,h)d\boldsymbol{x}. \tag{A.5}$$

Using Eqs. (2.16), (A.5), and integration by parts, we can transform Eq. (A.4) into

$$\frac{du_i}{dt} = \sum_j m_j \int \frac{\sigma^{\alpha\beta}(\boldsymbol{x})}{\rho^2(\boldsymbol{x})}[v^\alpha(\boldsymbol{x}) - v_i^\alpha]\Big[\frac{\partial}{\partial x_i^\beta} - \frac{\partial}{\partial x_j^\beta}\Big]W(|\boldsymbol{x}-\boldsymbol{x}_i|,h)W(|\boldsymbol{x}-\boldsymbol{x}_j|,h)d\boldsymbol{x}. \tag{A.6}$$

Finally, we formulate the time-development equation for $S^{\alpha\beta}/\rho$ according to the formulation of the induction equation for magnetic field described in Iwasaki and Inutsuka (2011). We simply differentiate $S^{\alpha\beta}/\rho$ and obtain

$$\frac{d}{dt}\Big(\frac{S^{\alpha\beta}}{\rho}\Big) = \frac{1}{\rho}\frac{dS^{\alpha\beta}}{dt} - \frac{S^{\alpha\beta}}{\rho^2}\frac{d\rho}{dt}. \tag{A.7}$$

We substitute Eqs. (2.6) and (2.9) into Eq. (A.7) and obtain

$$\frac{d}{dt}\Big(\frac{S^{\alpha\beta}}{\rho}\Big) = 2\mu\Big(\frac{\dot{\epsilon}^{\alpha\beta}}{\rho} - \frac{1}{3}\delta^{\alpha\beta}\frac{\dot{\epsilon}^{\gamma\gamma}}{\rho}\Big) + \frac{S^{\alpha\gamma}}{\rho}R^{\beta\gamma} + \frac{S^{\beta\gamma}}{\rho}R^{\alpha\gamma} + \frac{S^{\alpha\beta}}{\rho}\dot{\epsilon}^{\gamma\gamma}. \tag{A.8}$$

Note that $(\partial/\partial x^\gamma)v^\gamma = \dot{\epsilon}^{\gamma\gamma}$. We again define the time derivative of $S^{\alpha\beta}/\rho$ of the i-th particle by the convolution of Eq. (A.8):

$$\begin{aligned}\frac{d}{dt}\Big(\frac{S^{\alpha\beta}}{\rho}\Big)_i &\equiv \int \Big[\frac{d}{dt}\Big(\frac{S^{\alpha\beta}}{\rho}\Big)\Big](\boldsymbol{x})W(|\boldsymbol{x}-\boldsymbol{x}_i|,h)d\boldsymbol{x}\\ &= \int \Big[2\mu\Big(\frac{\dot{\epsilon}^{\alpha\beta}(\boldsymbol{x})}{\rho(\boldsymbol{x})} - \frac{1}{3}\delta^{\alpha\beta}\frac{\dot{\epsilon}^{\gamma\gamma}(\boldsymbol{x})}{\rho(\boldsymbol{x})}\Big)\\ &\quad + \frac{S^{\alpha\gamma}(\boldsymbol{x})}{\rho(\boldsymbol{x})}R^{\beta\gamma}(\boldsymbol{x}) + \frac{S^{\beta\gamma}(\boldsymbol{x})}{\rho(\boldsymbol{x})}R^{\alpha\gamma}(\boldsymbol{x}) + \frac{S^{\alpha\beta}(\boldsymbol{x})}{\rho(\boldsymbol{x})}\dot{\epsilon}^{\gamma\gamma}(\boldsymbol{x})\Big]W(|\boldsymbol{x}-\boldsymbol{x}_i|,h)d\boldsymbol{x}.\end{aligned} \tag{A.9}$$

The right hand side of Eq. (A.9) is composed of the following terms ($\dot{\epsilon}^{\alpha\beta}$ and $R^{\alpha\beta}$ are represented by the sums of velocity gradients):

$$\int \frac{1}{\rho(\boldsymbol{x})} \frac{\partial v^{\alpha}(\boldsymbol{x})}{\partial x^{\beta}} W(|\boldsymbol{x}-\boldsymbol{x}_i|, h) d\boldsymbol{x}, \tag{A.10}$$

$$\int \frac{S^{\alpha' \beta'}(\boldsymbol{x})}{\rho(\boldsymbol{x})} \frac{\partial v^{\alpha}(\boldsymbol{x})}{\partial x^{\beta}} W(|\boldsymbol{x}-\boldsymbol{x}_i|, h) d\boldsymbol{x}, \tag{A.11}$$

where α, β, α', and β' show arbitrary direction appearing in each term of Eq. (A.9). We notice that Eq. (A.11) is almost the same as the right hand side of Eq. (A.3), and thus we can do the same transformation as Eqs. (A.4), (A.5), and (A.6):

$$\begin{aligned}
&\int \frac{S^{\alpha' \beta'}(\boldsymbol{x})}{\rho(\boldsymbol{x})} \frac{\partial v^{\alpha}(\boldsymbol{x})}{\partial x^{\beta}} W(|\boldsymbol{x}-\boldsymbol{x}_i|, h) d\boldsymbol{x} \\
&= \sum_j m_j \int \frac{S^{\alpha' \beta'}(\boldsymbol{x})}{\rho^2(\boldsymbol{x})} [v^{\alpha}(\boldsymbol{x}) - v_i^{\alpha}] \Big[\frac{\partial}{\partial x_i^{\beta}} - \frac{\partial}{\partial x_j^{\beta}} \Big] W(|\boldsymbol{x}-\boldsymbol{x}_i|, h) W(|\boldsymbol{x}-\boldsymbol{x}_j|, h) d\boldsymbol{x}.
\end{aligned} \tag{A.12}$$

Using Eq. (2.11), Eq. (2.16), $\partial v_i^{\alpha}/\partial x^{\beta} = 0$, and the partial integration, Eq. (A.10) is transformed as

$$\begin{aligned}
&\int \frac{1}{\rho(\boldsymbol{x})} \frac{\partial v^{\alpha}(\boldsymbol{x})}{\partial x^{\beta}} W(|\boldsymbol{x}-\boldsymbol{x}_i|, h) d\boldsymbol{x} \\
&= \int \frac{1}{\rho(\boldsymbol{x})} \frac{\partial}{\partial x^{\beta}} (v^{\alpha}(\boldsymbol{x}) - v_i^{\alpha}) W(|\boldsymbol{x}-\boldsymbol{x}_i|, h) d\boldsymbol{x} \\
&= -\int (v^{\alpha}(\boldsymbol{x}) - v_i^{\alpha}) \frac{\partial}{\partial x^{\beta}} \Big(\frac{W(|\boldsymbol{x}-\boldsymbol{x}_i|, h)}{\rho(\boldsymbol{x})} \Big) d\boldsymbol{x} \\
&= \sum_j m_j \int \frac{1}{\rho^2(\boldsymbol{x})} (v^{\alpha}(\boldsymbol{x}) - v_i^{\alpha}) \Big[\frac{\partial}{\partial x_i^{\beta}} - \frac{\partial}{\partial x_j^{\beta}} \Big] W(|\boldsymbol{x}-\boldsymbol{x}_i|, h) W(|\boldsymbol{x}-\boldsymbol{x}_j|, h) d\boldsymbol{x}.
\end{aligned} \tag{A.13}$$

To evaluate the integrals in Eqs. (A.2), (A.6), (A.12), and (A.13), we make interpolated functions for physical quantities, especially the density. Here, a new convenient coordinate system is defined for the integration. We have the origin of the coordinate system at $(\boldsymbol{x}_i + \boldsymbol{x}_j)/2$, and the s-axis is defined to be parallel to the vector $\boldsymbol{x}_i - \boldsymbol{x}_j$. $\boldsymbol{s}_{\perp}$ denotes the component perpendicular to the s-axis of a vector $\boldsymbol{x}$. The vector $\boldsymbol{e}_{ij} \equiv (\boldsymbol{x}_i - \boldsymbol{x}_j)/|\boldsymbol{x}_i - \boldsymbol{x}_j|$ is defined to be the unit vector parallel to the s-axis, and $\Delta s_{ij} \equiv |\boldsymbol{x}_i - \boldsymbol{x}_j|$ as the distance between the i-th and j-th particles.

Essentially, Eqs. (A.2), (A.6), (A.12), and (A.13) are composed of the integration shown as

$$\int \frac{f(\boldsymbol{x})}{\rho^2(\boldsymbol{x})} W(|\boldsymbol{x}-\boldsymbol{x}_i|,h) W(|\boldsymbol{x}-\boldsymbol{x}_j|,h) d\boldsymbol{x}, \tag{A.14}$$

where $f(\boldsymbol{x})$ is an arbitrary physical quantity. Here, the weighted averaged physical quantity f^*_{ij} is defined as

$$\int \frac{f(\boldsymbol{x})}{\rho^2(\boldsymbol{x})} W(|\boldsymbol{x}-\boldsymbol{x}_i|,h) W(|\boldsymbol{x}-\boldsymbol{x}_j|,h) d\boldsymbol{x} = f^*_{ij} \int \frac{1}{\rho^2(\boldsymbol{x})} W(|\boldsymbol{x}-\boldsymbol{x}_i|,h) W(|\boldsymbol{x}-\boldsymbol{x}_j|,h) d\boldsymbol{x}. \tag{A.15}$$

If we interpolate $f(\boldsymbol{x})$ linearly in the direction parallel to $\boldsymbol{e}_{ij}$ and constant in the direction perpendicular to $\boldsymbol{e}_{ij}$, f^*_{ij} is expressed as

$$f^*_{ij} = \frac{f_i + f_j}{2} + s^*_{ij} \frac{f_i - f_j}{|\boldsymbol{x}_i - \boldsymbol{x}_j|}, \tag{A.16}$$

$$s^*_{ij} = \int_{-\infty}^{\infty} \frac{\sqrt{2}}{h\sqrt{\pi}} \frac{s}{\rho^2(s)} \exp\Big(-\frac{2s^2}{h^2}\Big) ds. \tag{A.17}$$

Then, $\rho^{-2}(\boldsymbol{r})$ is expanded linearly in the direction perpendicular to $\boldsymbol{e}_{ij}$ as

$$\rho^{-2}(\boldsymbol{x}) \approx \rho^{-2}(s) + \boldsymbol{s}_\perp \cdot \nabla \rho^{-2}(s). \tag{A.18}$$

Note that the second term of Eq. (A.18) vanishes through the integration due to the symmetric property of the kernel function. Eq. (A.15) is transformed using Eq. (A.18) as

$$\int \frac{f(\boldsymbol{x})}{\rho^2(\boldsymbol{x})} W(|\boldsymbol{x}-\boldsymbol{x}_i|,h) W(|\boldsymbol{x}-\boldsymbol{x}_j|,h) d\boldsymbol{x} = f^*_{ij} V^2_{ij} W(|\boldsymbol{x}_i-\boldsymbol{x}_j|,\sqrt{2}h), \tag{A.19}$$

where

$$V^2_{ij} = \int_{-\infty}^{\infty} \frac{\sqrt{2}}{h\sqrt{\pi}} \frac{1}{\rho^2(s)} \exp\Big(-\frac{2s^2}{h^2}\Big) ds. \tag{A.20}$$

To evaluate the integrals of Eqs. (A.17) and (A.20), we interpolate $1/\rho(s)$ using the density and its gradients of the i-th and j-th particles. For the convenience, we define the specific volume as $V(s) = 1/\rho(s)$ and calculate the specific volume and its gradients of the i-th particle as

$$
\begin{aligned}
V_i &= \frac{1}{\rho_i}, \\
\frac{\partial V_i}{\partial x_i^\alpha} &= -\frac{1}{\rho_i^2}\frac{\partial \rho_i}{\partial x_i^\alpha} = -\frac{1}{\rho_i^2}\sum_j m_j \frac{\partial}{\partial x_i^\alpha} W(|\boldsymbol{x}_i - \boldsymbol{x}_j|, h), \\
\frac{\partial^2 V_i}{\partial x_i^\alpha \partial x_i^\beta} &= \sum_j \frac{m_j}{\rho_j}\frac{\partial V_j}{\partial x_j^\alpha}\frac{\partial}{\partial x_i^\beta} W(|\boldsymbol{x}_i - \boldsymbol{x}_j|, h).
\end{aligned} \tag{A.21}
$$

We prepare three interpolation methods, that is, the linear, the cubic spline, and the quintic spline interpolation. For the linear interpolation, $V(s)$ is expressed as

$$
V(s) = C_{ij}s + D_{ij}, \tag{A.22}
$$

where

$$
\begin{aligned}
C_{ij} &= \frac{V_i - V_j}{\Delta s_{ij}}, \\
D_{ij} &= \frac{V_i + V_j}{2}.
\end{aligned} \tag{A.23}
$$

Then we achieve the expressions of V_{ij}^2 and s_{ij}^* for the linear interpolation as

$$
\begin{aligned}
V_{ij,\mathrm{linear}}^2 &= \frac{1}{4}h^2 C_{ij}^2 + D_{ij}^2, \\
s_{ij,\mathrm{linear}}^* &= \frac{h^2 C_{ij} D_{ij}}{2V_{ij,\mathrm{linear}}^2}.
\end{aligned} \tag{A.24}
$$

For the cubic spline interpolation, $V(s)$ is expressed as

$$
V(s) = A_{ij}s^3 + B_{ij}s^2 + C_{ij}s + D_{ij}, \tag{A.25}
$$

where

$$
\begin{aligned}
A_{ij} &= -2\frac{V_i - V_j}{\Delta s_{ij}^3} + \frac{V_i^{'} + V_j^{'}}{\Delta s_{ij}^2}, \\
B_{ij} &= \frac{1}{2}\frac{V_i^{'} - V_j^{'}}{\Delta s_{ij}}, \\
C_{ij} &= \frac{3}{2}\frac{V_i - V_j}{\Delta s_{ij}} - \frac{1}{4}(V_i^{'} + V_j^{'}), \\
D_{ij} &= \frac{1}{2}(V_i + V_j) - \frac{1}{8}(V_i^{'} - V_j^{'})\Delta s_{ij}, \\
V_i^{'} &= e_{ij}^{\alpha}\frac{\partial V_i}{\partial x_i^{\alpha}}, \\
V_j^{'} &= e_{ij}^{\alpha}\frac{\partial V_j}{\partial x_j^{\alpha}}.
\end{aligned} \tag{A.26}
$$

Then we achieve the expressions of V_{ij}^2 and s_{ij}^* for the cubic spline interpolation as

$$
\begin{aligned}
V_{ij,\text{cubic}}^2 &= \frac{15}{64}h^6 A_{ij}^2 + \frac{3}{16}h^4(2A_{ij}C_{ij} + B_{ij}^2) + \frac{1}{4}h^2(2B_{ij}D_{ij} + C_{ij}^2) + D_{ij}^2, \\
s_{ij,\text{cubic}}^* &= \frac{(15/32)h^6 A_{ij}B_{ij} + (3/8)h^4(A_{ij}D_{ij} + B_{ij}C_{ij}) + (1/2)h^2 C_{ij}D_{ij}}{V_{ij,\text{cubic}}^2}.
\end{aligned} \tag{A.27}
$$

Finally, for the quintic spline interpolation, $V(s)$ is expressed as

$$
V(s) = A_{ij}s^5 + B_{ij}s^4 + C_{ij}s^3 + D_{ij}s^2 + E_{ij}s + F_{ij}, \tag{A.28}
$$

where

$$
\begin{aligned}
A_{ij} &= 6\frac{V_i - V_j}{\Delta s_{ij}^5} - 3\frac{V_i^{'} + V_j^{'}}{\Delta s_{ij}^4} + \frac{1}{2}\frac{V_i^{''} - V_j^{''}}{\Delta s_{ij}^3}, \\
B_{ij} &= -\frac{1}{2}\frac{V_i^{'} - V_j^{'}}{\Delta s_{ij}^3} + \frac{1}{4}\frac{V_i^{''} + V_j^{''}}{\Delta s_{ij}^2}, \\
C_{ij} &= -5\frac{V_i - V_j}{\Delta s_{ij}^3} + \frac{5}{2}\frac{V_i^{'} + V_j^{'}}{\Delta s_{ij}^2} - \frac{1}{4}\frac{V_i^{''} - V_j^{''}}{\Delta s_{ij}}, \\
D_{ij} &= \frac{3}{4}\frac{V_i^{'} - V_j^{'}}{\Delta s_{ij}} - \frac{1}{8}(V_i^{''} + V_j^{''}), \\
E_{ij} &= \frac{15}{8}\frac{V_i - V_j}{\Delta s_{ij}} - \frac{7}{16}(V_i^{'} + V_j^{'}) + \frac{1}{32}(V_i^{''} - V_j^{''})\Delta s_{ij}, \\
F_{ij} &= \frac{1}{2}(V_i + V_j) - \frac{5}{32}(V_i^{'} - V_j^{'})\Delta s_{ij} + \frac{1}{64}(V_i^{''} + V_j^{''})\Delta s_{ij}^2,
\end{aligned} \tag{A.29}
$$

and

$$
\begin{aligned}
V_i^{''} &= e_{ij}^{\alpha} e_{ij}^{\beta} \frac{\partial^2 V_i}{\partial x_i^{\alpha} \partial x_i^{\beta}}, \\
V_j^{''} &= e_{ij}^{\alpha} e_{ij}^{\beta} \frac{\partial^2 V_j}{\partial x_j^{\alpha} \partial x_j^{\beta}}.
\end{aligned} \tag{A.30}
$$

Then we achieve the expressions of V_{ij}^2 and s_{ij}^* for the quintic spline interpolation as

$$
\begin{aligned}
V_{ij,\text{quintic}}^2 = & \frac{945}{1024} h^{10} A_{ij}^2 + \frac{105}{256} h^8 (2A_{ij}C_{ij} + B_{ij}^2) + \frac{15}{64} h^6 (2A_{ij}E_{ij} + 2B_{ij}D_{ij} + C_{ij}^2) \\
& + \frac{3}{16} h^4 (2B_{ij}F_{ij} + 2C_{ij}E_{ij} + D_{ij}^2) + \frac{1}{4} h^2 (2D_{ij}F_{ij} + E_{ij}^2) + F_{ij}^2, \\
s_{ij,\text{quintic}}^* = & \Big(\frac{945}{512} h^{10} A_{ij}B_{ij} + \frac{105}{128} h^8 (A_{ij}D_{ij} + B_{ij}C_{ij}) + \frac{15}{32} h^6 (A_{ij}F_{ij} + B_{ij}E_{ij} + C_{ij}D_{ij}) \\
& + \frac{3}{8} h^4 (C_{ij}F_{ij} + D_{ij}E_{ij}) + \frac{1}{2} h^2 E_{ij}F_{ij} \Big) / V_{ij,\text{quintic}}^2.
\end{aligned} \tag{A.31}
$$

Here, we introduce the final forms of EoM, EoE, and the time-evolution equation for the deviatoric stress tensor for the Godunov SPH method. EoM is expressed as

$$
\frac{dv_i^{\alpha}}{dt} = \sum_j 2m_j \sigma_{ij}^{\alpha\beta *} V_{ij}^2 \frac{\partial}{\partial x_i^{\beta}} W(|\boldsymbol{x}_i - \boldsymbol{x}_j|, \sqrt{2}h), \tag{A.32}
$$

where

$$
\begin{aligned}
\sigma_{ij}^{\alpha\beta *} &= -P_{ij}^* \delta^{\alpha\beta} + S_{ij}^{\alpha\beta *}, \\
S_{ij}^{\alpha\beta *} &= \frac{S_i^{\alpha\beta} + S_j^{\alpha\beta}}{2} + s_{ij}^* \frac{S_i^{\alpha\beta} - S_j^{\alpha\beta}}{|\boldsymbol{x}_i - \boldsymbol{x}_j|}.
\end{aligned} \tag{A.33}
$$

EoE is expressed as

$$
\frac{du_i}{dt} = \sum_j 2m_j \sigma_{ij}^{\alpha\beta *} V_{ij}^2 (v_{ij}^{\alpha *} - v_i^{\alpha *}) \frac{\partial}{\partial x_i^{\beta}} W(|\boldsymbol{x}_i - \boldsymbol{x}_j|, \sqrt{2}h), \tag{A.34}
$$

where

$$
v_i^{\alpha *} = v_i^{\alpha} + \frac{1}{2} \Delta t \frac{dv_i^{\alpha}}{dt}, \tag{A.35}
$$

for the conservation of the total energy. The time-evolution equation of the deviatoric stress tensor is expressed as

$$\frac{d}{dt}\Big(\frac{S^{\alpha\beta}}{\rho}\Big)_i = \sum_j 2\mu\Big(\dot{\epsilon}^{\alpha\beta}_{\rho,ij} - \frac{1}{3}\delta^{\alpha\beta}\dot{\epsilon}^{\gamma\gamma}_{\rho,ij}\Big) + S^{\alpha\gamma *}_{ij} R^{\beta\gamma}_{\rho,ij} + S^{\beta\gamma *}_{ij} R^{\alpha\gamma}_{\rho,ij} + S^{\alpha\beta *}_{ij}\dot{\epsilon}^{\gamma\gamma}_{\rho,ij}, \tag{A.36}$$

where,

$$\begin{aligned}
\dot{\epsilon}^{\alpha\beta}_{\rho,ij} &\equiv m_j V_{ij}^2\Big[(v^{\alpha *}_{ij} - v^{\alpha}_i)\frac{\partial}{\partial x^{\beta}_i} + (v^{\beta *}_{ij} - v^{\beta}_i)\frac{\partial}{\partial x^{\alpha}_i}\Big]W(|\boldsymbol{x}_i - \boldsymbol{x}_j|, \sqrt{2}h), \\
R^{\alpha\beta}_{\rho,ij} &\equiv m_j V_{ij}^2\Big[(v^{\alpha *}_{ij} - v^{\alpha}_i)\frac{\partial}{\partial x^{\beta}_i} - (v^{\beta *}_{ij} - v^{\beta}_i)\frac{\partial}{\partial x^{\alpha}_i}\Big]W(|\boldsymbol{x}_i - \boldsymbol{x}_j|, \sqrt{2}h).
\end{aligned} \tag{A.37}$$

Note that the deviatoric stress tensor itself is obtained from $(S^{\alpha\beta}/\rho)_i$ as $S^{\alpha\beta}_i = (S^{\alpha\beta}/\rho)_i\rho_i$.

According to Inutsuka (2002), we use the pressure resulted from the Riemann problem utilizing the physical values associated with the i-th and j-th particles for P^*_{ij}. The Riemann problem is introduced in the next section. Inutsuka (2002) also utilizes the velocity resulted from the Riemann problem for $v^{\alpha *}_{ij}$. The simulations for hydrodynamics work well with the velocity resulted from the Riemann problem. However, this may cause problems for elastic dynamics because of the difference of the equation of state, and it is safe to utilize the simple averaged value for $v^{\alpha *}_{ij}$ that is expressed as

$$v^{\alpha *}_{ij} = \frac{v^{\alpha}_i + v^{\alpha}_j}{2} + s^*_{ij}\frac{v^{\alpha}_i - v^{\alpha}_j}{|\boldsymbol{x}_i - \boldsymbol{x}_j|}. \tag{A.38}$$

If the cubic or quintic spline interpolations are used when the distance between two particles is much smaller than the smoothing length, V^2_{ij} may diverge due to the interpolation. However, V^2_{ij} should be about $1/\rho^2(\boldsymbol{x})$. Thus if V^2_{ij} obtained from the cubic or quintic spline interpolation is much larger than $1/\rho^2(\boldsymbol{x})$, we should use linear interpolation. We suggest that the linear interpolation should be used when V^2_{ij} becomes larger than $V^2_{ij,\mathrm{crit}}$ written as

$$V^2_{ij,\mathrm{crit}} = 10\Big(\frac{1}{\rho^2_{ij}}\Big), \tag{A.39}$$

where $\rho_{ij} = (\rho_i + \rho_j)/2$.

A.2 Riemann Solver

In this section, we will introduce how to calculate P^*_{ij} using the physical quantities associated with the i-th and j-th particles through the Riemann problem. We only introduce the Riemann

solver for the equation of state (EoS) $P = C_s^2(\rho - \rho_0)$, where C_s and ρ_0 are the parameters for this EoS. Please refer to, for example, van Leer (1979) for the Riemann solver for the ideal gas EoS.

We consider shock tube problems where the initial state (e.g., pressure or density) of right hand side is determined by the physical quantities of the i-th particle and the initial state of left hand side is determined by the physical quantities of the j-th particle. The waves are propagating to both the right and left directions. The waves are the shock wave or the rarefaction wave. A kind of "speed" in the mass coordinate for the shock wave and the rarefaction wave is written as

$$W_{s,D} = C_s \sqrt{\rho_D \Big(\rho_D + \frac{P^* - P_D}{C_s^2}\Big)} \ (P^* > P_D), \tag{A.40}$$

$$W_{s,D} = \frac{P_D - P^*}{C_s} \Big[\ln\Big(\frac{C_s^2 \rho_D}{P^* + C_s^2 \rho_0}\Big)\Big]^{-1} \ (P^* < P_D), \tag{A.41}$$

where D represents the direction of wave propagation and is replaced by R or L, and P^* represents the pressure around the contact discontinuity after the wave propagation. The quantities with D represent the quantities of the right or left hand side at the initial condition, i.e., the quantities of the i-th or j-th particle. If $P^* > P_D$, the shock wave propagates and thus Eq. (A.40) represents the speed of the shock wave, while if $P^* < P_D$, the rarefaction wave propagates and thus Eq. (A.41) represents a kind of speed of the rarefaction wave. Using $W_{s,\mathrm{L}}$ and $W_{s,\mathrm{R}}$, the pressure P^* and the velocity v^* at the contact discontinuity are written as

$$P^* = \frac{P_\mathrm{L}/W_{s,\mathrm{L}} + P_\mathrm{R}/W_{s,\mathrm{R}} + v_\mathrm{L} - v_\mathrm{R}}{1/W_{s,\mathrm{L}} + 1/W_{s,\mathrm{R}}}, \tag{A.42}$$

$$v^* = \frac{v_\mathrm{L} W_{s,\mathrm{L}} + v_\mathrm{R} W_{s,\mathrm{R}} + P_\mathrm{L} - P_\mathrm{R}}{W_{s,\mathrm{L}} + W_{s,\mathrm{R}}}, \tag{A.43}$$

where $P_\mathrm{R} = P_i$, $\rho_\mathrm{R} = \rho_i$, $v_\mathrm{R} = \boldsymbol{v}_i \cdot \boldsymbol{e}_{ij}$, $P_\mathrm{L} = P_j$, $\rho_\mathrm{L} = \rho_j$, and $v_\mathrm{L} = \boldsymbol{v}_j \cdot \boldsymbol{e}_{ij}$. P^* and v^* are determined through iterative calculations of Eq. (A.40) - Eq. (A.43). Five cycles of iterations with $P^* = (P_L + P_R)/2$ as the initial value are sufficient for the convergence. Finally, the converged P^* is used for P^*_{ij} in Eqs. (A.32) and (A.34).

However, P^* obtained from the above procedures has the first-order accuracy in space. For the Riemann solver with the second-order accuracy in space, we need to modify P_R, ρ_R, v_R, P_L, ρ_L, and v_L using the gradients of these physical quantities of the i-th and j-th particles. We skip

the explanation of the detailed procedures for this modification, and please refer to Inutsuka (2002). We just give a note that the gradient of the quantity f utilized for the Riemann solver should be calculated with

$$\frac{\partial f_i}{\partial x_i^\alpha} = \sum_j \frac{m_j(f_j - f_i)}{\rho_j} \frac{\partial}{\partial x_i^\alpha} W(|\boldsymbol{x}_i - \boldsymbol{x}_j|, h) \tag{A.44}$$

to avoid unphysical gradients nearby free surfaces.

We explained the Riemann solver for EoS for elastic body $P = C_s^2(\rho - \rho_0)$. However, impact simulations with rocky material utilize other EoS such as the tillotson EoS. In spite of the difference of EoS, usual EoS for rocky bodies behaves like the EoS for elastic body if the compression and the temperature raise due to impacts are moderate. Thus we can sill utilize the Riemann solver for $P = C_s^2(\rho - \rho_0)$ even if we utilize other EoS for rocky material. In this case, we approximate C_s and ρ_0 utilized for the Riemann solver using the physical values associated with the i-th and j-th particles. A possible way to calculate C_s and ρ_0 is as follows:

$$\begin{aligned} C_s &= \frac{C_{s,i} + C_{s,j}}{2}, \\ \rho_0 &= \frac{1}{2}[(\rho_i - P_i/C_s^2) + (\rho_j - P_j/C_s^2)]. \end{aligned} \tag{A.45}$$

Appendix B

Linear Stability Analysis for Godunov SPH Method

In this chapter, we will summarize the results of the linear stability analysis of the equations for the Godunov SPH method. This chapter is mainly based on Sugiura and Inutsuka (2016). In this linear stability analysis, we use the following simplification. We ignore the terms of the deviatoric stress tensor and set $S_i^{\alpha\beta} = 0$ because the deviatoric stress tensor generally prevents the clumping of SPH particles, which leads to prevent the tensile instability. We also ignore the Riemann solver and set $P_{ij}^* = (P_i + P_j)/2$ because numerical viscosity terms including the Riemann solver generally prevent numerical instabilities. We consider the cases that SPH particles are put on cubic lattices, and the smoothing length h is set to be the side length of the cubic lattices Δx. We conduct the linear stability analysis for the longitudinal perturbations because the tensile instability is the instability of compressional waves. We utilize the equation of state of $P = C_s^2(\rho - \rho_0)$. Unperturbed states have the uniform density and pressure, and all SPH particles have the same mass m.

B.1 Derivation of Dispersion Relations

In unperturbed states, particles are placed on the square lattices with the side lengths Δx. Unperturbed positions of particles are expressed as,

$$\overline{\boldsymbol{x}}_i = (\overline{x}_i, \overline{y}_i, \overline{z}_i). \tag{B.1}$$

We add the perturbation of positions in the x-direction. Then the positions of particles are represented as

$$\begin{aligned}\boldsymbol{x}_i &= (\overline{x}_i + \delta x_i, \overline{y}_i, \overline{z}_i),\\ \delta x_i &= \epsilon_x \exp[I(k\overline{x}_i - \omega t)],\end{aligned} \tag{B.2}$$

where ϵ_x is very small value, k and ω represent the wavenumber and frequency of the perturbation respectively, and I represents the imaginary unit. Hereafter, ϵ shows very small value, and we ignore second or higher order of ϵ.

From Eq. (B.2) and $(d/dt)\boldsymbol{x}_i = \boldsymbol{v}_i$, we can represent the velocity of the i-th particle as

$$\boldsymbol{v}_i = (-I\omega\delta x_i, 0, 0). \tag{B.3}$$

The density in unperturbed states is now defined as $\overline{\rho}$, and the density of the i-th particle is written as

$$\begin{aligned}\rho_i &= \overline{\rho} + \delta\rho_i,\\ \delta\rho_i &= \epsilon_\rho \exp[I(k\overline{x}_i - \omega t)].\end{aligned} \tag{B.4}$$

From Eq. (2.19), we can write $\delta\rho_i$ using δx_i as,

$$\begin{aligned}\delta\rho_i &= -I\overline{\rho}D\delta x_i,\\ D &\equiv \sum_j -\sin[k(\overline{x}_i - \overline{x}_j)]\frac{\partial}{\partial\overline{x}_i}W(|\overline{\boldsymbol{x}}_i - \overline{\boldsymbol{x}}_j|, h)\frac{m}{\overline{\rho}}.\end{aligned} \tag{B.5}$$

Then we can represent pressure of the i-th particle as

$$P_i = \overline{P} + \delta P_i = \overline{P} + C_s^2\delta\rho_i = \overline{P} - IC_s^2\overline{\rho}D\delta x_i, \tag{B.6}$$

where $\overline{P} = C_s^2(\overline{\rho} - \rho_0)$ represents the pressure in unperturbed states.

From Eq. (A.21), the specific volume is represented as

$$V_i = \frac{1}{\overline{\rho}}(1 + ID\delta x_i). \tag{B.7}$$

From Eq. (A.21), the x-component of the specific volume gradient is linearized as

$$\begin{aligned}\frac{\partial V_i}{\partial x_i} &= -\frac{1}{\rho_i^2}\frac{\partial \rho_i}{\partial x_i} \\ &\approx -\frac{1}{\overline{\rho}^2}\sum_j m(\delta x_i - \delta x_j)\frac{\partial^2}{\partial \overline{x_i}^2}W(|\overline{\boldsymbol{x}_i} - \overline{\boldsymbol{x}_j}|, h) = -\frac{1}{\overline{\rho}}C_\rho \delta x_i, \\ C_\rho &\equiv \sum_j (1 - \cos[k(\overline{x_i} - \overline{x_j})])\frac{\partial^2}{\partial \overline{x_i}^2}W(|\overline{\boldsymbol{x}_i} - \overline{\boldsymbol{x}_j}|, h)\frac{m}{\overline{\rho}}. \end{aligned} \tag{B.8}$$

The xx-component of the second derivative of V_i is linearized using Eq. (A.21) as

$$\frac{\partial^2 V_i}{\partial x_i^2} = \sum_j \frac{m}{\rho_j}\frac{\partial V_j}{\partial x_j}\frac{\partial}{\partial x_i}W(|\boldsymbol{x}_i - \boldsymbol{x}_j|, h) \approx -\frac{I}{\overline{\rho}}C_\rho D \delta x_i. \tag{B.9}$$

We then substitute linearized quantities into Eq. (A.32), and finally we obtain the dispersion relations (DRs) for the three interpolation methods. DR for the linear interpolation is expressed as

$$\omega^2_{\text{linear}} = -C_s^2 Da + \frac{\overline{P}}{\overline{\rho}}\Big[2Da + 2b\Big], \tag{B.10}$$

where

$$\begin{aligned} a &= \sum_{j\neq i} \sin[k(\overline{x_i} - \overline{x_j})]\frac{\partial}{\partial \overline{x_i}}W(|\overline{\boldsymbol{x}_i} - \overline{\boldsymbol{x}_j}|, \sqrt{2}h)\frac{m}{\overline{\rho}}, \\ b &= \sum_{j\neq i} (1 - \cos[k(\overline{x_i} - \overline{x_j})])\frac{\partial^2}{\partial \overline{x_i}^2}W(|\overline{\boldsymbol{x}_i} - \overline{\boldsymbol{x}_j}|, \sqrt{2}h)\frac{m}{\overline{\rho}}. \end{aligned} \tag{B.11}$$

DR for the cubic spline interpolation is expressed as

$$\omega^2_{\text{cubic}} = -C_s^2 Da + \frac{\overline{P}}{\overline{\rho}}\Big[2Da + 2b - \frac{1}{2}h^2 C_\rho c + \frac{1}{2}C_\rho d\Big], \tag{B.12}$$

where

$$\begin{aligned} c &= \sum_{j\neq i} \frac{\overline{x_i} - \overline{x_j}}{|\overline{\boldsymbol{x}_i} - \overline{\boldsymbol{x}_j}|^2}(1 - \cos[k(\overline{x_i} - \overline{x_j})])\frac{\partial}{\partial \overline{x_i}}W(|\overline{\boldsymbol{x}_i} - \overline{\boldsymbol{x}_j}|, \sqrt{2}h)\frac{m}{\overline{\rho}}, \\ d &= \sum_{j\neq i} (\overline{x_i} - \overline{x_j})(1 - \cos[k(\overline{x_i} - \overline{x_j})])\frac{\partial}{\partial \overline{x_i}}W(|\overline{\boldsymbol{x}_i} - \overline{\boldsymbol{x}_j}|, \sqrt{2}h)\frac{m}{\overline{\rho}}. \end{aligned} \tag{B.13}$$

DR for the quintic spline interpolation is expressed as

$$\begin{aligned}\omega^2_{\text{quintic}} =& -C_s^2 Da + \frac{\overline{P}}{\overline{\rho}}\Big[2Da + 2b + \frac{3}{8}h^4 C_\rho B_{1,4} + \frac{3}{16}h^4 C_\rho D A_{2,4} - \frac{3}{4}h^2 C_\rho B_{1,2} \\ & - \frac{1}{8}h^2 C_\rho D A_{2,2} + \frac{5}{8}C_\rho B_{1,0} + \frac{1}{16}C_\rho D A_{2,0}\Big], \end{aligned} \tag{B.14}$$

where

$$\begin{aligned} A_{n,m} &= \sum_j \frac{(\overline{x_i} - \overline{x_j})^n}{|\overline{\boldsymbol{x}_i} - \overline{\boldsymbol{x}_j}|^m} \sin[k(\overline{x_i} - \overline{x_j})] \frac{\partial}{\partial \overline{x_i}} W(|\overline{\boldsymbol{x}_i} - \overline{\boldsymbol{x}_j}|, \sqrt{2}h) \frac{m}{\overline{\rho}}, \\ B_{n,m} &= \sum_j \frac{(\overline{x_i} - \overline{x_j})^n}{|\overline{\boldsymbol{x}_i} - \overline{\boldsymbol{x}_j}|^m} (1 - \cos[k(\overline{x_i} - \overline{x_j})]) \frac{\partial}{\partial \overline{x_i}} W(|\overline{\boldsymbol{x}_i} - \overline{\boldsymbol{x}_j}|, \sqrt{2}h) \frac{m}{\overline{\rho}}. \end{aligned} \tag{B.15}$$

B.2 Results of Linear Stability Analysis

B.2.1 One-Dimensional Case

Here, we introduce the results of the linear stability analysis for the one-dimensional case. One dimension means that we only put SPH particles on one-dimensional string and use the Gaussian kernel for one dimension, i.e., we set $d_{\text{dim}} = 1$ in Eq. (2.12).

Figure B.1 shows the DRs for three interpolation methods with the positive unperturbed pressure (Fig. B.1a) and the negative unperturbed pressure (Fig. B.1b). As we notice from Fig. B.1a, ω^2 for the linear and cubic spline interpolations with the positive pressure is always positive for all wave numbers k including the Nyquist frequency $hk = \pi$, while ω^2 for the quintic spline interpolation with the positive pressure becomes negative around the Nyquist frequency. Note that the perturbations with negative ω^2 are unstable, since ω becomes pure imaginary and then the perturbations exponentially grow as we notice from Eq. (B.2). Therefore, the linear and cubic spline interpolations are stable with positive pressure, while the quintic spline interpolation is unstable with positive pressure. In contrast, Fig. B.1 shows that the linear and cubic spline interpolation are unstable with negative pressure, while the quintic spline interpolation is stable with negative pressure.

B.2.2 Two- and Three-Dimensional Case

Here, we introduce the results of the linear stability analysis for the two- and three-dimensional cases. Again, two dimensions mean that we put SPH particles on two-dimensional plane and

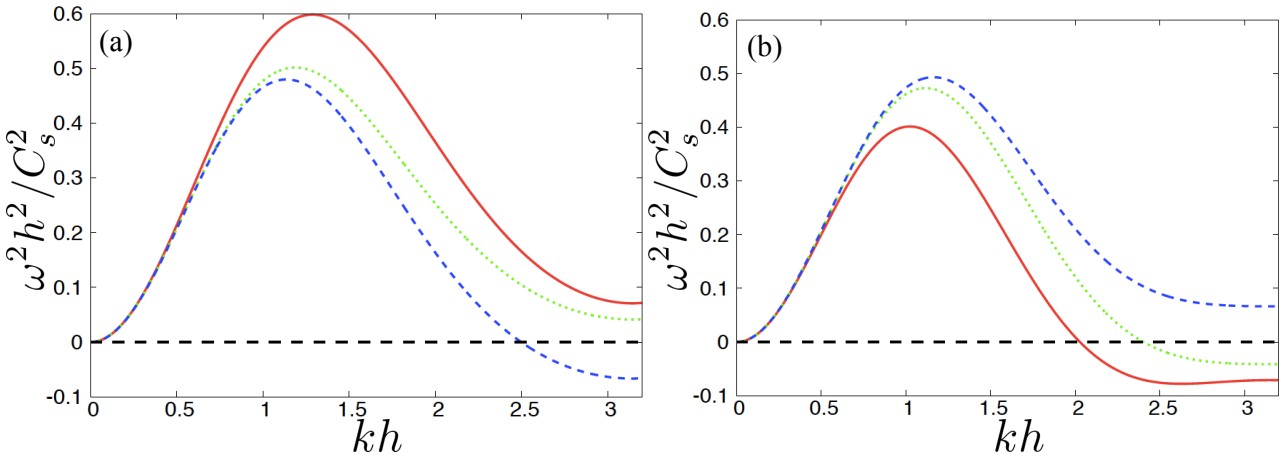

Figure B.1: DRs for the Godunov SPH method in a one-dimensional geometry. In both panels, the horizontal axis represents the wave number k of perturbations normalized by the smoothing length h, the vertical axis represents the square of the angular frequency ω of perturbations normalized by the sound speed C_s and the smoothing length h, the red solid curve shows DR for the linear interpolation, the green dotted curve shows that for the cubic spline interpolation, and the blue dashed curve shows that for the quintic spline interpolation. The panel (a) shows the DRs with the positive unperturbed pressure of $\overline{P} = 0.2C_s^2\overline{\rho}$, and the panel (b) shows those with the negative unperturbed pressure of $\overline{P} = -0.2C_s^2\overline{\rho}$.

use the Gaussian kernel for two dimensions, i.e., we set $d_{\rm dim} = 2$ in Eq. (2.12). Three dimensions mean usual setup of simulations.

Actually, the terms a and b (Eq. (B.12)) in the DR for the linear interpolation have the same values independent of the number of the spatial dimension. Thus the stability for the linear interpolation is the same independent of the number of the spatial dimension; even for two- and three-dimensional cases, the linear interpolation with positive pressure is stable while that with negative pressure is unstable.

Figure B.2 shows the DRs for the cubic and quintic spline interpolations in the two- and three-dimensional geometries with the positive pressure (Fig. B.2a) and the negative pressure (Fig. B.2b). As we notice from Fig. B.2a both cubic and quintic spline interpolations in both two- and three-dimensional geometries are unstable with the positive pressure. In contrast, Fig. B.2b shows that both cubic and quintic spline interpolations in both two- and three-dimensional geometries are stable with the negative pressure. Therefore, in two- and three-dimensional cases, the cubic and quintic spline interpolations are unstable with positive pressure and stable with negative pressure.

Summary of the discussion in Section B.2 leads to Table 2.1.

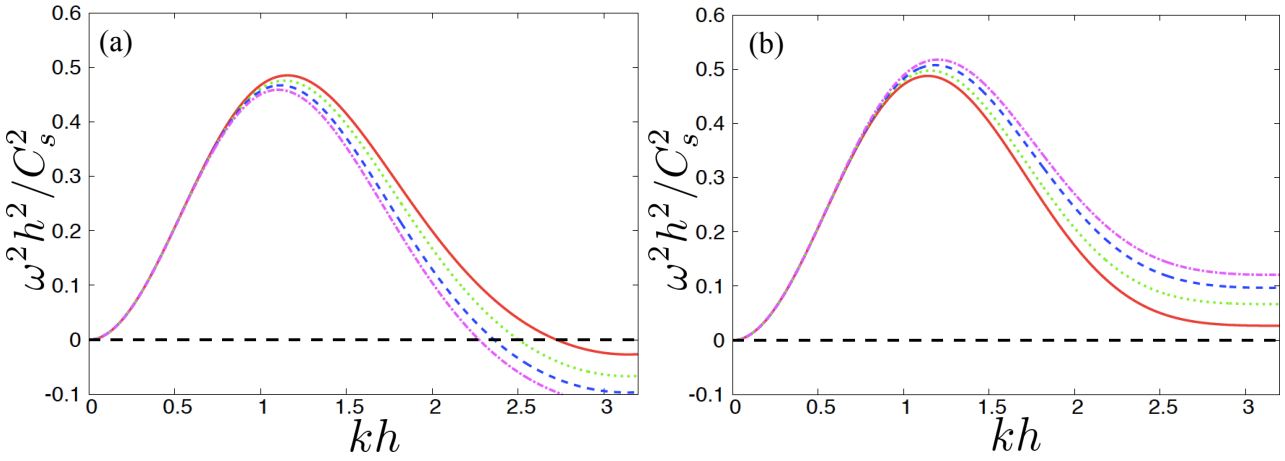

Figure B.2: DRs for the Godunov SPH method in two- and three-dimensional geometries. In both panels, the horizontal axis represents the wave number k of perturbations normalized by the smoothing length h, the vertical axis represents the square of the angular frequency ω of perturbations normalized by the sound speed C_s and the smoothing length h, the red solid curve shows the DR for the cubic spline interpolation in the two-dimensional case, the green dotted curve shows that in the three-dimensional case, the blue dashed curve shows the DR for the quintic spline interpolation in two-dimensional case, and the magenta chain curve shows that in the three-dimensional case. The panel (a) shows the DRs with the positive unperturbed pressure of $\overline{P} = 0.2C_s^2\overline{\rho}$, and the panel (b) shows those with the negative unperturbed pressure of $\overline{P} = -0.2C_s^2\overline{\rho}$.

B.3 Suppression of Tensile Instability with Godunov SPH Method

As a result of the analysis in above sections, we clarified the stability of the Godunov SPH method with the three interpolation methods in each dimensional geometry as shown in Table 2.1. This result suggests that if we select appropriate interpolation methods depending on the sign of pressure, we can avoid the tensile instability. Here, we propose the following way to select the interpolation methods for V_{ij}^2 in EoM (A.32), EoE (A.34), and the time-evolution equation for $S^{\alpha\beta}$ (A.36): V_{ij}^2 in one dimension becomes

$$V_{ij}^2 = \begin{cases} V_{ij,\mathrm{cubic}}^2 & \text{if } (P_i + P_j) > 0 \\ V_{ij,\mathrm{quintic}}^2 & \text{if } (P_i + P_j) < 0 \end{cases}, \tag{B.16}$$

while V_{ij}^2 in two and three dimensions becomes

$$V_{ij}^2 = \begin{cases} V_{ij,\text{linear}}^2 & \text{if } (P_i + P_j) > 0 \\ V_{ij,\text{cubic}}^2 & \text{if } (P_i + P_j) < 0 \end{cases} . \tag{B.17}$$

The correct selection of V_{ij}^2 depending on the sign of pressure as shown in Eq. (B.17) leads to the simulations of elastic bodies without the tensile instability as shown in Figs. 2.1 and 2.2.

Bibliography

C. Agnor and E. Asphaug. Accretion Efficiency during Planetary Collisions. *Astrophys. J.*, 613:L157–L160, October 2004. doi: 10.1086/425158.

C. B. Agnor, R. M. Canup, and H. F. Levison. On the Character and Consequences of Large Impacts in the Late Stage of Terrestrial Planet Formation. *Icarus*, 142:219–237, November 1999. doi: 10.1006/icar.1999.6201.

I. Alduán and M. A. Otaduy. Sph granular flow with friction and cohesion. In *Proc. of the ACM SIGGRAPH / Eurographics Symposium on Computer Animation*, 2011.

ALMA Partnership, C. L. Brogan, L. M. Pérez, T. R. Hunter, W. R. F. Dent, A. S. Hales, R. E. Hills, S. Corder, E. B. Fomalont, C. Vlahakis, Y. Asaki, D. Barkats, A. Hirota, J. A. Hodge, C. M. V. Impellizzeri, R. Kneissl, E. Liuzzo, R. Lucas, N. Marcelino, S. Matsushita, K. Nakanishi, N. Phillips, A. M. S. Richards, I. Toledo, R. Aladro, D. Broguiere, J. R. Cortes, P. C. Cortes, D. Espada, F. Galarza, D. Garcia-Appadoo, L. Guzman-Ramirez, E. M. Humphreys, T. Jung, S. Kameno, R. A. Laing, S. Leon, G. Marconi, A. Mignano, B. Nikolic, L.-A. Nyman, M. Radiszcz, A. Remijan, J. A. Rodón, T. Sawada, S. Takahashi, R. P. J. Tilanus, B. Vila Vilaro, L. C. Watson, T. Wiklind, E. Akiyama, E. Chapillon, I. de Gregorio-Monsalvo, J. Di Francesco, F. Gueth, A. Kawamura, C.-F. Lee, Q. Nguyen Luong, J. Mangum, V. Pietu, P. Sanhueza, K. Saigo, S. Takakuwa, C. Ubach, T. van Kempen, A. Wootten, A. Castro-Carrizo, H. Francke, J. Gallardo, J. Garcia, S. Gonzalez, T. Hill, T. Kaminski, Y. Kurono, H.-Y. Liu, C. Lopez, F. Morales, K. Plarre, G. Schieven, L. Testi, L. Videla, E. Villard, P. Andreani, J. E. Hibbard, and K. Tatematsu. The 2014 ALMA Long Baseline Campaign: First Results from High Angular Resolution Observations toward the HL Tau Region. *Astrophys. J.*, 808:L3, July 2015. doi: 10.1088/2041-8205/808/1/L3.

E. Asphaug. Similar-sized collisions and the diversity of planets. *Chem. Erde. / Geochem.*, 70: 199–219, 2010. doi: 10.1016/j.chemer.2010.01.004.

R.-L. Ballouz, D. C. Richardson, P. Michel, and S. R. Schwartz. Rotation-dependent Catastrophic Disruption of Gravitational Aggregates. *Astrophys. J.*, 789:158, July 2014. doi: 10.1088/0004-637X/789/2/158.

L. W. Bandermann and R. D. Wolstencroft. Energy changes in close planetary encounters. *Mon. Not. R. Astron. Soc.*, 152:377, 1971. doi: 10.1093/mnras/152.4.377.

M. T. Bannister, M. E. Schwamb, W. C. Fraser, M. Marsset, A. Fitzsimmons, S. D. Benecchi, P. Lacerda, R. E. Pike, J. J. Kavelaars, A. B. Smith, S. O. Stewart, S.-Y. Wang, and M. J. Lehner. Col-OSSOS: Colors of the Interstellar Planetesimal 1I/'Oumuamua. *Astrophys. J.*, 851:L38, December 2017. doi: 10.3847/2041-8213/aaa07c.

J. Barnes and P. Hut. A hierarchical O(N log N) force-calculation algorithm. *Nature*, 324: 446–449, December 1986. doi: 10.1038/324446a0.

W. Benz and E. Asphaug. Impact simulations with fracture. I - Method and tests. *Icarus*, 107: 98, January 1994. doi: 10.1006/icar.1994.1009.

W. Benz and E. Asphaug. Simulations of brittle solids using smooth particle hydrodynamics. *Comput. Phys. Comm.*, 87:253–265, May 1995. doi: 10.1016/0010-4655(94)00176-3.

W. Benz and E. Asphaug. Catastrophic Disruptions Revisited. *Icarus*, 142:5–20, November 1999. doi: 10.1006/icar.1999.6204.

R. P. Binzel, S. Xu, S. J. Bus, and E. Bowell. Origins for the near-earth asteroids. *Science*, 257 (5071):779–782, 1992. doi: 10.1126/science.257.5071.779.

T. Birnstiel, C. P. Dullemond, and F. Brauer. Gas- and dust evolution in protoplanetary disks. *Astron. Astrophys.*, 513:A79, April 2010. doi: 10.1051/0004-6361/200913731.

B. T. Bolin, H. A. Weaver, Y. R. Fernandez, C. M. Lisse, D. Huppenkothen, R. L. Jones, M. Jurić, J. Moeyens, C. A. Schambeau, C. T. Slater, Ž. Ivezić, and A. J. Connolly. APO Time-resolved Color Photometry of Highly Elongated Interstellar Object 1I/'Oumuamua. *Astrophys. J.*, 852:L2, January 2018. doi: 10.3847/2041-8213/aaa0c9.

J. Bonet and T.-S. Lok. Variational and momentum preservation aspects of smooth particle hydrodynamic formulations. *Comput. Methods Appl. Mech. Engrg.*, 180(1):97 – 115, 1999. doi: https://doi.org/10.1016/S0045-7825(99)00051-1.

W. F. Bottke, D. D. Durda, D. Nesvorný, R. Jedicke, A. Morbidelli, D. Vokrouhlický, and H. Levison. The fossilized size distribution of the main asteroid belt. *Icarus*, 175:111–140, May 2005. doi: 10.1016/j.icarus.2004.10.026.

D. T. Britt, D. Yeomans, K. Housen, and G. Consolmagno. *Asteroid Density, Porosity, and Structure*, pages 485–500. March 2002.

M. Bruck Syal, J. Rovny, J. M. Owen, and P. L. Miller. Excavating stickney crater at phobos. *Geophysical Research Letters*, 43(20):10,595–10,601, 2016. doi: 10.1002/2016GL070749.

J. A. Burns and V. S. Safronov. Asteroid nutation angles. *Mon. Not. R. Astron. Soc.*, 165:403, 1973. doi: 10.1093/mnras/165.4.403.

R. M. Canup. Origin of Terrestrial Planets and the Earth-Moon System. *Physics Today*, 57 (4):56–62, April 2004. doi: 10.1063/1.1752423.

M. Carroll and A. C. Holt. Suggested Modification of the P-α Model for Porous Materials. *Journal of Applied Physics*, 43:759–761, February 1972. doi: 10.1063/1.1661203.

S. Chandrasekhar. *Ellipsoidal figures of equilibrium*. 1969.

J. K. Chen, J. E. Beraun, and C. J. Jih. An improvement for tensile instability in smoothed particle hydrodynamics. *Comput. Mech.*, 23:279–287, 1999. doi: 10.1007/s004660050409.

G. S. Collins, H. J. Melosh, and B. A. Ivanov. Modeling damage and deformation in impact simulations. *Meteoritics and Planetary Science*, 39:217–231, February 2004. doi: 10.1111/j.1945-5100.2004.tb00337.x.

M. Ćuk. 1I/'Oumuamua as a Tidal Disruption Fragment from a Binary Star System. *Astrophys. J.*, 852:L15, January 2018. doi: 10.3847/2041-8213/aaa3db.

J. N. Cuzzi, R. C. Hogan, J. M. Paque, and A. R. Dobrovolskis. Size-selective Concentration of Chondrules and Other Small Particles in Protoplanetary Nebula Turbulence. *Astrophys. J.*, 546:496–508, January 2001. doi: 10.1086/318233.

C. de la Fuente Marcos and R. de la Fuente Marcos. Pole, Pericenter, and Nodes of the Interstellar Minor Body A/2017 U1. *Res. Notes AAS*, 1:5, December 2017. doi: 10.3847/2515-5172/aa96b4.

G. Domokos, A. Á. Sipos, G. M. Szabó, and P. L. Várkonyi. Formation of sharp edges and planar areas of asteroids by polyhedral abrasion. *Astrophys. J.*, 699(1):L13, 2009.

G. Domokos, A. Á. Sipos, G. M. Szabó, and P. L. Várkonyi. Explaining the elongated shape of 'Oumuamua by the eikonal abrasion model. *Res. Notes AAS*, 1(1):50, 2017.

M. Drahus, P. Guzik, W. Waniak, B. Handzlik, S. Kurowski, and S. Xu. Tumbling motion of 1I/'Oumuamua and its implications for the body's distant past. *Nature Astron.*, 2:407–412, May 2018. doi: 10.1038/s41550-018-0440-1.

B. T. Draine and H. M. Lee. Optical properties of interstellar graphite and silicate grains. *Astrophys. J.*, 285:89–108, October 1984. doi: 10.1086/162480.

J. Ďurech, V. Sidorin, and M. Kaasalainen. DAMIT: a database of asteroid models. *Astron. Astrophys.*, 513:A46, April 2010. doi: 10.1051/0004-6361/200912693.

P. Farinella, D. R. Davis, and F. Marzari. Asteroid Families, Old and Young. In T. Rettig and J. M. Hahn, editors, *Completing the Inventory of the Solar System*, volume 107 of *Astronomical Society of the Pacific Conference Series*, pages 45–55, 1996.

P. Farinella, D. Vokrouhlický, and W. K. Hartmann. Meteorite Delivery via Yarkovsky Orbital Drift. *Icarus*, 132:378–387, April 1998. doi: 10.1006/icar.1997.5872.

J. A. Fernandez. Mass removed by the outer planets in the early solar system. *Icarus*, 34: 173–181, April 1978. doi: 10.1016/0019-1035(78)90134-3.

M. Flock, S. Fromang, N. J. Turner, and M. Benisty. 3D Radiation Nonideal Magnetohydrodynamical Simulations of the Inner Rim in Protoplanetary Disks. *Astrophys. J.*, 835:230, February 2017. doi: 10.3847/1538-4357/835/2/230.

W. C. Fraser, P. Pravec, A. Fitzsimmons, P. Lacerda, M. T. Bannister, C. Snodgrass, and I. Smoli'c. The tumbling rotational state of 1I/'Oumuamua. *Nature Astron.*, 2 2018. doi: 10.1038/s41550-018-0398-z.

A. Fujiwara, G. Kamimoto, and A. Tsukamoto. Expected shape distribution of asteroids obtained from laboratory impact experiments. *Nature*, 272:602, April 1978. doi: 10.1038/272602a0.

A. Fujiwara, P. Cerroni, D. R. Davis, E. Ryan, M. di Martino, K. Holsapple, and K. Housen. Experiments and scaling laws for catastrophic collisions. In R. P. Binzel, T. Gehrels, and M. S. Matthews, editors, *Asteroids II*, pages 240–265, 1989.

A. Fujiwara, J. Kawaguchi, D. K. Yeomans, M. Abe, T. Mukai, T. Okada, J. Saito, H. Yano, M. Yoshikawa, D. J. Scheeres, O. Barnouin-Jha, A. F. Cheng, H. Demura, R. W. Gaskell, N. Hirata, H. Ikeda, T. Kominato, H. Miyamoto, A. M. Nakamura, R. Nakamura, S. Sasaki, and K. Uesugi. The Rubble-Pile Asteroid Itokawa as Observed by Hayabusa. *Science*, 312: 1330–1334, June 2006. doi: 10.1126/science.1125841.

H. Genda, E. Kokubo, and S. Ida. Merging Criteria for Giant Impacts of Protoplanets. *Astrophys. J.*, 744:137, January 2012. doi: 10.1088/0004-637X/744/2/137.

H. Genda, T. Fujita, H. Kobayashi, H. Tanaka, and Y. Abe. Resolution dependence of disruptive collisions between planetesimals in the gravity regime. *Icarus*, 262:58–66, December 2015. doi: 10.1016/j.icarus.2015.08.029.

R. A. Gingold and J. J. Monaghan. Smoothed particle hydrodynamics - Theory and application to non-spherical stars. *Mon. Not. R. Astron. Soc.*, 181:375–389, November 1977. doi: 10.1093/mnras/181.3.375.

M. Goeritz, T. Kenkmann, K. Wünnemann, and S. van Gasselt. Asymmetric Structure of Lunar Impact Craters Due to Oblique Impacts? In *Lunar and Planetary Science Conference*, volume 40 of *Lunar and Planetary Science Conference*, page 2096, March 2009.

D. Grady and M. Kipp. Continuum modelling of explosive fracture in oil shale. *Int. J. Rock Mech. Min. Sci. Geomech. Abstr.*, 17(3):147 – 157, 1980. doi: https://doi.org/10.1016/0148-9062(80)91361-3.

J. P. Gray, J. J. Monaghan, and R. P. Swift. Sph elastic dynamics. *Comput. Methods Appl. Mech. Engrg.*, 190(49):6641 – 6662, 2001. doi: https://doi.org/10.1016/S0045-7825(01)00254-7.

C. Hayashi. Structure of the Solar Nebula, Growth and Decay of Magnetic Fields and Effects of Magnetic and Turbulent Viscosities on the Nebula. *Prog. Theor. Phys. Suppl.*, 70:35–53, 1981. doi: 10.1143/PTPS.70.35.

C. Hayashi, K. Nakazawa, and Y. Nakagawa. Formation of the solar system. In D. C. Black and M. S. Matthews, editors, *Protostars and Planets II*, pages 1100–1153, 1985.

G. H. Heiken, D. T. Vaniman, and B. M. French. *Lunar sourcebook - A user's guide to the moon*. 1991.

W. Herrmann. Constitutive Equation for the Dynamic Compaction of Ductile Porous Materials. *Journal of Applied Physics*, 40:2490–2499, May 1969. doi: 10.1063/1.1658021.

A. Higuchi, E. Kokubo, and T. Mukai. Scattering of Planetesimals by a Planet: Formation of Comet Cloud Candidates. *Astron. J.*, 131:1119–1129, February 2006. doi: 10.1086/498892.

K. Hirayama. Groups of asteroids probably of common origin. *Astron. J.*, 31:185–188, October 1918. doi: 10.1086/104299.

M. J. Holman and P. A. Wiegert. Long-Term Stability of Planets in Binary Systems. *Astron. J.*, 117:621–628, January 1999. doi: 10.1086/300695.

K. R. Housen and K. A. Holsapple. On the fragmentation of asteroids and planetary satellites. *Icarus*, 84:226–253, March 1990. doi: 10.1016/0019-1035(90)90168-9.

K. R. Housen and K. A. Holsapple. Scale effects in strength-dominated collisions of rocky asteroids. *Icarus*, 142(1):21 – 33, 1999. doi: https://doi.org/10.1006/icar.1999.6206.

J. P. Huchra and M. J. Geller. Groups of galaxies. I - Nearby groups. *Astrophys. J.*, 257: 423–437, June 1982. doi: 10.1086/160000.

D. W. Hughes and G. H. A. Cole. The asteroidal sphericity limit. *Mon. Not. R. Astron. Soc.*, 277:99–105, November 1995. doi: 10.1093/mnras/277.1.99.

S. Ida. Stirring and dynamical friction rates of planetesimals in the solar gravitational field. *Icarus*, 88:129–145, November 1990. doi: 10.1016/0019-1035(90)90182-9.

S. Ida and J. Makino. Scattering of planetesimals by a protoplanet - Slowing down of runaway growth. *Icarus*, 106:210, November 1993. doi: 10.1006/icar.1993.1167.

S. Ida, R. M. Canup, and G. R. Stewart. Lunar accretion from an impact-generated disk. *Nature*, 389:353–357, September 1997. doi: 10.1038/38669.

S. Ida, T. Guillot, and A. Morbidelli. Accretion and Destruction of Planetesimals in Turbulent Disks. *Astrophys. J.*, 686:1292–1301, October 2008. doi: 10.1086/591903.

M. Ilgner and R. P. Nelson. Turbulent transport and its effect on the dead zone in protoplanetary discs. *Astron. Astrophys.*, 483:815–830, June 2008. doi: 10.1051/0004-6361:20079307.

S. Inutsuka. Reformulation of Smoothed Particle Hydrodynamics with Riemann Solver. *J. Comput. Phys.*, 179:238–267, June 2002. doi: 10.1006/jcph.2002.7053.

K. Iwasaki and S.-i. Inutsuka. Smoothed particle magnetohydrodynamics with a riemann solver and the method of characteristics. *Mon. Not. R. Astron. Soc.*, 418(3):1668–1688, 2011. doi: 10.1111/j.1365-2966.2011.19588.x.

M. Iwasawa, A. Tanikawa, N. Hosono, K. Nitadori, T. Muranushi, and J. Makino. Fdps: A novel framework for developing high-performance particle simulation codes for distributed-memory systems. In *Proceedings of the 5th International Workshop on Domain-Specific Languages and High-Level Frameworks for High Performance Computing*, WOLFHPC '15, pages 1:1–1:10, New York, NY, USA, 2015. ACM. ISBN 978-1-4503-4016-8. doi: 10.1145/2830018.2830019.

M. Iwasawa, A. Tanikawa, N. Hosono, K. Nitadori, T. Muranushi, and J. Makino. Implementation and performance of FDPS: a framework for developing parallel particle simulation codes. *Publ. Astron. Soc. Japan*, 68 (4):54 (1), 2016.

A. P. Jackson, D. Tamayo, N. Hammond, M. Ali-Dib, and H. Rein. Ejection of rocky and icy material from binary star systems: Implications for the origin and composition of 1I/'Oumuamua. *Mon. Not. R. Astron. Soc.*, March 2018. doi: 10.1093/mnrasl/sly033.

D. Jewitt, J. Luu, J. Rajagopal, R. Kotulla, S. Ridgway, W. Liu, and T. Augusteijn. Interstellar interloper 1I/2017 U1: Observations from the NOT and WIYN telescopes. *Astrophys. J.*, 850(2):L36, 2017.

A. Johansen, J. Blum, H. Tanaka, C. Ormel, M. Bizzarro, and H. Rickman. The Multifaceted Planetesimal Formation Process. *Protostars and Planets VI*, pages 547–570, 2014.

M. Jutzi. SPH calculations of asteroid disruptions: The role of pressure dependent failure models. *Planetary and Space Science*, 107:3–9, March 2015. doi: 10.1016/j.pss.2014.09.012.

M. Jutzi and E. Asphaug. The shape and structure of cometary nuclei as a result of low-velocity accretion. *Science*, 348:1355–1358, June 2015. doi: 10.1126/science.aaa4747.

M. Jutzi and W. Benz. Formation of bi-lobed shapes by sub-catastrophic collisions. A late origin of comet 67P's structure. *Astron. Astrophys.*, 597:A62, January 2017. doi: 10.1051/0004-6361/201628964.

M. Jutzi, W. Benz, and P. Michel. Numerical simulations of impacts involving porous bodies. I. Implementing sub-resolution porosity in a 3D SPH hydrocode. *Icarus*, 198:242–255, November 2008. doi: 10.1016/j.icarus.2008.06.013.

M. Jutzi, P. Michel, and W. Benz. A large crater as a probe of the internal structure of the E-type asteroid Steins. *Astron. Astrophys.*, 509:L2, January 2010. doi: 10.1051/0004-6361/200913549.

M. Kaasalainen and J. Torppa. Optimization Methods for Asteroid Lightcurve Inversion. I. Shape Determination. *Icarus*, 153:24–36, September 2001. doi: 10.1006/icar.2001.6673.

M. Kaasalainen, J. Torppa, and K. Muinonen. Optimization Methods for Asteroid Lightcurve Inversion. II. The Complete Inverse Problem. *Icarus*, 153:37–51, September 2001. doi: 10.1006/icar.2001.6674.

M. Kaasalainen, T. Kwiatkowski, M. Abe, J. Piironen, T. Nakamura, Y. Ohba, B. Dermawan, T. Farnham, F. Colas, S. Lowry, P. Weissman, R. J. Whiteley, D. J. Tholen, S. M. Larson, M. Yoshikawa, I. Toth, and F. P. Velichko. CCD photometry and model of MUSES-C target (25143) 1998 SF36. *Astron. Astrophys.*, 405:L29–L32, July 2003. doi: 10.1051/0004-6361:20030819.

A. Kataoka, H. Tanaka, S. Okuzumi, and K. Wada. Fluffy dust forms icy planetesimals by static compression. *Astron. Astrophys.*, 557:L4, September 2013. doi: 10.1051/0004-6361/201322151.

M. Kato, Y.-I. Iijima, M. Arakawa, Y. Okimura, A. Fujimura, N. Maeno, and H. Mizutani. Ice-on-ice impact experiments. *Icarus*, 113(2):423 – 441, 1995. doi: https://doi.org/10.1006/icar.1995.1032.

Y. Kitamura, M. Momose, S. Yokogawa, R. Kawabe, M. Tamura, and S. Ida. Investigation of the Physical Properties of Protoplanetary Disks around T Tauri Stars by a 1 Arcsecond

Imaging Survey: Evolution and Diversity of the Disks in Their Accretion Stage. *Astrophys. J.*, 581:357–380, December 2002. doi: 10.1086/344223.

Z. Knezevic, A. Lemaître, and A. Milani. *The Determination of Asteroid Proper Elements*, pages 603–612. March 2002.

M. M. Knight, S. Protopapa, M. S. P. Kelley, T. L. Farnham, J. M. Bauer, D. Bodewits, L. M. Feaga, and J. M. Sunshine. On the rotation period and shape of the hyperbolic asteroid 1I/ʻ Oumuamua (2017 U1) from its lightcurve. *Astrophys. J.*, 851(2):L31, 2017.

H. Kobayashi and S. Ida. The Effects of a Stellar Encounter on a Planetesimal Disk. *Icarus*, 153:416–429, October 2001. doi: 10.1006/icar.2001.6700.

H. Kobayashi and H. Tanaka. From Planetesimal to Planet in Turbulent Disks. II. Formation of Gas Giant Planets. *Astrophys. J.*, 862:127, August 2018. doi: 10.3847/1538-4357/aacdf5.

H. Kobayashi, S. Ida, and H. Tanaka. The evidence of an early stellar encounter in Edgeworth Kuiper belt. *Icarus*, 177:246–255, September 2005. doi: 10.1016/j.icarus.2005.02.017.

H. Kobayashi, H. Tanaka, and S. Okuzumi. From Planetesimals to Planets in Turbulent Protoplanetary Disks. I. Onset of Runaway Growth. *Astrophys. J.*, 817:105, February 2016. doi: 10.3847/0004-637X/817/2/105.

E. Kokubo and H. Genda. Formation of Terrestrial Planets from Protoplanets Under a Realistic Accretion Condition. *Astrophys. J.*, 714:L21–L25, May 2010. doi: 10.1088/2041-8205/714/1/L21.

E. Kokubo and S. Ida. Orbital evolution of protoplanets embedded in a swarm of planetesimals. *Icarus*, 114:247–257, April 1995. doi: 10.1006/icar.1995.1059.

E. Kokubo and S. Ida. On Runaway Growth of Planetesimals. *Icarus*, 123:180–191, September 1996. doi: 10.1006/icar.1996.0148.

E. Kokubo and S. Ida. Oligarchic Growth of Protoplanets. *Icarus*, 131:171–178, January 1998. doi: 10.1006/icar.1997.5840.

E. Kokubo and S. Ida. Formation of Protoplanets from Planetesimals in the Solar Nebula. *Icarus*, 143:15–27, January 2000. doi: 10.1006/icar.1999.6237.

E. Kokubo and S. Ida. Formation of Protoplanet Systems and Diversity of Planetary Systems. *Astrophys. J.*, 581:666–680, December 2002. doi: 10.1086/344105.

R. G. Kraus, L. E. Senft, and S. T. Stewart. Impacts onto H $_2$O ice: Scaling laws for melting, vaporization, excavation, and final crater size. *Icarus*, 214:724–738, August 2011. doi: 10.1016/j.icarus.2011.05.016.

K. A. Kretke, D. N. C. Lin, P. Garaud, and N. J. Turner. Assembling the Building Blocks of Giant Planets Around Intermediate-Mass Stars. *Astrophys. J.*, 690:407–415, January 2009. doi: 10.1088/0004-637X/690/1/407.

K. Krohn, R. Jaumann, D. Elbeshausen, T. Kneissl, N. Schmedemann, R. Wagner, J. Voigt, K. Otto, K. D. Matz, F. Preusker, T. Roatsch, K. Stephan, C. A. Raymond, and C. T. Russell. Asymmetric craters on Vesta: Impact on sloping surfaces. *Planetary and Space Science*, 103:36–56, November 2014. doi: 10.1016/j.pss.2014.04.011.

W. Kwon, L. W. Looney, and L. G. Mundy. Resolving the Circumstellar Disk of HL Tauri at Millimeter Wavelengths. *Astrophys. J.*, 741:3, November 2011. doi: 10.1088/0004-637X/741/1/3.

E. Lajeunesse, J. B. Monnier, and G. M. Homsy. Granular slumping on a horizontal surface. *Physics of Fluids*, 17(10):103302, 2005. doi: 10.1063/1.2087687.

M. A. Lange and T. J. Ahrens. The dynamic tensile strength of ice and ice-silicate mixtures. *J. Geophys. Res.*, 88(B2):1197–1208, 1983. doi: 10.1029/JB088iB02p01197.

B. Lawn. *Fracture of Brittle Solids*. Cambridge Solid State Science Series. Cambridge University Press, 2 edition, 1993. doi: 10.1017/CBO9780511623127.

Z. M. Leinhardt and S. T. Stewart. Collisions between Gravity-dominated Bodies. I. Outcome Regimes and Scaling Laws. *Astrophys. J.*, 745:79, January 2012. doi: 10.1088/0004-637X/745/1/79.

Z. M. Leinhardt, D. C. Richardson, and T. Quinn. Direct N-body Simulations of Rubble Pile Collisions. *Icarus*, 146:133–151, July 2000. doi: 10.1006/icar.2000.6370.

Z. M. Leinhardt, R. A. Marcus, and S. T. Stewart. The Formation of the Collisional Family Around the Dwarf Planet Haumea. *Astrophys. J.*, 714:1789–1799, May 2010. doi: 10.1088/0004-637X/714/2/1789.

A. Leleu, M. Jutzi, and M. Rubin. The peculiar shapes of Saturn's small inner moons as evidence of mergers of similar-sized moonlets. *Nature Astron.*, 2:555–561, July 2018. doi: 10.1038/s41550-018-0471-7.

L. D. Libersky and A. G. Petschek. Smooth particle hydrodynamics with strength of materials. In H. E. Trease, M. F. Fritts, and W. P. Crowley, editors, *Advances in the Free-Lagrange Method Including Contributions on Adaptive Gridding and the Smooth Particle Hydrodynamics Method*, volume 395 of *Lecture Notes in Physics, Berlin Springer Verlag*, pages 248–257, 1991.

E. M. Lifshitz, A. M. Kosevich, and L. P. Pitaevskii. Chapter ii - the equilibrium of rods and plates. In E. Lifshitz, A. Kosevich, and L. Pitaevskii, editors, *Theory of Elasticity (Third Edition)*, pages 38 – 86. Butterworth-Heinemann, Oxford, third edition edition, 1986. ISBN 978-0-08-057069-3. doi: https://doi.org/10.1016/B978-0-08-057069-3.50009-7.

C. H. Lineweaver and M. Norman. The Potato Radius: a Lower Minimum Size for Dwarf Planets. *ArXiv e-prints*, April 2010.

L. B. Lucy. A numerical approach to the testing of the fission hypothesis. *Astron. J.*, 82: 1013–1024, December 1977. doi: 10.1086/112164.

J. S. Mathis, W. Rumpl, and K. H. Nordsieck. The size distribution of interstellar grains. *Astrophys. J.*, 217:425–433, October 1977. doi: 10.1086/155591.

K. J. Meech, R. Weryk, M. Micheli, J. T. Kleyna, O. R. Hainaut, R. Jedicke, R. J. Wainscoat, K. C. Chambers, J. V. Keane, A. Petric, L. Denneau, E. Magnier, T. Berger, M. E. Huber, H. Flewelling, C. Waters, E. Schunova-Lilly, and S. Chastel. A brief visit from a red and extremely elongated interstellar asteroid. *Nature*, 552:378–381, December 2017. doi: 10.1038/nature25020.

H. J. Melosh, E. V. Ryan, and E. Asphaug. Dynamic fragmentation in impacts - Hydrocode simulation of laboratory impacts. *J. Geophys. Res.*, 97:14, September 1992. doi: 10.1029/92JE01632.

P. Michel and D. C. Richardson. Collision and gravitational reaccumulation: Possible formation mechanism of the asteroid Itokawa. *Astron. Astrophys.*, 554:L1, June 2013. doi: 10.1051/0004-6361/201321657.

P. Michel, W. Benz, P. Tanga, and D. C. Richardson. Collisions and Gravitational Reaccumulation: Forming Asteroid Families and Satellites. *Science*, 294:1696–1700, November 2001. doi: 10.1126/science.1065189.

P. Michel, M. Jutzi, D. C. Richardson, and W. Benz. The Asteroid Veritas: An intruder in a family named after it? *Icarus*, 211:535–545, January 2011. doi: 10.1016/j.icarus.2010.10.012.

P. Michel, A. Morbidelli, and W. F. Bottke. Origin and dynamics of near earth objects. *Comptes Rendus Physique*, 6(3):291 – 301, 2005. doi: https://doi.org/10.1016/j.crhy.2004.12.013. The Near Earth Objects : possible impactors of the Earth.

M. Micheli, D. Farnocchia, K. J. Meech, M. W. Buie, O. R. Hainaut, D. Prialnik, N. Schörghofer, H. A. Weaver, P. W. Chodas, J. T. Kleyna, R. Weryk, R. J. Wainscoat, H. Ebeling, J. V. Keane, K. C. Chambers, D. Koschny, and A. E. Petropoulos. Non-gravitational acceleration in the trajectory of 1I/2017 U1 ('Oumuamua). *Nature*, 559:223–226, June 2018. doi: 10.1038/s41586-018-0254-4.

T. Michikami, A. Hagermann, H. Miyamoto, S. Miura, J. Haruyama, and P. Lykawka. Impact cratering experiments in brittle targets with variable thickness: Implications for deep pit craters on mars. *Planetary and Space Science*, 96:71 – 80, 2014. doi: https://doi.org/10.1016/j.pss.2014.03.010.

T. Michikami, A. Hagermann, T. Kadokawa, A. Yoshida, A. Shimada, S. Hasegawa, and A. Tsuchiyama. Fragment shapes in impact experiments ranging from cratering to catastrophic disruption. *Icarus*, 264(Supplement C):316 – 330, 2016. doi: https://doi.org/10.1016/j.icarus.2015.09.038.

T. Michikami, T. Kadokawa, A. Tsuchiyama, A. Hagermann, T. Nakano, K. Uesugi, and S. Hasegawa. Influence of petrographic textures on the shapes of impact experiment fine fragments measuring several tens of microns: Comparison with Itokawa regolith particles. *Icarus*, 302:109–125, March 2018. doi: 10.1016/j.icarus.2017.10.040.

A. Milani, A. Cellino, Z. Knežević, B. Novaković, F. Spoto, and P. Paolicchi. Asteroid families classification: Exploiting very large datasets. *Icarus*, 239:46–73, September 2014. doi: 10.1016/j.icarus.2014.05.039.

H. Mizuno. Formation of the Giant Planets. *Prog. Theor. Phys.* , 64:544–557, August 1980. doi: 10.1143/PTP.64.544.

H. Mizuno, K. Nakazawa, and C. Hayashi. Instability of a gaseous envelope surrounding a planetary core and formation of giant planets. *Prog. Theor. Phys.* , 60:699–710, September 1978. doi: 10.1143/PTP.60.699.

H. Mizutani, Y. Takagi, and S.-I. Kawakami. New scaling laws on impact fragmentation. *Icarus*, 87:307–326, October 1990. doi: 10.1016/0019-1035(90)90136-W.

J. J. Monaghan. An introduction to SPH. *Comput. Phys. Comm.*, 48:89–96, January 1988. doi: 10.1016/0010-4655(88)90026-4.

J. J. Monaghan. Smoothed particle hydrodynamics. *Annu. Rev. Astron. Astrophys.*, 30:543–574, 1992. doi: 10.1146/annurev.aa.30.090192.002551.

J. J. Monaghan. SPH without a Tensile Instability. *J. Comput. Phys.*, 159:290–311, April 2000. doi: 10.1006/jcph.2000.6439.

A. Morbidelli and D. Vokrouhlický. The Yarkovsky-driven origin of near-Earth asteroids. *Icarus*, 163:120–134, May 2003. doi: 10.1016/S0019-1035(03)00047-2.

S. Mori, T. Muranushi, S. Okuzumi, and S.-i. Inutsuka. Electron Heating and Saturation of Self-regulating Magnetorotational Instability in Protoplanetary Disks. *Astrophys. J.*, 849:86, November 2017. doi: 10.3847/1538-4357/aa8e42.

M. Nagasawa, S. Ida, and H. Tanaka. Excitation of Orbital Inclinations of Asteroids during Depletion of a Protoplanetary Disk: Dependence on the Disk Configuration. *Icarus*, 159: 322–327, October 2002. doi: 10.1006/icar.2002.6925.

A. Nakamura and A. Fujiwara. Velocity Distribution of Fragments in Collisional Breakup. In A. C. Levasseur-Regoud and H. Hasegawa, editors, *IAU Colloq. 126: Origin and Evolution of Interplanetary Dust*, volume 173 of *Astrophysics and Space Science Library*, page 379, 1991.

D. P. O'Brien and R. Greenberg. The collisional and dynamical evolution of the main-belt and NEA size distributions. *Icarus*, 178:179–212, November 2005. doi: 10.1016/j.icarus.2005.04.001.

K. Ohtsuki. Evolution of random velocities of planetesimals in the course of accretion. *Icarus*, 98:20–27, July 1992. doi: 10.1016/0019-1035(92)90202-I.

K. Ohtsuki, G. R. Stewart, and S. Ida. Evolution of Planetesimal Velocities Based on Three-Body Orbital Integrations and Growth of Protoplanets. *Icarus*, 155:436–453, February 2002. doi: 10.1006/icar.2001.6741.

J. D. O'Keefe and T. J. Ahrens. Cometary and meteorite swarm impact on planetary surfaces. *J. Geophys. Res.*, 87:6668–6680, August 1982a. doi: 10.1029/JB087iB08p06668.

J. D. O'Keefe and T. J. Ahrens. *The interaction of the Cretaceous/Tertiary Extinction Bolide with the atmosphere, ocean, and solid Earth*. 1982b. doi: 10.1130/SPE190.

S. Okuzumi and C. W. Ormel. The Fate of Planetesimals in Turbulent Disks with Dead Zones. I. The Turbulent Stirring Recipe. *Astrophys. J.*, 771:43, July 2013. doi: 10.1088/0004-637X/771/1/43.

S. Okuzumi, H. Tanaka, H. Kobayashi, and K. Wada. Rapid Coagulation of Porous Dust Aggregates outside the Snow Line: A Pathway to Successful Icy Planetesimal Formation. *Astrophys. J.*, 752:106, June 2012. doi: 10.1088/0004-637X/752/2/106.

C. W. Ormel and J. N. Cuzzi. Closed-form expressions for particle relative velocities induced by turbulence. *Astron. Astrophys.*, 466:413–420, May 2007. doi: 10.1051/0004-6361:20066899.

C. W. Ormel and S. Okuzumi. The Fate of Planetesimals in Turbulent Disks with Dead Zones. II. Limits on the Viability of Runaway Accretion. *Astrophys. J.*, 771:44, July 2013. doi: 10.1088/0004-637X/771/1/44.

S. J. Ostro, R. Scott, Hudson, M. C. Nolan, J.-L. Margot, D. J. Scheeres, D. B. Campbell, C. Magri, J. D. Giorgini, and D. K. Yeomans. Radar observations of asteroid 216 kleopatra. *Science*, 288(5467):836–839, 2000. doi: 10.1126/science.288.5467.836.

J.-M. Petit, A. Morbidelli, and J. Chambers. The Primordial Excitation and Clearing of the Asteroid Belt. *Icarus*, 153:338–347, October 2001. doi: 10.1006/icar.2001.6702.

C. Pinte, W. R. F. Dent, F. Ménard, A. Hales, T. Hill, P. Cortes, and I. de Gregorio-Monsalvo. Dust and Gas in the Disk of HL Tauri: Surface Density, Dust Settling, and Dust-to-gas Ratio. *Astrophys. J.*, 816:25, January 2016. doi: 10.3847/0004-637X/816/1/25.

R. W. Potter, J. W. Head, D. Guo, J. Liu, and L. Xiao. The apollo peak-ring impact basin: Insights into the structure and evolution of the south poleaitken basin. *Icarus*, 306:139 – 149, 2018. doi: https://doi.org/10.1016/j.icarus.2018.02.007.

P. Pravec, A. W. Harris, and T. Michalowski. *Asteroid Rotations*, pages 113–122. 2002.

P. W. Randles and L. D. Libersky. Smoothed particle hydrodynamics: Some recent improvements and applications. *Comput. Methods Appl. Mech. Engrg.*, 139(1):375 – 408, 1996. doi: https://doi.org/10.1016/S0045-7825(96)01090-0.

S. N. Raymond, P. J. Armitage, A. Moro-Martín, M. Booth, M. C. Wyatt, J. C. Armstrong, A. M. Mandell, F. Selsis, and A. A. West. Debris disks as signposts of terrestrial planet formation. *Astron. Astrophys.*, 530:A62, June 2011. doi: 10.1051/0004-6361/201116456.

S. N. Raymond, P. J. Armitage, D. Veras, E. V. Quintana, and T. Barclay. Implications of the interstellar object 1I/'Oumuamua for planetary dynamics and planetesimal formation. *Mon. Not. R. Astron. Soc.*, 476:3031–3038, May 2018. doi: 10.1093/mnras/sty468.

D. C. Richardson, T. Quinn, J. Stadel, and G. Lake. Direct Large-Scale N-Body Simulations of Planetesimal Dynamics. *Icarus*, 143:45–59, January 2000. doi: 10.1006/icar.1999.6243.

D. C. Richardson, Z. M. Leinhardt, H. J. Melosh, W. F. Bottke, Jr., and E. Asphaug. *Gravitational Aggregates: Evidence and Evolution*, pages 501–515. March 2002.

D. C. Richardson, P. Elankumaran, and R. E. Sanderson. Numerical experiments with rubble piles: equilibrium shapes and spins. *Icarus*, 173:349–361, February 2005. doi: 10.1016/j.icarus.2004.09.007.

D. P. Rubincam. Radiative Spin-up and Spin-down of Small Asteroids. *Icarus*, 148:2–11, November 2000. doi: 10.1006/icar.2000.6485.

V. S. Safronov. *Evoliutsiia doplanetnogo oblaka.* 1969.

I. Satō, L. Šarounová, and H. Fukushima. Size and Shape of Trojan Asteroid Diomedes from Its Occultation and Photometry. *Icarus*, 145:25–32, May 2000. doi: 10.1006/icar.1999.6316.

S. R. Schwartz, P. Michel, M. Jutzi, S. Marchi, Y. Zhang, and D. C. Richardson. Catastrophic disruptions as the origin of bilobate comets. *Nature Astron.*, 2:379–382, May 2018. doi: 10.1038/s41550-018-0395-2.

L. D. G. Sigalotti and H. López. Adaptive kernel estimation and sph tensile instability. *Comput. Math. Appl*, 55(1):23 – 50, 2008. doi: https://doi.org/10.1016/j.camwa.2007.03.007.

F. Spoto, A. Milani, and Z. Kneževiá. Asteroid family ages. *Icarus*, 257:275 – 289, 2015. doi: https://doi.org/10.1016/j.icarus.2015.04.041.

D. J. Stevenson. Formation of the giant planets. *P & SS*, 30:755–764, August 1982. doi: 10.1016/0032-0633(82)90108-8.

K. Sugiura and S. Inutsuka. An extension of Godunov SPH: Application to negative pressure media. *J. Comput. Phys.*, 308:171–197, March 2016. doi: 10.1016/j.jcp.2015.12.030.

K. Sugiura and S. Inutsuka. An extension of Godunov SPH II: Application to elastic dynamics. *J. Comput. Phys.*, 333:78–103, March 2017. doi: 10.1016/j.jcp.2016.12.026.

K. Sugiura, H. Kobayashi, and S. Inutsuka. Toward understanding the origin of asteroid geometries. Variety in shapes produced by equal-mass impacts. *Astron. Astrophys.*, 620:A167, 2018a. doi: https://doi.org/10.1051/0004-6361/201833227.

K. Sugiura, H. Kobayashi, and S. Inutsuka. Collisional Elongation: Possible Origin of Extremely Elongated Shape of 1I/′Oumuamua. *submitted to Icarus*, 2018b.

T. Suyama, K. Wada, and H. Tanaka. Numerical Simulation of Density Evolution of Dust Aggregates in Protoplanetary Disks. I. Head-on Collisions. *Astrophys. J.*, 684:1310–1322, September 2008. doi: 10.1086/590143.

J. W. Swegle, D. L. Hicks, and S. W. Attaway. Smoothed Particle Hydrodynamics Stability Analysis. *J. Comput. Phys.*, 116:123–134, January 1995. doi: 10.1006/jcph.1995.1010.

S. Z. Takahashi and S.-i. Inutsuka. Two-component Secular Gravitational Instability in a Protoplanetary Disk: A Possible Mechanism for Creating Ring-like Structures. *Astrophys. J.*, 794:55, October 2014. doi: 10.1088/0004-637X/794/1/55.

S. Z. Takahashi and S.-i. Inutsuka. An Origin of Multiple Ring Structure and Hidden Planets in HL Tau: A Unified Picture by Secular Gravitational Instability. *Astron. J.*, 152:184, December 2016. doi: 10.3847/0004-6256/152/6/184.

J. H. Tillotson. Metallic equations of state for hypervelocity impact. *General Atomic Rept.*, GA-3216:1–142, 1962.

R. T. Tominaga, S.-i. Inutsuka, and S. Z. Takahashi. Non-linear development of secular gravitational instability in protoplanetary disks. *Publ. Astron. Soc. Japan*, 70:3, January 2018. doi: 10.1093/pasj/psx143.

T. Ueda, H. Kobayashi, T. Takeuchi, D. Ishihara, T. Kondo, and H. Kaneda. Size Dependence of Dust Distribution around the Earth Orbit. *Astron. J.*, 153:232, May 2017. doi: 10.3847/1538-3881/aa5ff3.

B. v. Leer. Towards the ultimate conservative difference scheme. v. a second-order sequel to godunov's method. *J. Comput. Phys.*, 32(1):101 – 136, 1979. doi: https://doi.org/10.1016/0021-9991(79)90145-1.

J. B. Walsh. The Effect of Cracks on the Compressibility of Rocks. *J. Geophys. Res.*, 70: 381–389, January 1965. doi: 10.1029/JZ070i002p00381.

K. J. Walsh and D. C. Richardson. Binary near-earth asteroid formation: Rubble pile model of tidal disruptions. *Icarus*, 180(1):201 – 216, 2006. doi: https://doi.org/10.1016/j.icarus.2005.08.015.

K. J. Walsh, D. C. Richardson, and P. Michel. Rotational breakup as the origin of small binary asteroids. *Nature*, 454:188–191, July 2008. doi: 10.1038/nature07078.

K. J. Walsh, A. Morbidelli, S. N. Raymond, D. P. O'Brien, and A. M. Mandell. A low mass for Mars from Jupiter's early gas-driven migration. *Nature*, 475:206–209, July 2011. doi: 10.1038/nature10201.

W. A. Weibull. A statistical theory of the strength of materials (transl.). *Ingvetenks. Akad. Handl. (Stockholm)*, 151:5–45, 1939.

S. J. Weidenschilling. Aerodynamics of solid bodies in the solar nebula. *Mon. Not. R. Astron. Soc.*, 180:57–70, July 1977. doi: 10.1093/mnras/180.1.57.

S. J. Weidenschilling, D. Spaute, D. R. Davis, F. Marzari, and K. Ohtsuki. Accretional Evolution of a Planetesimal Swarm. *Icarus*, 128:429–455, August 1997. doi: 10.1006/icar.1997.5747.

G. W. Wetherill. Occurrence of giant impacts during the growth of the terrestrial planets. *Science*, 228:877–879, May 1985. doi: 10.1126/science.228.4701.877.

G. W. Wetherill and G. R. Stewart. Accumulation of a swarm of small planetesimals. *Icarus*, 77:330–357, February 1989. doi: 10.1016/0019-1035(89)90093-6.

F. L. Whipple. On certain aerodynamic processes for asteroids and comets. In A. Elvius, editor, *From Plasma to Planet*, page 211, 1972.

D. P. Whitmire, J. J. Matese, L. Criswell, and S. Mikkola. Habitable Planet Formation in Binary Star Systems. *Icarus*, 132:196–203, March 1998. doi: 10.1006/icar.1998.5900.

Q.-Z. Ye, Q. Zhang, M. S. P. Kelley, and P. G. Brown. 1I/2017 U1 (‘ Oumuamua) is hot: Imaging, spectroscopy, and search of meteor activity. *Astrophys. J.*, 851(1):L5, 2017.

V. Zappalá, P. Bendjoya, A. Cellino, P. Farinella, and C. Froeschlé. Asteroid families: Search of a 12,487-asteroid sample using two different clustering techniques. *Icarus*, 116(2):291 – 314, 1995. doi: https://doi.org/10.1006/icar.1995.1127.